

HEAT TRANSFER DISTRIBUTION OF IMPINGING METHANE-AIR PREMIXED FLAME JETS

Thesis

Submitted in partial fulfillment of the requirement for the degree of

DOCTOR OF PHILOSOPHY

by

KADAM ANIL RAMKISHANRAO

Reg. No. 148052ME14F17



DEPARTMENT OF MECHANICAL ENGINEERING
NATIONAL INSTITUTE OF TECHNOLOGY KARNATAKA
SURATHKAL, MANGALORE – 575025

JULY 2019

HEAT TRANSFER DISTRIBUTION OF IMPINGING METHANE-AIR PREMIXED FLAME JETS

Thesis

Submitted in partial fulfillment of the requirement for the degree of

DOCTOR OF PHILOSOPHY

by

KADAM ANIL RAMKISHANRAO

Under the Guidance of

Dr. KUMAR G N

Associate Professor



DEPARTMENT OF MECHANICAL ENGINEERING
NATIONAL INSTITUTE OF TECHNOLOGY KARNATAKA
SURATHKAL, MANGALORE – 575025

JULY 2019

DECLARATION

I hereby *declare* that the Research Thesis entitled “**HEAT TRANSFER DISTRIBUTION OF IMPINGING METHANE-AIR PREMIXED FLAME JETS**” which is being submitted to the **National Institute of Technology Karnataka, Surathkal** in partial fulfillment of the requirements for the award of the Degree of **Doctor of Philosophy in Mechanical Engineering** is a *bonafide report of the research work carried out by me*. The material contained in this Research Thesis has not been submitted to any University or Institution for the award of any degree.

Register Number: **148052ME14F17**

Name of the Research Scholar: **KADAM ANIL RAMKISHANRAO**

Signature of the Research Scholar:

Department of Mechanical Engineering

Place: NITK, Surathkal

Date: 08/07/2019

C E R T I F I C A T E

This is to *certify* that the Research Thesis entitled “**HEAT TRANSFER DISTRIBUTION OF IMPINGING METHANE-AIR PREMIXED FLAME JETS**” submitted by **KADAM ANIL RAMKISHANRAO** (**Register Number: 148052ME14F17**) as the record of the research work carried out by him, is *accepted as the Research Thesis submission* in partial fulfillment of the requirements for the award of degree of Doctor of Philosophy.

R e s e a r c h G u i d e

Dr. KUMAR G N

Associate Professor

Department of Mechanical Engineering

National Institute of Technology Karnataka, Surathkal

Chairman-DRPC

Department of Mechanical Engineering

National Institute of Technology Karnataka, Surathkal

Date:

DEDICATED TO
MY BELOVED
FAMILY MEMBERS

ACKNOWLEDGEMENT

This thesis becomes a reality with the kind support and help of many individuals. I would like to thank all of them at this moment.

It is a great pleasure for me to express my deep sense of gratitude to my supervisors **Dr. Vijaykumar Hindasageri and Dr. Kumar G N**, for their excellent inspiring guidance, valuable suggestions and encouragement rendered throughout the course of my thesis work. I am thankful to Professor **Dr. Shrikantha S. Rao**, Professor and Head, Department of Mechanical Engineering, for support and providing facilities required for the successful completion of this research work. I take this opportunity to acknowledge the former HODs, Mechanical engineering, **Dr. T P Ashok babu, Dr. Gangadharan K.V. and Dr. Narendranath S.**, for their support and encouragement. I wish to thank my RPAC members **Dr. N. Gnanasekaran and Dr. Shashi Bhushan Arya** for their valuable suggestions during my project assessment meet.

My deepest gratitude to **Prof. S. V. Prabhu, IIT Mumbai** for his valuable guidance and words of advice.

I am extremely grateful to **Lieutenant commander Ritesh Kumar Parida and Chetankumar** for helping me to establish the experimental setup at Navy base, Ezimala, Kerala.

I acknowledge my parents, **Kadam Ramkishanrao Munjaji and Kadam Shobha Ramkishanrao** for their inspiration and support throughout my studies. Words cannot explain my gratitude to my wife **Kalpna (Rani)** and son **Aaryan** for supporting me and making my stay pleasant always. I am grateful to my brother **Sunil**, sisters **Rekha and Smita**, my sister- in - law **Archana** and my brother-in-laws **Vijay Tate and Chandrakant Pawar** for always encouraging and believing in me. I extend my sincere thanks to my **in-laws** and entire **Jadhav family** for their kind support. I am very thankful to my owner **Mr. Suresh Devadiga**, his wife **Hemavathi** and daughters (**Seema and Sushma**) for taking care of my family.

My special thanks to my friends **Madagonda Biradar, Vasishta, Shashikumar C M, Dr. Venkatesh Lamani, Dr. Harshakumar, Dr. Avdhoot, Dr. Vignesh, Dr.**

Shivaprasad K V, Thippeswamy, Kotresha, Vishweshwara, Narendran, Nuthanprasad, Prakash Jadhav, Deepak Kolke, Jagadish, Vasu, Rudramoorthy, Raouf Tajik, Libin, Santhosh, Jayashish Pandey, Abhishek Patil, Sanjay, Praveen T. R., Shankar Kodate, Kalinga, Santhosh Chavan, Abdul Buradi, Tabish Wahidhi, Shrijith, Jeena Joseph, Vishwas, Balu Patil, Amit, Ajinkya, Kartheek, Achyutha and list seems to be endless.

I am extremely thankful to the department of Mechanical Engineering, NITK, Faculty and non- teaching staff for providing all the facilities to carry out my research work.

I acknowledge with gratitude to all others who have helped directly or indirectly in completing my thesis successfully.

Finally, I am greatly indebted to almighty for giving me this opportunity.

Kadam Anil Ramkishanrao

ABSTRACT

Flame jets find importance in industrial and household applications like metal and glass melting/forming and cook stoves respectively. Heat transfer distribution of impinging flame jet was compared with that of the impinging air jet based on the experimental data reported in literature for methane-air flame jet and air jet impingement for Reynolds number, $Re = 600$ to 1400 and the non-dimensional nozzle tip to impingement plate distance, $Z/d = 2$ to 6 . The comparative data based on mapping experimental data reported in literature suggested that there is a good agreement between the Nusselt numbers for higher Z/d near stagnation region. However, away from the stagnation region, the Nusselt number for flame jet is higher than that of air jet for similar operating conditions of Re and Z/d . A CFD simulation for impinging air jet and impinging flame jet was carried out using FLUENT software to explain the physics and reason for the deviations observed in experimental data. A scale analysis was carried out to identify the dominant forces and their influence on the heat transfer distribution on the impingement plate.

Heat transfer from impinging flame jets to a flat plate has been assumed to be one-dimensional in most of the investigations and without radiation loss treatment. In the present work, the exact nature of diffusion of heat in the plate is investigated via solution to multidimensional heat conduction problem. Two procedures have been employed – Duhamel theorem and three dimensional transient analytical inverse heat conduction problem (IHCP). The Duhamel theorem which is analytical model for transient one dimensional heat conduction was applied and its application failed the check of linearity requirement of the convection rate equation. From the solution by analytical IHCP for transient three dimensional heat conduction, the distribution of wall heat flux and the wall temperature was perfectly linear. This check confirmed that three dimensional approach has to be used. Experimental data is then analyzed by the three dimensional analytical IHCP for short and larger time intervals. It was found that for short time data, heat transfer coefficient and the reference temperature have oscillatory distribution along the radial direction on the impingement plate and for larger time data the oscillations die out. However, at larger time, radiation loss from the impingement plate becomes significant. The effect of variation in thermal conductivity of the impingement plate with the temperature on heat transfer coefficient and reference temperature is discussed. A

novel method was developed to correct the heat transfer coefficient and reference temperature to incorporate radiation losses. The deviation in heat transfer coefficient and reference temperature estimated without considering variable thermal conductivity and radiation loss for large time interval was upto 50%.

The scope of the present technique is examined through its application to impinging jets with various configurations. The present study covers the applications of hot jet, cold jet and multiple jets with distinct Reynolds numbers and the nozzle-to-plate spacing and results confirms the validity of technique to impinging jets as well. Effect of plate thickness on the accuracy of the present technique is also studied. Upto 5 mm thick plates can be used in impinging jet applications without compromising much on accuracy. Use of present technique significantly reduces the experimental cost and time since it works on transient data of just few seconds

Experiments were carried out on ribbed plates with three different geometrical shaped rib elements i.e. circular, rectangular and triangular. In addition, numerical simulations were performed to study flow field on and around ribs. During the experiments, Reynolds numbers varied from 600 to 1800 and burner tip to target plate distance from 2 to 4. Heat transfer coefficients were found lower whereas reference temperatures were observed higher on ribbed surfaces than smooth surfaces. Obstruction to the flow, flow separation and decrease in momentum are the reasons attributed for lower heat transfer rate to the ribbed surfaces.

Keywords: Flame jet, air jet, IHCP, ribs, CFD, heat transfer coefficient, reference temperature

TABLE OF CONTENTS

TABLE OF CONTENTS	i
LIST OF TABLES	v
LIST OF FIGURES	vi
NOMENCLATURE	xiii
1 INTRODUCTION	1
1.1 Introduction.....	1
1.2 Characteristic Regions In Impinging Flame Jet.....	1
1.3 Modes of heat transfer in impinging flame jet.....	3
1.3.1 Convection	4
1.3.2 Conduction.....	4
1.3.3 Radiation	4
1.3.4 Thermochemical heat release (TCHR or chemical recombination or simply recombination)	5
1.3.5 Boiling and Condensation.....	6
1.4 Applications	6
1.5 Organization of thesis	8
2 LITERATURE SURVEY	9
2.1 Introduction.....	9
2.2 Typical experimental test rig used in flame impingement study	9
2.3 Parameters affecting heat transfer characteristics of the flame	10
2.3.1 Effect of the configuration of impinging flame jets.....	10
2.3.2 Effect of Oxidizer and fuel	10
2.3.3 Effect of Nozzle-plate spacing (H/d)	13
2.3.4 Effect of Reynolds number (Re)	14
2.3.5 Effect of Equivalence Ratio (ϕ)	15
2.3.6 Effect of Firing Rate	17
2.3.7 Effect of TCHR.....	17

2.3.8	Effect of Burner geometry	18
2.3.9	Effect of type of flame	21
2.3.10	Effect of Mixture temperature	22
2.3.11	Effect of Multiple jets.....	23
2.3.12	Effect of Type of jet	24
2.3.13	Effect of Surface characteristics of the impinging plate	26
2.4	Measurement Techniques in flame jet impingement	27
2.4.1	Total heat flux measurement (Baukal 2000).....	27
2.4.2	Temperature measurement (Baukal 2000).....	30
2.4.3	Gas velocity (Baukal 2000)	34
2.4.4	Static pressure measurement (Baukal 2000).....	36
2.4.5	The composition of gas species measurement (Baukal 2000)	36
2.5	Evaluation of isothermal jets in relevance with flame jets	36
2.5.1	Analysis of the experimental data reported in the literature	37
2.6	Numerical studies in flame jet impingement	43
2.7	Inverse investigations in the field of jet impingement.....	44
2.8	The literature on ribbed surfaces.....	46
2.9	Summary of the Literature review	48
2.10	Motive and Scope for the present work	49
2.10.1	Simultaneous estimation of heat convection coefficient (h) and reference Temperature (T_{ref})	51
2.11	Objectives of the present investigation	52
2.12	Closure	52
3	EXPERIMENTAL AND NUMERICAL METHODOLOGY	53
3.1	Introduction.....	53
3.2	Experimental set-up	53
3.3	Data reduction:.....	56
3.4	Numerical methodology.....	58
3.4.1	CFD simulation for flame jet impingement	58
3.4.2	CFD simulation for air jet impingement.....	61
3.4.3	CFD simulation for heat diffusion by conduction	64

3.5	Closure	64
4	ANALYTICAL SOLUTIONS TO HEAT CONDUCTION PROBLEM	65
4.1	Introduction.....	65
4.2	Formulation of the heat conduction problem.....	65
4.3	Solution methodologies to one dimensional (1-D) heat conduction problem	67
4.3.1	Convection boundary condition on flame side	67
4.3.2	Time dependent temperature boundary condition on flame side.....	68
4.4	Solution methodology to three dimensional (3-D) heat conduction problem	69
4.4.1	Solution by inverse approach.....	70
4.5	Closure	77
5	RESULTS AND DISCUSSION	79
5.1	Introduction.....	79
5.2	Heat transfer distribution of impinging flame and air jets – A comparative study.....	79
5.2.1	Validation of CFD simulation for Flame jet impingement.....	80
5.2.2	Comparison through numerical analysis.....	81
5.2.3	Comparison through Scale analysis	91
5.3	Simultaneous estimation of heat transfer coefficient and reference temperature from impinging flame jets.....	94
5.3.1	Validation of experimental set-up.....	94
5.3.2	Validation of Analytical methods	96
5.3.3	Verification of 1-D approximation	100
5.3.4	Transient front surface temperature and heat flux estimation	100
5.3.5	Heat transfer coefficient and reference temperature for real time experimental data	108
5.3.6	Radiation loss correction procedure.....	112
5.3.7	Effect of variable thermal conductivity and radiation correction	115
5.4	Heat transfer from impinging jets	118
5.4.1	Validation of numerical procedure	118

5.4.2	Linearity check between heat flux and wall temperature for simulation data.....	120
5.4.3	Heat transfer characteristics of impinging jets.....	120
5.4.4	Effect of Thickness on 3-D IHCP solution.....	124
5.5	Heat transfer distribution of premixed methane-air laminar flame jets impinging on ribbed surfaces.....	128
5.5.1	Experimental procedure.....	129
5.5.2	Data Smoothing.....	133
5.5.3	Heat transfer coefficient and Reference temperature at Re 1000 and $Z/d=3$	133
5.5.4	Heat transfer coefficient and Reference temperature at Re 1400 and $Z/d=4$	136
5.5.5	Heat transfer coefficient and Reference temperature for Rectangular ribbed plate at various Reynolds number and Z/d	139
5.5.6	CFD Simulation results.....	143
6	CONCLUSIONS AND SCOPE FOR FUTURE WORK.....	147
6.1	Conclusions.....	147
6.2	Key contributions of the present work.....	148
6.3	Scope for future work.....	149
	APPENDIX A.....	151
	APPENDIX B.....	159
	APPENDIX C.....	168
	REFERENCES.....	170

LIST OF TABLES

Table 2.1 Applications of different configurations of flame impinging jets	12
Table 2.2 Effect of preheating on adiabatic flame temperature (Tajik et al. 2015).....	22
Table 2.3 Summary of techniques used for total heat flux measurement	32
Table 3.1 Specifications of flowmeters	53
Table 3.2 Specifications of Thermal camera	56
Table 4.1 Possible Boundary conditions in flame jet impingement	66
Table 4.2 Boundary conditions assumed in Feng et al. (2011).....	70
Table 4.3 Reformed Boundary conditions for non-dimensionalized equation	72
Table 5.1 Magnitude of different forces (N/m^3) involved in flame jets and air jets....	93
Table 5.2 Mechanical and thermal properties of SS 316 material.....	133

LIST OF FIGURES

Figure 1.1 a) Characteristic regions in impinging flame jet b) Flow zones of the free jet region	2
Figure 1.2 Modes of heat transfer in impinging jet	3
Figure 1.3 Applications of impinging flame jets	7
Figure 2.1 General flame impingement experimental set up.....	9
Figure 2.2 Parameters affecting heat transfer characteristics of the flame	11
Figure 2.3 Influence of Nozzle-plate spacing (H/d); (a) Heat flux and (b) surface temperature for methane/air premixed flame at $Re = 1400$, $\phi = 1.0$ and tube diameter = 10 mm (Chander and Ray, 2006)	13
Figure 2.4 Cause and effect diagram for higher H/d	14
Figure 2.5 Influence of Reynolds Number (Re); (a) Heat flux and (b) surface temperature for methane/air premixed flame at $H/d = 4$, $\phi = 1.0$ and tube diameter = 10 mm (Chander and Ray, 2006)	15
Figure 2.6 Influence of equivalence ratios (ϕ); (a) Heat flux and (b) surface temperature for methane/air premixed flame at $Re = 1400$, $H/d = 4$ and tube diameter = 10 mm. (Chander and Ray, 2006)	16
Figure 2.7 Influence of equivalence ratios on impinging methane/air flame shapes for $Re = 1400$, $H/d = 4$ and at various; (a) $\phi = 0.8$ (b) $\phi = 0.9$ (c) $\phi = 1.0$ (d) $\phi = 1.1$ (e) $\phi = 1.2$ and (f) $\phi = 1.5$ (Chander and Ray 2006)	16
Figure 2.8 TCHR factor as a function of surface temperature for various mixtures (Cremers et al., 2010)	18
Figure 2.9 Influence of burner geometry on exit velocity profiles at $Re = 600$ and diameter = 10 mm (Chander and Ray, 2006).....	19
Figure 2.10 Influence of burner geometry; (a) heat flux and (b) surface temperature for $Re = 1000$, $H/d = 6$, $\phi = 1.0$ and 10 mm diameter (Chander and Ray 2006).....	20

Figure 2.11 Influence of burner geometry; (a) heat flux and (b) surface temperature for Re = 1000, H/d = 3, $\phi = 1.0$ and 10 mm diameter (Chander and Ray 2006).....	20
Figure 2.12 Influence of burner geometry; (a) heat flux and (b) surface temperature for Re = 1000, H/d = 2, $\phi = 1.0$ and 10 mm diameter (Chander and Ray 2006).....	20
Figure 2.13 Different types of flame (Baukal 2000).....	21
Figure 2.14 Cause and effect diagram for preheating the mixture	22
Figure 2.15 Influence of mixture temperature on flame cone length for different Reynolds number at $\phi = 1$ (Tajik et al., 2015)	23
Figure 2.16 Heat transfer distribution for a single circular premixed flame jet with induced swirl and twin flame jets without swirl at $\phi = 1$, Re = 1200 and H/d = 2 (Huang et al., 2006)	25
Figure 2.17 Measurement techniques for Impinging Flame Jets	28
Figure 2.18 Heat flux measurement using a calorimeter	29
Figure 2.19 Heat flux measurement using heat flux sensor.....	30
Figure 2.20 Comparison of Nusselt number distribution of impinging air jets with impinging flame jets for varying Re at Z/d = 2	39
Figure 2.21 Comparison of Nusselt number distribution of impinging air jets with impinging flame jets for varying Re at Z/d = 4	40
Figure 2.22 Comparison of Nusselt number distribution of impinging air jets with impinging flame jets for varying Re at Z/d = 6	41
Figure 2.23 Comparison of Nusselt number and Effectiveness distribution of impinging air jets with impinging flame jets at various configuration (Kuntikana and Prabhu, 2016))	42
Figure 2.24 Normally impinging circular jet; d=13.4 mm; Z/d = 1.5 a) Nu distribution Time-averaged b) Nu Time-trace (O'Donovan, 2005)	50
Figure 3.1 Schematic of experimental Set-up.....	54

Figure 3.2 Experimental laboratory set-up	55
Figure 3.3 Physical model with boundary conditions.....	58
Figure 3.4 Adaptive mesh near the wall	59
Figure 3.5 Boundary layer mesh near the wall	61
Figure 4.1 Schematic diagram of the three dimensional plate impinged by a flame jet.....	65
Figure 4.2 Plate with convection boundary condition	68
Figure 4.3 Plate with time dependent temperature boundary condition	68
Figure 4.4 Geometry considered in Feng et al. (2011)	70
Figure 5.1 Comparison of Numerical results with Experimental results.....	80
Figure 5.2 Comparison of velocity vectors of impinging air jets with impinging flame jets from the tip of burner to the impingement plate for $Re = 600$ and $Z/d =$ 2 ; a) along the tube axis, b) normal to the tube axis	82
Figure 5.3 Comparison of velocity vector of impinging air jets with impinging flame jets from the tip of burner to the impingement plate for $Re = 1000$ and Z/d $= 2$; a) along the tube axis, b) normal to the tube axis.....	83
Figure 5.4 Comparison of velocity vector of impinging air jets with impinging flame jets from the tip of burner to the impingement plate for $Re = 1400$ and Z/d $= 2$; a) along the tube axis, b) normal to the tube axis.....	84
Figure 5.5 Comparison of velocity vector of impinging air jets with impinging flame jets from the tip of burner to the impingement plate for $Re = 600$ and $Z/d =$ 4 ; a) along the tube axis, b) normal to the tube axis	85
Figure 5.6 Comparison of velocity vector of impinging air jets with impinging flame jets from the tip of burner to the impingement plate for $Re = 1000$ and Z/d $= 4$; a) along the tube axis, b) normal to the tube axis.....	86
Figure 5.7 Comparison of velocity vector of impinging air jets with impinging flame jets from the tip of burner to the impingement plate for $Re = 1400$ and Z/d $= 4$; a) along the tube axis, b) normal to the tube axis.....	87

Figure 5.8 Comparison of velocity vector of impinging air jets with impinging flame jets from the tip of burner to the impingement plate for $Re = 600$ and $Z/d = 6$; a) along the tube axis, b) normal to the tube axis	88
Figure 5.9 Comparison of velocity vector of impinging air jets with impinging flame jets from the tip of burner to the impingement plate for $Re = 1000$ and $Z/d = 6$; a) along the tube axis, b) normal to the tube axis.....	89
Figure 5.10 Comparison of velocity vector of impinging air jets with impinging flame jets from the tip of burner to the impingement plate for $Re = 1400$ and $Z/d = 6$; a) along the tube axis, b) normal to the tube axis	90
Figure 5.11 Comparison of Laminar burning velocity with published data	94
Figure 5.12 Comparison of critical velocity gradient parameter with that of Hindasageri et al. (2012).....	95
Figure 5.13 Comparison of the analytically estimated heat transfer coefficient with reported experimental values at $Z/d = 4$	96
Figure 5.14 a) Linear fit approximation to transient temperature data at stagnation point b) Comparison of Duhamel results with Remie et al. (2008) for $Re = 1334$ at $Z/d = 4$ for transient heat flux data	97
Figure 5.15 Front surface temperature (a) Simulation result (b) Calculated by IHCP code (c) Percentage of deviation	98
Figure 5.16 Front surface heat flux (a) Simulation result (b) Calculated by IHCP code (c) Percentage of deviation.....	99
Figure 5.17 Heat flux vs. corresponding impingement side wall temperature a) at $r/d = 0$ and b) at $r/d = 3$ for the experimental data.....	100
Figure 5.18 Matching of (a) front temperature (b) heat flux computed by 3-D IHCP solution with simulation results. The direction of arrow indicates the increasing value of t from 0.5 to 5 sec in steps of 0.5.	101
Figure 5.19 Comparison of heat flux in case of hot laminar jet impingement.	103

Figure 5.20 Comparison of (a) front surface temperature (b) wall heat flux in case of cold laminar jet impingement. The direction of arrow indicates the increasing value of t from 0.5 to 5 sec in steps of 0.5 sec.....	103
Figure 5.21 Comparison of (a) front surface temperature (b) wall heat flux in case of heating application of a turbulent jet. The direction of arrow indicates the increasing value of t from 1 to 8 sec in steps of 1 sec.....	104
Figure 5.22 Comparison of (a) front surface temperature (b) wall heat flux in case of cooling application of a turbulent jet. The direction of arrow indicates the increasing value of t from 1 to 8 sec in steps of 1 sec.....	105
Figure 5.23 Comparison of (a) front surface temperature, (b) heat flux computed from 3-D IHCP solution (c) heat flux computed from 3-D IHCP + Duhamel for $Re = 1000, Z/d=4$	106
Figure 5.24 Temperature gradient from impingement (front) surface for $Re = 1000, Z/d=4$	107
Figure 5.25 Comparison of heat flux computed from two point scheme for $Re = 1000, Z/d=4$	108
Figure 5.26 Experimental (a) Surface temperature (b) Flux by two point scheme c) Flux vs Wall temperature at $r/d = 0$ and 3 for 2 to 10 sec data d) Estimated heat transfer coeff e) Estimated reference temp (Mixture conditions $\phi=1, 2$ bar, 300K).....	110
Figure 5.27 Heat transfer contour maps for square and rectangular tube flame jets .	111
Figure 5.28 a) Wall heat flux vs wall temperature with and without radiation loss b) Linearity in slope of quadratic fit	113
Figure 5.29 a) Extrapolation of flux b) Corrected wall temperature (T_w^*).....	114
Figure 5.30 a) Corrected heat transfer coefficient (h^*) b) Corrected reference temperature (T_{ref}^*)	114
Figure 5.31 Effect of radiation loss and variable thermal conductivity on h and Tref for the experimental data of $Re = 1000$ and 1600 and $Z/d = 4$	117

Figure 5.32 Comparison of numerically simulated (a) Front temperature and (b) wall heat flux data	118
Figure 5.33 Comparison of simulated Nusselt number with Guo et al. (2017).....	119
Figure 5.34 Linear fit at (a) $r/d=0$ (b) $r/d=1$ (c) $r/d=2$ (d) $r/d=3$ (e) $r/d=4$ (f) $r/d=5$	121
Figure 5.35 Comparison of estimated a) Heat transfer coefficient and b) Reference temperature with applied profile via UDF for hot jet	122
Figure 5.36 Comparison of estimated a) Front temperature with simulation data and b) heat convection coefficient with applied profile via UDF for cold jet. The direction of arrow indicates the increasing value of t from 0.5 to 5 sec in steps of 0.5 sec.....	123
Figure 5.37 Comparison of estimated a)Front temperature with simulated data and b)heat transfer coefficient with applied profile via UDF for multiple jet. The direction of arrow indicates the increasing value of t from 0.5 to 5 sec in steps of 0.5 sec.	124
Figure 5.38 Comparison of estimated a) front surface temperature with simulated data and b) Heat convection coefficient with applied profile via UDF for 3 mm plate. The direction of arrow indicates the increasing value of t from 1 to 10 sec in steps of 1 sec.	125
Figure 5.39 Comparison of estimated a)Front surface temperature with simulated data and b) heat convection coefficient with applied profile via UDF for 5 mm plate. The direction of arrow indicates the increasing value of t from 3 to 12 sec in steps of 1 sec.	126
Figure 5.40 Comparison of estimated a) Front surface temperature with simulated data and b) heat convection coefficient with applied profile via UDF for 7 mm plate. The direction of arrow indicates the increasing value of t from 5 to 14 sec in steps of 1 sec.	127
Figure 5.41 Comparison of estimated Front surface temperature with simulated data for 10 mm plate.	128

Figure 5.42 Schematic of the test plate	129
Figure 5.43 Schematic of ribbed plates considered in present investigation.....	131
Figure 5.44 Photographs of actual (manufactured) ribbed plates	132
Figure 5.45 Heat transfer coefficient and Reference temperature for various shaped ribbed surfaces at Re 1000 and $Z/d=3$	135
Figure 5.46 Heat flux at the impingement side for rectangular ribbed plate at Re 1000 and $Z/d=3$. The direction of arrow indicates the increasing value of time from 0.2 to 22.6 sec in steps of 2.8 sec.	136
Figure 5.47 Heat transfer coefficient and Reference temperature for various shaped ribbed surfaces at Re 1400 and $Z/d=4$	138
Figure 5.48 Heat transfer coefficient and Reference temperature for Rectangular ribbed plate at different Reynolds number and $Z/d=2$	140
Figure 5.49 Heat transfer coefficient and Reference temperature for Rectangular ribbed plate at different Reynolds number and $Z/d=3$	141
Figure 5.50 Heat transfer coefficient and Reference temperature for Rectangular ribbed plate at different Reynolds number and $Z/d=4$	143
Figure 5.51 Temperature contour for square ribbed plate at Re 1400, $Z/d=4$ and $\phi=1$	143
Figure 5.52 Streamlines in the stagnation and wall jet region at Re 1400 and $Z/d=4$	144

NOMENCLATURE

c_p	specific heat (kJ/kg.K)
d	burner diameter (m)
g	acceleration due to gravitation (m/s^2)
h	heat transfer coefficient (W/m^2K)
k	thermal conductivity ($W/m.K$)
k_{eff}	effective thermal conductivity ($W/m.K$)
L_f	flame cone height (m)
\dot{m}	mixture mass flow rate (kg/s)
\dot{m}_{fu}	fuel mass flow rate (kg/s)
M	molecular weight (kg/kmol)
Nu	Nusselt number
p	pressure (Pa)
Pr	Prandtl number
q''	heat flux(W/m^2K)
r, z	coordinate directions
Re	Reynolds number
S_u	burning velocity (m/s)
t	time (s)
T	temperature (K)
u	average mixture velocity (m/s)
u_e	average velocity at the burner exit (m/s)
V	velocity (m/s)
X	distance between the tip of the nozzle to impingement plate (m)
x, r	cylindrical coordinate axes
Y	mass fraction (.)
Z	location of the impingement plate from the burner tip (m)

Greek Symbols

α	thermal diffusivity (m ² /s)
β	constant
δ	boundary layer thickness (m)
Δp	gauge pressure on the reattachment surface (Pa)
ΔT	$T_{mix} - T_{\infty}$ (K)
ε	kinetic energy dissipation rate (m ² /s ³)
ϕ	equivalence ratio
λ	thermal conductivity (W/m.K)
η	Effectiveness
μ	laminar absolute viscosity (Pa-s)
μ_{eff}	effective viscosity (Pa-s)
μ_t	turbulent absolute viscosity (Pa-s)
ν	kinematic viscosity (m ² /s)
ω	angular velocity (rad/s)
ρ	density (kg/m ³)
σ_{ε}	turbulent Prandtl number for kinetic energy dissipation rate, ε
σ_k	turbulent Prandtl number for turbulent kinetic energy, k

Subscripts/ superscripts

adf	adiabatic flame
aw	adiabatic wall
C	chemical
d	diameter
D_H	hydraulic diameter (m)
f	flame
fu	fuel
e	edge of the boundary layer in uniform flow

<i>eff</i>	effective
<i>i</i>	i^{th} species
∞	ambient
<i>init</i>	initial
<i>j</i>	j^{th} species
<i>mix</i>	mixture
<i>o</i>	stagnation point
<i>ox</i>	oxidizer
<i>pr</i>	products
<i>ref</i>	reference
<i>s</i>	surface
<i>w</i>	wall

Abbreviations

CFD	computational fluid dynamics
GRI	gas research institute
IHCP	inverse heat conduction problem
TCHR	thermochemical heat release

Chapter 1

1 INTRODUCTION

1.1 INTRODUCTION

Impinging flame jets find importance in many industrial and household applications like metal and glass melting/forming and cook stoves respectively. They are preferred over the induction heating techniques due to their high convective heat transfer, improved product quality, rapid heating response, possibility to heat locally, smaller demand of the primary fuel and quick switching on and off period. Heat transfer distribution from an impinging flame jet is observed as bell shaped with maximum at the centerline of the jet and subsequently reduces in wall jet region. This bell shape brings the non-uniformity in the heat transfer distribution over the target plate.

1.2 CHARACTERISTIC REGIONS IN IMPINGING FLAME JET

Different characteristic regions of the impinging axisymmetric flame jet, the flame jet region, the free jet region, the stagnation flow region and the wall jet region on a flat plate are illustrated in Figure 1.1(a). In the flame jet region, unburnt gas from nozzle gets expanded due to reaction of gases in the flame front. In the next free jet region due to shear interaction between gas and surrounding fluid, there is an entrainment of surrounding fluid which results in increase in mass flow rate, decrease in jet temperature and non-uniform radial velocity. However, effect of impingement plate is not notable in this region (Van der Meer 1987). Free jet region can be divided into three zones as shown in Figure 1.1(b). First potential core zone where velocity of fluid remains the same and constant as that of nozzle exit velocity. Second is developing zone where due to shear action, there is decay of axial velocity profile. Third is fully developed zone where axial velocity profile is fully developed. Further stagnation region is characterized by pressure gradient due to which flow radially accelerates and axially decelerates. As heat transfer is maximum in this region, it is needed more attention and so extensively studied.

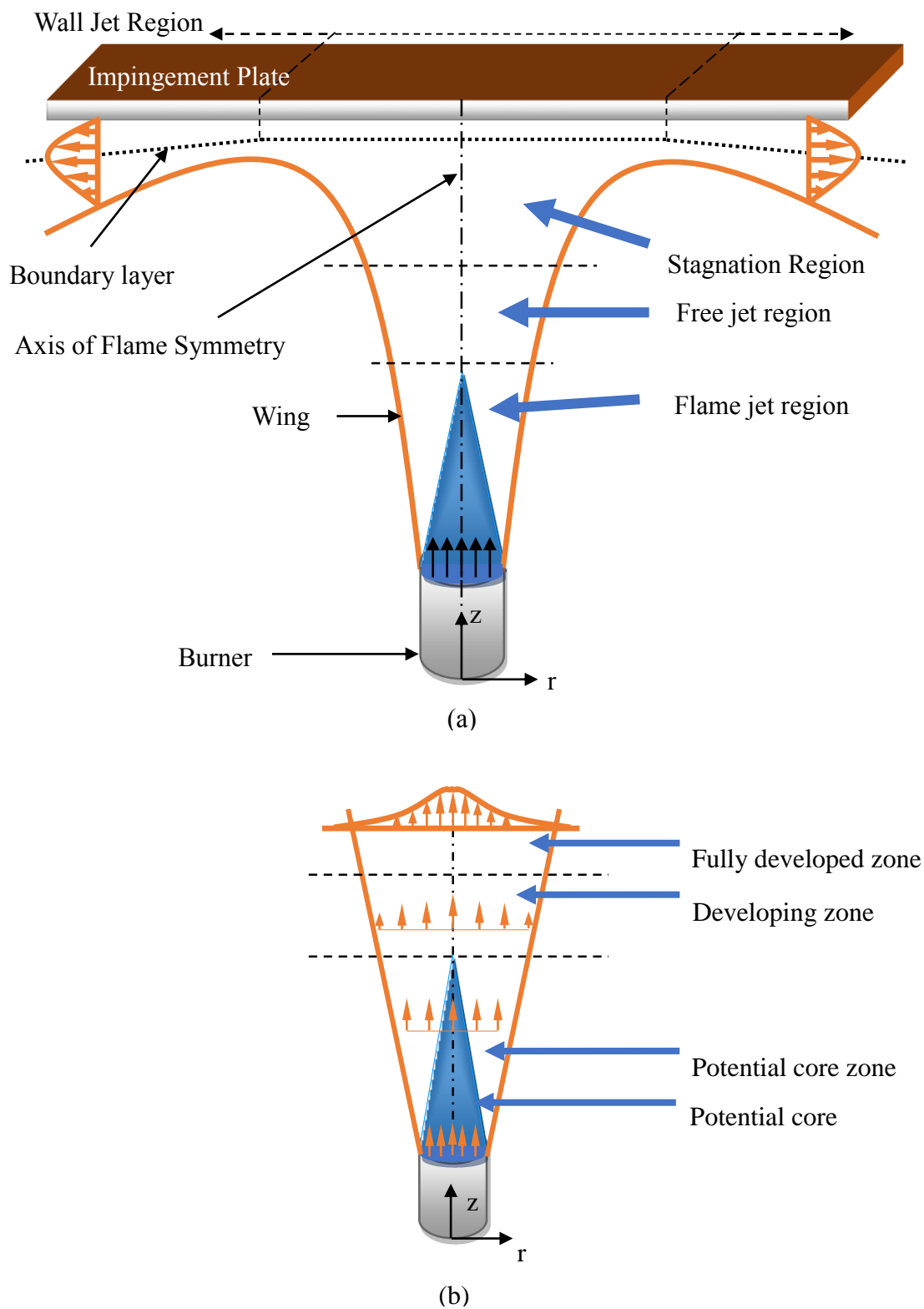


Figure 1.1 a) Characteristic regions in impinging flame jet b) Flow zones of the free jet region

This region is bounded by the flow where static pressure is more than distant ambient pressure and after that wall jet region starts. Here bulk flow radially flows along the surface in decelerating direction (Viskanta 1993). Flow behavior of impinging flame jets are very comparable with hot inert jets, thus flame jets are generally approximated by hot inert jets. The basic difference between these jets is the presence of a reaction zone in the stagnation region and viscous boundary layer in the flame jet.

1.3 MODES OF HEAT TRANSFER IN IMPINGING FLAME JET

Figure 1.2 depicts six heat transfer mechanisms that have been distinguished in previous flame impingement studies: convection (forced and natural), conduction (steady-state and transient), radiation (surface, luminous, and non-luminous), thermochemical heat release (TCHR) (equilibrium, catalytic, and mixed), water vapor condensation and boiling (internal and external). Contribution by each during impingement depends upon thermal and flow conditions. Detailed description of these modes can be found in Baukal (2000).

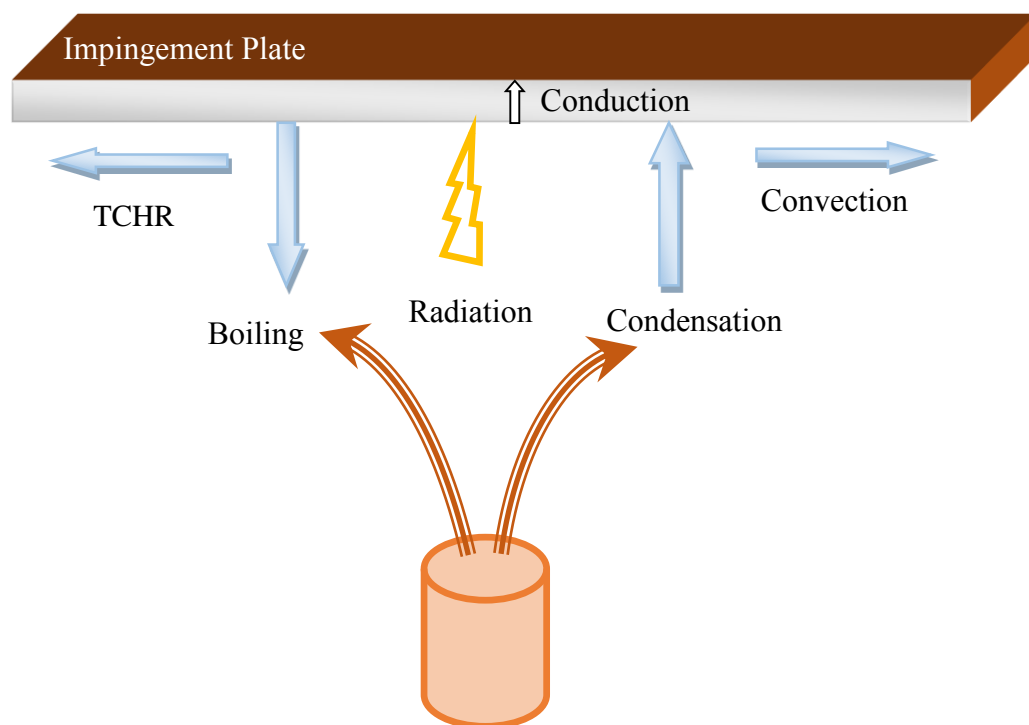


Figure 1.2 Modes of heat transfer in impinging jet

1.3.1 Convection

It is considered as a predominant mechanism when target placed in open space is at ambient condition and flame temperature is less than 1800 K since heat release by TCHR is negligible. Convective heat transfer is dependent on several factors like the aerodynamics of the jet, the turbulence intensity, burner tip to impingement surface spacing, geometry of the target, air fuel mixture, equivalence ratio, TCHR and whether the jet is a premixed or diffusion flame.

Many flame impingement studies are carried out for different geometries. Semi-analytical relations have been derived for the heat transfer at the stagnation point based on velocity gradient. From potential flow theory, the axial velocity decreases near the stagnation point and the radial velocity increases. Natural convection is significant mode of heat transfer for flame jets with low Reynolds number like buoyant diffusion flames.

1.3.2 Conduction

Conduction heat transfer is very important mode from heat flux calculation point of view. Several steady state techniques are used to estimate heat flux distribution at the impingement side. In case of steady state heat conduction, plate temperature is approximately constant as it is getting cooled from other side with the help of coolant in case of high thermal conductivity objects. Whereas, in case of transient heat conduction, target temperature changes non-linearly. Transient heat transfer distribution within the object helps in understanding the thermal stresses developed in the targets. In few studies, transient temperature distribution is also used to estimate heat flux distribution at the impingement side.

1.3.3 Radiation

The influence of radiation is considered if target is placed in isolation or in enclosure. In isolation, two components contribute to the thermal radiation heat transfer at the impingement plate: Nonluminous radiation and luminous radiation. Nonluminous radiation is generated due to carbon dioxide and water vapor produced by combustion

of gaseous fuel. Magnitude of radiation produced by the burnt gases depends on the gas temperature, the optical path length through the gas, partial pressures and concentration of each emitting species. Luminous radiation is a significant component of the radiation heat transfer where the amount of soot formation is high as in case of solid and liquid fuels. In case of gaseous fuel, this mechanism is considered important for either fuel rich flame or diffusion flame, which has tendency to form soot. Soot particle radiations can be assumed approximately same as black body radiation.

1.3.4 Thermochemical heat release (TCHR or chemical recombination or simply recombination)

Among all the alternative names, TCHR includes the aspects of thermodynamics, chemical reactions and exothermic energy release, suggested by Baukal and Gebhart (1996). Flame jets can be produced by using oxy rich fuel which leads into higher burning velocity that ultimately results in higher temperature. Moreover, absence of N_2 which acts as heat sink in combustion products results in a higher flame temperature. At higher temperature, many combustion products contain free radicals due to dissociation of species and degree of dissociation goes on increasing as temperature increases. When flame impinges on cooler surface, these products cool down by losing energy exothermically to form more stable products. During this radical recombination, additional heat releases known as thermochemical heat release (TCHR). It can have same magnitude as that of convection at high temperature. As TCHR is very difficult to separate out from convection, its effect is considered along with convection.

Two mechanisms are observed in TCHR, namely equilibrium TCHR and catalytic TCHR. In gas phase, chemical reaction takes place in the boundary layer. When free radical experiences less diffusion rate comparative to the chemical reaction rate, chemical reactions occur in the boundary layer, before reaching the surface giving no difference in heating rate. Hence gives equilibrium effect and consequently equilibrium TCHR. whereas, if dissociated species have insufficient time to react before reaching the surface, catalytic TCHR happens at the surface. Since these reactions occur at the surface, material of surfaces may catalytically accelerate the reactions known as catalytic TCHR.

1.3.5 Boiling and Condensation

In many studies, to estimate heat transfer from the impingement target, target surfaces are cooled from the non-impingement side. This boiling and condensation may occur on surface during flame impingement unknowingly. Internal and External boiling can occur when flame impinges on wet surfaces. Internal boiling occurs on the opposite side of impinging surface where coolant gets heated above its boiling temperature. Due to impinging flame, if there is condensed water on cold surface, gets heated above the boiling point, known as external boiling. Condensation of water vapors in the products of combustion can also occur if target surface temperature is less than dew point temperature of water vapor.

1.4 APPLICATIONS

Impinging flame jets are widely used in so many industrial as well as domestic applications. Many studies are carried out in this field to find the effect of different parameters on heat transfer characteristics of impinging flame jets and suitable explanations are also presented. Despite of the available studies the research should be continued for presenting more efficient way of using the energy and getting the maximum out of it.

Some typical applications of flame impingement jets are metal melting, glass processing, fabrication and assembly applications etc. Fig. 1.3 illustrates some of the direct industrial applications of impinging flame jets, although many more could be added, even subjects like aerospace vehicles re-entering the atmosphere can be described as impinging jets (Cremer et al. 2010).

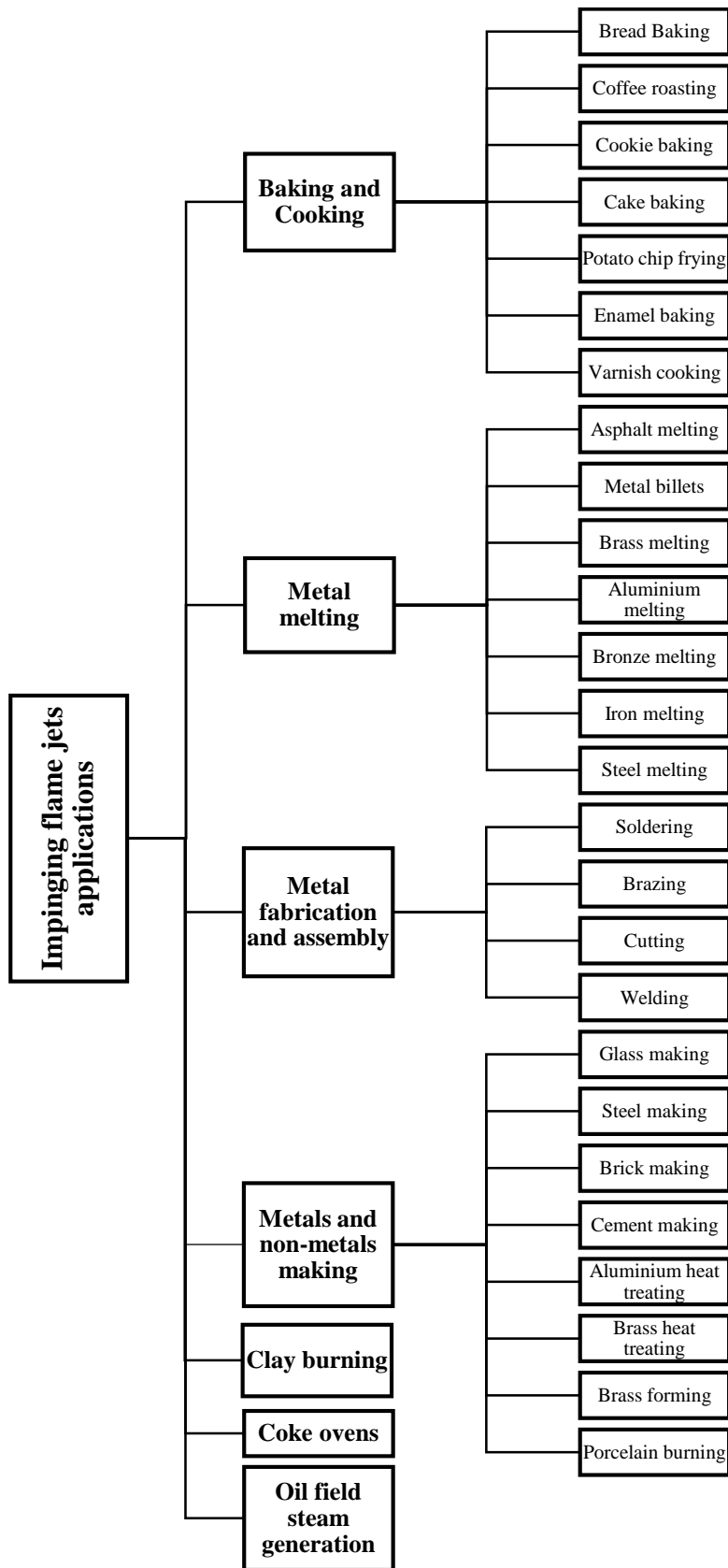


Figure 1.3 Applications of impinging flame jets

1.5 ORGANIZATION OF THESIS

This thesis organized into six chapters to help the reader in understanding the nature of present work, as follows.

Chapter 1 provides the brief introduction about the impinging flame jet through identification of its nature and wide applications in industries as well as domestic field. This chapter also describes all the modes of heat transfer involved in impinging flame jets.

Chapter 2 deals with review of literature pertaining to flame jet impingement studies. Extensive literature is appraised to find research gap. Reviewed Literature is mapped with the respective objective and presented in sequence with the framed objectives.

Chapter 3 describes experimental set up used in the present study along with the its validation in terms of flame stability check. All instruments required during experimentation are identified and their usage are explained in this chapter. This chapter also deals with the data reduction related to flame impingement study. Numerical approach adopted in current research work is briefed as well in same chapter.

Chapter 4 presents all the analytical methods employed in the current study to estimate the transient heat flux at the impingement side. Nature of heat transfer to and from the jet is explored through one dimensional to multi-dimensional assumption.

Chapter 5 contains all the results in sequence with the objectives followed by the elaborative discussion and it is presented in four stages. Heat transfer characteristics of flame and air jet are compared, analyzed and presented in first stage. In second stage, results from analytical methods applied to flame jets to estimate heat transfer coefficient and reference temperature are synthesized. Effect of variable thermal conductivity and radiation correction is also presented in same stage. Later in third stage, heat transfer characteristics of impinging jets by inverse approach is discussed. In last stage, results related to ribbed surface are presented.

Chapter 6 presents concluding remarks of the present investigations and discusses the scope for future work.

Chapter 2

2 LITERATURE SURVEY

2.1 INTRODUCTION

Rapid heating techniques have become increasingly popular as they save energy and improves the quality of the hot product. Thus, many investigators have shown interest in studying impingement of flame gases onto cold surfaces. Reviews are written on impinging flame jets by Chander and Ray (2005), Viskanta (1993) and Baukal and Gebhart (1996).

2.2 TYPICAL EXPERIMENTAL TEST RIG USED IN FLAME IMPINGEMENT STUDY

Figure 2.1 shows the typical schematic for the flame impingement test rig. Heat generation part consists of a burner and it can be of any size. Several geometries of different size and material are tried as a burner to improve the heat transfer rate.

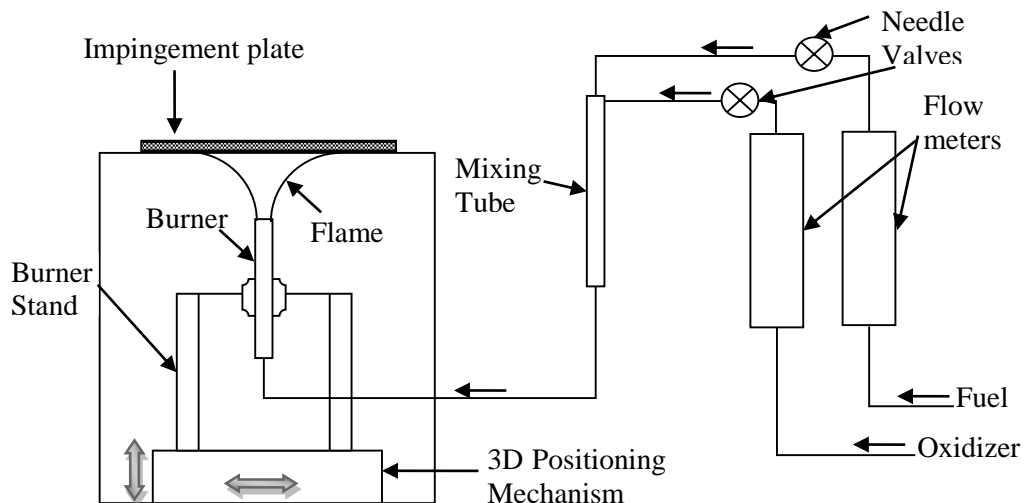


Figure 2.1 General flame impingement experimental set up

The flow of fuel and oxidizer is controlled by flow meters. A range of flow regulators from standard mass flow controller (MFC) to simple flow meters like Rotameters,

venturi meter and orifice meter has been used in the literature. Before burner, air and methane are mixed in mixing tube and then ignited mixture produces a flame which impinges on a plate. Again plates of different geometry and material are studied as impingement surface. 3-D positioning mechanism facilitates the movement of the burner in horizontal as well as vertical direction. Heat flux measurement techniques are discussed further in detail.

2.3 PARAMETERS AFFECTING HEAT TRANSFER CHARACTERISTICS OF THE FLAME

Figure 2.2 shows parameters affecting on heat transfer characteristics of flame and their effect are summarized below.

2.3.1 Effect of the configuration of impinging flame jets

Review by Chander and Ray (2005) has summarized the five different configurations of impinging flame jets. It includes flame impinging normal to a cylinder, flame impinging normal to a hemispherical nosed cylinder, flame impinging normal to plane surfaces, flame striking parallel to plane surfaces and flame striking at some angle to plane surfaces. Applications of these configurations are explained in Table 2.1.

A comprehensive study has been carried out on flame impinging normal to plane surface since it has been widely used in the industrial application and it was found that stagnation point coincides with the point of intersection of the axis of burner and plane surface. Moreover, due to the presence of a cool central core of unreacted mixture in the flame, stagnation region found cooler than the maximum temperature. In case of flame jet impinging at different angles of incidence, stagnation point did not coincide with the point of intersection of the axis of burner and plane surface. Stagnation point found shifted towards the uphill side of the jet.

2.3.2 Effect of Oxidizer and fuel

The type of oxidizer and fuel is the most critical parameter in flame impingement study as it directly affects heat transfer to plate from the flame. Air has been used as an oxidizer in most of the studies.

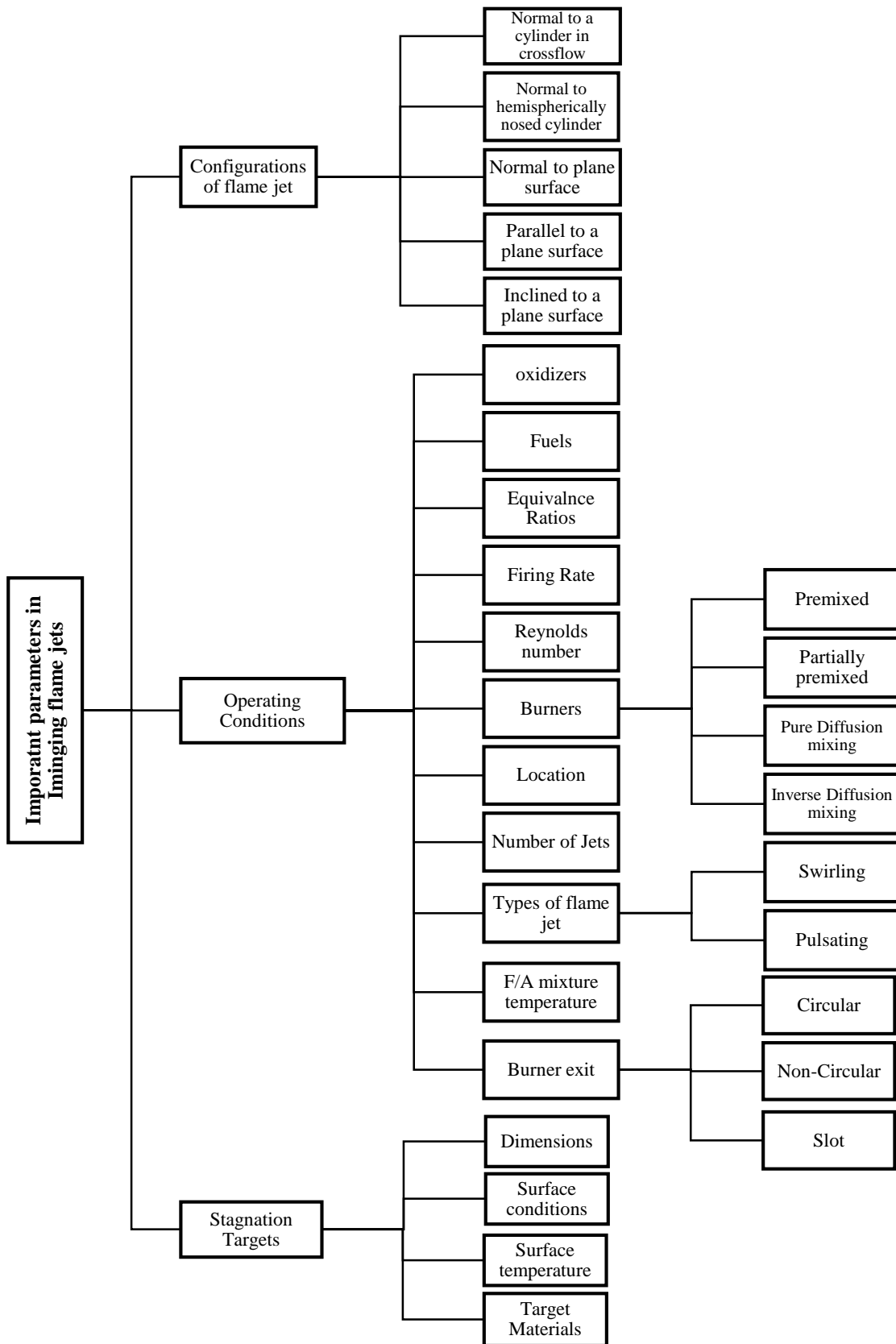
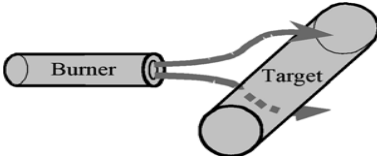
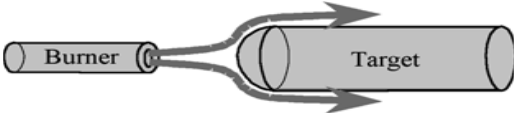
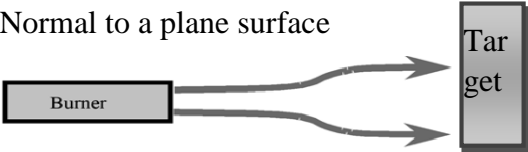



Figure 2.2 Parameters affecting heat transfer characteristics of the flame

Table 2.1 Applications of different configurations of flame impinging jets

Flame impinging Configurations (Baukal 2000)	Applications
<p>Normal to a cylinder</p> 	<p>Heating round metal billets, and in fires impinging on pipes in chemical plants</p>
<p>Normal to a hemispherical nosed cylinder</p> 	<p>Important in aerospace applications.</p>
<p>Normal to a plane surface</p> 	<p>Melting of scrap metal, shaping glass and heating metal bars, metal fabrication and assembly applications</p>
<p>Parallel to a plane surface</p> 	<p>Important in-flight application (Aerofoil surface)</p>

The flame temperature and the degree of dissociation of species in combustion products depend upon the type of oxidizer used. Baukal (2000) has explained that the adiabatic flame temperatures for stoichiometric methane-air mixture and stoichiometric methane-oxygen mixture are 2220 K and 3054 K respectively. Products of combustion for stoichiometric methane-air adiabatic flame essentially contain no unreacted fuel or dissociated species whereas methane-oxygen adiabatic flame has approximately 23 volume % unreacted fuel and 18 volume % dissociated species. These products cool down near boundary layer by relieving heat exothermically known as TCHR which is considerably larger as convective heat transfer.

Literature shows that either natural gas or methane is used in most of the studies. Many combinations of oxidizer, fuel and equivalence ratios can be possible. The carbon to hydrogen weight ratios in the fuel decides the tendency of soot formation. Thus proper

consideration must be given for choosing the combination of fuel, oxidizer and equivalence ratio so soot formation may be less leading to less deposition on the surface, maximizing heat transfer to the surface.

2.3.3 Effect of Nozzle-plate spacing (H/d)

Although the length of the primary cone can be adjusted to vary heat transfer rate to the plates, the dimensionless axial separation distance between burner exit and plate must be varied to get the more uniform rate. It has a substantial effect on resulting heat transfer to the plate and it is an essential parameter from a stability point of view. Larger separation distance produces less flame temperature and lower heat flux attributed to more surrounding cool air entrainment into the flame and more widening of flame. Maximum heat flux and temperature occurs at stagnation point and decreases along radial direction producing comparatively more uniform heat transfer profile at the surface.

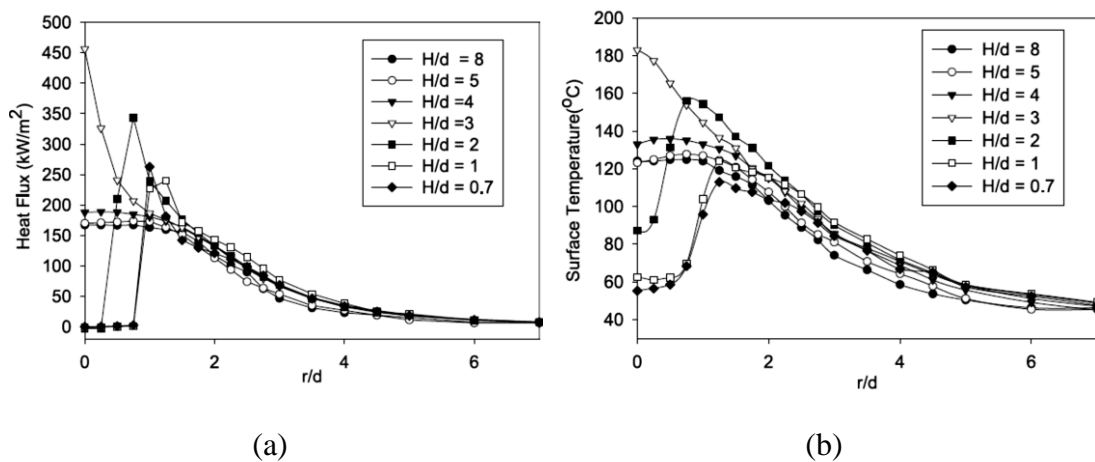


Figure 2.3 Influence of Nozzle-plate spacing (H/d); (a) Heat flux and (b) surface temperature for methane/air premixed flame at $\text{Re} = 1400$, $\phi = 1.0$ and tube diameter =10 mm (Chander and Ray, 2006)

Figure 2.3 (a) and (b) shows the effect of H/d on heat flux and surface temperature respectively at non-dimensional radial distance r/d for methane-air flame impinging on the surface at $\text{Re}=1400$, $\phi=1$, as reported by Chander and Ray (2006). Instability in flame may occur at larger separation distances because of buoyancy effect.

At shorter distances, the heat flux rate and the temperature are higher due to less air entrainment and less widening of flame. At $H/d = 3$, the inner reaction zone is just touching to the surface resulting maximum heat flux rate and surface temperature. Further reduction in separation distance results in shifting the point of maximum heat flux and surface temperature away from stagnation point in the radial direction as inner reaction cone spreads around the stagnation point and reaction zone touches the surface at some distance away from stagnation point. At shorter distances, it has been observed that heat flux at the stagnation point reduces to zero value or even negative. This is due to impingement of unburnt cold mixture directly on stagnation region. Cause and effect at higher H/d is summarized in Figure 2.4.

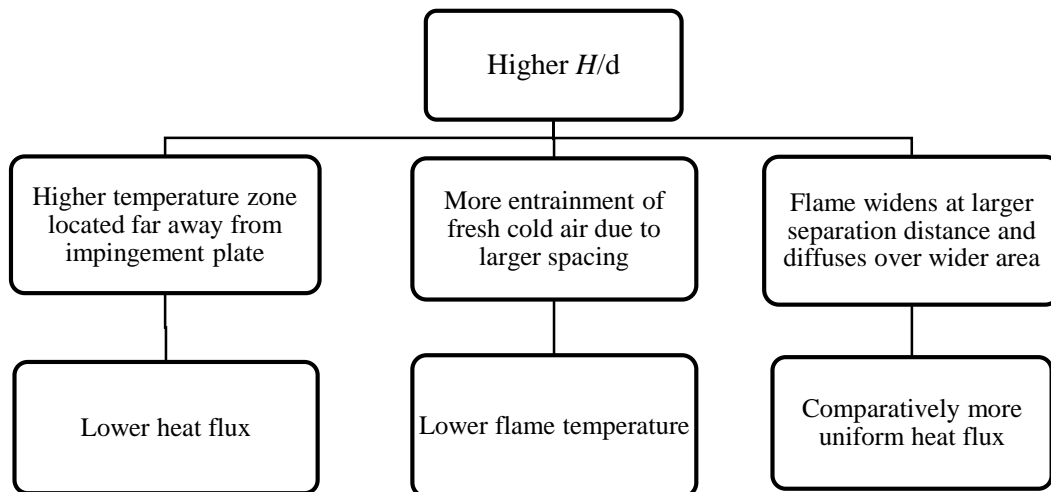


Figure 2.4 Cause and effect diagram for higher H/d

2.3.4 Effect of Reynolds number (Re)

It has been observed that the range of Reynolds number used in the study of flame impingement varies from very low, i.e. 300 to very high, i.e. 35000. It has a significant influence on the heat transfer rate to the plate. It directly affects flame length (both primary and reaction). High Reynolds numbers have been used mostly to study diffusion flames, while Reynolds number up to 2500 have been used to laminar premixed flames. Figure 2.5 (a) and (b) shows the consequence of Reynolds number on heat flux and surface temperature distribution along the radial direction for methane-air flame for tube burner of 10 mm diameter for $H/d=4$ and $\phi=1$.

At lower Reynolds number, high temperature zone located far away from the plate. Thus heat flux and surface temperatures are lower in values. As Reynolds number increases further, flame cone height also increases results in an increase in heat flux and surface temperature values not only at stagnation region but also in wall jet region. It attributes to more convective heat transfer. At Reynolds number 1600, flame cone comes in contact with surface giving maximum heat flux value 461kW/m^2 . Maximum heat flux point shifts away from stagnation point for Reynolds number higher than 1600. It happens because inner cone intercepted by surface and it spreads out towards wall jet region. At very high Reynolds number, it has been observed that heat flux at the stagnation point reduces to zero value or even negative. This is due to impingement of unburnt cold mixture directly on stagnation region.

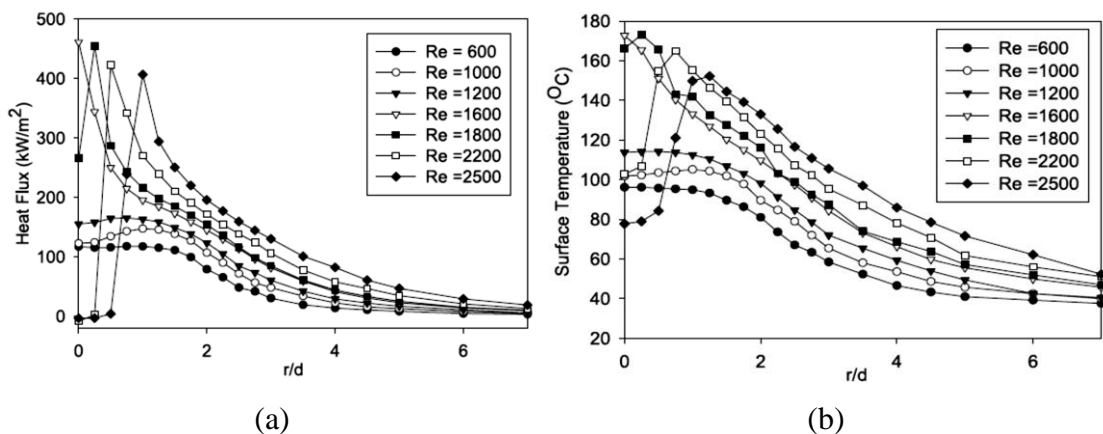


Figure 2.5 Influence of Reynolds Number (Re); (a) Heat flux and (b) surface temperature for methane/air premixed flame at $H/d = 4$, $\phi = 1.0$ and tube diameter = 10 mm (Chander and Ray, 2006)

2.3.5 Effect of Equivalence Ratio (ϕ)

Many researchers have studied the effect of a wide range of equivalence ratio on heat transfer rate. The trend of heat flux and surface temperature profiles over non-dimensional radial distance is shown in Figure 2.6 for the range of equivalence ratios from the lean mixture ($\phi = 0.8$) to rich mixture ($\phi = 1.5$) as reported by Chander and Ray (2006).

The degree of dissociation in combustion products and the sooting tendency is directly depended upon equivalence ratio. Stoichiometric ($\phi = 1$) or near stoichiometric mixture has highest flame temperature as it is complete combustion with no soot production. Hence, it produces nonluminous radiation. The rich mixture ($\phi < 1$) produces both luminous and nonluminous thermal radiations due to the presence of soot particle in combustion products, whereas lean ($\phi > 1$) mixture produces nonluminous radiation due to the absence of soot particles. At lean mixture, the maximum heat flux and surface temperature occur at the stagnation point.

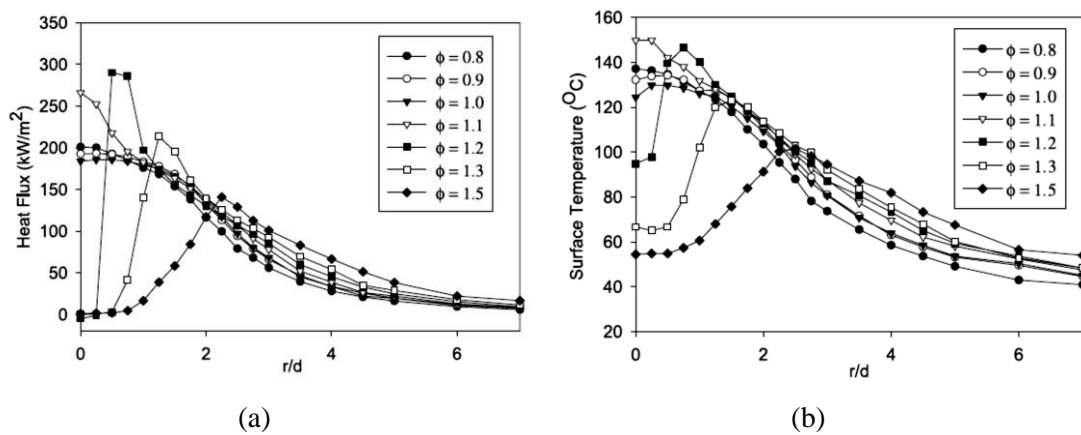


Figure 2.6 Influence of equivalence ratios (ϕ); (a) Heat flux and (b) surface temperature for methane/air premixed flame at $\text{Re} = 1400$, $H/d = 4$ and tube diameter = 10 mm. (Chander and Ray, 2006)

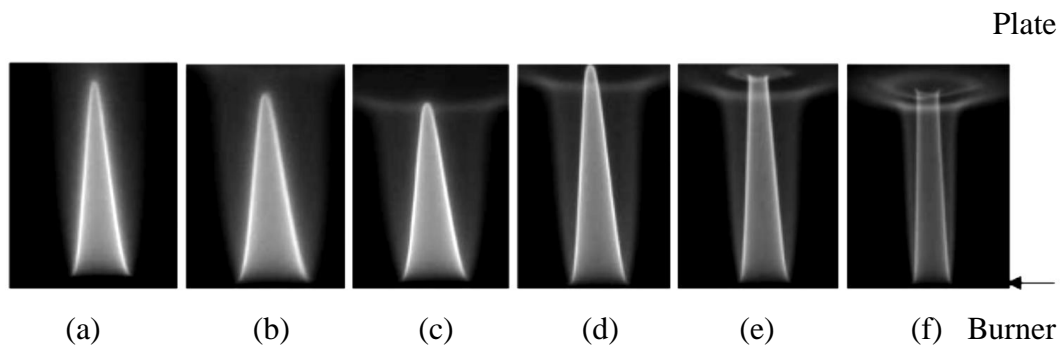


Figure 2.7 Influence of equivalence ratios on impinging methane/air flame shapes for $\text{Re} = 1400$, $H/d = 4$ and at various; (a) $\phi = 0.8$ (b) $\phi = 0.9$ (c) $\phi = 1.0$ (d) $\phi = 1.1$ (e) $\phi = 1.2$ and (f) $\phi = 1.5$ (Chander and Ray 2006)

As shown in Figure 2.7, longer length of flame was observed at lean mixture $\phi = 0.8$ than stoichiometric mixture which is the reason for having heat flux and surface temperature more at $\phi = 0.8$ than $\phi = 1$. However, adiabatic flame temperature found lower at $\phi = 0.8$ than $\phi = 1$. Maximum heat flux at stagnation has been observed at $\phi = 1.1$. This is attributed to the highest adiabatic flame temperature of flame at $\phi = 1.1$. This happens on account of complete combustion of stoichiometric or near to stoichiometric mixture which gets produced as entrainment air mixes with the already rich mixture. Further increase in equivalence ratio results in a shift of maximum heat flux point away from stagnation point owing to interception to the reaction cone which spreads the flame towards wall jet region.

2.3.6 Effect of Firing Rate

Firing rates are governed by Reynolds number and equivalence ratio. The researchers have used a wide range of firing rates from 5 kW to 25 kW and it has been observed that for larger heat flux rate higher firing rates need to be used. It was also found that separation distance between flame and surface did not have any influence on the heat flux rate at higher firing rate. It has also been seen that flame length increases with the firing rate. Chander and Ray (2005) have reviewed the effect of firing rates used by investigators.

2.3.7 Effect of TCHR

Effect of TCHR is frequently neglected in case of fuel-air mixture flames and total heat transfer is assumed from the only mode of convective heat transfer. Besides, for oxy-fuel flames, this phenomenon is so important that it was held responsible for more than 50% heat transfer to the surface along with the convection. As explained in section 1.3.4, it is the extra heat released due to dissociation and exothermically recombination of reactions. Its effect on species concentration as well as on temperature distribution in the stagnation boundary layer is observed by Cremers et al. (2010). Thus, TCHR effect is considered in terms of TCHR-factor which is a multiplication factor for convective heat transfer and it is defined by Cremers et al. (2010) as Equation (2.1)

$$a_{TCHR} = \frac{q_{convective} + q_{TCHR}}{q_{convective}} \quad (2.1)$$

Figure 2.8 shows the variation in TCHR factor as a function of surface temperature for various mixtures and it is observed that for lower temperature, the factor is in the range of 1.7 to 2.2. Especially, TCHR factor for H₂ – O₂ is almost twice at a lower temperature, if neglected would be misleading for heat transfer calculation. Heat transfer rate from the flame to the plate is given by Equation (2.2)

$$q_{Total} = a_{TCHR} q_{convection} \quad (2.2)$$

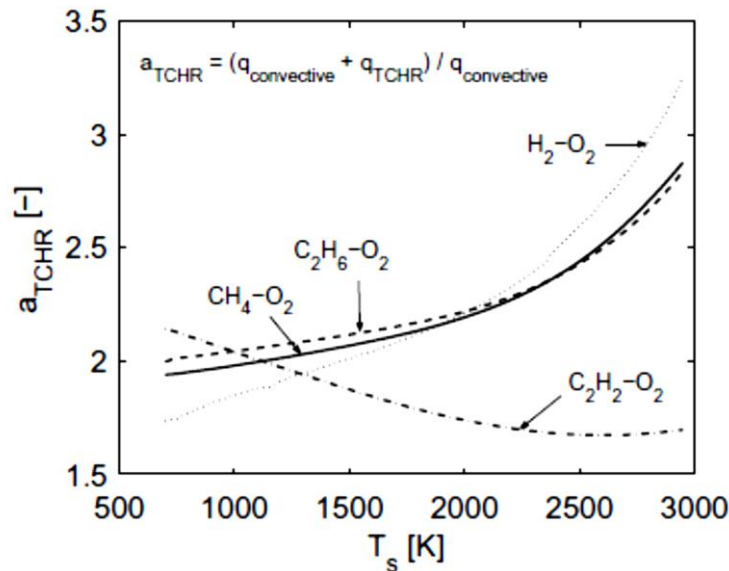


Figure 2.8 TCHR factor as a function of surface temperature for various mixtures (Cremers et al., 2010)

2.3.8 Effect of Burner geometry

Among circular, noncircular and slot burner, the axisymmetric circular burner has received most of the research interest. Dong et al. (2002) investigated the effect of slot burner and it was found that the slot flame jet produces a uniform heat flux profile and larger averaged heat fluxes than the circular flame jet. Chander and Ray (2006) have also studied the effect of burner geometry on heat flux distribution and considered three types of geometries as, tube, nozzle and orifice. Figure 2.9 shows the variation in exit velocity profiles for tube, nozzle and orifice. Tube length was sufficient to get a

parabolic profile at the exit. For nozzle and orifice, velocity profiles were observed almost flat. Among two, nozzle exit profile was flatter owing to a high-velocity component present at the orifice edge. As exit velocity profiles were different, variation in flame shape and heat transfer characteristics were observed. Figures 2.10 to 2.12 show the heat flux and surface temperature distribution for geometries at three different separation distances i.e. $H/d = 6, 3$ and 2 respectively. Maximum stagnation point heat flux was found for $H/d = 3$ in case of tube burner because of flame cone just touching the surface and parabolic nature of velocity profile at the exit of tube burner. Among geometries, tube burner produced higher heat flux at the stagnation region whereas higher flux was observed for orifice burner in wall jet region.

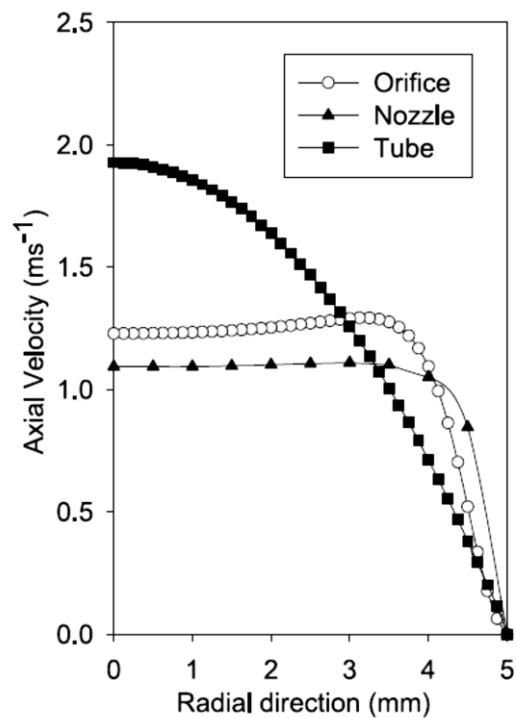


Figure 2.9 Influence of burner geometry on exit velocity profiles at $Re = 600$ and diameter = 10 mm (Chander and Ray, 2006)

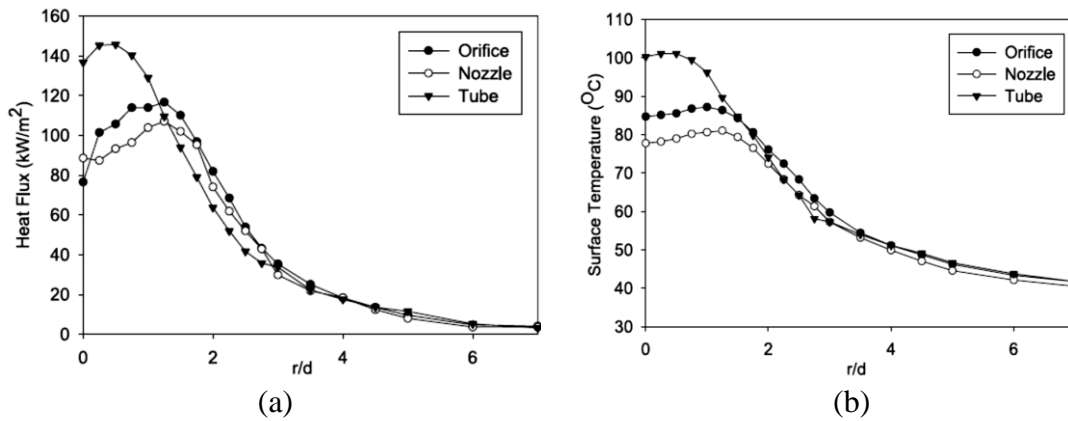


Figure 2.10 Influence of burner geometry; (a) heat flux and (b) surface temperature for $\text{Re} = 1000$, $H/d = 6$, $\phi = 1.0$ and 10 mm diameter (Chander and Ray 2006)

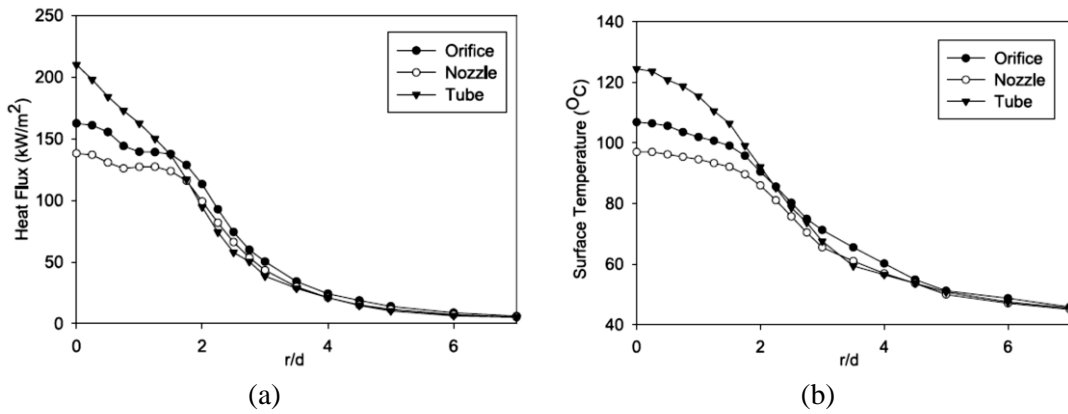


Figure 2.11 Influence of burner geometry; (a) heat flux and (b) surface temperature for $\text{Re} = 1000$, $H/d = 3$, $\phi = 1.0$ and 10 mm diameter (Chander and Ray 2006)

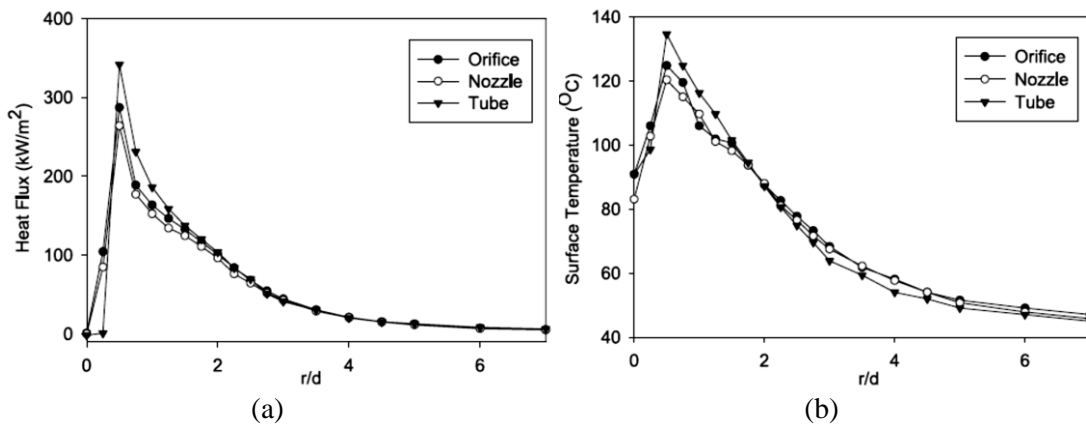


Figure 2.12 Influence of burner geometry; (a) heat flux and (b) surface temperature for $\text{Re} = 1000$, $H/d = 2$, $\phi = 1.0$ and 10 mm diameter (Chander and Ray 2006)

2.3.9 Effect of type of flame

Flames produced after combustion are of different types. Figure 2.13 shows different types of flame depends upon how fuel and oxidizer are mixed. To produce premixed flames, fuel and the oxidizer needs to get mixed before combustion. These flames are of shorter length but produce higher heating rates than diffusion flames. Hence premixed flames are preferred over diffusion flame in the flame impinging application. However, due to high temperature regions, non-uniform heating of surface takes place.

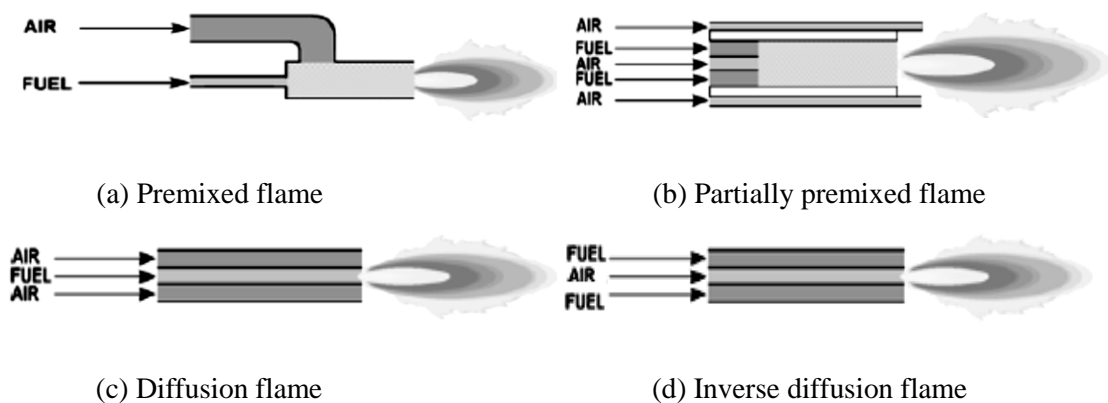


Figure 2.13 Different types of flame (Baukal 2000)

In diffusion flame, fuel and oxidizer flow separately through the burner and at the exit, these two diffuse into each other. Flame speed solely depends upon the rate of diffusion. Thus, diffusion flames burn slower and produce more soot than premixed flames. Generally, oxy-fuel flames are diffusion flames, primarily for safety reason, to prevent flashback. To lessen the chance of flashback which can be with the fully premixed flame and to stabilize flame, a portion of fuel can be mixed with an oxidizer to produce a partially premixed flame. An inverse diffusion flame (IDF) is a non-premixed flame that consists of inner air flow surrounded by fuel flow. This structure helps in better mixing of fuel-air as inner air flow creates strong entrainment of the surrounding flame jet results in shorter flame length and less soot emission. IDF has the same advantages of shorter flame height and higher heating rate as that of partial or fully premixed flame. Moreover, in basic, it is a diffusion flame; therefore it has no danger of flashback as that of premixed flame.

2.3.10 Effect of Mixture temperature

Tajik et al. (2015) have investigated the effect of the preheated mixture on heat transfer characteristics in case of premixed methane-air flame impingement on a flat plate. Electric energy was used to preheat the mixture. Besides it, energy from spent flame or low-grade energy can be used to preheat the mixture.

It can be noted from Figure 2.14 that effect of preheating was not only on flame cone height but also on adiabatic flame temperature.

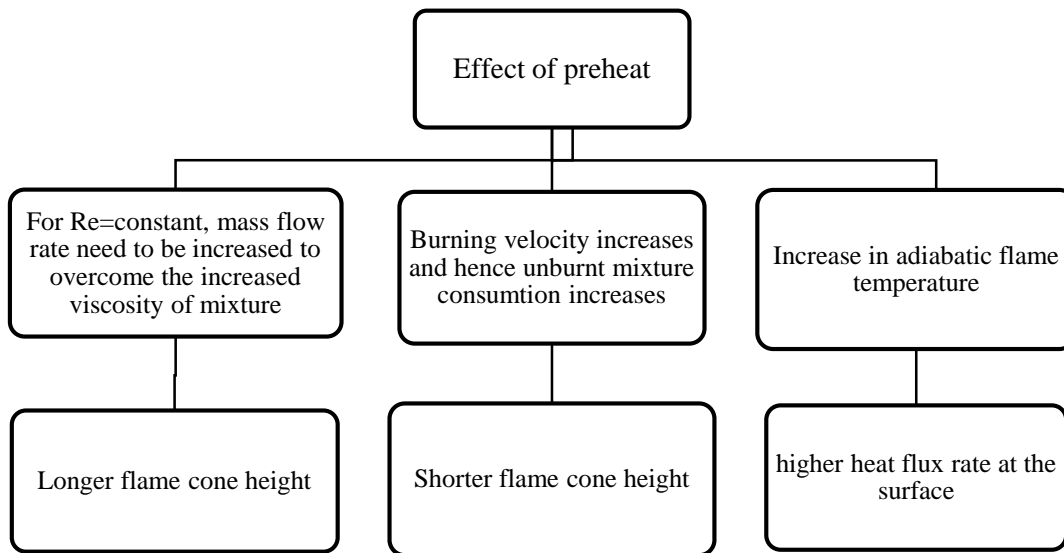


Figure 2.14 Cause and effect diagram for preheating the mixture

Table 2.2 Effect of preheating on adiabatic flame temperature (Tajik et al. 2015)

ϕ	$T_{adf}(K)$		
	$\Delta T = 0 K$	$\Delta T = 50 K$	$\Delta T = 100 K$
0.75	1919	1954	1989
1	2225	2250	2274
1.25	2097	2130	2164
1.5	1905	1940	1974

The adiabatic flame temperature was calculated from fundamentals at different preheated mixture temperatures and equivalence ratios shown in Table 2.2. It can be seen from the Figure 2.15 that for same Reynolds number and with variable mixture mass flow rate, flame cone length always increases. The reason behind this increase in length was attributed to the increase in mass flow rate to maintain the same Reynolds number.

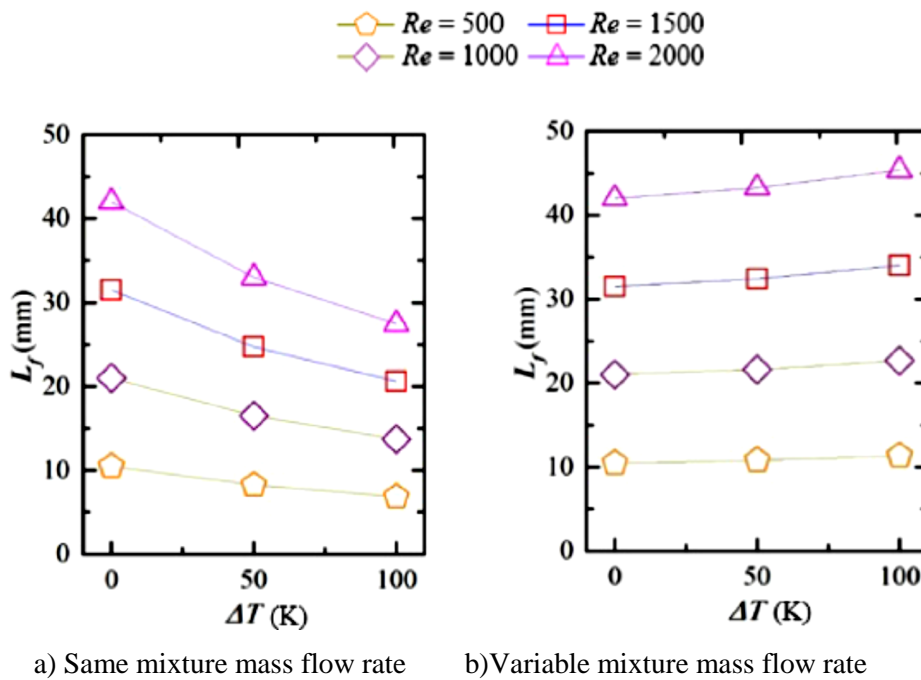


Figure 2.15 Influence of mixture temperature on flame cone length for different Reynolds number at $\phi = 1$ (Tajik et al., 2015)

2.3.11 Effect of Multiple jets

Intense, quick and uniform heating is a requirement in glass and many more industrial applications to ensure the quality of treatment. One way of getting it is making use of multiple jets instead of single set. It has been observed that multiple jets not only ensures uniform heating but also increases the heat transfer rate to the plate. Review by Chander and Ray (2005) has summarized the use of an array of the jet by different investigators in their study. Chander and Ray (2007) have detailed studied the staggered array of three impinging flame jet. Parametric study on staggered array leads to a conclusion that maximum heat transfer rate obtained when inner reaction cone was just touching the surface of the plate and average heat fluxes were high at small separation

distances and at small inter-jet spacing but the heat flux distribution was quite non-uniform. In view of a balance, a moderate H/d of 5 and a small S/d of 3 was found to be the optimum configuration in their study. Li et al. (2011) investigated the effect of twin and triple inline nozzle on heat transfer characteristics and observed that highest total heat flux obtained was at moderate $S/d=5$.

Although the use of multiple jets enhances heat flux rates and uniformity in the heat flux distribution, to get the optimum configuration for a particular case is always challenging. This is due to a large number of parameters like burner shape, jet arrangement, axial separation distance, inter-jet spacing, geometry and inclination of the impingement surface, initial flow field and turbulence intensity in the jet affects the optimization process.

2.3.12 Effect of Type of jet

Flame jet can be categorized as laminar and turbulent based on nature at the burner exit. Among them, the laminar flame has been studied mostly due to its simplicity. Furthermore, laminar flames are relatively stable than those of turbulent flames. Study on turbulent is limited but important as it influences flame structure, stability and heat transfer characteristics. These flames reduce stagnation point heat flux with uniformity in heat flux distribution over the plate and responsible for axial velocity decay as well.

To get quick higher heat transfer rate with less pollution, flame impingement has been studied by many researchers. Still, it has been remained a challenge to design an optimum system which could be used in industrial as well as domestic application. Single impinging flame jet found setback due to its non-uniform heating of the impingement surface. A number of arrays of the jet have been used as a solution which was also found less interest owing to the interaction between adjacent jets which induced operational difficulties.

To overcome this problem, swirling jets have been investigated and found considerably more uniform. Although more work is on swirling diffusion flame jet operated at high flow and high pressure conditions, recently many researchers have reported the study on swirling premixed flame operated at various conditions. Huang et al. (2006) have

studied the heat-transfer characteristics of a circular premixed air/butane impinging laminar flame jet with swirl induced and compared with the heat transfer by twin flame jet studied by Dong et al. (2004) as shown in Figure 2.16.

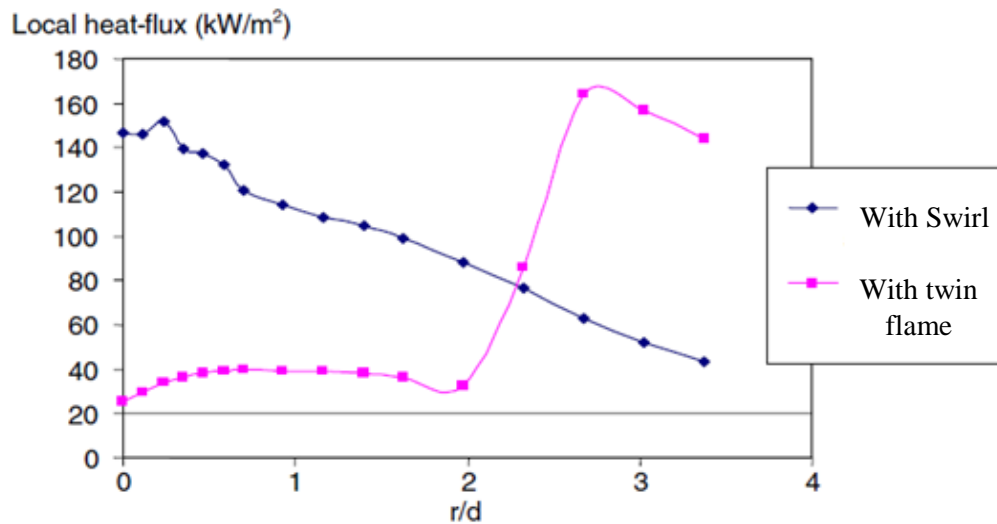


Figure 2.16 Heat transfer distribution for a single circular premixed flame jet with induced swirl and twin flame jets without swirl at $\phi = 1$, $Re = 1200$ and $H/d = 2$ (Huang et al., 2006)

Thermal performance of an array of three identical premixed circular flame jet with induced swirl has been studied by Zhao et al. (2009) and suggested that at shorter separation distance complete combustion and more uniform heat flux distribution can be achieved. Luo et al. (2010) have conducted experiments to study the effects of the different operational parameter on a swirling premixed flame impinging vertically normal to a horizontal plate and found that complete combustion which is due to better surrounding air entrainment and mixing. Heat transfer characteristics of the premixed swirling flame of CNG-air was studied by Singh et al. (2012) and observed a dip in the flux at and around the stagnation point. To overcome the drawback of non-uniformity in the heat flux distribution due to a dip in heat flux, Singh et al. (2014) have proposed a dual flame burner with inner non-swirling and outer swirling flame. In that case, it has been observed that the inner non-swirling flame was able to cover partially region at and around stagnation point. But it was observed that there was still a region where the heating was low on the impingement surface.

2.3.13 Effect of Surface characteristics of the impinging plate

Surface characteristics are varied among the studies over the flame impingement on impingement surfaces. Surface characteristics involve dimension, surface treatment, material and surface temperature. Cylindrical cylinders, thin circular disks, square and rectangular plates have been used as the target surfaces. Baukal and Gebhart (1997), has extensively studied the effect of surface conditions on heat transfer characteristics of oxygen-enhanced natural gas flames impinging normal to water-cooled metal disk. Five surface treatments (untreated, polished, blackened, alumina coated, and platinum coated) under similar operating conditions were investigated.

To understand varying emissivity effect, surfaces such as untreated, polished and blackened were considered. Highest heat fluxes were found for blackened surfaces whereas the polished surfaces had the lowest heat fluxes. The untreated surfaces experienced fluxes between those of the blackened and the polished surfaces. However, the largest difference in the heat fluxes between the polished and the blackened surfaces was only 9.8%. Surfaces of varying catalyticity were also investigated and it was noticed that platinum coated surface has 12% more heat flux than the alumina-coated surface. Contribution in heat flux of TCHR from surface catalytic reactions found relatively very small.

Li et al. (2010) have extensively studied the effect of plate temperature by conducting experiments with premixed LPG-air impinging on a flat plate. Plate temperature was maintained at three different temperatures 38°C, 58°C and 78°C by controlling circulating cooling water and at each temperature, a parametric study has been carried out to see the effect on heat transfer and emission. The increment in surface temperature with the increment in initial impingement plate temperature was observed. At the same time, there was a significant reduction in heat flux with an increase in the impingement plate temperature. Highest heat flux received by the plate was at 38°C whereas lowest heat flux received was at 78°C. Effect of impingement plate temperature was also found on emission characteristics. Lower CO emission and higher NO_x emission was attributed to enhanced combustion due to high impingement plate temperature.

2.4 MEASUREMENT TECHNIQUES IN FLAME JET IMPINGEMENT

The measurement technique is a very key and critical element of the experimental study. It decides the quality of the study. Figure 2.17 illustrates various measurement techniques used by researchers for flame impingement studies and same are elaborated as follows.

2.4.1 Total heat flux measurement (Baukal 2000)

In many heating applications as well as in studies, the heat flux is the most significant and intrigued parameter. The total heat flux to the surface has been measured by two methods: Steady-state and transient. Along with the working principle, advantages, disadvantages and present status of these techniques is summarized in Table 2.3.

2.4.1.1 Steady State Methods

Researchers found three ways to calculate heat flux under steady state.

I) First method - If the surface is uncooled: In this method, to measure heat flux, energy balance has been used for the uncooled surface. Radiative heat transfer is added to convective heat transfer from the flame to get total heat flux to the surface. Radiative heat transfer from the flame with surface and without surface is measured by thermopile and radiative heat transfer from the flame to the surface is calculated by subtracting the first measurement from the later one. Sensible heat gain by the surface is then added to radiative heat gain by the surface to calculate total heat flux to the surface.

II) Second Method – If the surface is cooled: In this method, sensible heat gain by a coolant which cools the rear side of the impinging surface has been used to calculate heat flux. Once steady state has been achieved, flow rate and temperature rise are measured. Thermocouples are generally provided on the surface to confirm the steady state, illustrated in Figure 2.18.

III) Third method-Measurement by cooled gages: In this method, heat flux has been measured directly by using heat flux gages whose hot and cold ends are exposed to flame and water respectively. These gages are generally made up of high conductivity material like copper and flushed with the surfaces always.

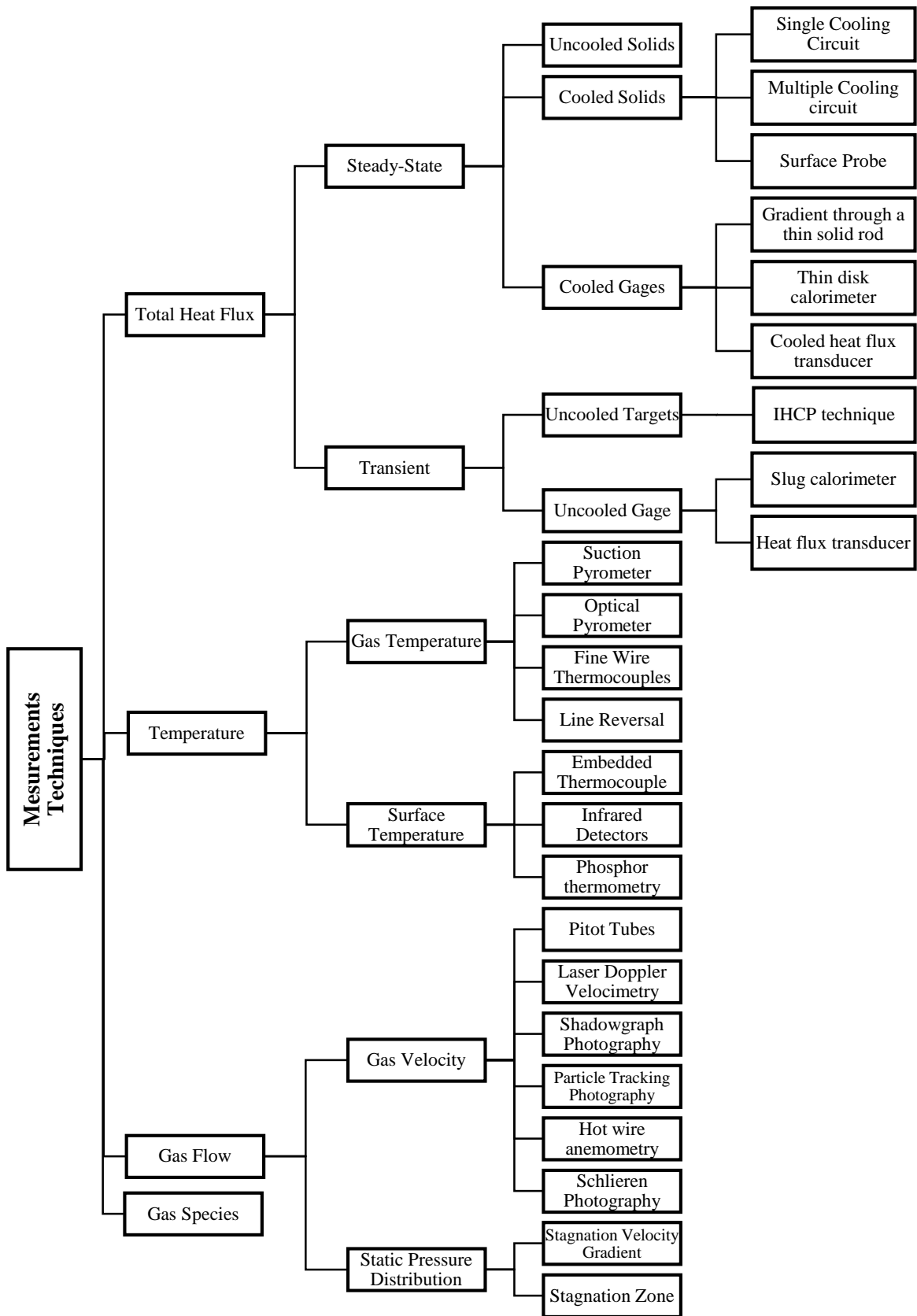


Figure 2.17 Measurement techniques for Impinging Flame Jets

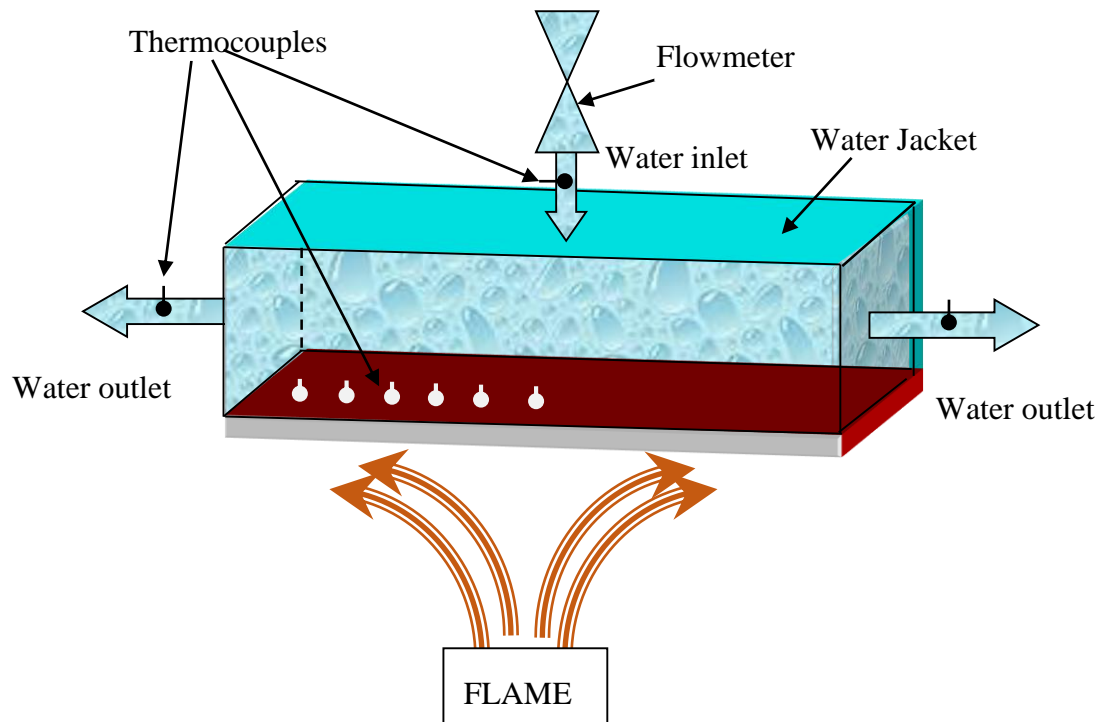


Figure 2.18 Heat flux measurement using a calorimeter

2.4.1.2 Transient methods

Two transient methods have been used in literature.

I) First Method – If the surface is uncooled (IHCP Technique): In this method, the uncooled surface is allowed to reach a certain temperature or else heated for a specific amount of time. Sensible heat gain by the surface, in either case, gives flux. Using the recorded temperature, the transient heat flux is determined indirectly. The temperature profiles are measured at or near impingement surface by using a number of thermocouples and then inverse conduction heat transfer computational technique is used to estimate transient heat flux.

II) Second Method – Measurement by uncooled gages: In the second method, heat flux gages embedded in uncooled surfaces gives flux directly. Transient heat flux can be calculated by knowing sensible heat gain of the gages. Gages made up of high thermal conductivity material. It is generally flush with the impingement plate at the center. Heat flux distribution over impingement surface was found either moving the plate in

x-y plane against flame or moving flame against the plate with the help of the three-dimensional positioner as shown in Figure 2.19.

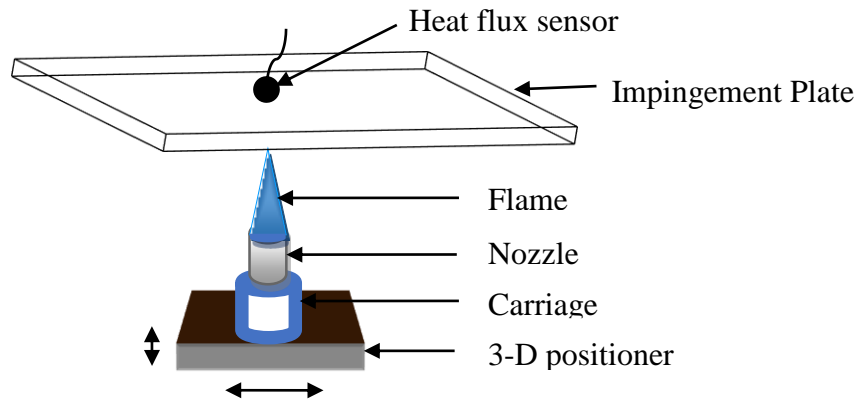


Figure 2.19 Heat flux measurement using heat flux sensor

2.4.2 Temperature measurement (Baukal 2000)

In the study of flame impingement, gas temperature and surface temperature are the most critical parameters to be measured to understand the heat transfer phenomenon.

2.4.2.1 Gas/mixture temperature measurement

It has been observed that gas temperature is not needed if heat flux is the only parameter of interest. However, to understand the temperature profile across the jet which decides flow uniformity and also results in entrainment of surrounding air, gas temperatures are required. Following are the techniques found in the literature.

D) Suction pyrometer: Gases from flame are sucked into the sampling tubes and the temperature is measured by using thermocouple placed inside this tube. Bare thermocouple introduces the error in measurement due to the radiative heat exchange between the thermocouple and its surrounding. Thus, in standard pyrometer, the thermocouple is always surrounded by a radiation shield made of ceramic or high temperature metal. However, there is always a possibility of happening active chemical reactions inside the probe for highly dissociated gases.

II) Optical techniques: In recent studies, researchers were more concerned about heat flux rather than flame/gas temperature. Of the few studies, mostly thermocouples were used to measure the gas temperature. Qi et al. in 2006 and 2008 have used reference-beam interferometry (RBI) with the set-up of a Michelson interferometer and a Mach–Zehnder Interferometry respectively to study the axisymmetric temperature fields of a flame jet.

III) Fine Wire Thermocouples: Fine wire thermocouples have been used to measure the flame temperature due to their inherent properties like fast response time, low cost and simple in use. It was observed that thermocouple to some extent always disturbs the flame and is always vulnerable to errors due to radiation loss from the bead and conduction loss along the length of thermocouple wire. Hindsageri et al. (2013) came with a numerical procedure to recover these losses. They observed that there exist a limit for the length of lead wire for which error in temperature measurement remains constant for further increase in the length of lead wire.

Table 2.3 Summary of techniques used for total heat flux measurement

Measurement Techniques	Working Principle	Advantages	Disadvantages/Remark
Steady State methods			
1. If surface is uncooled	<ul style="list-style-type: none"> ▪ Energy Balance at surface 	<ul style="list-style-type: none"> ▪ Very Simple ▪ Low in cost 	<ul style="list-style-type: none"> ▪ Determines only average flux ▪ Accuracy depends on exactness in surface emissivity
Current Status: Currently not in use. Used in earlier studies i.e. 1950s			
2. If surface is cooled	<ul style="list-style-type: none"> ▪ Heat balance of coolant 	<ul style="list-style-type: none"> ▪ Very Simple in working ▪ Doesn't need calibration 	<ul style="list-style-type: none"> ▪ Determines only average flux ▪ Requires uniform heating of the surface ▪ Coolant for higher temperature applications difficult to get
Current Status: mostly used. In studies, single cooling circuit has been used for small surfaces. Multiple cooling circuits have been used for large			
3. Measurement by cooled gages	<ul style="list-style-type: none"> ▪ Directly measures the heat flux 	<ul style="list-style-type: none"> ▪ Simple and low in cost ▪ Has more accuracy ▪ Gives local heat flux 	<ul style="list-style-type: none"> ▪ Needs calibration ▪ Cooling required at higher temperature
Current status: mostly used. In studies, three different ways have been used.			
i. Gradient through a thin solid rod: hot end of the thin rod is embedded with the surface. Thermocouples, placed along rod, are used to determine axial temperature gradient, which is assumed to be linear. Generally rod is insulated to suppress the interaction with the surroundings. Heat flux is calculated by using one dimensional heat conduction equation. Used in 1970s.			
ii. Thin disk calorimeter: A thin water cooled disk, usually copper, is embedded with the surface. Since it works same as calorimeter, heat flux is calculated using sensible heat gain by water. Used in very few studies in 1990s.			

- iii. Water cooled heat flux transducer: In the transducer, a proportional voltage is generated for received heat flux. This transducer is also generally embedded with the surface. Heat received by the transducer is continuously removed by cooling water. Thus has maximum operating temperature around 200°C irrespective of applied heat flux. Used in 1970s.

Transient Methods

- | | | | |
|--|---|---|--|
| 1. If surface is uncooled (IHCP Technique) | <ul style="list-style-type: none"> ▪ Using the recorded temperatures, transient heat flux is determined indirectly | <ul style="list-style-type: none"> ▪ Very Simple and low in cost ▪ Doesn't need calibration | <ul style="list-style-type: none"> ▪ Usually suffers from poor spatial resolution ▪ Accuracy depends on accurate thermal conductivity as a function of temperature ▪ Need very rapid instrument response time |
|--|---|---|--|

Current Status: Earlier used i.e. 1970s. Later, as it was commonly suffered from poor spatial resolution, use of this method reduced. Heat flux gages took their place. But recently Hindasageri et al. (2014) introduced novel technique to estimate transient heat flux using IHCP method where the transient temperature of impingement surface has been recorded using Thermal camera.

- | | | | |
|----------------------------------|--|---|---|
| 2. Measurement by uncooled gages | <ul style="list-style-type: none"> ▪ Transient heat flux is calculated by knowing sensible heat gain of the gages | <ul style="list-style-type: none"> ▪ Technique is simple ▪ Gives transient local heat flux ▪ Can be used for high temperature flames | <ul style="list-style-type: none"> ▪ Does need calibration ▪ Need very rapid instrument response time |
|----------------------------------|--|---|---|

Current Status: Mostly used. In literature, two different ways have been used.

- i. Slug Calorimeter: A very high thermal conductivity material is used to form the slug. Thus, thermal capacity of slug can be assumed as isothermal. Then, sensible heat gain of the slug gives heat flux received.
 - ii. Heat flux Transducer: In the transducer, a proportional voltage is generated for received heat flux. This transducer is also generally embedded with the surface.
-

2.4.2.2 Surface temperature measurement

In almost all flame impingement studies, surface temperatures are measured to observe temperature distribution along the plate. Following are the different ways to measure the surface temperatures.

I) Embedded thermocouples: The temperature distribution along the radial direction of impingement surface was generally obtained by embedding thermocouples at distant places. In recent studies, it has been observed that local surface temperature is measured by the heat flux sensor itself. Nowadays, heat flux sensor comes with the provision to measure temperature as well. Temperature distribution over impingement surface can be found either moving the plate in x-y plane against flame or moving flame against the plate with the help of the three-dimensional positioner.

II) Infrared Detectors: In early studies on combustion applications, pyrometer has been used to track the surface temperature of the object. A pyrometer is remote sensing temperature detector works on the infrared energy emitted by the surface. However, it gives only track of a point on the surface being under investigation. Recently imaging technology has been introduced in a newer device known as a thermal infrared camera with which entire temperature profile of surface can be captured. This infrared camera comes in various configuration (pixels and max temperature limit) with provision to capture images as well as transient temperature distribution over the surface. Norteshaur and Millan (2000), Loubat et al. (2004) and Hindasageri et al. (2014) have used thermal imaging camera based temperature readings at the non-impingement side in their IHCP techniques to estimate heat flux from the flame to the plate. Hindasageri et al. (2014) even could capture the images of flame impingement side while estimating adiabatic wall temperature.

2.4.3 Gas velocity (Baukal 2000)

Gas velocity is not needed while studying heat transfer characteristic of impinging flame jets. However, it is an important parameter in comparison of experimental data with the analytical results. Furthermore, the velocity profile may be used to verify

whether the jet is fully developed or not before impinging on the plate. Following are the methods considered by researchers in their study for the velocity measurement.

I) Pitot Tubes: To measure total and static pressure in a flow, Pitot tube and Prandtl tubes have been used respectively. Pitot tube has one end open to the flow and another end is connected to a pressure transducer. The tube is aligned in the flow, thus blocks the fluid flow and brought to rest gives total or stagnation pressure. In the case of Prandtl tube, the hole is on the sides of the tube and when it is aligned with the flow, it measures static pressure. The two probes may be combined, as a Pitot-static probe or simply Pitot tube which measures the difference between total and static pressure, i.e. dynamic pressure. Fluid velocity can be computed from this pressure.

Though the use of Pitot tube is very simple and at lower cost, its use is very limited while studying the turbulent fluctuations. Also, these tubes are intrusive to the flow which makes them unfavorable in case of highly circulating flow studies.

II) Laser Doppler Velocimetry (LDV): This is also known as Laser Doppler anemometry (LDA), an optical technique to measure gas velocities. Doppler shift produced by fluid particles detected by receiving optics. Further processing of signals gives the velocity of the particle. This technique has many advantages over the Pitot tube like extraordinary temporal resolution, less intrusive to the flow, can be used near to the wall to capture boundary layer flows and can also measure multidimensional velocity fields. New fiber-optic techniques make optical alignment easier than before. However, an LDV system is expensive.

III) Shadowgraph Photography: It is an old optical technique. Shadowgraph measures deflection as well as the displacement of the light beam at the exit plane of the apparatus. With this principle technique, flame cross-section area can be captured and further processing with known gas flow rate and temperature, average gas velocity can be obtained.

IV) Particle Tracking Photography: This is also an old technique used to measure the velocity of the fluid particle. As the name suggests, individual particles are tracked, so this technique is a Lagrangian approach. Whereas Particle Image Velocimetry (PIV), is a Eulerian method that measures the velocity field of a fluid at a grid.

V) Hot-wire anemometry: It is the most well-known thermal anemometer. The core of the anemometer is an exposed hot wire either heated up by a constant current or maintained at a constant temperature. In either case, the heat lost to fluid convection is a function of the fluid velocity.

VI) Schlieren Photography: This technique employs variation in refractive index with density to map a thermal or a species concentration field. Schlieren, shadowgraph and interferometry techniques have been used for many years to study the distribution of density gradients within a transparent medium. Of these methods, the Schlieren technique combines relatively low cost with high sensitivity. Flame velocity can be measured with the help of the flame area method and Schlieren image.

2.4.4 Static pressure measurement (Baukal 2000)

Static pressure distribution is a crucial parameter along with the heat transfer characteristics for an impinging jet flow on delicate target. Besides, it helps in determining the extent of stagnation region and stagnation velocity gradient (β_s). Static pressure distribution is not uniform in case of impinging jet flows. This is due to rapid deceleration and deflection of the impinging jet. Static pressure has been measured by either Pitot tube or inclined differential manometer attached to very small pressure tapping (1mm) in literature.

2.4.5 The composition of gas species measurement (Baukal 2000)

Gas composition is helpful in deciding combustion effectiveness. The concentration of gas species close to the target surface aids in determining the amount of thermochemical heat release from the radical species in advance. Gas analyzers or infrared imaging technique have been used to determine the gas composition.

2.5 EVALUATION OF ISOTHERMAL JETS IN RELEVANCE WITH FLAME JETS

Impinging flame jets are commonly approximated by hot inert jets since the flow behavior of both types of jets is comparable. Impinging jets are always preferred to enhance heat transfer rate as it yielded high local and averaged heat convection

coefficients. Therefore, applications of impinging jets are wide-ranging from cooling to heating in industrial as well as the domestic field. These applications include electrical and electronic cooling, turbine blade cooling, combustion wall cooling, drying of paper, heating of metal ingots, heat treatment of glass, etc. A plentiful of research on the impinging hot/cold jet can be found in the literature. Exclusive reviews on experimental studies (Jambunathan et al., 1992, Viskanta 1993) have reported the effect of parameters such as Reynolds number (Re), the nozzle-to-plate spacing, nozzle geometry, turbulence intensity on the heat transfer characteristic of an impinging jet. The characteristic regions of impinging isothermal jet and flame jet are same.

2.5.1 Analysis of the experimental data reported in the literature

According to Viskanta (1993), the aerodynamics of a single flame jet is very similar to the aerodynamics of a single isothermal jet. Experiments by Meer (1987) showed that the radial velocity gradients at the stagnation point are found to be equal. He also reported that the flame jet axial velocity decays slightly faster than in the isothermal jet. Meer (1987) also reported that if the properties of the burnt gases are taken at the temperature corresponding to the average enthalpy in the boundary layer formed on the plate, then the Nusselt number distribution of flame jets matches reasonably well with isothermal jets. The main difference between these jets is the presence of a reaction zone in the stagnation region and the viscous boundary layer.

Figures 2.20, 2.21 and 2.22 show the comparison of experimental Nusselt number for flame and air jets reported by Hindasageri *et al.* (2014) and Katti *et al.* (2011) respectively. The technique for obtaining the heat flux in both the cases is different. However, the heat transfer coefficient (h) being the phenomenon constant does not change based on the linear rate equation for heat flux given in Equation (2.3).

$$q'' = h(T_w - T_{aw}) \quad (2.3)$$

The functional form with then on dimensionalized parameters is given Equation (2.4).

$$Nu = f(Re, Pr) \quad (2.4)$$

For the flame and air jets the Prandtl number (Pr) is almost the same (0.71-0.75), hence the comparison of a Nusselt number by fixing Reynolds number same makes sense.

Nusselt number is calculated by Equation (2.5) where d is the diameter of the nozzle and k is the thermal conductivity of jet.

$$Nu = \frac{hd}{k} \quad (2.5)$$

For the smallest $Z/d = 2$, it is observed that the Nusselt number for the flame jet is higher than that of air jet by up to 60% except for the cases ($Re = 1000, 1200$ and 1400) when the premixed inner cone of the flame touches the impingement plate. For $Z/d = 4$ and 6 , there is a good matching of a Nusselt number near the stagnation region for some cases of Re . However, away from the stagnation region, the Nusselt number for flame jets is always higher as compared to air jets. It is further observed from Figures 2 and 3 that this difference between Nusselt number for flame and air jets away from the stagnation region is more for lower Re . Furthermore, at the stagnation point, the ratio of Nusselt number for flame jets to that of air jets decreases with the increase in Re .

Recently, Kuntikana and Prabhu (2016) compared the Nusselt number and effectiveness distribution from cold jet (at ambient temperature), hot jet (at 100°C) and flame jet shown in Figure 2.23. It was observed that the Nusselt number distribution for the hot and cold jet at fixed Reynolds number is not dependent on jet temperature for a proper reference temperature of the hot jet. Non dimensionalized reference temperature in terms of Effectiveness (η) was defined as given in Equation (2.6).

$$\eta = \frac{T_{ref} - T_\infty}{T_{jet} - T_\infty} \quad (2.6)$$

Nusselt number distribution of flame jet almost matched with isothermal jets whereas effectiveness is found lower attributed to more entrainment of surrounding air.

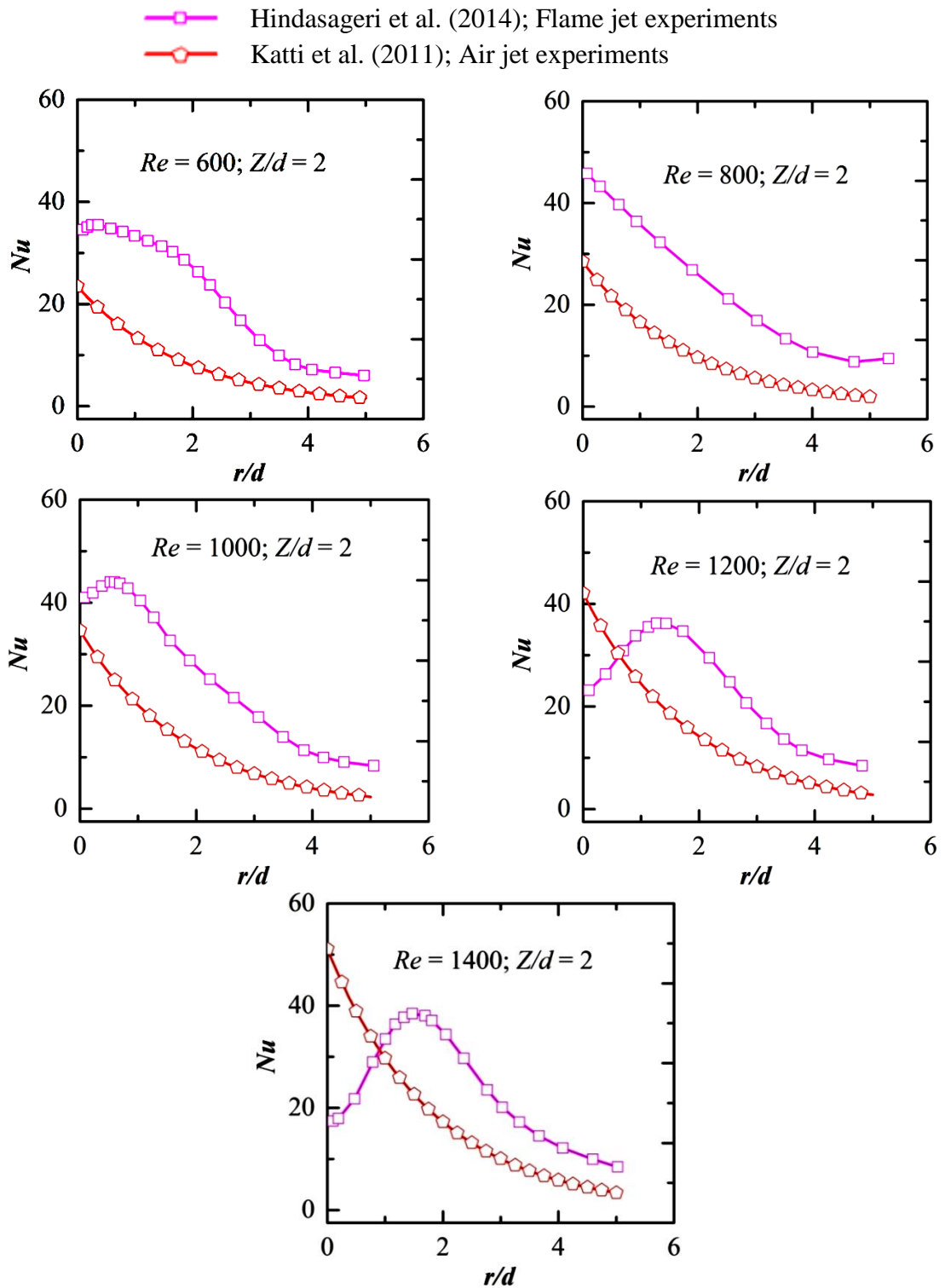


Figure 2.20 Comparison of Nusselt number distribution of impinging air jets with impinging flame jets for varying Re at $Z/d = 2$

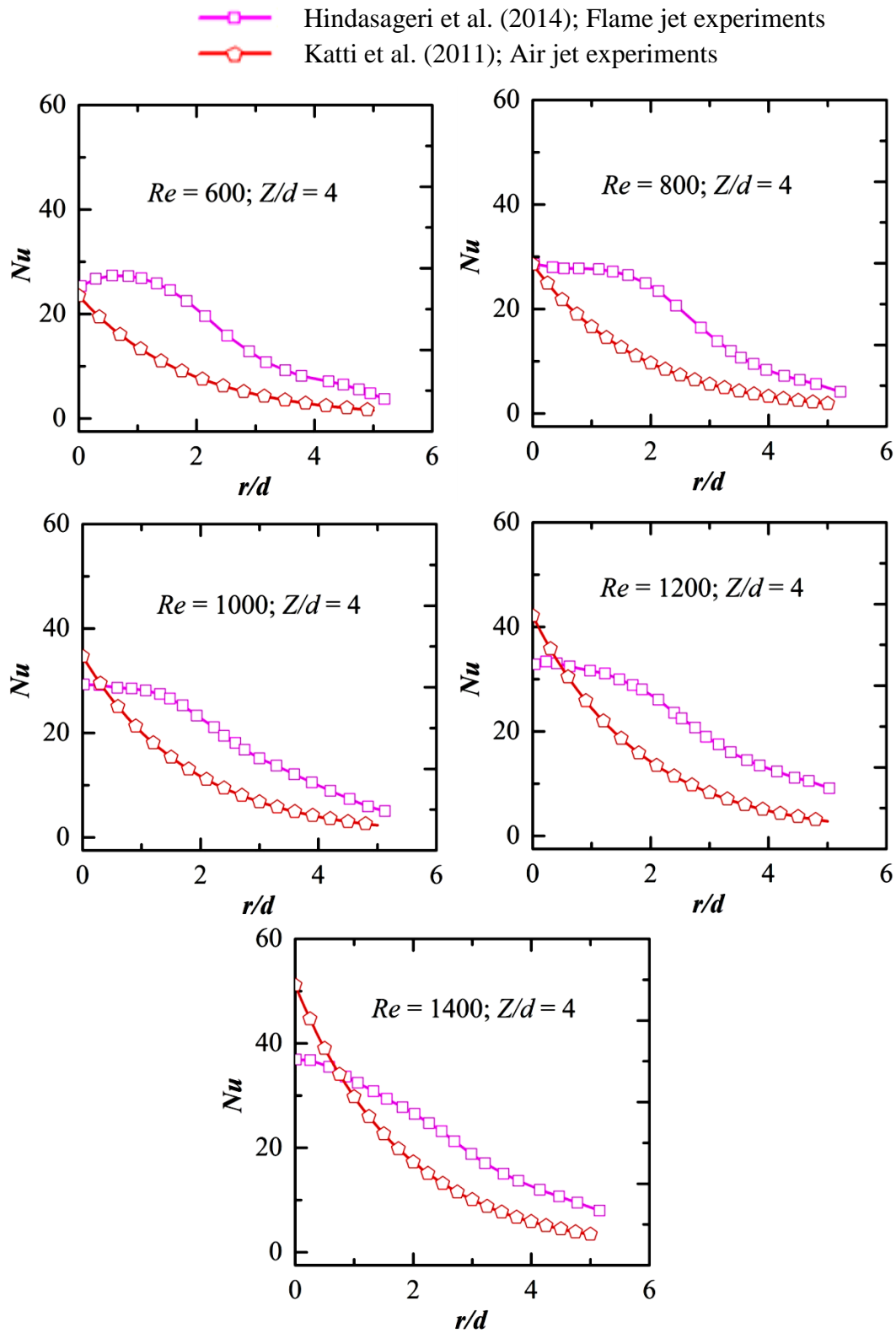


Figure 2.21 Comparison of Nusselt number distribution of impinging air jets with impinging flame jets for varying Re at $Z/d = 4$

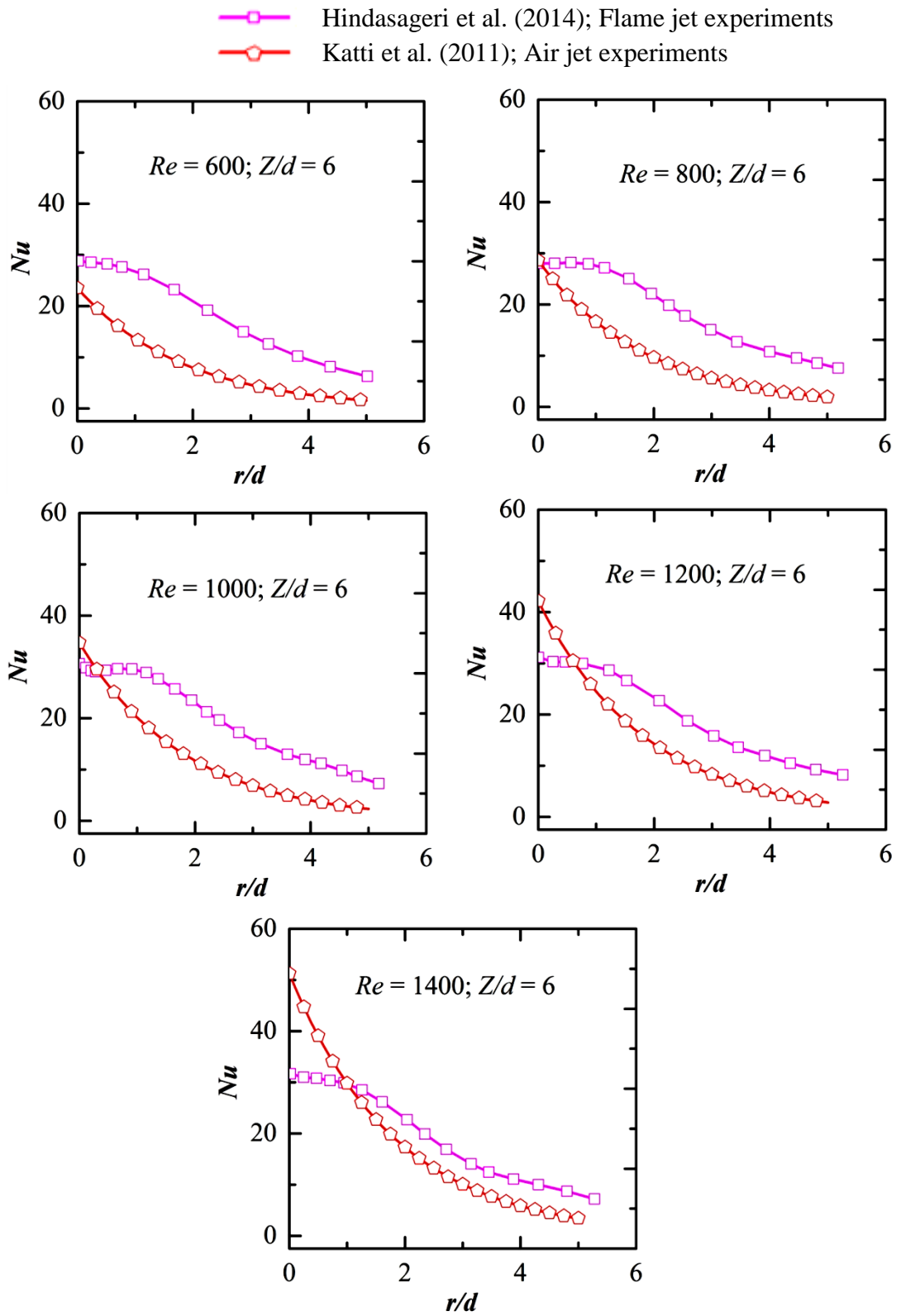


Figure 2.22 Comparison of Nusselt number distribution of impinging air jets with impinging flame jets for varying Re at $Z/d = 6$

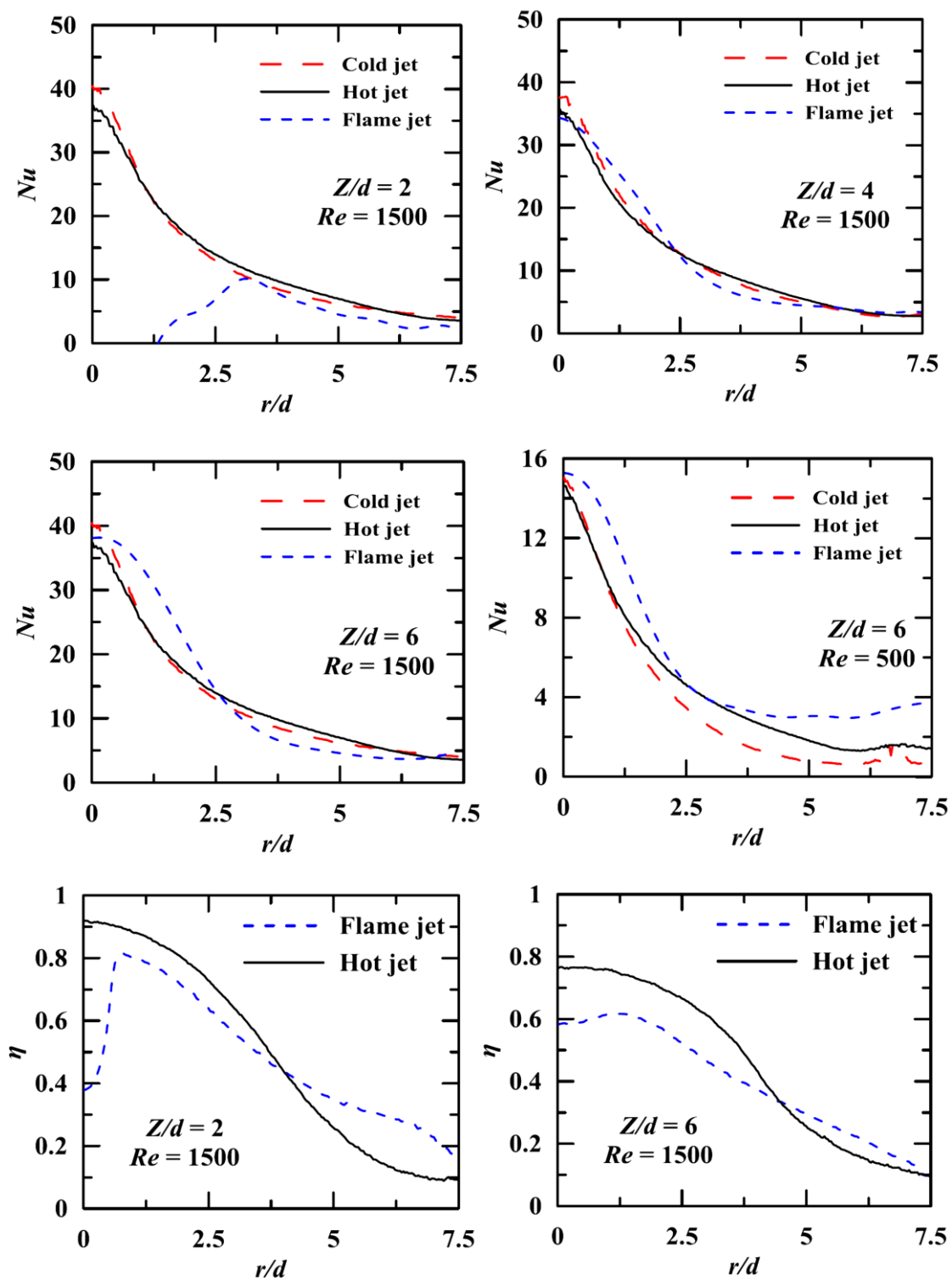


Figure 2.23 Comparison of Nusselt number and Effectiveness distribution of impinging air jets with impinging flame jets at various configuration (Kuntikana and Prabhu, 2016))

2.6 NUMERICAL STUDIES IN FLAME JET IMPINGEMENT

As flame jets application are wide, it is very important to know the heat transferred to the target object by the flames. Along with experimental studies, few numerical investigations are found in the literature aiming to optimize the existing system and to authorize new possible designs. The advancements in computer hardware and associated Softwares have inspired many numerical studies on flame jet impingement in recent time.

Conolly and Davies (1972) investigated the heat transfer at the stagnation point of a blunt body submerged in flames with the help of numerical solutions to the appropriate boundary layer conservation equations. The results for forced convective heat transfer coefficient were compared with the experimental results and it was observed that numerical results were in good agreement to experimental values.

Exergy and entropy generation analysis of Methane–air flame jet impingement process was carried out numerically by Som et al. (2007). A global two-step chemical kinetics and RNG k - ϵ model was used to analyze turbulent flames. The numerically obtained Nusselt number was fairly in agreement with the experimental result.

Chander and Ray (2008) studied laminar methane-air flame jet heat transfer at the stagnation point numerically as well as experimentally. A reduced reaction mechanism of 16 species and 25 reactions were employed in the Fluent software to obtain the results. A numerical procedure adopted in the study is well explained and achieved results for heat flux were in a good match with experimental values.

Chander and Ray (2011) conducted a numerical and experimental study on the occurrence of an off-stagnation peak in heat flux and explained that the shift in peak heat flux from stagnation point is due to the corresponding peak in axial velocity profile.

Hindasageri et al. (2015 and 2016) and Tajik et al. (2015) used the 30 species skeletal reaction mechanism GRI Mech 3.0 developed by Lu and Law (2018) for Methane-air combustion in their respective studies.

A numerical investigation by Jarray et al. (2016) on premixed Methane-air flame jet impingement employed Zimont combustion model along with a realizable k - ϵ model to

take care of turbulence kinetics in fireproof test applications. Heat flux and effectiveness were compared with experimental results and was in good agreement. This was the only transient numerical study on a flame jet is found in the literature.

2.7 INVERSE INVESTIGATIONS IN THE FIELD OF JET IMPINGEMENT

Estimation of the heat flux from known transient temperature distribution is an Inverse problem. The solution to these inverse heat conduction problem would estimate transient heat transfer to or from impinging jets. In the literature of jet impingement, various 1-D, 2-D and 3-D inverse heat conduction (IHC) models for linear as well as for non-linear cases can be found.

Wikstrom et al. (2007) have inversely retrieved transient surface temperature and heat flux of the slab from the history of temperatures at the interior points with the 1-D heat conduction model. A spectral method was used to get the ordinary differential equation (ODE) from 1-D transient Partial differential equation (PDE). Further, with the help of a numerical method that ODE was solved.

Haghighi et al. (2009) employed 3-D IHC approach to estimate unknown boundary heat flux of thick functionally graded plates. The forward problem was solved using a mixed finite element and differential quadrature method while the conjugate gradient method (CGM) in conjunction with the adjoint problem was applied to solve the inverse problem.

Feng et al. (2010) have used Laplace transform to one-dimensional heat conduction and obtained expression relating temperature and heat flux on the front and back surface. Later, ad hoc approximations assumed earlier to the transfer functions are replaced by better approximations through iterations in his follow-up work (Feng et al. 2010). Further, Feng et al. (2011) have come up with the new technique as a solution to the three-dimensional inverse heat conduction problem where transfer functions were elaborated in terms of polynomial through Hadamard Factorization theorem. These polynomials were handled through an iterative procedure. Further, the technique is validated for constant but non-uniform heat flux application.

Ryfa and Bialecki (2011) introduced a technique based on the superposition principle with which the spatial distribution of heat convection coefficient is possible to estimate from transient temperature measurements. Heat convection coefficient was retrieved explicitly (directly) and implicitly (indirectly), i.e. through estimation of surface temperature and heat flux respectively. The assumption of linear variation between temporal heat flux and temperature over the entire period of measurement is approximated by linear spline in their follow up study (Ryfa and Bialecki, 2011) and concluded that performance of explicit technique was better than its implicit counterpart.

Both Cui et al. (2012) and R. Dou et al. (2016) used the same approach to estimate transient heat flux from the measured temperature inside the slab. Heat flux was treated as an optimization variable in both the studies. The optimization problem was solved further by minimizing the differences between the estimated temperatures and the measured ones. For sensitivity analysis, the earlier study made use of the complex-variable-differentiation method while later study employed the Levenber–Marquardt approach.

Lu et al. (2012) claimed development of a fast, robust and efficient algorithm which combines advantages of the conjugate gradient based iterative-type and Tikhonov-type of regularization methods. The algorithm was validated through a couple of simulation cases along with an experimental case study.

Hao et al. (2013) have proposed an algorithm for 1-D heat conduction problem which determines time-dependent heat flux applied to a slab from surface temperature history. The algorithm was established through an analytical solution to Fourier equation using Duhamel theorem which considers the effect of time dependent boundary condition. To demonstrate the validity of algorithm, results for same input are compared with a widely used Cook-Felderman algorithm which works on the semi-infinite concept.

Both Duda (2015) and Jaremkiwicz (2018) employed inverse space marching technique based on finite element control volume in order to estimate transient temperature distribution of whole thick walled complex shaped element from the known temperature at few selected points inside or outside of the element. Local heat

flux and heat convection coefficient were also estimated at unknown boundary edge with the same technique.

2.8 THE LITERATURE ON RIBBED SURFACES

Effect of ribbed surfaces on the heat transfer is exclusively studied in jet impingement studies. Different shapes and sizes of the rib are considered by the researchers. Triangular, semicircular, rectangular, square-shaped ribs are considered in different configurations studied by the researchers. Configurations are characterized by the pitch to width ratio (dia), height to width ratio (dia).

Gau and Lee (1992) did experiments to study flow structure and heat transfer from slot jet to the rib roughened surfaces. Square rib (3mm) elements were glued over the length of the plate for two different pitch to width ratio (P/W) and studied them for the various Reynolds numbers, slot width (D) and jet to plate spacing (Z/d). At a higher mass flow rate (larger dimension of slot width for same Reynolds number), significant heat transfer enhancement is observed in rib roughened surfaces.

Miyake et al. (1994) investigated the heat transfer augmentation from axisymmetric circular impinging jet for concentric rib configuration for different height to jet diameter ratio and pitch to height ratio. They highlighted the importance of distance between the stagnation point and rib along with the pitch to height ratio for enhancement of heat transfer rate in stagnation and wall jet region.

Gau and Lee (2000) carried out experiments to understand the flow behavior and heat transfer rate from slot jet impinging on the triangular ribbed flat surface. At a higher mass flow rate, significant heat transfer enhancement is observed in rib roughened surfaces. It was found that triangular rib geometry has more advantage over the rectangular ribs for heat transfer augmentation.

Son et al. (2005) Studied cylindrical, diamond-shaped and hexagonal rib elements for maximizing the heat transfer with minimal pressure loss in case of cross flow. It was found that hexagonal rib helped in the enhancement of heat transfer by 10% with minimal pressure loss.

Son et al. (2005) (Fillet radii) compared the heat transfer from rib element having a sharp edge with a rounded edge. Sharp-edged rib performance was observed better than round edged rib.

Wang et al. (2011) optimized the location of the rib in cross-flow jet impingement to control the heat transfer. Rib with rectangular cross section was placed such a manner that flow reattachment region coincides with the jet impingement region and heat transfer enhancement found was significant.

Caliskan and Baskaya (2012) considered V-shaped rib roughened arrays for multiple circular jet impingement. A significant increase in overall heat transfer rate is observed with 4-35% increment in stagnation point Nusselt number value.

Kito et al. (2012) worked on the spacing between the ribs to optimize it for single Reynolds number. Experiments were conducted with the single rib to identify the optimum location of it from stagnation point. Later considering the phenomenon of reattachment, the minimum distance between the first and second rib was identified.

Nantadusit et al. (2012) studied heat transfer characteristics of the transverse perforated ribs under constant single Reynolds Number. Ribs performance was examined for perforations made at different locations and inclination of perforations on the rib. It was observed that inclined perforated ribs improved the heat transfer rate significantly than the straight perforated and solid ribs.

Caliskan (2013) also studied the effect of perforations in rib over solid one and it was observed that perforated ribs have higher heat transfer rate.

Labbe (2013) with Large Eddy Simulation, successfully captured all possible vortices on and around rib element. Reattachment and recirculation zone are clearly identified which helps in understanding the flow and heat transfer phenomenon in jet impingement on the ribbed surface.

Tan et al. (2014) Studied the effect of the orthogonal, V-shaped and inverted V-shaped ribbed surfaces on the laterally averaged heat transfer in semi-confined channel with four transverse ribs and found that averaged heat transfer is more up to 30% than the smooth surface and more uniform in case of the inverted V-shaped ribbed surface.

2.9 SUMMARY OF THE LITERATURE REVIEW

Massive theoretical and experimental research on flame jet impingement is covered in the literature. A broad overview from all the perspective is presented covering all the parameters affecting heat transfer, employed measurement techniques and heat augmentation techniques. Based on the literature review, the following observations are made:

- Typically the heat transfer coefficient under an impinging jet has a bell-shaped distribution with a maximum value at the stagnation point, followed by a rapid decrease with radial distance from the jet centreline.
- This also leads to the non-uniformity of heat transfer rate, which is a big disadvantage of jet impingement.
- Even though active research is simultaneously being carried out on both the flame and air jets, a proper comparison of impingement heat transfer distribution for the two cases lacks in the literature.
- The knowledge of reference temperature is essential to estimate the proper value of the heat transfer coefficient. However, the estimation of the reference temperature is not straightforward as the flame jet temperature is not the same as that of the surroundings and further varies along the radial direction on the impingement plate.
- Nusselt number distribution and hence heat convection coefficient remains the same from the time of impingement till the steady state achieved when the jet parameters remain constant.
- Most of the reported experimental data assume one-dimensional heat diffusion in the impingement plate citing the thinness of the plate used. A quantitative description of the one dimensional/ multi-dimensional nature of heat diffusion in the impingement plate is not available in the literature.
- Studies using semi-infinite medium concept (Hindasageri et al. 2014) have been used for spatially varying heat transfer distribution while the analytical solution is that for spatially constant heat transfer boundary condition.
- For the reported transient three dimensional analytical and experimental studies mostly numerical IHCP procedure has been adopted (Loubat et al. 2004, Hindasageri et al. 2014).

- Furthermore, the effect of radiation loss from the impingement plate has not been addressed in the literature.
- The effect of the ribbed surface on heat transfer distribution in case of flame jet impingement has not been studied yet.

2.10 MOTIVE AND SCOPE FOR THE PRESENT WORK

Most of studies on impinging jet have reported steady state heat transfer distribution over the impinging target. On the other hand, work on impinging jet heat transfer in transient condition is very scarce. The studies concerning the thermal stresses and its consequences on the material performance requires the understanding of transient state of the impinging target.

Apart from experiments, the simplest way to get transient temperature distribution and thus transient heat transfer is through the numerical simulations assuming jet impingement as conjugate problem. From literature, it is concluded that no numerical model is perfect in predicting the heat transfer from impinging flame and air jets and choosing a turbulence model is still required skillful tactics considering an accuracy and computation time required. Thus, one can only choose better performing turbulence model over the others for a particular application where accuracy can be compromised in some extent. The applications such as cooling of critical high-temperature turbine blade, thermal protection to launch pad, vertical/short take-off and landing jet devices and thermal management of electronic equipment where accuracy is requisite, it is worth to find a tool alternative to simulation.

Instead solving conjugate problem, fluid flow model can be decoupled from conduction in the solid. Ryfa and Bialecki [2011] suggested that it is possible to replace this decoupled model with experimentally estimated boundary conditions such as temperature (Dirichlet type), heat flux (Neumann type) or heat convection coefficient and reference temperature (Robin type). Though temperature boundary condition appears easier to apply, it is hard to implement it as it involves large transient temperature data at the impinging side which is tough to get without disturbing the flow. The application of heat flux boundary condition sometime becomes cumbersome and inconvenient as heat flux measurement techniques (naphthalene sublimation technique,

calorimeter technique, and heat flux sensors) are less accurate and costliest. Besides, these (Dirichlet and Neumann) boundary conditions cannot be generalized, because, as and when material and impinging fluid properties changes, temperature and flux also changes. Thus, the most appropriate boundary condition in view of generalization is Robin boundary condition. The reference temperature either can be measured directly or can be estimated (analytically) whereas heat convection coefficient can only be estimated (analytically). Moreover, heat convection coefficient and reference temperature can be generalized with the help of dimensionless Nusselt number and effectiveness respectively.

Nusselt number distribution for unsteady and steady state in impinging jets is experimentally studied by O'Donovan (2005). Experimental results of O'Donovan (2005) for normally impinging circular jet of diameter 13.4 mm at $Z/d = 1.5$ is shown in Figure 2.24. Figure 2.24a shows micro-foil heat flux sensor measured time-averaged data over entire r/d whereas Figure 2.24b illustrates hot Film Sensor measured time-trace data of Nusselt number at location with green markers in Figure 2.24a. Thus, it can be concluded that Nusselt number distribution and hence heat convection coefficient remains same from the time of impingement till the steady state achieved when the jet parameters remains constant. Similar observation is reported in numerical study on jet impingement by Ryfa and Bialecki (2011).

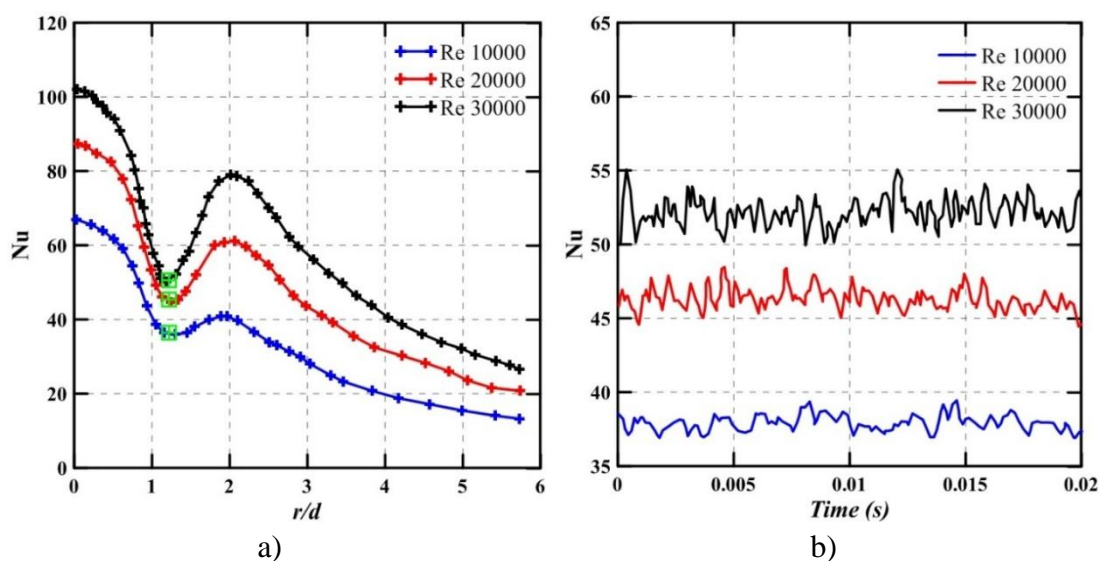


Figure 2.24 Normally impinging circular jet; $d=13.4$ mm; $Z/d = 1.5$ a) Nu distribution Time-averaged b) Nu Time-trace (O'Donovan, 2005)

2.10.1 Simultaneous estimation of heat convection coefficient (h) and reference Temperature (T_{ref})

Estimation of heat transfer from impinging flame jets has been extensively studied with techniques ranging from simple calorimeter, heat flux sensors to application of inverse conduction problems. While the former two methods would provide heat flux data, the latter is useful in obtaining the proper heat transfer coefficient and reference temperature required for any engineering purpose. The knowledge of reference temperature is essential to estimate the proper value of the heat transfer coefficient as per Equation (2.7).

$$q'' = h(T_{ref} - T_w) \quad (2.7)$$

However, the estimation of reference temperature is not straightforward as the flame jet temperature is not same as that of the surroundings and further varies along the radial direction on the impingement plate. In most considered thin foil technique in jet impingement studies, linearity (of the form, $mx + c = y$) between surface heat flux and corresponding surface temperature is used to find out heat convection coefficient and the reference temperature simultaneously as per Equation 2.8. It is obtained by rearranging Equation (2.7).

$$-\frac{q''}{h} + T_{ref} = T_w \quad (2.8)$$

Accordingly, inverse of slope and intercept of the linear fit gives heat convection coefficient and reference temperature respectively. Multiple values of heat flux and temperature are required to fit the line and those have been usually obtained by conducting several steady state experiments.

Instead steady state values, transient heat flux and corresponding wall temperatures can be utilized in Equation 2.8 to obtain heat convection coefficient and reference temperature simultaneously. These transient values of heat flux and corresponding temperatures can only be obtained through application of Inverse heat conduction (IHC) problem without disturbing the flow at the impingement side.

2.11 OBJECTIVES OF THE PRESENT INVESTIGATION

The main objective of the current reaserch work is to find heat transfer distribution of impinging Methane-air premixed flame jets and details of the objectives are as follows:

1. To review and analyze the literature pertaining to heat transfer characteristics of premixed flame jets
2. To Study and analyze the heat transfer distribution of impinging methane-air flame jet and air jet impingement
 - 2.1 To compare the experimental data reported in literature for methane-air flame jet and air jet impingement
 - 2.2 To carry out numerical investigation for studying the flow pattern of methane-air flame jet and air jet impingement
3. To develop an analytical method for estimation of heat transfer distribution of impinging flame jets based on transient measurements
 - 3.1 To estimate heat transfer coefficient and refernce temperature simultaneoulsy using solution to one dimensional/multi-dimensional heat condcuton problem
 - 3.2 To establish a procedure to correct radiation loss from impingement plate
4. To determine the heat transfer distribution of impinging flame jets in case of ribbed surfaces
 - 4.1 To compare heat transfer coefficient and reference temperature of ribbed surfaces with smooth surfaces
 - 4.2 To conduct numerical investigation for understanding the flow physics on and around rib elements

2.12 CLOSURE

A detailed analysis of literature is carried out in this chapter. Fundamental, as well as parametric issues, were observed. Based on the research gaps, objectives are enlisted. In the next chapter, the experimental setup and the instruments used for experimentation is elucidated.

Chapter 3

3 EXPERIMENTAL AND NUMERICAL METHODOLOGY

3.1 INTRODUCTION

This chapter describes the experimental setup and the instruments used to perform the experiments. The discussion includes the validation of the experimental set-up along with the calibration of each instrument used during experimentation. Numerical procedure adopted in the present work is also explained in brief.

3.2 EXPERIMENTAL SET-UP

Figure 3.1 is the schematic of experimental set up used in the study on flame jet impingement heat transfer. It consists of two venturimeters and two orificemeters which are used as flowmeters. To measure air flow rate, venturimeters are used whereas for measurement of methane flow rate orificemeters are used. The flow rate of methane is almost 5 % of mixture flow rate (for equivalence ratio=1.0), thus to obtain measurable head in water manometer, orificemeters are employed. According to the requirement of higher and lower mass flow rates, different flowmeters are used. Table 3.1 gives the specifications of flowmeters used in the set-up.

Table 3.1 Specifications of flowmeters

Device	Throat/Orifice diameter (mm)	Remark
Venturi meter	1.5	used to regulate lower air flow rate. Thus named as AVL (Air Venturimeter for lower flow rate)
	2.5	used to regulate a higher air flow rate. Thus named as AVH (Air Venturimeter for higher flow rate)
Orificemeter	0.5	used to regulate lower methane flow rate. Thus named as MOL (Methane Orificemeter for lower flow rate)
	1	used to regulate higher methane flow rate. Thus named as MOH (Methane Orificemeter for higher flow rate)

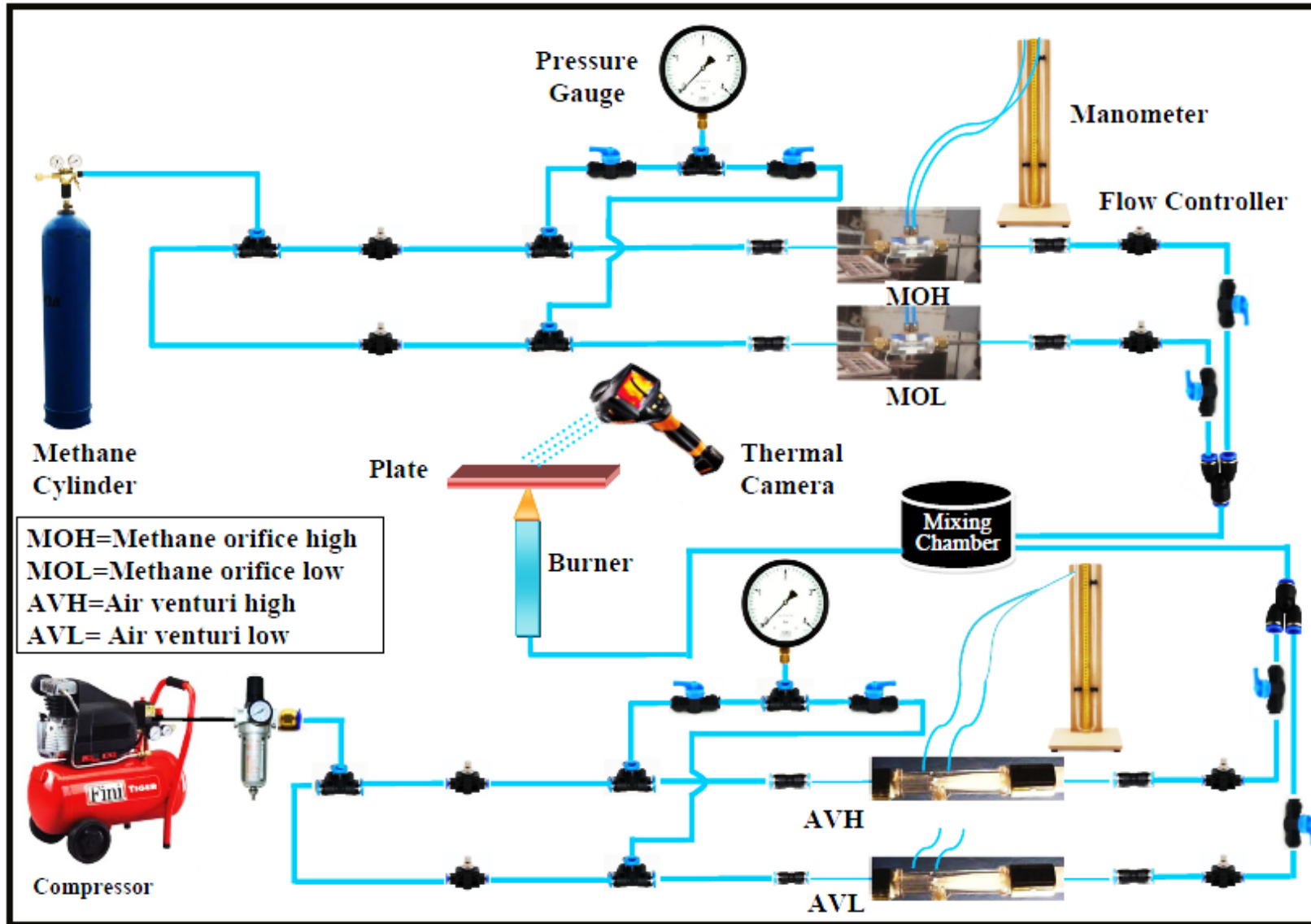


Figure 3.1 Schematic of experimental Set-up

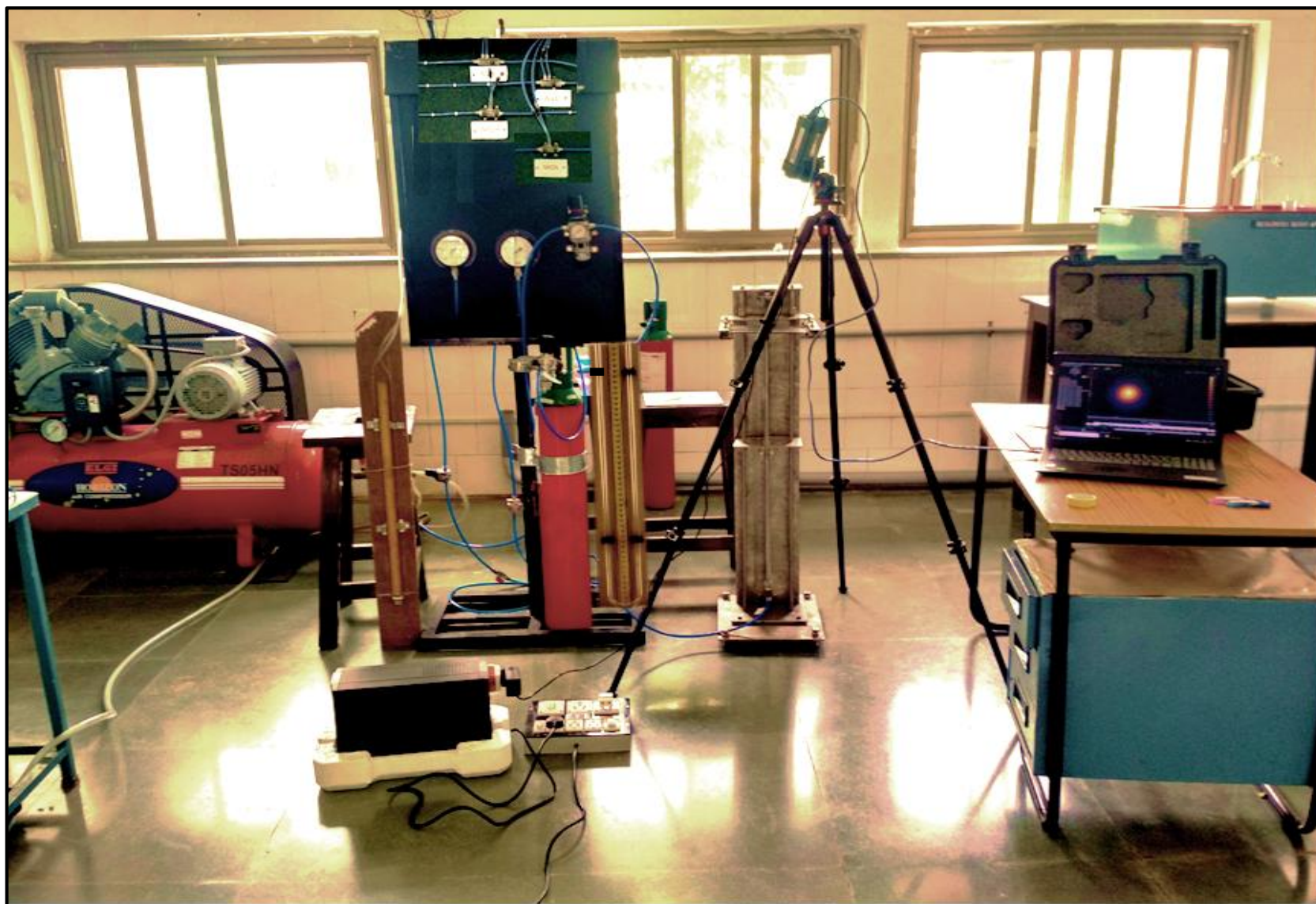


Figure 3.2 Experimental laboratory set-up

Design of flowmeters is discussed in detail in Appendix A.1. Flowmeters are operated at 2 bar gauge pressure to avoid leakages into the flow line. Additionally, the entire flow line is operated with push-fit fittings to ensure leak-free operation. Even differential manometer is designed with transparent acrylic tubing fitted with push-fit fittings at its end. The ratio of burner tube length to diameter is maintained at least 80 to ensure fully developed flow.

The venturimeters and orificemeters are directly calibrated with DryCal Defender calibrators, BIOS International make. During calibration, operating pressure in the flowmeter was maintained at 2 bar gauge pressure and flow was regulated with the downstream valve after which calibrator was connected. Details of the calibration and operating range for flowmeters are presented in Appendix A.2 and A.3 respectively.

The temperature distribution of the plate from the non-impingement side is measured with the help of thermal infrared (IR) camera A325sc, FLIR make. Specifications of this thermal camera are given in Table 3.2. Calibration details for the thermal camera are presented in Appendix A.4.

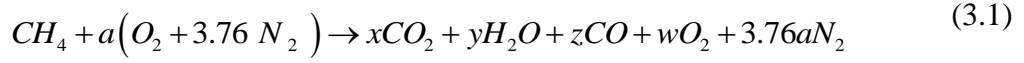
Table 3.2 Specifications of Thermal camera

Model	FLIR A325sc
Detector	Uncooled Microbolometer
Spectral range	7.5 – 13.0 μm
Pixel Resolution	320 \times 240
Digital Data Streaming	Gigabit Ethernet (60 Hz)
Minimum focus distance	0.2 m
Temperature range	-20°C to 2000°C
Accuracy	\pm 2% of reading
Frames per second	60

3.3 DATA REDUCTION:

The thermal properties for methane gas are referred from NIST data source, while properties of air are referred from Zografos et al. (1987). The chemical balance equation for the combustion of methane and air is as per Equation (3.1).

Chemical balance equation:



For $\phi = 1$, $a = 2$ and when ϕ is not equal to 1, $a = 2 / \phi$. Here, ϕ is the equivalence ratio.

The air/fuel (A/F) ratio and equivalence ratio (ϕ) are given by Equation (3.2) and Equation (3.3) respectively.

$$\frac{A}{F} = \frac{\dot{m}_{air}}{\dot{m}_{fuel}} \quad (3.2)$$

$$\phi = \frac{(A/F)_{stoic}}{(A/F)_{act}} \quad (3.3)$$

Mixture density and Mixture viscosity is calculated as per Equation (3.4) and Equation (3.5) respectively.

$$\rho_{mix} = \sum Y_i \rho_i = Y_{air} \frac{P_{air}}{R_{air} T_{air}} + Y_{CH_4} \frac{P_{CH_4}}{R_{CH_4} T_{CH_4}} \quad (3.4)$$

$$(At \phi = 1, Y_{CH_4} = 0.054, Y_{air} = 0.946)$$

$$\mu_m = \frac{\sum \mu_i X_i \sqrt{M_i}}{\sum X_i \sqrt{M_i}} \quad (3.5)$$

Mixture Reynolds number at the exit of burner is calculated as per Equation (3.6)

$$Re = \frac{\rho_{mix} \bar{u} d}{\mu} \quad (3.6)$$

Where, the average velocity (\bar{u}) of the mixture is given by Equation (3.7)

$$\bar{u} = \frac{\dot{m}_{mix}}{\rho_{mix} A} \quad (3.7)$$

The uncertainties estimated by the method of Moffat (1985) are presented in Appendix B.

3.4 NUMERICAL METHODOLOGY

Apart from experiments, the simplest way to get transient temperature distribution and thus transient heat transfer is through the numerical simulations assuming jet impingement as a conjugate problem. This section discusses the numerical treatment adopted in present work to study flame jet and air jet impingement. For all the cases discussed in this section, two dimensional axisymmetric CFD simulations are carried out using Fluent 14.5 software and numerical modeling is done in Gambit 2.4.6.

3.4.1 CFD simulation for flame jet impingement

The numerical procedure adopted in the present study is the same as that employed in Chander and Ray (2008). The physical domain and the boundary conditions for the impinging jet are shown in Figure 3.3.

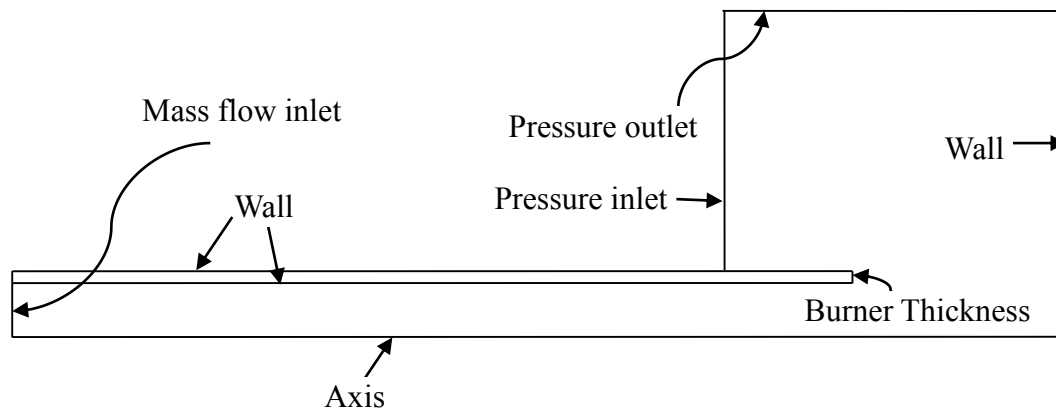


Figure 3.3 Physical model with boundary conditions

The adaptive meshing technique available in FLUENT is used to refine the grid only at the region of high interest as shown in Figure 3.4. This saves computational time. The coarse grid away from the premixed cone is of 1 mm size and the fine grid is 0.125 mm size near the inner premixed cone. The grid independence test is carried out by varying the grid size near the impingement plate from 0.125 mm to 0.0625 mm. Change in heat flux value at the stagnation point is found only 1.5 kW/m² for Re 1000, Z/d=4. A CFD simulation using the 30 species skeletal reaction mechanism of GRI Mech 3.0 developed by Lu and Law (2008) is used to obtain numerical solution for two dimensional axisymmetric case.

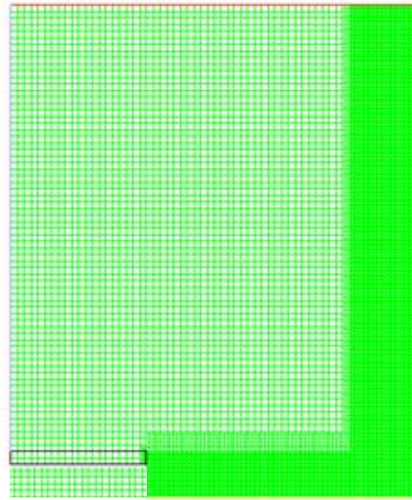


Figure 3.4 Adaptive mesh near the wall

The segregated solver, steady state model with volumetric reaction is selected for the present numerical simulation. Laminar finite rate turbulence-chemistry interaction is selected with stiff chemistry solver. Volumetric reactions with multicomponent diffusion are selected in the FLUENT software. The solution is initially solved for cold flow by unselecting the energy and species equations in the solver. After 100 iterations of cold flow a small region above the tube exit is patched to a temperature of 2000K and then the solution is iterated by selecting the energy and species equations. The solution is iterated until the convergence criterion of 10^{-6} for continuity and species equations and 10^{-7} for energy equation is met. Flame impinging on a wall is always maintained at 300 K to get the heat exchanged with it.

Governing Equations

The governing equations for the two dimensional axisymmetric reacting flows are given in Equations (3.8-3.12). The energy equation is derived from the principle of conservation of mass. The momentum equations are derived from the Newton's second law of motion. The energy equation is derived from the first law of thermodynamics. The species conservation equation is derived from the fact that the net change in individual species is equal to the individual molecule diffusion in the mixture (due to concentration gradient) and production/generation (ω_i) from chemical reactions. Due to chemical exothermic/endothermic reactions there is either heat generation or heat

absorption and this phenomenon is quantified through the volumetric heat generation term (\dot{q}''').

The terms u , v and w represent bulk fluid velocity along the coordinate directions (x , r for axisymmetric case and x , y , z for the three dimensional case). The term h_s represents the sensible enthalpy of the mixture. The term Y_i represents the individual mass fraction the reactants/ products. The term D_i represents the individual species diffusion coefficient.

Continuity Equation:

$$\frac{\partial(\rho u)}{\partial x} + \frac{1}{r} \frac{\partial(\rho v r)}{\partial r} = 0 \quad (3.8)$$

x -momentum Equation:

$$\begin{aligned} \frac{\partial(\rho u u)}{\partial x} + \frac{1}{r} \frac{\partial(\rho u v r)}{\partial r} = & -\frac{\partial p}{\partial x} + \frac{\partial p}{\partial x} \left(\frac{4}{3} \mu \frac{\partial u}{\partial x} \right) + \rho g_x \\ & + \frac{1}{r} \frac{\partial}{\partial r} \left(r \mu \frac{\partial u}{\partial r} \right) - \frac{\partial}{\partial x} \left(\frac{2\mu}{3r} \frac{\partial(vr)}{\partial r} \right) + \frac{1}{r} \frac{\partial}{\partial r} \left(r \mu \frac{\partial v}{\partial r} \right) \end{aligned} \quad (3.9)$$

r -momentum Equation:

$$\begin{aligned} \frac{\partial(\rho u v)}{\partial x} + \frac{1}{r} \frac{\partial(\rho v v r)}{\partial r} = & -\frac{\partial p}{\partial r} + \frac{\partial}{\partial x} \left(\mu \frac{\partial u}{\partial r} \right) - \frac{1}{r} \frac{\partial}{\partial r} \left(\frac{2r\mu}{3} \frac{\partial u}{\partial x} \right) + \frac{\partial}{\partial x} \left(\mu \frac{\partial v}{\partial x} \right) \\ & + \frac{1}{r} \frac{\partial}{\partial r} \left(\frac{4r\mu}{3} \frac{\partial v}{\partial r} \right) - \frac{1}{r} \frac{\partial}{\partial r} \left(\frac{2}{3} \mu v \right) \end{aligned} \quad (3.10)$$

Energy Equation:

$$\frac{\partial(\rho u h_s)}{\partial x} + \frac{1}{r} \frac{\partial(\rho v h_s r)}{\partial r} = \frac{\partial}{\partial x} \left(k \frac{\partial T}{\partial x} \right) + \frac{1}{r} \frac{\partial}{\partial r} \left(k \frac{\partial T}{\partial r} r \right) + \dot{q}''' \quad (3.11)$$

Species conservation Equation:

$$\frac{\partial(\rho u Y_i)}{\partial x} + \frac{1}{r} \frac{\partial(\rho v r Y_i)}{\partial r} = \frac{\partial}{\partial x} \left(D_i \frac{\partial(\rho Y_i)}{\partial x} \right) + \frac{1}{r} \frac{\partial}{\partial r} \left(D_i r \frac{\partial(\rho Y_i)}{\partial r} \right) + \omega_i \quad (3.12)$$

3.4.2 CFD simulation for air jet impingement

In present study, simulations are carried out for laminar as well as turbulent jets. Before going for unsteady heating or cooling of the plate, steady state solution was obtained in both the studies. Other than front surface, remaining all surfaces are assumed insulated.

3.4.2.1 Laminar Jet

Physical model and boundary conditions employed for simulating laminar jet are similar as mentioned in Figure 3.5. Boundary layer mesh is generated near the wall surface as shown in Figure 3.5. First layer height is kept 0.1 mm along with growth factor of 1.2. Total 10 number of rows are included in boundary layer. The grid independence test is carried out by varying the grid size near the impingement plate from 0.1 mm to 0.0125 mm.

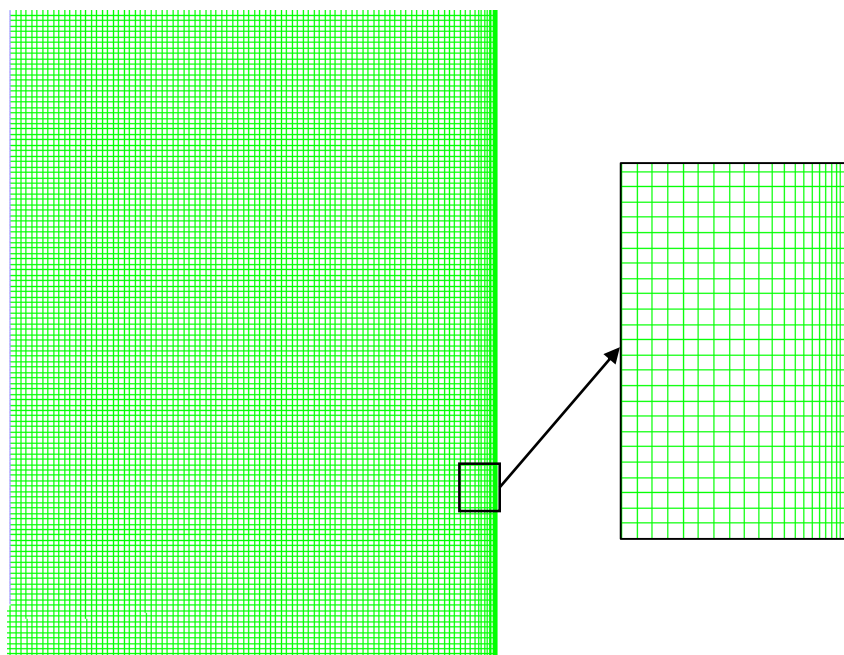


Figure 3.5 Boundary layer mesh near the wall

Governing Equations

The governing equations for the two dimensional axisymmetric laminar flows are given in Equations (3.13-3.16).

Continuity Equation:

$$\frac{\partial u}{\partial x} + \frac{1}{r} \frac{\partial (rv)}{\partial r} = 0 \quad (3.13)$$

x -momentum Equation:

$$\begin{aligned} \rho \left(u \frac{\partial u}{\partial x} + v \frac{\partial v}{\partial r} \right) = & -\frac{\partial p}{\partial x} + \frac{1}{r} \left[\frac{\partial}{\partial x} \left(r\mu \frac{\partial u}{\partial x} \right) + \frac{\partial}{\partial r} \left(r\mu \frac{\partial u}{\partial r} \right) \right] \\ & + \frac{\partial}{\partial x} \left(\mu \frac{\partial u}{\partial r} \right) + \frac{1}{r} \frac{\partial}{\partial r} \left(r\mu \frac{\partial v}{\partial x} \right) \end{aligned} \quad (3.14)$$

r -momentum Equation:

$$\begin{aligned} \rho \left(u \frac{\partial v}{\partial x} + v \frac{\partial v}{\partial r} \right) = & -\frac{\partial p}{\partial r} + \frac{1}{r} \left[\frac{\partial}{\partial x} \left(r\mu \frac{\partial v}{\partial x} \right) + \frac{\partial}{\partial r} \left(r\mu \frac{\partial v}{\partial r} \right) \right] \\ & - 2\mu \frac{v}{r^2} + \frac{\partial}{\partial x} \left(\mu \frac{\partial u}{\partial r} \right) + \frac{1}{r} \frac{\partial}{\partial r} \left(r\mu \frac{\partial v}{\partial x} \right) \end{aligned} \quad (3.15)$$

Energy Equation:

$$\frac{\partial (\rho u h_s)}{\partial x} + \frac{1}{r} \frac{\partial (\rho v h_s r)}{\partial r} = \frac{\partial}{\partial x} \left(k \frac{\partial T}{\partial x} \right) + \frac{1}{r} \frac{\partial}{\partial r} \left(k \frac{\partial T}{\partial r} r \right) \quad (3.16)$$

3.4.2.2 Turbulent Jet

For the numerical modelling of turbulent impinging jets, the numerical procedure similar to Guo et al. (2017) is considered. Turbulence models such as RNG κ - ϵ , SST κ - ω , realizable κ - ϵ , and Reynolds stress model were considered in their study to simulate jet impingement. Through the comparative evaluation of various turbulence models, better performing RNG κ - ϵ turbulence model was used in Guo et al. (2017) and here same is adopted to simulate turbulent impinging jet. Again physical model and boundary conditions employed for simulating laminar jet are similar as mentioned in Figure 3.3. For all the turbulent jet simulations, boundary layer mesh is attached to the impingement wall (Figure 3.5) and y^+ value less than 2 is always maintained.

Governing Equations

The governing equations for the two dimensional axisymmetric turbulent flows are given in Equations (3.17-3.22).

Continuity Equation:

$$\frac{\partial u}{\partial x} + \frac{1}{r} \frac{\partial (rv)}{\partial r} = 0 \quad (3.17)$$

x -momentum Equation:

$$\begin{aligned} \rho \left(u \frac{\partial u}{\partial x} + v \frac{\partial v}{\partial r} \right) = & -\frac{\partial p}{\partial x} + \frac{1}{r} \left[\frac{\partial}{\partial x} \left(r \mu_{eff} \frac{\partial u}{\partial x} \right) + \frac{\partial}{\partial r} \left(r \mu_{eff} \frac{\partial u}{\partial r} \right) \right] \\ & + \frac{\partial}{\partial x} \left(\mu_{eff} \frac{\partial u}{\partial r} \right) + \frac{1}{r} \frac{\partial}{\partial r} \left(r \mu_{eff} \frac{\partial v}{\partial x} \right) \end{aligned} \quad (3.18)$$

r -momentum Equation:

$$\begin{aligned} \rho \left(u \frac{\partial v}{\partial x} + v \frac{\partial v}{\partial r} \right) = & -\frac{\partial p}{\partial r} + \frac{1}{r} \left[\frac{\partial}{\partial x} \left(r \mu_{eff} \frac{\partial v}{\partial x} \right) + \frac{\partial}{\partial r} \left(r \mu_{eff} \frac{\partial v}{\partial r} \right) \right] \\ & - 2 \mu_{eff} \frac{v}{r^2} + \frac{\partial}{\partial x} \left(\mu_{eff} \frac{\partial u}{\partial r} \right) + \frac{1}{r} \frac{\partial}{\partial r} \left(r \mu_{eff} \frac{\partial v}{\partial x} \right) \end{aligned} \quad (3.19)$$

Energy Equation:

$$\frac{\partial (\rho u h_s)}{\partial x} + \frac{1}{r} \frac{\partial (\rho v h_s r)}{\partial r} = \frac{\partial}{\partial x} \left(k \frac{\partial T}{\partial x} \right) + \frac{1}{r} \frac{\partial}{\partial r} \left(k \frac{\partial T}{\partial r} r \right) \quad (3.20)$$

Equation for Turbulent kinetic energy:

$$\rho \left(u \frac{\partial k}{\partial x} + v \frac{\partial k}{\partial r} \right) = \frac{\partial}{\partial x} \left(\frac{\mu_t}{\sigma_k} \frac{\partial k}{\partial x} \right) + \frac{1}{r} \frac{\partial}{\partial r} \left(r \frac{\mu_t}{\sigma_k} \frac{\partial k}{\partial r} \right) + G_k - \rho \varepsilon \quad (3.21)$$

Equation for dissipation rate:

$$\rho \left(u \frac{\partial \varepsilon}{\partial x} + v \frac{\partial \varepsilon}{\partial r} \right) = \frac{\partial}{\partial x} \left(\frac{\mu_t}{\sigma_\varepsilon} \frac{\partial \varepsilon}{\partial x} \right) + \frac{1}{r} \frac{\partial}{\partial r} \left(r \frac{\mu_t}{\sigma_\varepsilon} \frac{\partial \varepsilon}{\partial r} \right) + C_1 \frac{\varepsilon}{k} G_k - \rho C_2 \frac{\varepsilon^2}{k} \quad (3.22)$$

Where viscous dissipation term (G_k) is given as Equation (3.25)

$$G_k = \mu_t \left\{ 2 \left[\left(\frac{\partial u}{\partial x} \right)^2 + \left(\frac{\partial v}{\partial r} \right)^2 + \left(\frac{v}{r} \right)^2 \right] + \left(\frac{\partial u}{\partial r} + \frac{\partial v}{\partial x} \right)^2 \right\} \quad (3.23)$$

and effective dynamic viscosity is defined as Equation (3.24)

$$\mu_{eff} = \mu + \mu_t \quad \text{where } \mu_t = C\mu \frac{k^2}{\varepsilon} \quad (3.24)$$

Constants values are given in Equation (3.25)

$$C_\mu = 0.09, C_1 = 1.45, C_2 = 1.9, \sigma_k = 1.0, \sigma_\varepsilon = 1.3 \text{ and } Pr_t = 1.0 \quad (3.25)$$

3.4.3 CFD simulation for heat diffusion by conduction

Heat conduction simulations are carried out in both cases, flame jet and air jet impingement. The axisymmetric approach is used for transient conduction model. The grid has been successively refined so as to get a grid independent result. A boundary layer mesh is attached on the impingement side and 45000 cells are sufficient for grid independency. The typical variations of h and T_{ref} is taken from the reported data and fed to numerical code via UDF.

Governing Equations

In absence of flow, Energy equation (Equation 3.26) is suffice for the heat conduction analysis through the plate.

Energy Equation:

$$\frac{\partial(\rho u h_s)}{\partial x} + \frac{1}{r} \frac{\partial(\rho v h_s r)}{\partial r} = \frac{\partial}{\partial x} \left(k \frac{\partial T}{\partial x} \right) + \frac{1}{r} \frac{\partial}{\partial r} \left(k \frac{\partial T}{\partial r} r \right) \quad (3.26)$$

3.5 CLOSURE

This chapter provided the details about experimental set-up and instruments required for smooth conduction of the experiments. This chapter also has introduced the numerical procedure adopted during simulation study. The next chapter explains about the analytical methods used in the present work.

Chapter 4

4 ANALYTICAL SOLUTIONS TO HEAT CONDUCTION PROBLEM

4.1 INTRODUCTION

Most of the reported experimental data reported assumes one-dimensional heat diffusion in the impingement plate citing the thinness of the plate. However, there is no study that classifies the one and multi-dimensional nature of heat diffusion in the impingement plate. In this chapter, the various analytical solutions to multi-dimensional conduction problem are presented which are further used to estimate the heat transfer coefficient and the reference (adiabatic wall) temperature for impinging methane-air premixed flame jets of different adiabatic flame temperature and Reynolds numbers.

4.2 FORMULATION OF THE HEAT CONDUCTION PROBLEM

Figure 4.1 is the schematic diagram of the three dimensional plate impinged by a flame jet.

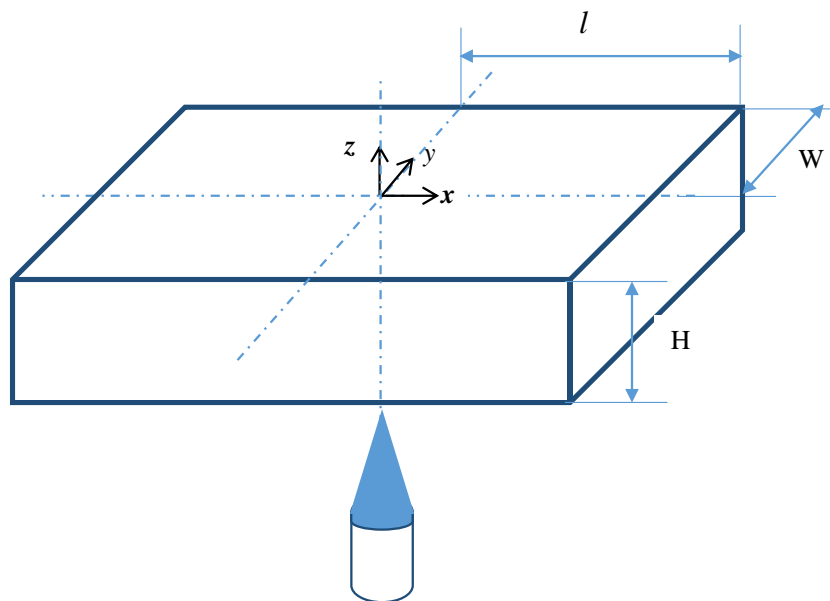


Figure 4.1 Schematic diagram of the three dimensional plate impinged by a flame jet

The generalized multi-dimensional heat conduction problem with constant material properties ($k, \rho C$) for flame jet impinging on a flat plate can be mathematically expressed as given in Equation (4.1).

$$\rho C \frac{\partial T}{\partial t} = k \left(\frac{\partial^2 T}{\partial x^2} + \frac{\partial^2 T}{\partial y^2} + \frac{\partial^2 T}{\partial z^2} \right) \quad (4.1)$$

Table 4.1 Possible Boundary conditions in flame jet impingement

Location	Boundary condition	Description
At $t = 0$	$T(x, y, z, t) = T_\infty$	Initial
At $x = 0, y = 0, z$	$\frac{\partial T}{\partial n} = 0$	Symmetry
At $x = \frac{l}{2}, y = \frac{w}{2}, z$	$\frac{\partial T}{\partial n} = 0$ OR $-k \frac{\partial T}{\partial n} = h_{NC}(T - T_\infty)$	Insulated OR loss by natural convection
At $x, y, z = H$	$-k \frac{\partial T}{\partial n} = h(T_{ref} - T) + \sigma \varepsilon (T^4 - T_\infty^4)$ OR $\frac{\partial T}{\partial n} = 0$	loss by natural convection + Radiation loss OR Insulated
At $x, y, z = 0$	$k \frac{\partial T}{\partial z} = h_f (T_{ref} - T_\infty)$ OR $T(x, y, H, t) = F(x, t)$	Forced convection due to flame jet OR Time dependent temperature

* n is the direction along x, y and z axes

The different possible boundary conditions are listed in Table 4.1. At the sections (planes normal to x and y axes) passing through the impingement point, the symmetry condition is applied. The side and top surfaces of the plate can either be modeled as natural convection or insulated boundary. The flame side surface further can be modeled as forced convection or time dependent temperature boundary condition.

4.3 SOLUTION METHODOLOGIES TO ONE DIMENSIONAL (1-D) HEAT CONDUCTION PROBLEM

The solution of Equation 4.1 can be written as Equation 4.2 by the method of the Separation of variables (SOV) (Mackowski, 2011). In general, SOV can be applied directly to transient problems that have homogeneous boundary conditions and a homogeneous differential equations. Optionally, solution can be expressed as product of three 1-D transient problems as given in Equation 4.3 (Mackowski, 2011).

$$T(x, y, z, t) = u(x) v(y) w(z) p(t) \quad (4.2)$$

Or

$$T(x, y, z, t) = u(x, t) v(y, t) w(z, t) \quad (4.3)$$

For the case of insulated boundaries at $x = y = W$ and thin plate assumption, the temperature distribution becomes independent of x and y. However, the effect of natural convection on these sides can be studied by appropriate assumption of natural convection heat transfer coefficient. In subsequent section, forced convection and time dependent boundary conditions at the impingement side are considered in the perspective of 1-D heat diffusion.

4.3.1 Convection boundary condition on flame side

Figure 4.2 describes the convection boundary condition at the heating side. The temperature distribution solution for one dimensional heat diffusion with forced convection boundary at flame side is obtained by SOV and is given in Equation 4.4.

$$T(z, t) = \sum_{n=1}^{\infty} \frac{(-2)(-1)^n Bi_f (\lambda_n^2 + Bi_f^2)^{1/2}}{\lambda_n (\lambda_n^2 + Bi_f (1 + Bi_f))} \cos(\lambda_n z) e^{-(\lambda_n^2)t} \quad (4.4)$$

where $Bi_f = \frac{h_f H}{k}$

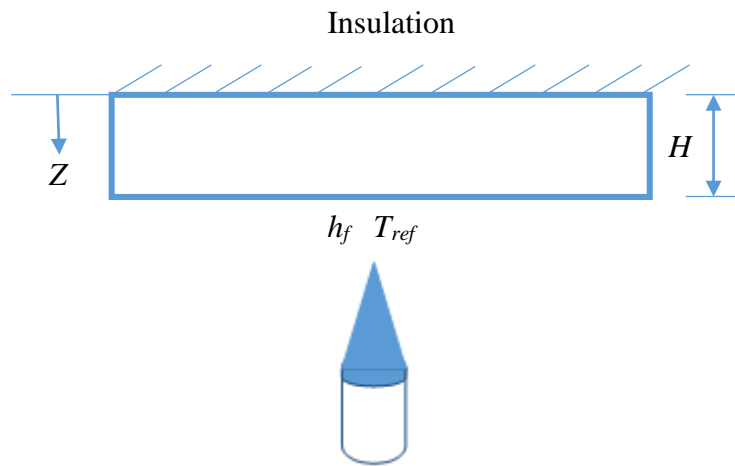


Figure 4.2 Plate with convection boundary condition

4.3.2 Time dependent temperature boundary condition on flame side

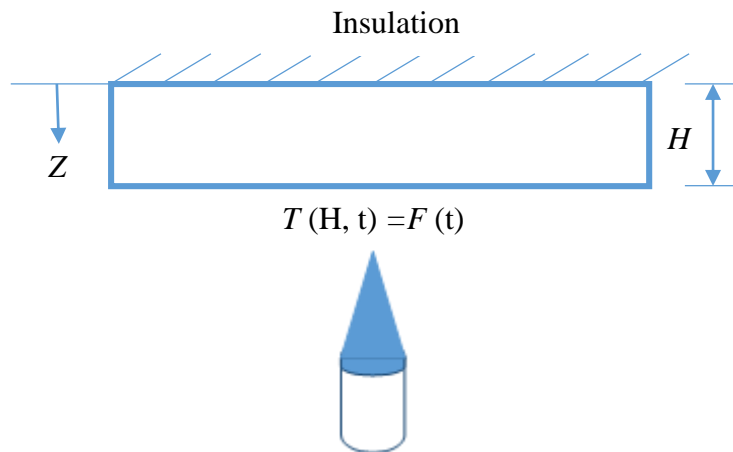


Figure 4.3 Plate with time dependent temperature boundary condition

As shown in Figure 4.3, the flame side wall temperature varies with time and hence the temperature distribution solution for one dimensional heat diffusion is obtained by the application of Duhamel's theorem (Mackowski, 2011) as given in Equation 4.5.

$$T(z, t) = T_\infty + \underbrace{\int_0^t F(t) \frac{\partial U(z, t - \tau)}{\partial t} d\tau}_{\text{continuous part}} + \underbrace{\sum_{n=1}^{\infty} U(z, t - \tau)}_{\text{Initial jump}} \times D_0 \quad (4.5)$$

$U(z, t)$ is the fundamental solution given in Equation (4.5) and τ is dummy variable of integration.

$$U(z, t) = 1 + \frac{4}{\pi} \sum_{n=1}^{\infty} \frac{(-1)^n}{(2n-1)} \cos(\lambda_n z) e^{-(\lambda_n^2)t} \quad (4.6)$$

D_0 is the initial disturbance (jump) and $F(t)$ is the continuous function for time dependent temperature boundary condition and ' λ_n ' are the infinite roots of transcendental equation $\cos(\lambda H) = 0$ which arises after applying time dependent boundary condition. Here for this relation, roots can be obtained in general form as given in Equation (4.7)

$$\lambda_n = \frac{1}{2}(2n-1) \frac{\pi}{H} \quad n=1,2,3,\dots \quad (4.7)$$

The wall heat flux at any time t is obtained by Eq. (4.8).

$$q(z, t) = -k \left(\frac{\partial T(z, t)}{\partial z} \right)_{z=H} \quad (4.8)$$

The thermal conductivity, k for Equation (4.8) is taken at average temperature of flame side and back side surfaces.

4.4 SOLUTION METHODOLOGY TO THREE DIMENSIONAL (3-D) HEAT CONDUCTION PROBLEM

It is understood that heat flux calculation considering 1-D approximation is not sufficient. Consideration of diffusion of heat in other directions requires more sophisticated method. Thus, solution to three-dimensional inverse heat conduction problem described by Feng et al. (2011) is studied in this section.

4.4.1 Solution by inverse approach

The method described by Feng et al. (2011) solves three dimensional heat conduction equation (Equation 4.1) with time dependent boundary condition for plate having small thicknesses.

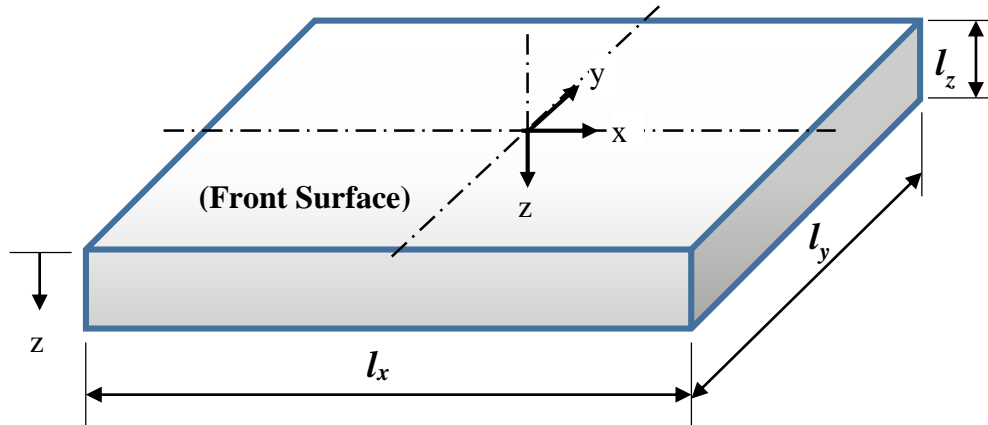


Figure 4.4 Geometry considered in Feng et al. (2011)

Figure 4.4 shows the geometry considered in their study. Mathematical formulation of boundary conditions used is summarized in Table 4.2.

Table 4.2 Boundary conditions assumed in Feng et al. (2011)

Location	Boundary condition	Description
At $x=0$ & $x=l_x$	$\frac{\partial T}{\partial x} = 0$	Insulation
At $y=0$ & $y=l_y$	$\frac{\partial T}{\partial y} = 0$	Insulation
At $z=l_z$	$\frac{\partial T}{\partial z} = 0$	Insulation
At $z=0$	$-k \frac{\partial T}{\partial z} = q(x, y, t)$	Heat flux to be estimated

Adiabatic conditions at back (non-impingement) surface and at all four side surfaces in x and y direction have been assumed. The solution to the inverse heat conduction problem assumes temperature independent material properties (k, ρ and C).

To simplify further, dimensionless variables are introduced as Equation (4.9).

$$t = t_c \tau, \quad x = l_z X, \quad y = l_z Y, \quad z = l_z Z \quad (4.9)$$

Where l_z is plate thickness

and at the same time heat flux and temperature are assumed with dimensions of temperature as given in Equations (4.10) and (4.11) respectively.

$$q(x, y, t) = \frac{k}{l_z} f(X, Y, \tau) \quad (4.10)$$

$$T(x, y, z, t) = \theta(X, Y, Z, \tau) \quad (4.11)$$

Where

$$t_c = \frac{\rho C_p l_z^2}{k}$$

and $f(X, Y, \tau)$ is the normalized front surface heat flux with unit K.

With above all substitutions the three dimensional heat conduction Equation (4.1) gets transformed as Equation (4.12).

$$\frac{\partial \theta}{\partial \tau} = \frac{\partial^2 \theta}{\partial X^2} + \frac{\partial^2 \theta}{\partial Y^2} + \frac{\partial^2 \theta}{\partial Z^2} \quad (4.12)$$

and the corresponding boundary conditions also get changed as given in Table 4.3.

Further, normalized temperature and normalized heat flux are defined through modal representation as per Equations (4.13) and (4.14) respectively.

$$\theta(X, Y, Z, \tau) = \sum_{m,n=0,1,\dots} \theta_{mn}(\tau, Z) \cos \frac{m\pi X}{L_x} \cos \frac{n\pi Y}{L_y} \quad (4.13)$$

$$f(X, Y, Z, \tau) = \sum_{m,n=0,1,\dots} f_{mn}(\tau) \cos \frac{m\pi X}{L_x} \cos \frac{n\pi Y}{L_y} \quad (4.14)$$

Table 4.3 Reformed Boundary conditions for non-dimensionalized equation

Location	Boundary condition
At $X = 0$ & $X = L_x$	$\frac{\partial \theta}{\partial X} = 0$
At $Y = 0$ & $Y = L_y$	$\frac{\partial \theta}{\partial Y} = 0$
At $Z = 1$	$\frac{\partial \theta}{\partial Y} = 0$
At $Z = 0$	$-\frac{\partial \theta}{\partial Z} = f(X, Y, \tau)$

Where $L_x = l_x / l_z$ and $L_y = l_y / l_z$

These expressions are nothing but Fourier series expansions of the temperature and heat flux in X and Y directions respectively.

These substitutions produces a one-dimensional heat conduction equation as expressed in Equation (4.15).

$$\frac{\partial^2 \theta_{mn}}{\partial Z^2} - C_{mn}^2 \theta_{mn} - \frac{\partial \theta_{mn}}{\partial \tau} = 0 \text{ for } m, n = 0, 1, 2, \dots \quad (4.15)$$

Where

$$C_{mn}^2 = \left(\frac{m\pi}{L_x} \right)^2 + \left(\frac{n\pi}{L_y} \right)^2$$

Heat flux boundary condition at $Z=0$ and the adiabatic boundary condition at $Z=1$ gets changed to Equations (4.16) and Equation (4.17) respectively.

$$-\frac{\partial \theta_{mn}}{\partial Z} = f_{mn}(\tau) \quad (4.16)$$

$$\frac{\partial \theta_{mn}}{\partial Z} = 0 \quad (4.17)$$

The function $\theta_{mn}(\tau, Z)$ represents modal temperature.

Laplace transform has been used to solve Equation (4.15) which yields second order ordinary differentiation equation with two unknown coefficients. These two unknown coefficients can be found with any two of the four possible quantities on the two surfaces. Once these coefficients are known, remaining two quantities can be found easily.

Linear relationship between the Laplace transform of the temperature and heat flux of the front surface and back surface has been established through thermal quadrupole and it is expressed as equation.

$$\begin{bmatrix} \Theta_{mn}(S, 0) \\ \Phi_{mn}(S, 0) \end{bmatrix} = \begin{bmatrix} \cosh \sqrt{S + C_{mn}^2} & \frac{1}{\sqrt{S + C_{mn}^2}} \sinh \sqrt{S + C_{mn}^2} \\ \sqrt{S + C_{mn}^2} \sinh \sqrt{S + C_{mn}^2} & \cosh \sqrt{S + C_{mn}^2} \end{bmatrix} \times \begin{bmatrix} \Theta_{mn}(S, 1) \\ \Phi_{mn}(S, 1) \end{bmatrix} \quad (4.18)$$

Where

$\Theta_{mn}(S, 0)$ = Laplace transform of the modal temperature of the front surface

$\Theta_{mn}(S, 1)$ = Laplace transform of the modal temperature of the back surface

$\Phi_{mn}(S, 0)$ = Laplace transform of the modal heat flux of the front surface

$\Phi_{mn}(S, 1)$ = Laplace transform of the modal heat flux of the back surface

Since back surface is assumed adiabatic, relationship Equation (4.18) gets simplified to Equation (4.19) and (4.20)

$$\Theta_{mn}(S, 0) = \cosh \sqrt{S + C_{mn}^2} \times \Theta_{mn}(S, 1) \quad (4.19)$$

and

$$\Phi_{mn}(S, 0) = \sqrt{S + C_{mn}^2} \sinh \sqrt{S + C_{mn}^2} \times \Theta_{mn}(S, 1) \quad (4.20)$$

Equation (4.19) and (4.20) gives front surface temperature and heat flux based on back surface temperature in Laplace domain. These are known as transfer functions. Only inverse Laplace of above equations gives the meaningful quantities in the time domain. Thus, these transfer functions are expanded as infinite product of simple polynomials based on Hadamard Factorization Theorem. Then simple straightforward inverse of polynomials are found. Infinite product expansions and its further simplification for hyperbolic cosine term is given in Equation (4.21) and Equation (4.22) respectively.

$$\cosh \sqrt{S + C_{mn}^2} = \prod_{k=1}^{\infty} \left\{ 1 + \frac{S + C_{mn}^2}{[(2k-1)\pi/2]^2} \right\} \quad (4.21)$$

$$\cosh \sqrt{S + C_{mn}^2} = \cosh C_{mn} \times \prod_{k=1}^{\infty} \left\{ 1 + \frac{S}{[(2k-1)\pi/2]^2 + C_{mn}^2} \right\} \quad (4.22)$$

and similarly infinite product expansion for hyperbolic sine function is given by Equation (4.23).

$$\frac{\sinh \sqrt{S + C_{mn}^2}}{\sqrt{S + C_{mn}^2}} = \frac{\sinh C_{mn}}{C_{mn}} \times \prod_{k=1}^{\infty} \left\{ 1 + \frac{S}{[k\pi]^2 + C_{mn}^2} \right\} \quad (4.23)$$

Substituting Equation (4.22) and Equation (4.23) into Equations (4.19) and Equation (4.20), Equation (4.24) and Equation (4.25) are obtained in Laplace domain.

$$\Theta_{mn}(S, 0) = \cosh C_{mn} \times \prod_{k=1}^{\infty} \left\{ 1 + \frac{S}{[(2k-1)\pi/2]^2 + C_{mn}^2} \right\} \times \Theta_{mn}(S, 1) \quad (4.24)$$

$$\Phi_{mn}(S, 0) = \frac{\sinh C_{mn}}{C_{mn}} \times (S + C_{mn}^2) \times \prod_{k=1}^{\infty} \left\{ 1 + \frac{S}{[k\pi]^2 + C_{mn}^2} \right\} \times \Theta_{mn}(S, 1) \quad (4.25)$$

Corresponding equations in the time domain are expressed as Equation (4.26) and Equation (4.27).

$$\theta_{mn}(\tau, 0) = \cosh C_{mn} \times \prod_{k=1}^{\infty} \left\{ 1 + \frac{1}{[(2k-1)\pi/2]^2 + C_{mn}^2} \frac{d}{d\tau} \right\} \times \theta_{mn}(\tau, 1) \quad (4.26)$$

$$f_{mn}(\tau) = \frac{\sinh C_{mn}}{C_{mn}} \left(\frac{d}{d\tau} + C_{mn}^2 \right) \prod_{k=1}^{\infty} \left\{ 1 + \frac{1}{[k\pi]^2 + C_{mn}^2} \frac{d}{d\tau} \right\} \theta_{mn}(\tau, 1) \quad (4.27)$$

Above Equations (4.26) and (4.27) contain derivative of infinite order. As k becomes large, the coefficient associated with derivative term becomes small. Therefore approximation has been obtained by truncating the infinite product and it is implemented through iterative scheme. Initial approximation is given by following Equations (4.28) and (4.29).

$$\theta_{mn}^{(1)}(\tau, 0) = \cosh C_{mn} \left[\theta_{mn}(\tau, 1) + \frac{1}{[\pi/2]^2 + C_{mn}^2} \frac{d\theta_{mn}(\tau, 1)}{d\tau} \right] \quad (4.28)$$

$$f_{mn}^{(1)}(\tau) = \frac{\sinh C_{mn}}{C_{mn}} \left[\frac{d\theta_{mn}(\tau, 1)}{d\tau} + C_{mn}^2 \theta_{mn}(\tau, 1) \right] \quad (4.29)$$

From these initial approximations, the successive approximations were obtained using iterations as per Equations (4.30) and (4.31).

$$\theta_{mn}^{(K+1)}(\tau, 0) = \left[\theta_{mn}^{(K)}(\tau, 0) + \frac{1}{[(2K+1)\pi/2]^2 + C_{mn}^2} \frac{d\theta_{mn}^{(K)}(\tau, 0)}{d\tau} \right] \quad (4.30)$$

$$f_{mn}^{(K+1)}(\tau) = f_{mn}^{(K)}(\tau) + \frac{1}{C_{mn}^2 + (K\pi)^2} \frac{df_{mn}^{(K)}(\tau)}{d\tau} \quad (4.31)$$

For $K = 1, 2, 3 \dots$

Thus, from back side modal temperature, the front side temperature and heat flux can be estimated using the iterative Equations (4.30) and (4.31).

In order to use above mentioned iterative scheme, the function of $\theta_{mn}(\tau, Z)$ and its first order derivative is required. Therefore, Savitzky-Golay method for data smoothing and

differentiation is used. Convolution weights used for smoothing and differentiation are given in Appendix C.

Required modal temperature on the back surface for the iterative scheme can be obtained as per the Equation (4.32)

$$\theta_{mn}(\tau, 1) = \frac{2^{2-(\delta_{0m}+\delta_{0n})}}{L_x L_y} \int_0^{L_x} \int_0^{L_y} \theta(X, Y, 1, \tau) \cos \frac{m\pi X}{L_x} \cos \frac{n\pi Y}{L_y} dX dY \quad (4.32)$$

Where δ_{0m} and δ_{0n} are Kronecker delta, $m=0,1,2,\dots,M$ and $n=0,1,2,\dots,N$.

If sensors placed at the back surface are at the centre of uniformly distributed rectangular grid then above Equation (4.32) can be written as Equation (4.33).

$$\theta_{nm}(\tau, 1) = \frac{2^{2-(\delta_{0m}+\delta_{0n})}}{L_x L_y} \sum_i \sum_j \theta(X_i, Y_j, 1, \tau) \cos \frac{m\pi X_i}{L_x} \cos \frac{n\pi Y_j}{L_y} \delta X_i \delta Y_j \quad (4.33)$$

Where (X_i, Y_j) is the center of the $(i, j)^{\text{th}}$ grid and δX_i and δY_j are the sides of the grid.

Above Equation (4.33) is valid for general mode numbers. For $(m, n) = (0, 0)$, it was suggested to use the Equation (4.34) which assumes constant uniform front surface heat flux.

$$\theta_{00}(\tau, Z) = f_{00}^0 \left[\tau + \frac{Z^2}{2} - Z + \frac{1}{3} - \frac{2}{\pi^2} \sum_{k=1}^{\infty} \frac{\cos(k\pi Z)}{k^2} e^{-(k\pi)^2 \tau} \right] \quad (4.34)$$

If the back side is distributed into $I \times J$ rectangular grids, then (X_i, Y_j) is given by Equation (4.35).

$$(X_i, Y_j) = \left(\left(i - \frac{1}{2} \right) \frac{L_x}{I}, \left(j - \frac{1}{2} \right) \frac{L_y}{J} \right) \quad (4.35)$$

As total sensor measurements are $I \times J$, total modes cannot be more than number of sensors. Therefore, to avoid aliasing, following condition (Equation 4.36) must be satisfied.

$$(M+1)(N+1) \leq I \cdot J \quad (4.36)$$

Once the front modal temperature and modal flux is known then normalized temperature and normalized heat flux can be obtained from the Equation (4.13) and Equation (4.14) respectively. Finally 2-D distribution of front temperature and front heat flux can be recovered from the Equation (4.10) and Equation (4.11) respectively.

4.5 CLOSURE

This chapter discussed physical model for real time situation in flame jet impingement and then analytical methods to solve 1-D and 3-D heat conduction problem are presented. Next chapter deals with the application and feasibility of these methods to real time experimental data to estimate heat transfer coefficient and reference temperature.

Chapter 5

5 RESULTS AND DISCUSSION

5.1 INTRODUCTION

At first, Heat transfer distribution of impinging flame jet is compared with that of the impinging air jet and a proper physical explanation for certain deviations in heat transfer distribution between flame and air jets is given. Then, analytical solutions to one dimensional and three dimensional heat conduction problem are verified with the help of numerical data. Need of a solution to three dimensional heat conduction problem in case of flame jet impingement where lateral temperature gradients are considerable is also addressed. Application of three dimensional solution is extended to real time flame impingement experimental data to estimate heat transfer coefficient and reference temperature simultaneously. Later, impinging jets with different configurations are also characterized with the help of this three dimensional solution. At the end numerical as well as experimental results for ribbed surfaces are presented. A circular, rectangular and triangular geometries of ribbed elements are considered with different aspect ratios in view of maximizing the heat transfer to the plate.

5.2 HEAT TRANSFER DISTRIBUTION OF IMPINGING FLAME AND AIR JETS – A COMPARATIVE STUDY

In this section, a comparison between heat transfer distributions of impinging flame jet with impinging air jet is presented using the experimental results of Nusselt number distribution of impinging flame jet of Hindasageri et al. (2014) and impinging air jet of Katti et al. (2011). CFD simulation for impinging flame and air jets is carried out using software Fluent to understand the physics. A scale analysis is further carried out to understand the dominant forces and their influence on the impingement heat transfer characteristics.

5.2.1 Validation of CFD simulation for Flame jet impingement

Two dimensional axisymmetric CFD simulations are carried out for flame jet impingement analysis. Numerical procedure is detailed in section 3.5.1. Figure 5.1 shows the comparison of heat flux between the present numerical results with published experimental results of Chander and Ray (2006). Heat flux sensor has been used to measure heat flux at the impingement side in Chander and Ray (2006).

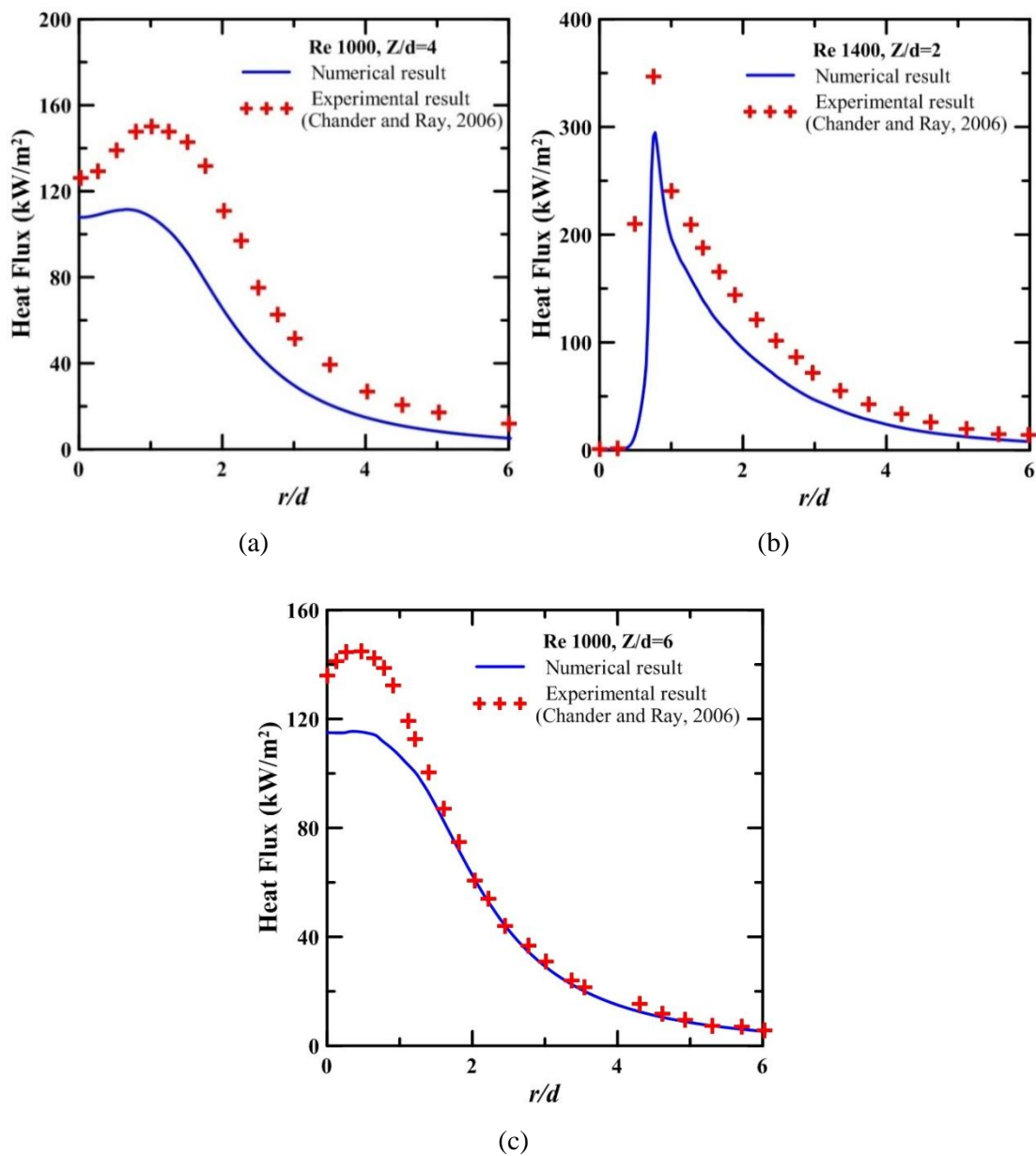


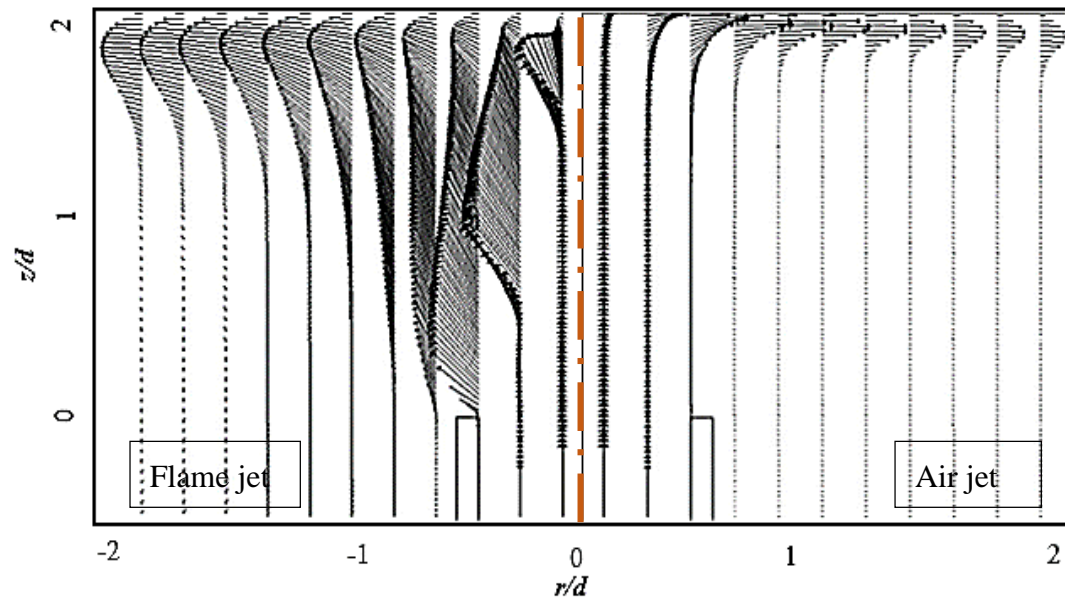
Figure 5.1 Comparison of Numerical results with Experimental results

Numerical results for heat flux are under predicting the experimentally measured heat flux at all Z/d . However, it can be seen from Figure 5.1 b that numerical simulation is able to pick the peak in the heat flux profile accurately at lower Z/d . Maximum deviation in stagnation heat flux value of is found 15% in case of $Re = 1000$ and $Z/d=4$ (Figure 5.1a). Heat flux prediction at $r/d > 2$ is good for $Re = 1000$, $Z/d=6$ (Figure 5.1c). Shorter flame lengths are observed in numerical simulations. The reason for shorter flame length could be the reduced reaction mechanism used in numerical simulation.

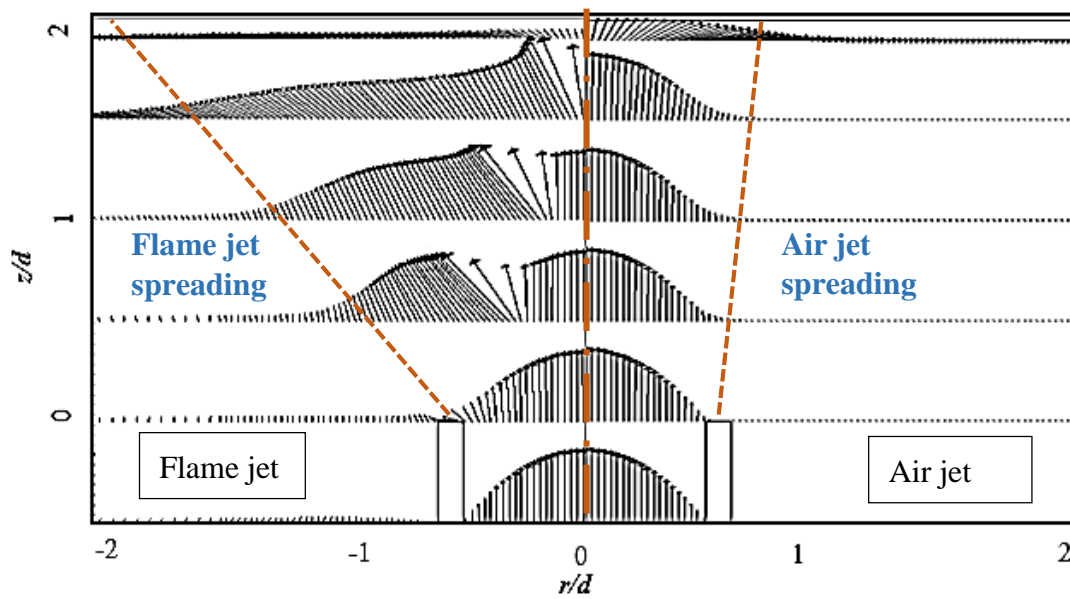
5.2.2 Comparison through numerical analysis

The velocity vectors along radial and axial directions for $Re = 600, 1000$ and 1400 for all Z/d is shown in Figures 5.2 to 5.10. It is observed that for flame jet there is sudden increase in radial velocity on the conical flame front surface. This speeding up of the jet on the flame front surface is due to burning of the mixture which results in density reduction of 7 times (for methane-air flame) across the flame front. For mass conservation, this should imply a corresponding increase in burnt gas velocity. From the present CFD simulations, it is observed that on the flamefront surface the burnt gas speed relative to the unburnt side of the jet is around 40 to 50% higher. Also, this sudden increase in velocity is in a direction normal to the flame front surface. Hence, the radial spreading of the flame jet is much higher than that of the air jet. Another reason that can be attributed to this higher radial spreading of the flame jet is due to the diffusion of burnt species in the presence of the radial concentration gradient.

At the smallest $Z/d = 2$, due to the sudden increase in the velocity on the flame front surface the heat transfer distribution is higher (Figure 5.2) on the impingement plate provided if the inner premixed cone of the flame doesnot touch the impingement plate. For $Z/d = 4$ and 6 , it is observed that due to excessive radial spreading of the flame jet, the axial momentum decreases and therefore the ratio of Nusselt number for flame jet to that of air jet at stagnation region decreases, this is more particularly true for higher Reynolds number ($Re = 1000$ and 1400). However, away from the stagnation region, the Nusselt number distribution for flame jet is higher than that of air jet due to lateral spreading of the flame jet and gain in momentum due to burning on the flamefront surface of the premixed cone.

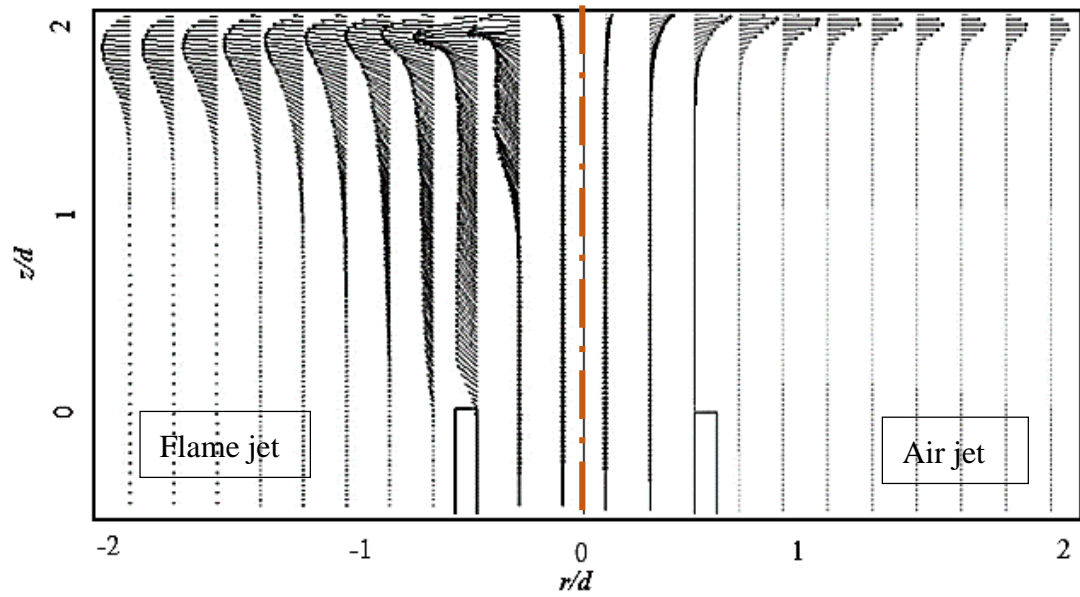


(a)

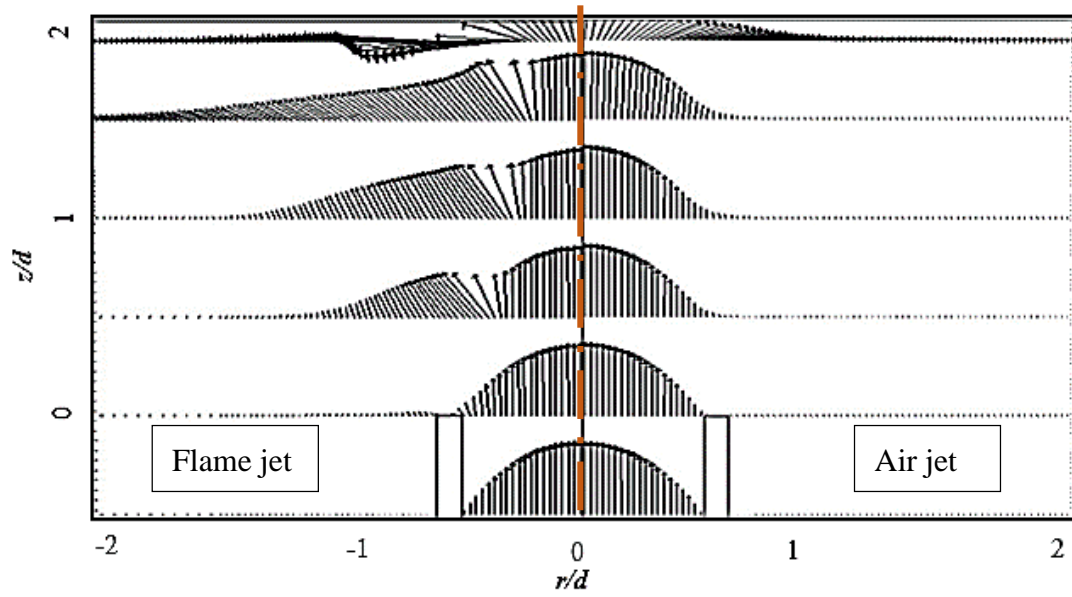


(b)

Figure 5.2 Comparison of velocity vectors of impinging air jets with impinging flame jets from the tip of burner to the impingement plate for $Re = 600$ and $Z/d = 2$;
 a) along the tube axis, b) normal to the tube axis



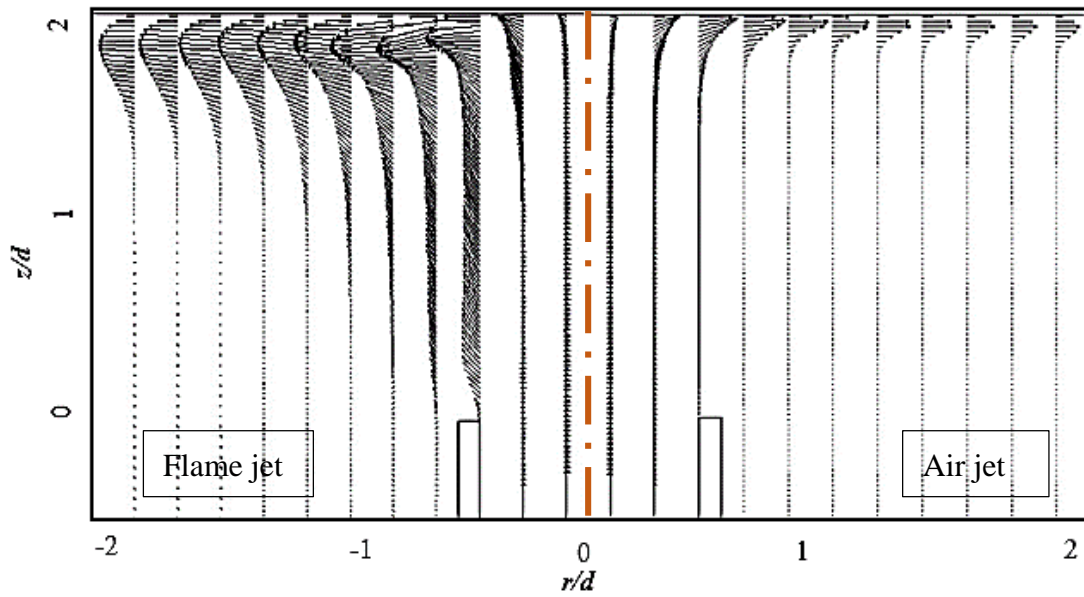
(a)



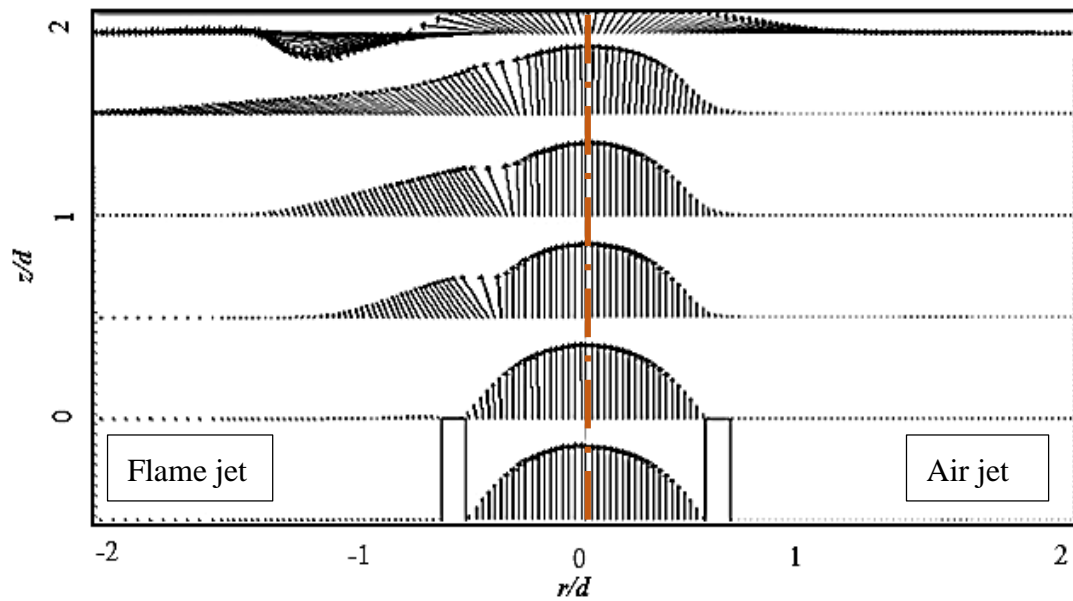
(b)

Figure 5.3 Comparison of velocity vector of impinging air jets with impinging flame jets from the tip of burner to the impingement plate for $Re = 1000$ and $Z/d = 2$;

a) along the tube axis, b) normal to the tube axis

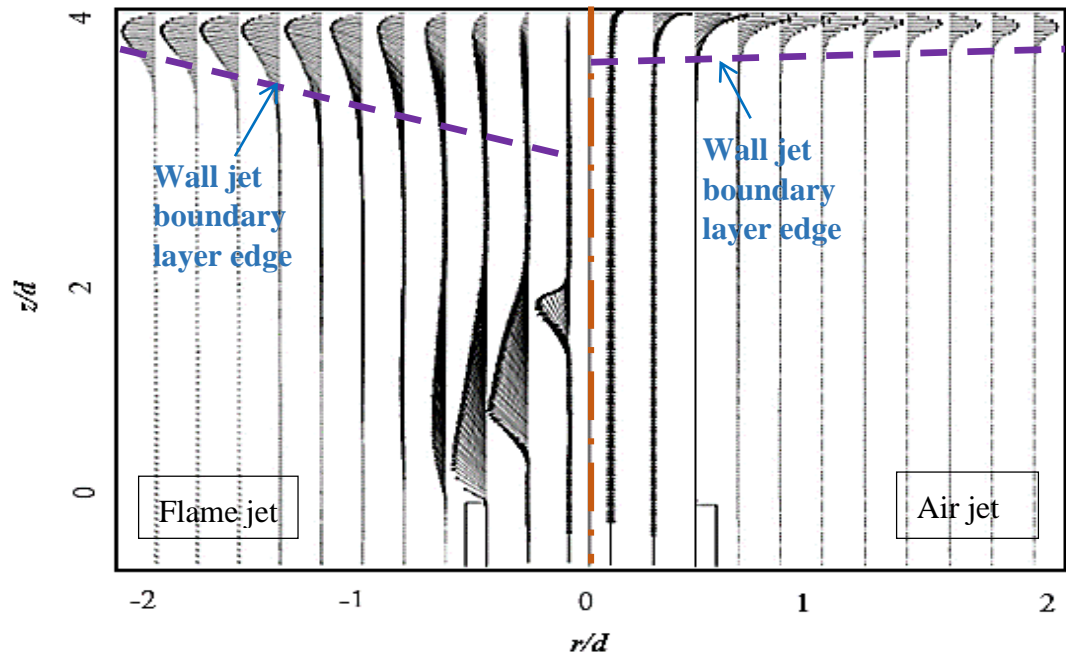


(a)

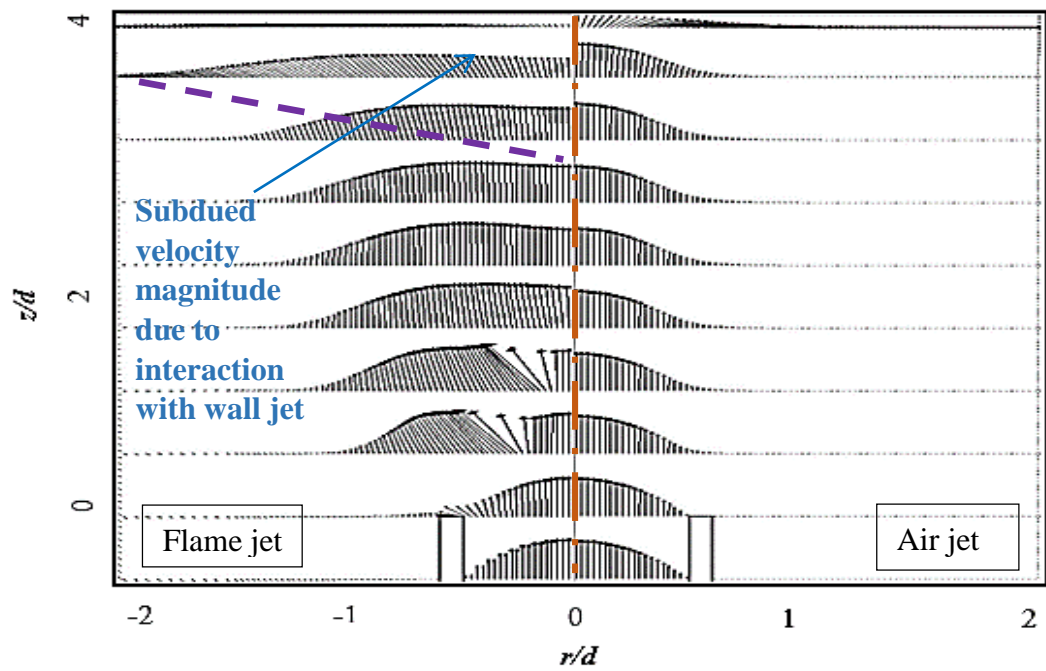


(b)

Figure 5.4 Comparison of velocity vector of impinging air jets with impinging flame jets from the tip of burner to the impingement plate for $Re = 1400$ and $Z/d = 2$;
 a) along the tube axis, b) normal to the tube axis

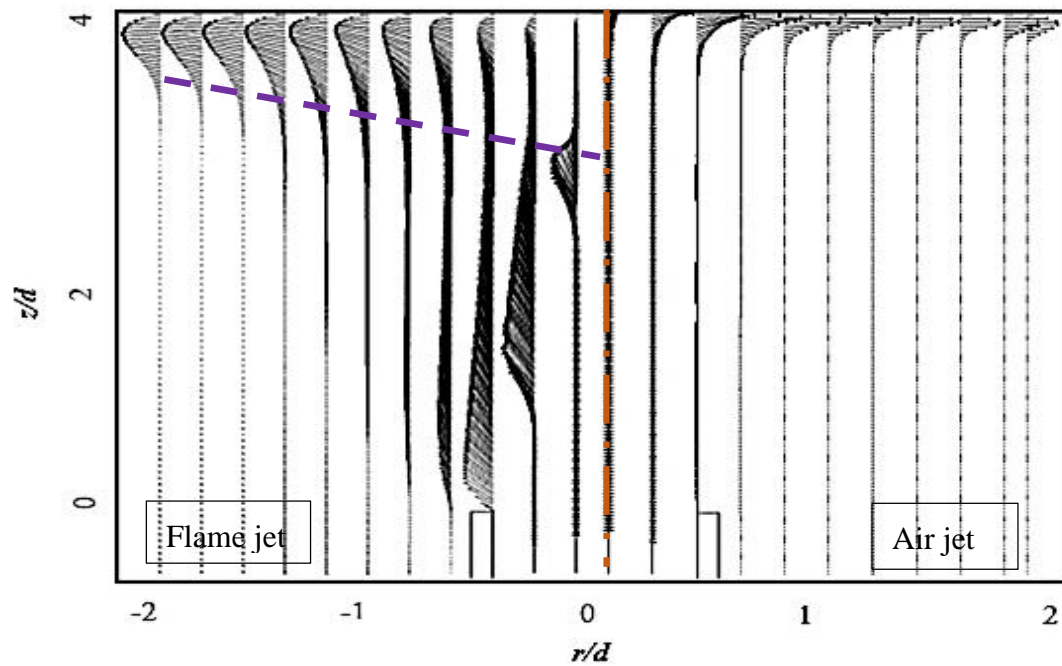


(a)

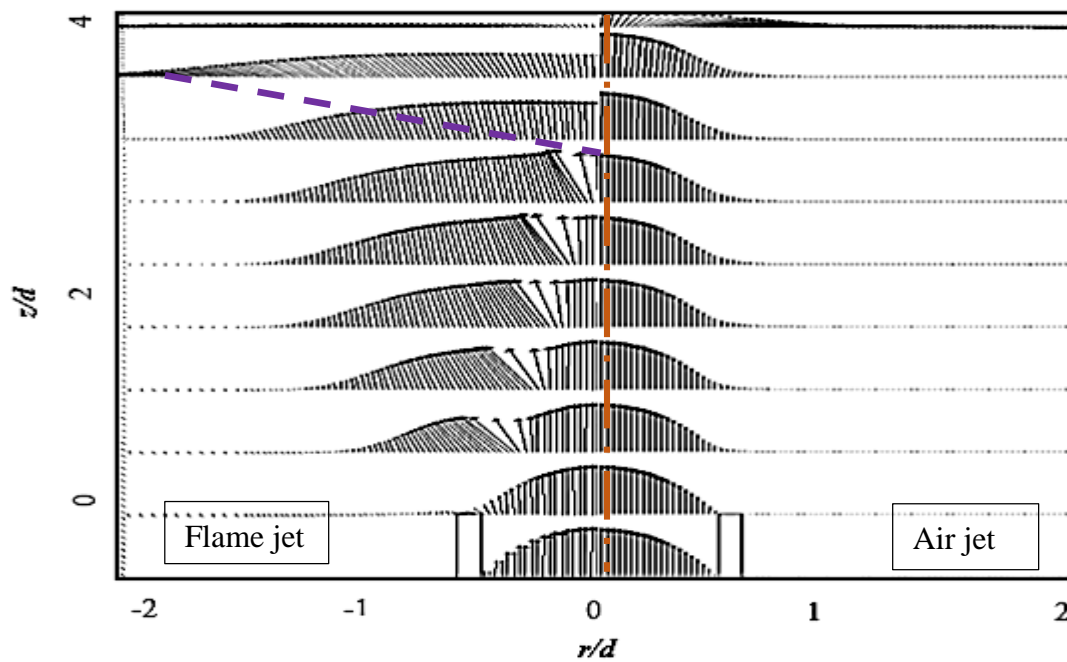


(b)

Figure 5.5 Comparison of velocity vector of impinging air jets with impinging flame jets from the tip of burner to the impingement plate for $Re = 600$ and $Z/d = 4$;
 a) along the tube axis, b) normal to the tube axis

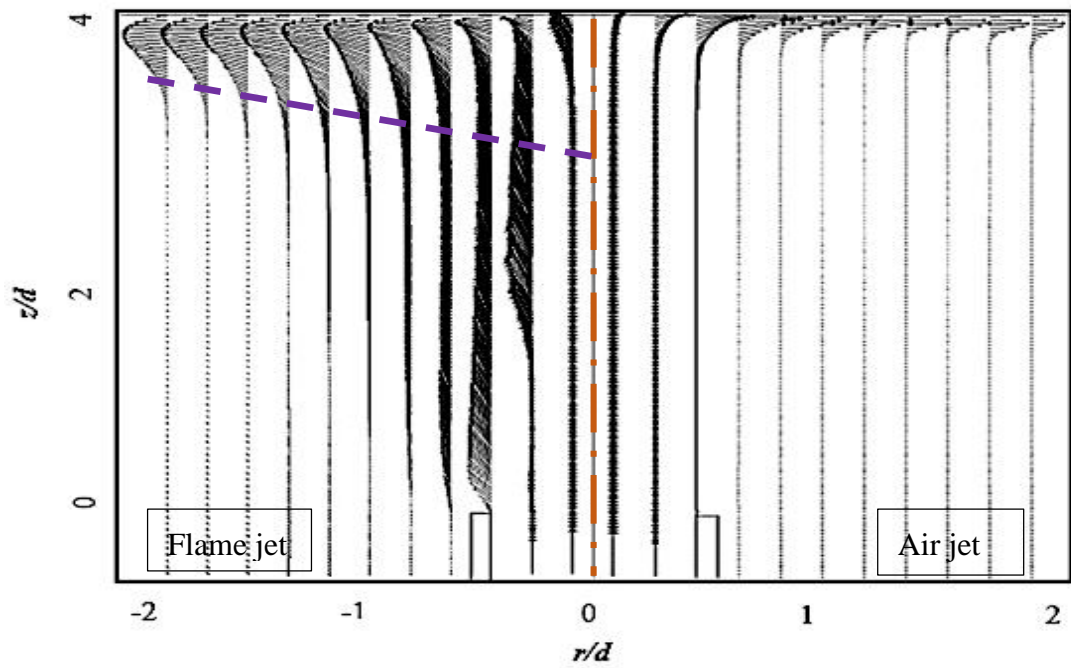


(a)

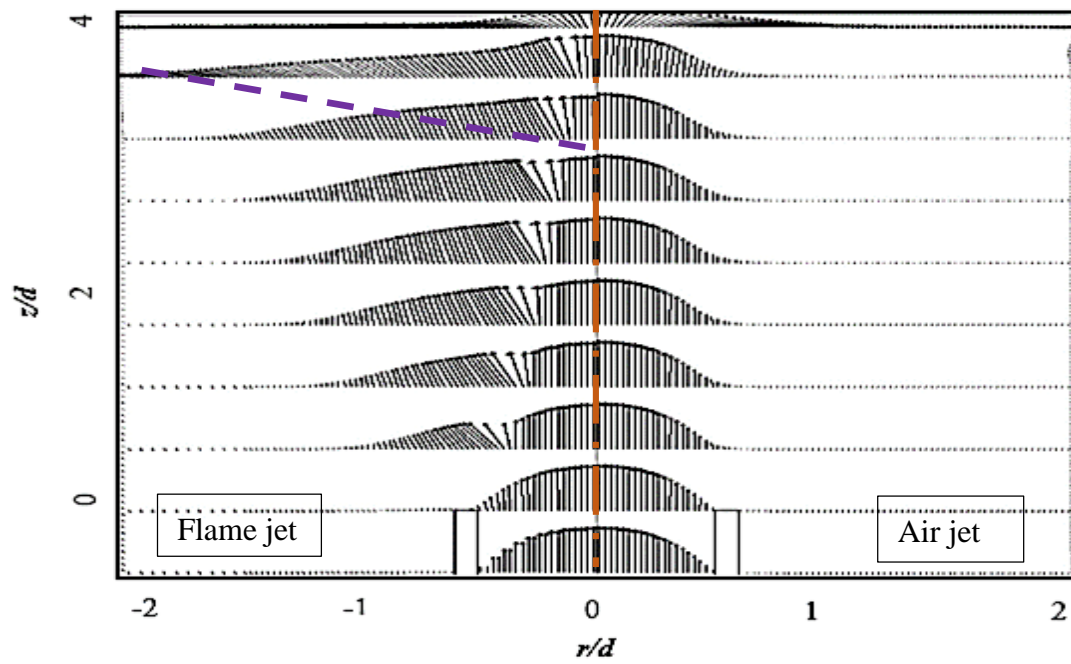


(b)

Figure 5.6 Comparison of velocity vector of impinging air jets with impinging flame jets from the tip of burner to the impingement plate for $Re = 1000$ and $Z/d = 4$;
 a) along the tube axis, b) normal to the tube axis



(a)



(b)

Figure 5.7 Comparison of velocity vector of impinging air jets with impinging flame jets from the tip of burner to the impingement plate for $Re = 1400$ and $Z/d = 4$;
 a) along the tube axis, b) normal to the tube axis

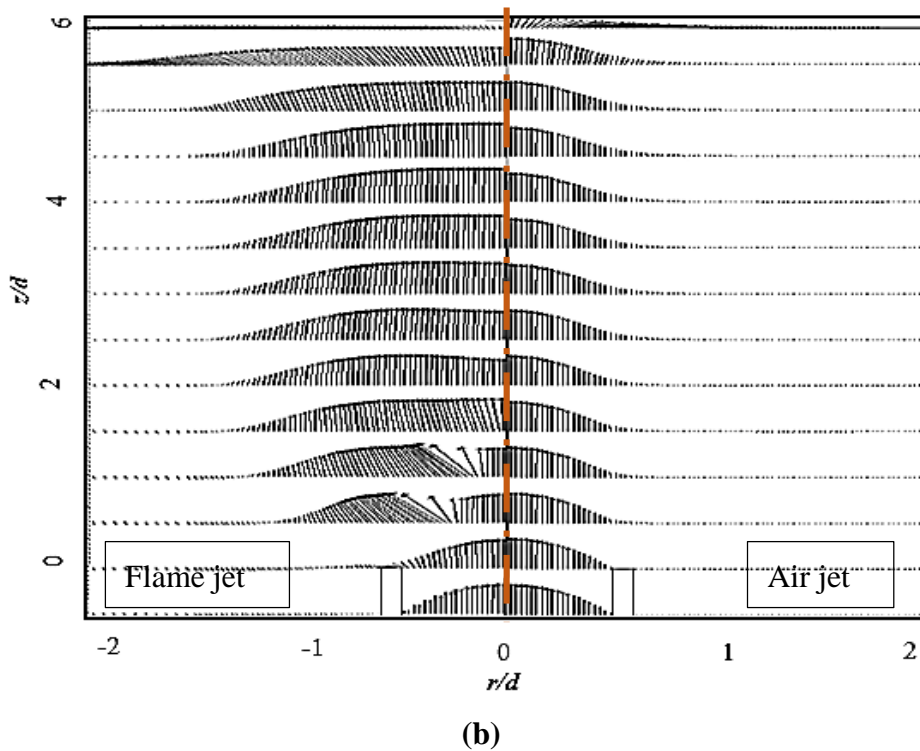
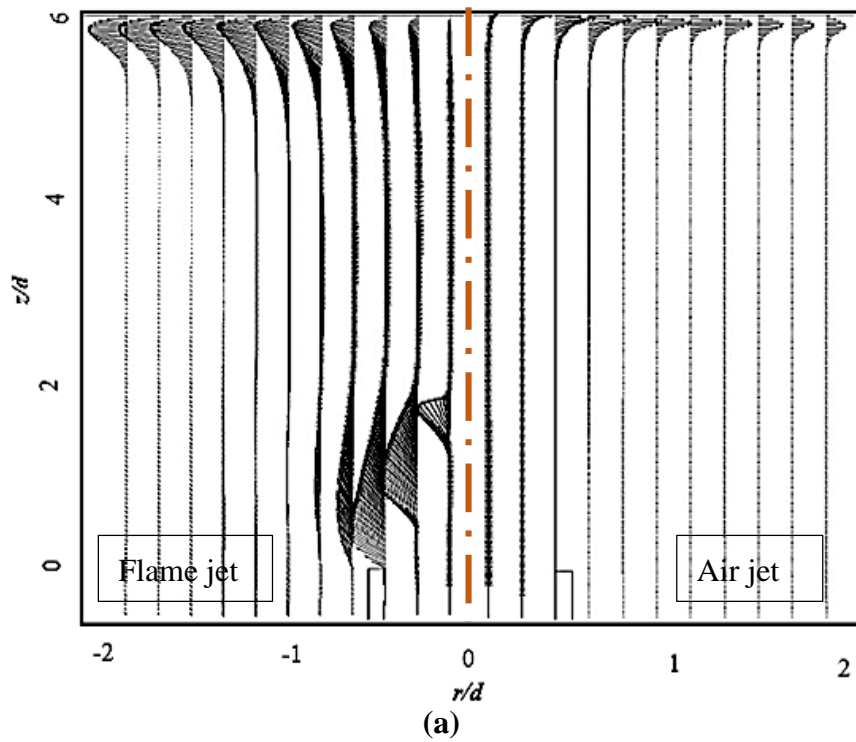


Figure 5.8 Comparison of velocity vector of impinging air jets with impinging flame jets from the tip of burner to the impingement plate for $Re = 600$ and $Z/d = 6$;
 a) along the tube axis, b) normal to the tube axis

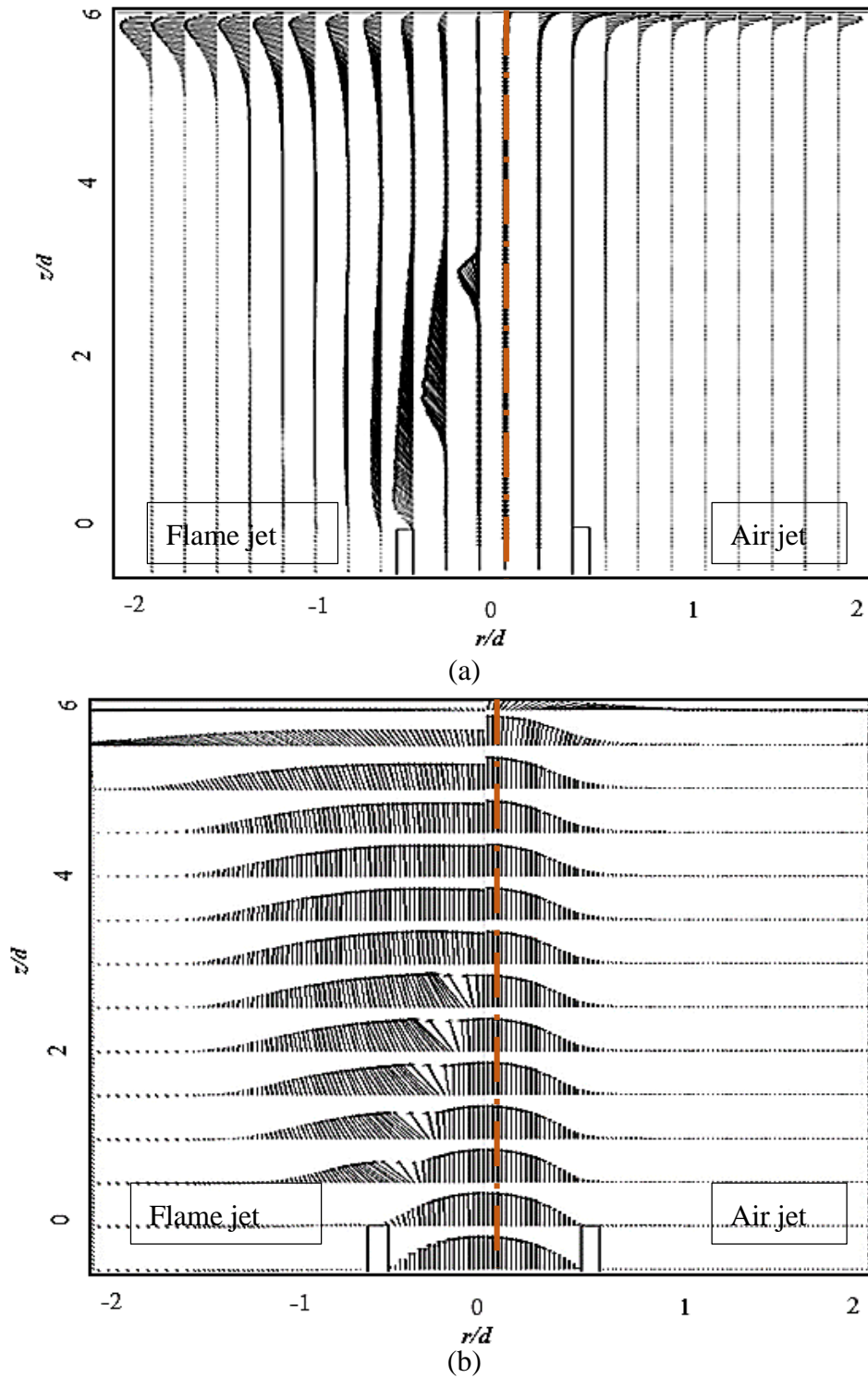


Figure 5.9 Comparison of velocity vector of impinging air jets with impinging flame jets from the tip of burner to the impingement plate for $Re = 1000$ and $Z/d = 6$;
 a) along the tube axis, b) normal to the tube axis

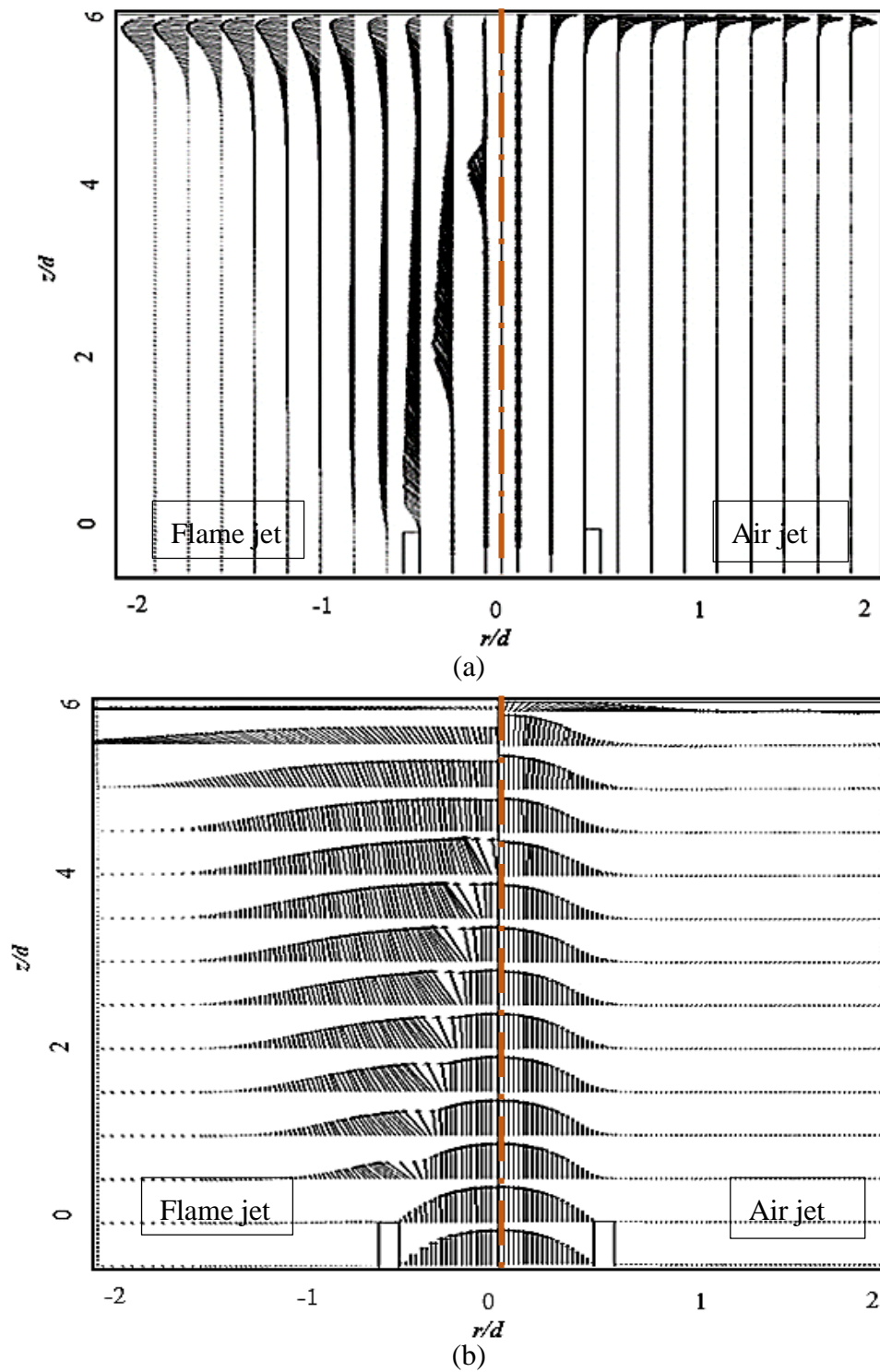


Figure 5.10 Comparison of velocity vector of impinging air jets with impinging flame jets from the tip of burner to the impingement plate for $Re = 1400$ and $Z/d = 6$;
 a) along the tube axis, b) normal to the tube axis

From Figure 5.5 for $Re = 600$ and $Z/d = 4$, the flame jet Nusselt number is slightly higher compared to the air jet. However, the axial velocity vectors near the impingement plate appear to be subdued (lower) for flame jet as compared to the air jet. The reason for this subdued nature of velocity vectors near the impingement plate for the flame jet is due to the presence of the much wider boundary layer region.

Figure 5.5 shows the boundary layer edges marked on the velocity vector plots for flame and air jets. From theoretical calculations ($Re = ud/\nu$) it can be shown that the boundary layer thickness ($\delta = 5x/\sqrt{Re}$) for flame jet is three times that of the air jet for the same jet exit velocity. This is due to the kinematic viscosity variations (Hindasageri et al. 2014) for flame and air jets ($\nu_{flame}/\nu_{air} \sim 10$). For $Z/d = 4$ and $Re = 1000$ and 1400 , it is observed that the flame cone tip is closer to the impingement plate and the velocity vectors diverge in radial direction thereby losing axial momentum. Hence, for these cases the Nusselt number for flame jet is lower at the stagnation region as compared to that for the air jet. Furthermore, the observations for $Z/d = 6$ is similar to that of $Z/d = 4$.

An interesting contradiction for Nusselt number distribution for $Z/d = 2$ and those for $Z/d = 4$ and 6 is that for $Z/d = 2$, the Nusselt number is always significantly higher excluding the cases where the inner premixed cone touches the impingement plate. A reasonable explanation for this is the fact that for larger Z/d , the momentum gained due to burning on the flame front surface decays due to radial spreading and this decay increases with the increase in Z/d . Hence, for $Z/d = 2$, the decay in axial velocity is lesser and therefore results in significantly higher Nusselt number for flame jet as compared to air jet.

5.2.3 Comparison through Scale analysis

An observation that could not be explained through the CFD simulation is at low Re (600 and 800) for all Z/d , the Nusselt number for flame jet is higher than that of air jet when compared to that at high Re (1200 and 1400). Such an observation can be explained by understanding the dominant forces and their influence on the impingement heat transfer distribution. A scale (order of magnitude) analysis of the z - momentum

equation is carried out. Equation (5.1) is the momentum equation along the axial (z) direction for the two dimensional axisymmetric jet.

$$\underbrace{\rho \left(u_r \frac{\partial u_z}{\partial r} + u_z \frac{\partial u_z}{\partial z} \right)}_{\text{Inertia-force}} = \underbrace{-\frac{\partial P}{\partial z}}_{\text{Pressure-force}} + \underbrace{\rho g_z}_{\text{Body-force}} + \underbrace{\mu \left[\frac{1}{r} \frac{\partial}{\partial r} \left(r \frac{\partial u_z}{\partial r} \right) + \frac{\partial u_z^2}{\partial z^2} \right]}_{\text{Viscous-force}} \quad (5.1)$$

The inertia force is balanced by the pressure, viscous (frictional) and body force terms. The viscous dissipation in axial direction is negligible as compared to the radial direction. The appropriate scales for Equation (5.1) are as follows.

Air jet:

$$u_r \sim 0, u_z \sim u_e, r \sim R, \rho \sim \rho_\infty$$

Flame jet:

$$u_r \sim 0, u_z \sim 1.5u_e, r \sim 2R, \rho \sim \rho_f$$

The flame jet is found to spread much wider than the air jet and therefore, the maximum radial distance for air jet is taken as R and for flame jet is taken as $2R$ based on observations made in the CFD simulations. Furthermore, the flame jet velocity increases on the flame front surface and hence an appropriate factor of 1.5 times for u_e (average mixture velocity at tube exit) is taken for flame jets based on the observations made in the CFD simulations. Applying the appropriate scales, the Equation (5.1) for air and flame jets simplifies as given in Equations (5.2) and (5.3).

$$\rho_\infty \frac{u_e^2}{Z} = \rho_\infty g + \frac{\mu_\infty u_e}{R^2} \quad (5.2)$$

$$\rho_f \frac{u_e^2}{Z} = (\rho_f - \rho_\infty)g + \frac{\mu_f u_e}{4R^2} \quad (5.3)$$

It is important to note that for air jet, the body force opposes the inertia due to gravitational force while for the flame jet, the body force (buoyancy force) adds to the inertia. Table 5.1 gives the order of magnitudes of each of the forces for flame and air

jets at $Re = 600$ and 1400 for $Z/d = 4$ and 6 . For $Z/d = 2$, the premixed flame cone (unburnt mixture volume) is very close or partly touches the impingement plate. Hence, the scaling concept is applicable to only higher Z/d . The flame properties required at reference temperature are taken from Hinasageri et al. (2014).

The data given in Table 5.1 supports the experimental observations in Figures 2.21 and 2.22. At $Z/d = 4$ and $Re = 600$, the net force is of same magnitude and is in agreement with the Nusselt number distribution in Figure 2.21. However, at $Z/d = 4$ and $Re = 1400$, the net force for air jet is higher as compared to flame jet and this is also in agreement with the Nusselt number distribution in Figure 2.21. This is due to significantly higher inertia force at $Re = 1400$ and the other forces are negligible (one order of magnitude lower). A similar inference can be made through Table 5.1 and Figure 5.3 for $Re = 600$ and 1400 at $Z/d = 6$.

Table 5.1 Magnitude of different forces (N/m^3) involved in flame jets and air jets

Forces	$Z/d = 4$				$Z/d = 6$			
	$Re = 600$		$Re = 1400$		$Re = 600$		$Re = 1400$	
	Air jet	Flame jet	Air jet	Flame jet	Air jet	Flame jet	Air jet	Flame jet
Inertia	29	17	144	84	19.4	11.25	96.5	56
Viscous	-0.7	-7.5	-1.7	-16.7	-0.7	-7.5	-1.7	-16.7
Body	-11	8.5	-11	8.5	-11	8.5	-11	8.5
Net	17.3	18	131.3	75.8	7.7	12.3	83.8	47.8

5.3 SIMULTANEOUS ESTIMATION OF HEAT TRANSFER COEFFICIENT AND REFERENCE TEMPERATURE FROM IMPINGING FLAME JETS

In this section, analytical solutions to multi-dimensional conduction problem are used to estimate the heat transfer coefficient and the reference (adiabatic wall) temperature for impinging flame jets. A new procedure to correct the radiation loss from the impingement plate is presented. The effect of thermal conductivity variations with temperature for the impingement plate is also discussed.

5.3.1 Validation of experimental set-up

Confirmation to the calibration procedure applied to flowmeters is done by validating the experimental results for laminar burning velocity and flame stability limits.

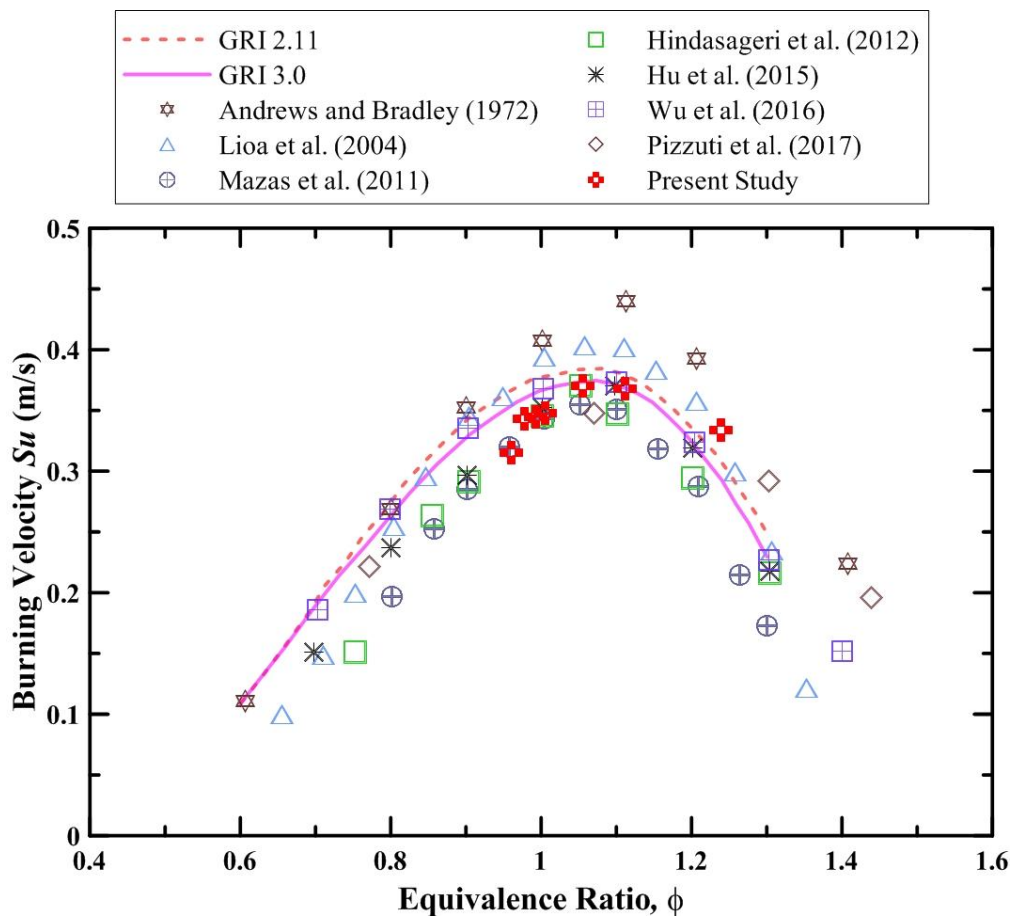


Figure 5.11 Comparison of Laminar burning velocity with published data

Here, the inner cone is approximated as a right circular cone with base radius (r) and slant height (l). On applying a mass flux balance would result in an expression for burning velocity (Su) as given in Equation (5.4)

$$Su = \frac{r}{l} u_m \quad (5.4)$$

Figure 5.11 compares the result for laminar burning velocity estimated from present set-up with well-known published data. It can be observed that estimated laminar burning velocities are in good match with published data.

Another way of validation of the experimental set-up is by confirming the flame stability limits. For stable flame, there is a requirement of the certain mass flow rate of methane and air in the mixture. Beyond that certain proportion of methane and air in the mixture, flame flashback or blowoff occurs. The blowoff limit governed by the critical velocity gradient (g_b) is given by Equation 5.5.

$$g_b = \frac{8\bar{u}}{d} \quad (5.5)$$

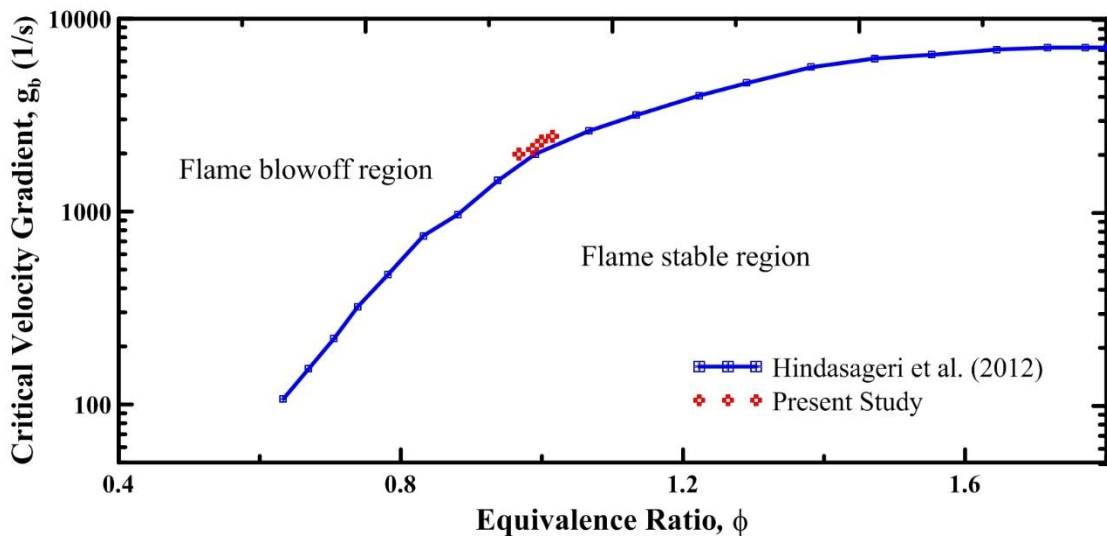


Figure 5.12 Comparison of critical velocity gradient parameter with that of Hindasageri et al. (2012)

Estimated critical velocity gradient for present experimental set-up with 10 mm diameter stainless steel tube burner is compared in Figure 5.12 and it is in a good agreement with Hindasageri et al. (2012) data.

5.3.2 Validation of Analytical methods

The one dimensional/ multidimensional solutions to heat conduction problem are validated before applying them to real time experimental data.

5.3.2.1 Convection boundary condition on flame side

The temperature distribution for convection boundary condition is in implicit form and also non-linear. Hence, it is not possible to estimate the heat transfer coefficient and reference temperature simultaneously.

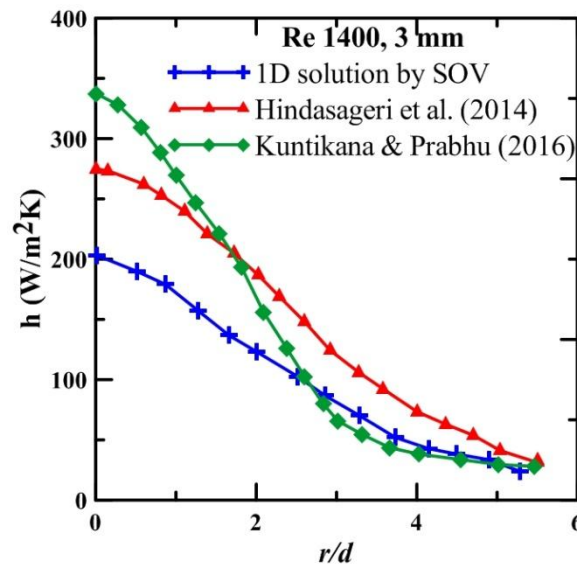


Figure 5.13 Comparison of the analytically estimated heat transfer coefficient with reported experimental values at $Z/d = 4$

However, if the reference temperature is known by direct measurement then the heat transfer coefficient can be computed iteratively by an initial guess and comparing the analytically computed back side wall temperature with that of experimental measurements. Figure 5.13 shows the comparison heat transfer coefficient estimated by the analytical 1D SOV with that of experimental values for $Re=1400$ at $Z/d = 4$. The deviations are attributed to averaging of heat flux and wall temperature data reported in Hindasageri et al. (2014) and Kuntikana and Prabhu (2016).

5.3.2.2 Time dependent temperature boundary condition on flame side

The comparison of front surface heat flux obtained by Duhamel theorem is done with numerical heat flux data for methane-oxygen flame of Remie et al. (2008) for $Z/d = 0.5$, $Re = 1334$. The temperature distribution for Remie et al. (2008) is based on one dimensional heat conduction in the plate and the forcing functions at any 'r' can be obtained by assuming a linear curve fit approximation to transient temperature distribution data at that 'r'.

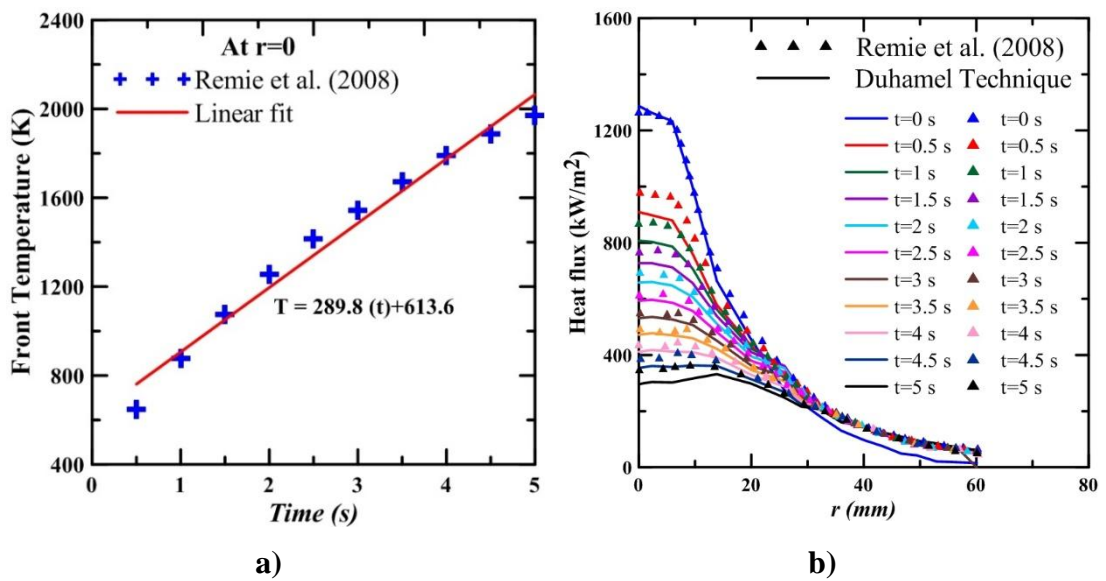
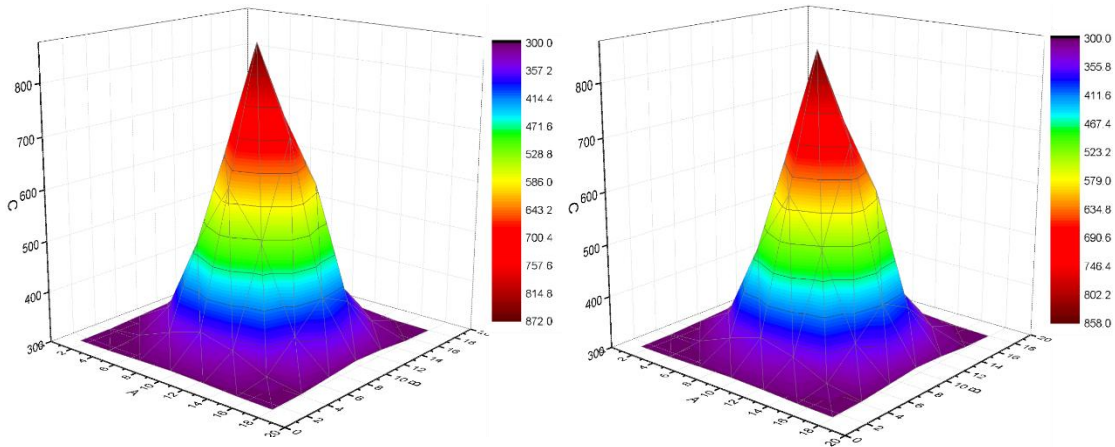


Figure 5.14 a) Linear fit approximation to transient temperature data at stagnation point b) Comparison of Duhamel results with Remie et al. (2008) for $Re = 1334$ at $Z/d = 4$ for transient heat flux data

Figure 5.14a shows approximated linear fit to the transient temperature data at stagnation point ($r = 0$). Figure 5.14b shows the comparison of wall heat flux data on impingement side obtained by Duhamel theorem and numerical heat flux data of Remie et al. (2008) for methane-oxygen flame jet. The deviations are within 4%. Hence, this comparison with numerical data (Remie et al., 2008) ascertains the correctness of the Duhamel procedure employed in the present work.

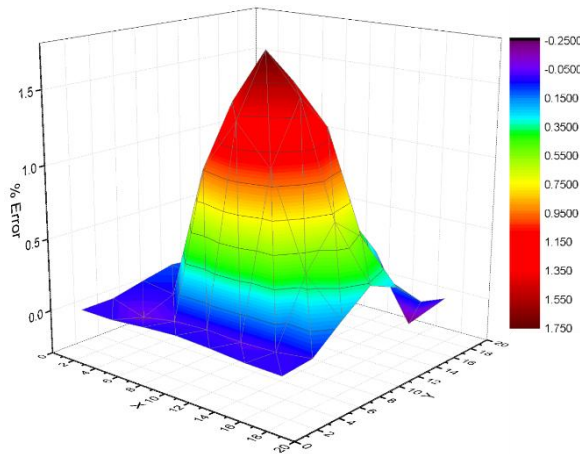
5.3.2.3 Three dimensional IHCP solution

The procedure employing method of Feng et al. (2011) is validated with the numerically simulated data obtained in Ansys, Fluent CFD Software.



(a)

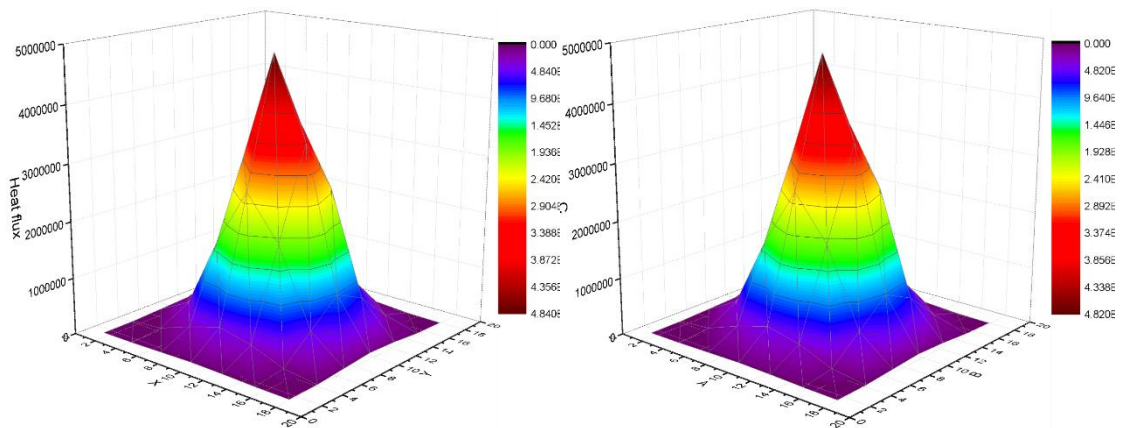
(b)



(c)

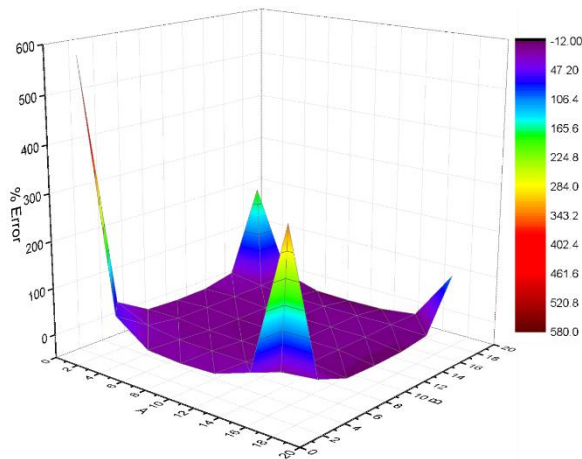
Figure 5.15 Front surface temperature (a) Simulation result (b) Calculated by IHCP code (c) Percentage of deviation

The IHCP solution of Feng et al. (2011) is validated for constant but non-uniform surface heat flux applied to a plate having three dimensional geometry. To validate the code, 3 mm thick and 60 mm square steel plate having constant thermal conductivity 16.27 (W/mK), density 8030(kg/m³) and specific heat 502.48 (J/kgK) is considered. Constant but non-uniform heat flux profile is applied on the front surface. Except front surface, all other surfaces are insulated and corresponding to these boundary condition numerical solution is obtained by commercial finite volume package Ansys (fluent).



(a)

(b)



(c)

Figure 5.16 Front surface heat flux (a) Simulation result (b) Calculated by IHCP code
(c) Percentage of deviation

Then, back side surface temperature is given as input to the IHCP code. Assuming 7 by 7 sensor array at the back side, corresponding modal temperature is calculated. Savitzky-Golay method using seven points fitted with fourth order polynomial is used for smoothing and differentiation the data.

Figure 5.15 shows the comparison of calculated front surface temperature with simulation result along with % deviation. Maximum deviation found is 1.74%. Front surface heat flux comparison is shown in Figure 5.16. Except corner points, at all other points IHCP code predicts heat flux well with maximum deviation 8%.

5.3.3 Verification of 1-D approximation

With 1-D approximation, heat conduction problem for convection and time dependent boundary conditions are solved and heat flux are obtained. Further, the heat transfer coefficient and the reference temperatures can be obtained simultaneously by curve fitting the transient heat flux data for the corresponding impingement side wall temperature.

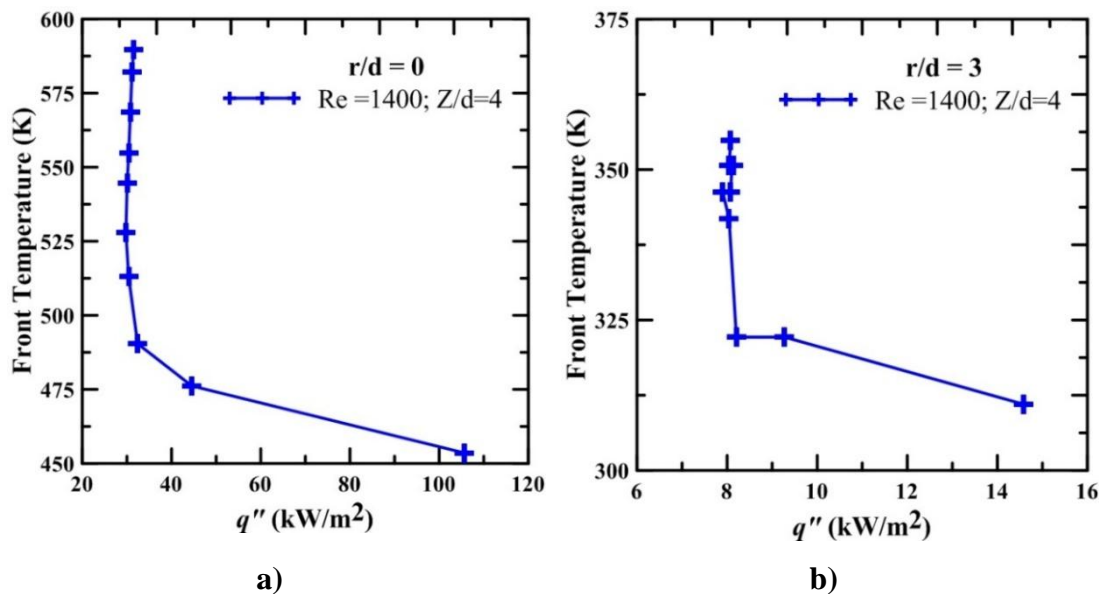


Figure 5.17 Heat flux vs. corresponding impingement side wall temperature a) at $r/d = 0$ and b) at $r/d = 3$ for the experimental data

In case of convection boundary condition, need of reference temperature beforehand rules out its further consideration as it is contrary to the purpose of having them evaluated simultaneously. However, heat flux obtained by the application of Duhamel theorem to experimental data of $Re = 1400$ at $Z/d = 4$ are plotted against corresponding front temperature in Figure 5.17. It can be seen that the application of Duhamel theorem fails the test of linear relationship requirement (of the form, $mx + c = y$ where m is slope and c is the y intercept of the graph of x vs y) of wall heat flux and wall temperature.

5.3.4 Transient front surface temperature and heat flux estimation

As stated in 2.10.1, to estimate heat transfer coefficient and reference temperature simultaneously, transient temperatures and corresponding heat flux values at the

impingement are required. Moreover all the numerical cases carried out are two dimensional axisymmetric with transient formulations. Thus, 3-D IHCP solution is applied for 2-D axisymmetric case.

5.3.4.1 Three dimensional IHCP solution

The inverse solution to three dimensional conduction problem (Feng et al., 2011) is restructured to work for two dimensional heat conduction problem. This reformed solution is then validated with the use of numerically simulated data for hot jet.

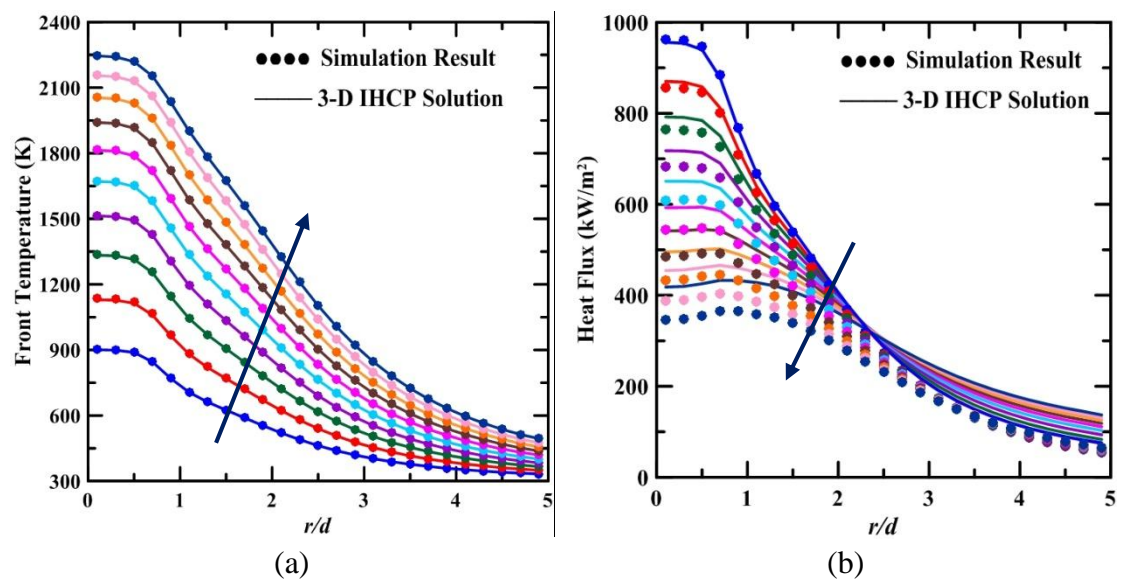


Figure 5.18 Matching of (a) front temperature (b) heat flux computed by 3-D IHCP solution with simulation results. The direction of arrow indicates the increasing value of t from 0.5 to 5 sec in steps of 0.5.

A plate of 1 mm thickness and 60 mm width having constant thermal conductivity 1.05 (W/mK), density 2250 (kg/m^3) and specific heat 780 (J/kgK) is considered as target plate. The numerical procedure is mentioned in the section 3.5.2.1 and its validation along with configuration of the plate and jet is given in section 5.4.1.1. The laminar impinging jet having temperature 3000 K at $\text{Re}=1333$, $Z/d=4$ is assumed impinging on a target plate. Impinging gas properties are assumed same as mentioned in Remie et al. (2008). Plate is assumed at 300 K initially. Numerically determined back surface temperatures are used as input to inverse solution to obtain front surface temperatures and corresponding heat flux magnitudes.

Figure 5.18a shows the comparative analysis of inversely estimated front temperatures with the numerically simulated data. The match between them is within 1%. The comparative plot for estimated heat flux is illustrated in Figure 5.18b and it can be observed that there is an overestimation in the heat flux values for larger time. The reason behind this over estimation is constant heat flux assumption at $(m, n) = (0, 0)$ in the inverse solution.

5.3.4.2 3-D IHCP solution + Duhamel Theorem

Constant heat flux assumption at $(m, n) = (0, 0)$ over estimates the heat flux data. Thus, 3-D IHCP solution is improved with the help of Duhamel's theorem. The time dependent continuous function $F(t)$ can be obtained by using appropriate fit to the transient front modal temperatures estimated by 3-D IHCP solution at $(m, n) = (0, 0)$. Here, second order polynomial is used to fit the transient front modal temperatures. Then the front modal heat flux at $(m, n) = (0, 0)$ is obtained by application of Duhamel's theorem.

Exclusive validation is done in this section for this method. Hot as well as cold impinging jets are characterized with the help of this solution. Laminar and turbulent jets with varying nozzle to plate spacing (Z/d) and Reynolds numbers are considered. A plate of 1 mm thickness and 60 mm width having constant thermal conductivity 1.05 (W/mK), density 2250 (kg/m^3) and specific heat 780 (J/kgK) is considered as target plate for both type impinging jets.

Laminar Jet

The laminar impinging jet at $\text{Re}=1333$, $Z/d=4$ is considered for heating as well as cooling application. Impinging gas properties are assumed same as mentioned in Remie et al. (2008). Impinging gas is assumed at 3000 K in case of heating application. Plate is assumed at 300 K initially. With the Exception for initial few seconds, present technique has succeeded in catching all the temporal variation in front surface heat flux along radial direction of the plate as shown in Figure 5.19. Maximum deviation of 4% is found for the stagnation heat flux value at 0.5 sec.

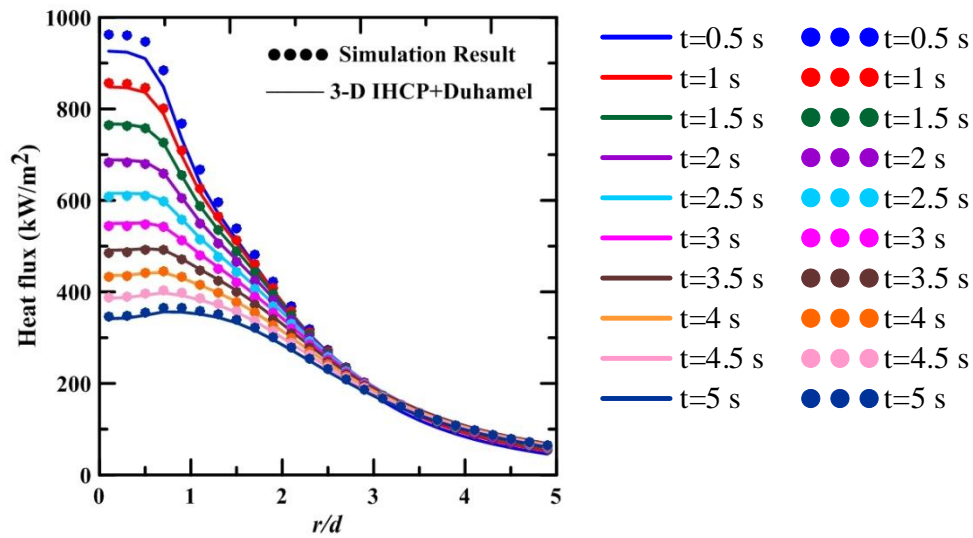


Figure 5.19 Comparison of heat flux in case of hot laminar jet impingement.

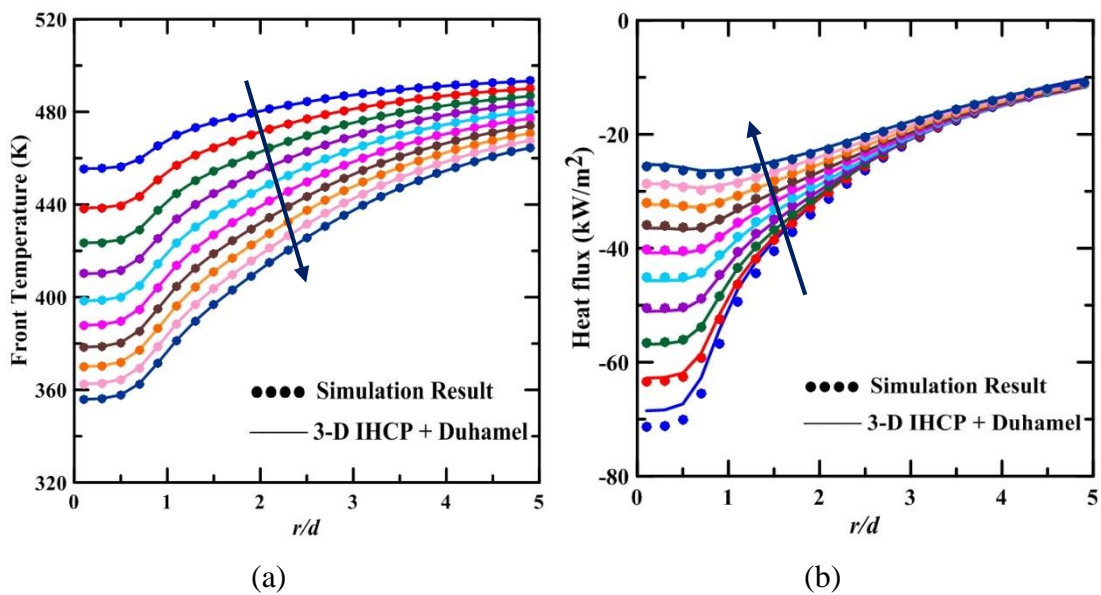


Figure 5.20 Comparison of (a) front surface temperature (b) wall heat flux in case of cold laminar jet impingement. The direction of arrow indicates the increasing value of t from 0.5 to 5 sec in steps of 0.5 sec.

For the cooling application, a plate is considered at 500 K and laminar jet at 300 K is assumed impinging on it. Figure 5.20 compares the results for front surface temperature and wall heat flux estimated by present technique with simulation results. Again similar agreement in the results can be observed as that in heating application.

Turbulent jet

The numerical procedure adopted for turbulent jet impinging flame jets is similar as described in Guo et al. (2017) and its details are already discussed in section 3.5.2.2. The turbulent impinging jet at $Re=34000$, $Z/d=4$ is considered for heating as well as cooling application. Impinging gas properties are assumed same as mentioned in Guo et al. (2017).

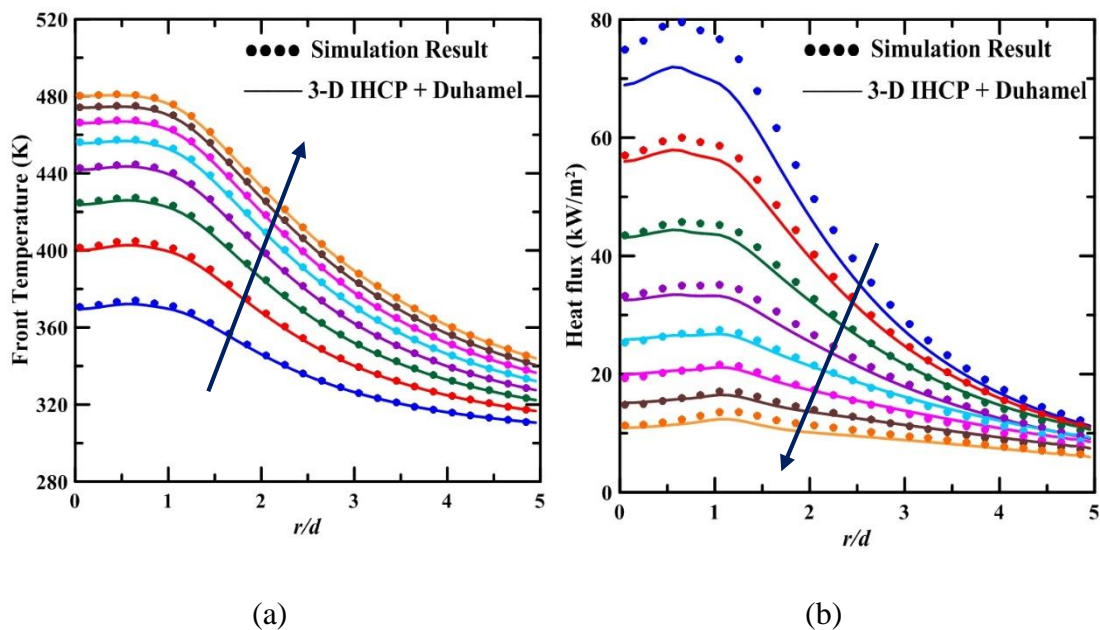


Figure 5.21 Comparison of (a) front surface temperature (b) wall heat flux in case of heating application of a turbulent jet. The direction of arrow indicates the increasing value of t from 1 to 8 sec in steps of 1 sec.

In case of heating application, the plate is considered initially at 300 K and turbulent jet at 500 K assumed impinging on it. While for the cooling application, turbulent jet at 293 K is considered impinging on a plate at 673 K. The results of heating and cooling application for front surface temperature and wall heat flux are shown in Figure 5.21 and Figure 5.22 respectively. The estimated data is in good match with the simulated data.

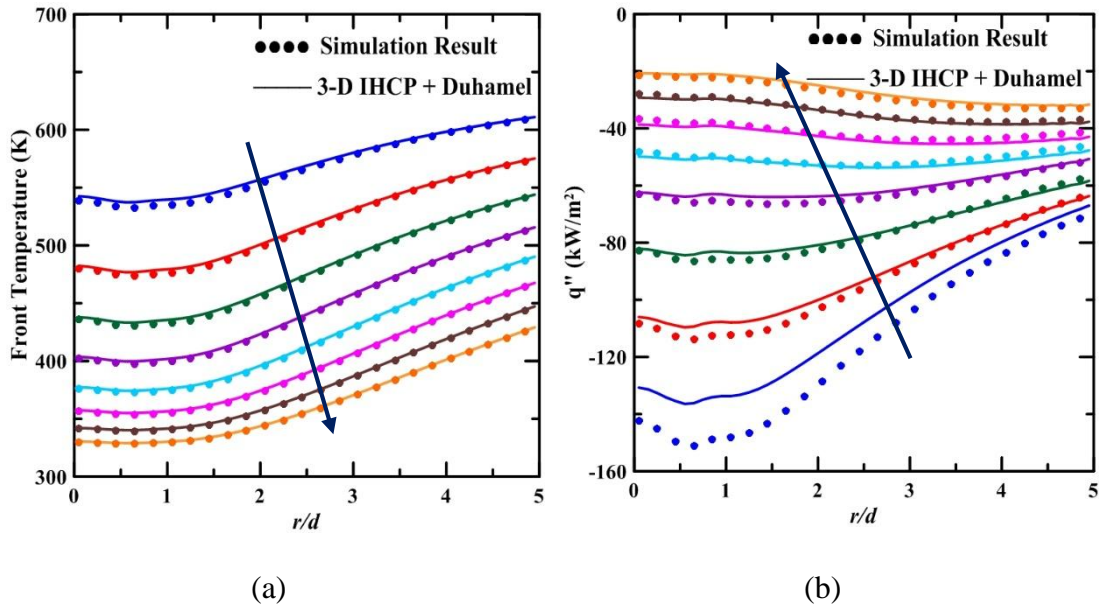


Figure 5.22 Comparison of (a) front surface temperature (b) wall heat flux in case of cooling application of a turbulent jet. The direction of arrow indicates the increasing value of t from 1 to 8 sec in steps of 1 sec.

Flame jet

Further, the three dimensional IHCP code employing the procedure of Feng *et al.* (2011) and Duhamel theorem has been validated for flame jet with numerically simulated data using Ansys Fluent software. A steel plate of 3 mm thick and 60 mm width having constant thermal conductivity 16.27 (W/mK), density 8030 (kg/m^3) and specific heat 502.48 (J/kgK) is considered. Except the front surface, all other surfaces are insulated. A forward numerical code or transient axisymmetric heat conduction problem is run in Fluent with heat transfer coefficient and reference temperature as a convection boundary condition via user defined function. The typical variations of heat transfer coefficient and reference temperature are taken from the reported experimental data of Hindasageri *et al.* (2014) for $\text{Re}=1000$, $Z/d=4$ for circular tube burner. The obtained back side transient temperatures at 25 positions along the length of plate (60 mm) are given as input to the analytical IHCP method and the front side wall temperatures and wall heat flux are obtained. Plots of wall temperature and wall heat flux for varying r/d obtained by numerically simulated data and 3-D IHCP solution are shown in Figure 5.23a and Figure 5.23b respectively.

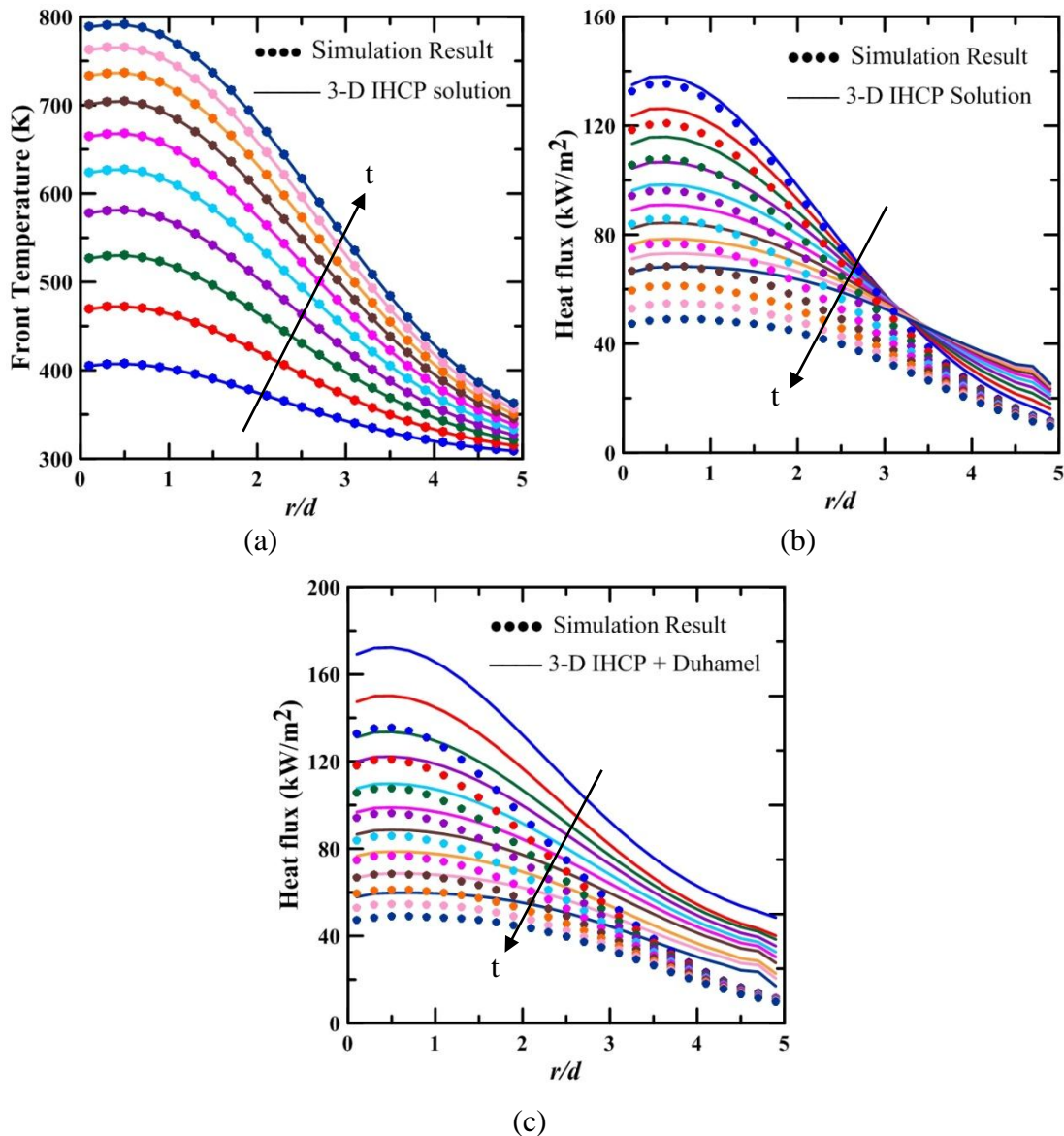


Figure 5.23 Comparison of (a) front surface temperature, (b) heat flux computed from 3-D IHCP solution (c) heat flux computed from 3-D IHCP + Duhamel for $Re = 1000$, $Z/d=4$

The obtained temperature data match within 1% but the heat flux data is overestimated for larger time. This over estimate by the 3-D IHCP solution is due to constant heat flux assumption at $(m, n) = (0, 0)$. Also at larger r/d , the prediction is poor.

Further 3-D IHCP solution with Duhamel technique is applied to get the front flux. Figure 5.23c compares the heat flux computed from the mixed technique with simulated flux. Over estimation in computed data over the r/d is clearly visible. This time,

improved solution is largely failed to recover temporal variation of heat flux over the entire r/d . This is in contrast with the results for impinging jets. Reason behind this contrast is attributed to large lateral temperature gradient produced by the impinging flame jet over the plate. Effect of these large lateral gradients on heat conduction is not possible to capture by this technique. Thus, an alternate approach is proposed to estimate heat flux accurately as stated in subsequent section.

5.3.4.3 3-D IHCP solution + Temperature gradient

An alternate procedure is considered in this work to estimate the transient heat flux accurately at the front surface by numerically computing the gradient by finite difference method.

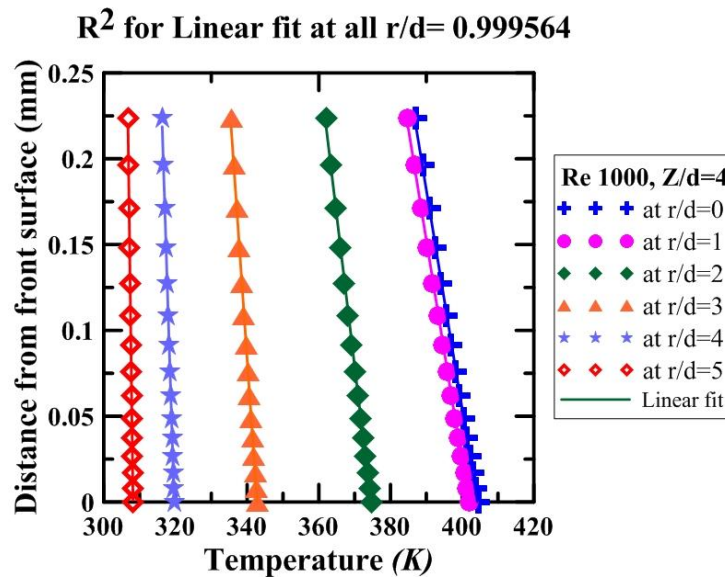


Figure 5.24 Temperature gradient from impingement (front) surface for $Re = 1000$,
 $Z/d=4$

Two finite differences schemes are considered here - two point (Equation 5.6) and three point (Equation 5.7) of first order and second order accuracies respectively.

$$\frac{dT}{dx} = \frac{T(x+h) - T(x)}{h} \quad (5.6)$$

$$\frac{dT}{dx} = \frac{-3T(x) + 4T(x+h) - T(x+2h)}{2h} \quad (5.7)$$

The temperature gradient near the wall upto non-dimensional $z = 0.2$ is found to be linear (Figure 5.24) and a simple slope of first order approximation would be accurate. Comparison of the heat flux with temperature gradient computed from two point and three point schemes has good agreement with deviations of less than 1%. Using the first order finite difference scheme, the heat flux obtained is in excellent agreement with numerically simulated heat flux data of Fluent software as shown in Figure 5.25. Hence for further applications only first order finite difference scheme is considered.

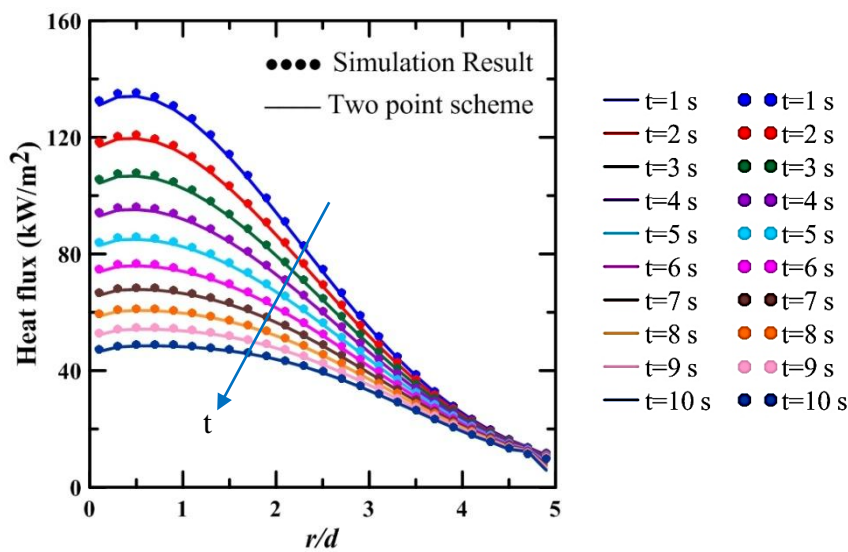


Figure 5.25 Comparison of heat flux computed from two point scheme for $Re = 1000$, $Z/d=4$

5.3.5 Heat transfer coefficient and reference temperature for real time experimental data

In this section, two point scheme is used to estimate heat flux at the impinging side to characterize circular and non-circular impinging flame jets. Further, heat transfer coefficient and reference temperatures are estimated simultaneously with the help of thin foil technique.

5.3.5.1 Circular jet

The two point scheme for temperature gradient estimation is applied to real time experimental data for $Re = 1000$ and 1600 at $Z/d=4$ for circular tube burner for 3 mm

plate thickness. For the analysis purpose 25 sensors are assumed along the radial direction over the length of 50 mm from stagnation point. Back side data is sampled up to 10 sec in the step of 2 sec. Thermo physical properties $k_V = 0.8956 (1+1.675e-3 T)$ W/m K and $\alpha = 8.04e-8$ for quartz plate are considered (Hindasageri et al. 2014). Back surface temperature data is given as input to the 3-D IHCP solution to compute front surface temperature of the plate. The temperature gradient is taken between $z = 0$ (Plate thickness=3 mm) and $z=0.05$ mm (Plate thickness=2.95 mm) from the front surface. The estimated front surface temperature and surface heat flux is shown in Figure 5.26a and Figure 5.26b for $Re = 1000$ at $Z/d = 4$. The raw experimental data obtained from the thermal IR camera has temporal and spatial fluctuations and hence the experimental data has to be smoothed to have any meaningful result. The raw data is smoothed with the help of 4th order polynomial and then given as input to 3-D IHCP solution. It is also found that small noise in the estimated front surface temperature, arised due to small noise present in input data even after smoothing, can result in large fluctuations in heat flux estimation. Hence, the temperature obtained from 3-D IHCP solution is further smoothed by 7th order polynomial fit to get front surface heat flux. The linear rate law is again used to get the reference temperature and the heat transfer coefficient. From Figure 5.26c, the fit of front surface temperature against corresponding heat flux is found to be linear at various r/d and is shown for specific values of $r/d = 0$ and 3 in Figure 5.26c.

The flame jet structure is highly oscillatory, therefore the heat transfer coefficient and reference temperature estimated tend to exhibit oscillatory pattern for smaller time interval as the heat flux is computed from temperature gradient of this oscillatory data. This observation is also seen in the data reported by Loubat et al. (2004). Various set of data with different time interval are assessed to estimate heat transfer coefficient and reference temperature for $Re = 1000$ and 1600 at $Z/d = 4$. Data from initial transient of 2 sec to 10 sec in an interval of 2 sec and higher transient 5 sec to 50 sec in an interval of 5 sec is shown in Figure 5.26d and Figure 5.26e. At larger times, the oscillations die and a gradual decrease of both heat transfer coefficient and reference temperature is observed as shown in Figure 5.26d and Figure 5.26e.

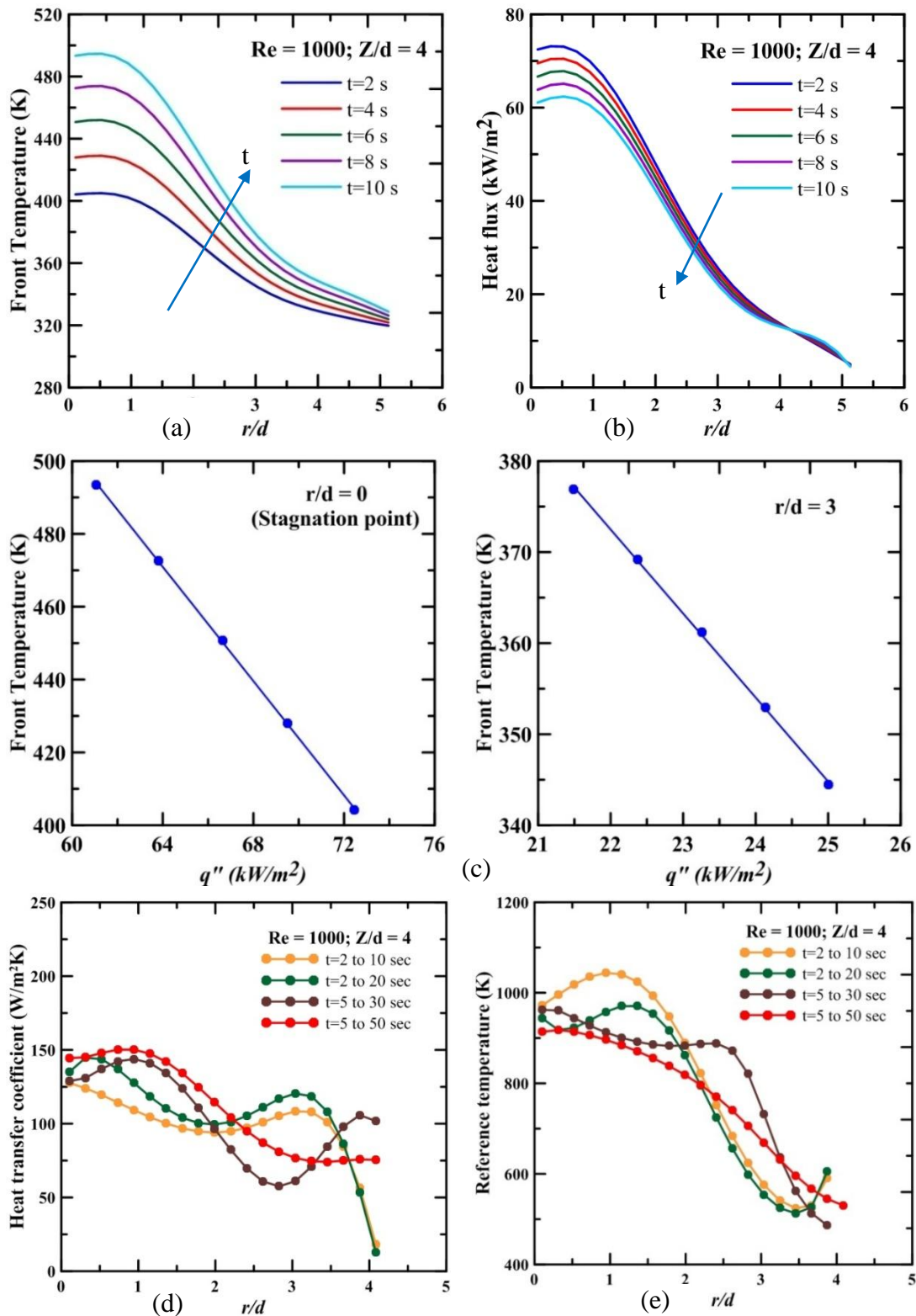


Figure 5.26 Experimental (a) Surface temperature (b) Flux by two point scheme (c) Flux vs Wall temperature at $r/d = 0$ and 3 for 2 to 10 sec data (d) Estimated heat transfer coeff (e) Estimated reference temp (Mixture conditions $\phi=1$, 2 bar, 300K)

5.3.5.2 Non-circular flame jets

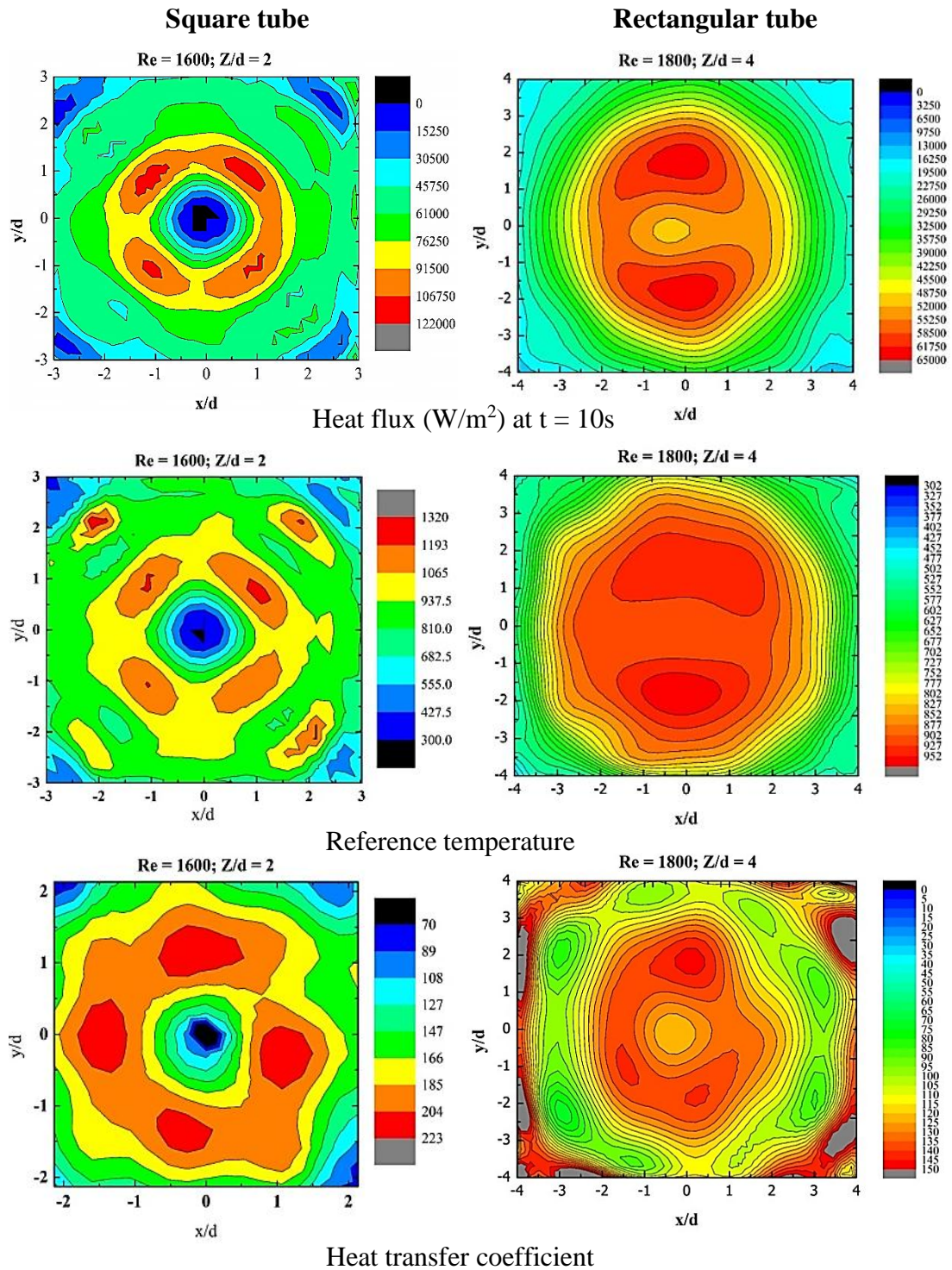


Figure 5.27 Heat transfer contour maps for square and rectangular tube flame jets

The successful implementation of three dimensional IHCP method of Feng et al. (2011) prompted to test this method for non-circular flame jets which have non-symmetric spatial variations of wall temperature. Two cases of flame jets - ensuing from square tube (10 mm X 10 mm) of hydraulic diameter 10mm with $Z/d = 2$ and $Re = 1600$ and rectangular tube (19 mm X 9 mm) of hydraulic diameter 12.21mm with $Z/d = 4$ and $Re = 1800$ are considered. A 4th order polynomial fit with least square fit accuracy of 99% is used to capture the spatial variations in input experimental temperature data. The heat flux, heat transfer coefficient and reference temperature contour maps for square and rectangular burners are shown in Figure 5.27. The observed contour patterns are in agreement with reported work of Hindasageri et al. (2016) on axis switching.

5.3.6 Radiation loss correction procedure

From Figure 5.26d and Figure 5.26e it is observed that the estimated reference temperature for larger time interval data is lower than that at smaller time interval while the estimated heat transfer coefficient has opposite trend. This is attributed to the radiation loss from the impingement plate.

To demonstrate this, two dimensional axisymmetric transient heat conduction simulation is carried out for typical h and T_{ref} values of Hindasageri et al. (2014) taken as input in the numerical model. Figure 5.28a shows that at smaller time interval of upto 5 sec, there is no significant difference in the slopes of the two lines. This is expected since at lower temperatures, the radiation contribution is insignificant and becomes significant at higher time intervals due to the fourth power dependence of temperature. It is clear that reference temperature is under predicted and the heat transfer coefficient is over predicted when radiation loss is neglected. These deviations of reference temperature and the heat transfer coefficient can be corrected by applying the following simple procedure.

It is observed that the slope of plot of wall temperature vs wall heat flux decreases steadily in the presence of radiation loss. A second order polynomial curve fit function can be applied to this decay of slope ($m(q'')$). The derivative of this curve fit polynomial function would give the slope of the polynomial at any point on the curve.

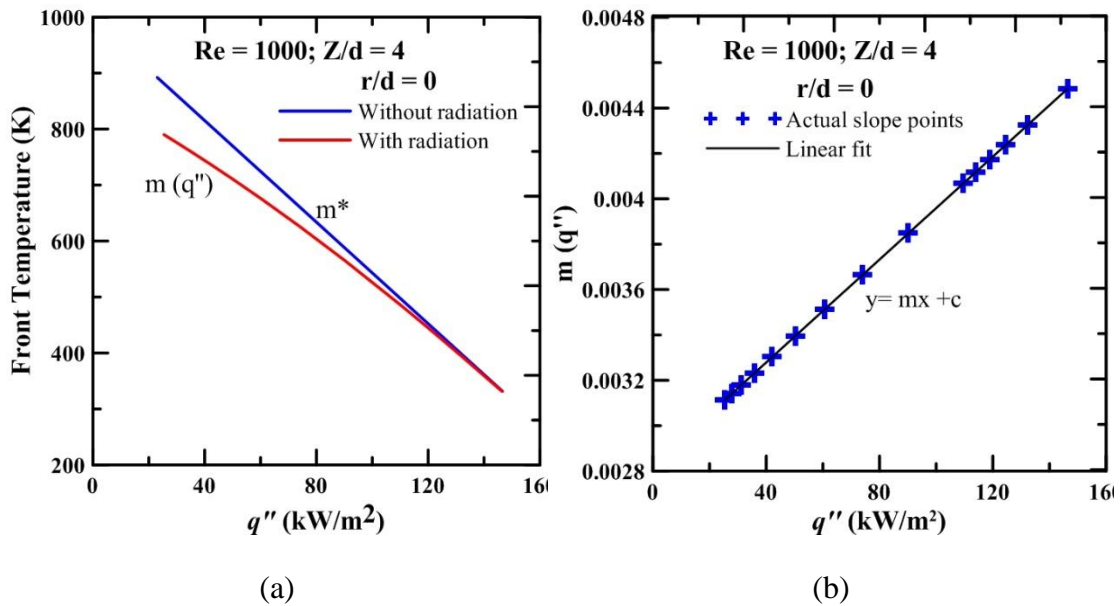


Figure 5.28 a) Wall heat flux vs wall temperature with and without radiation loss b) Linearity in slope of quadratic fit

If the real time experimental data were to be free from oscillations then the slope of this polynomial at early time interval would have given the required corrected reference temperature (T_{ref}^*) and the heat transfer coefficient (h^*). Since, non-oscillatory values of h and T_{ref} are possible only at larger time, slope ($m(q'')$) of quadratic function fitted to larger time data is plotted against q'' . It is obvious that derivative of quadratic function (ax^2+bx+c) is always linear ($2ax+b$) as shown in Figure 5.28b.

The slope (m^*) which is to be found out would be on same linear line and it corresponds to initial flux value. Hence, wall Heat flux at different time intervals is plotted in Figure 5.29a and extrapolated back for $t = 0$. The corrected slope (m^*) can be now used to get the corrected reference temperature (T_{ref}^*) by computing the corrected wall temperature (T_w^*) at larger time that corresponds to smaller heat flux value as shown in Figure 5.29b. This corrected wall temperature and corresponding wall heat flux along with the corrected slope ($m^* = 1/h^*$) can be used to get the corrected reference temperature (T_{ref}^*) by using Eq. (24). Obtained T_{ref}^* and h^* by this simple procedure is in good agreement with the numerically simulated data as shown in Figure 5.30a and Figure 5.30b.

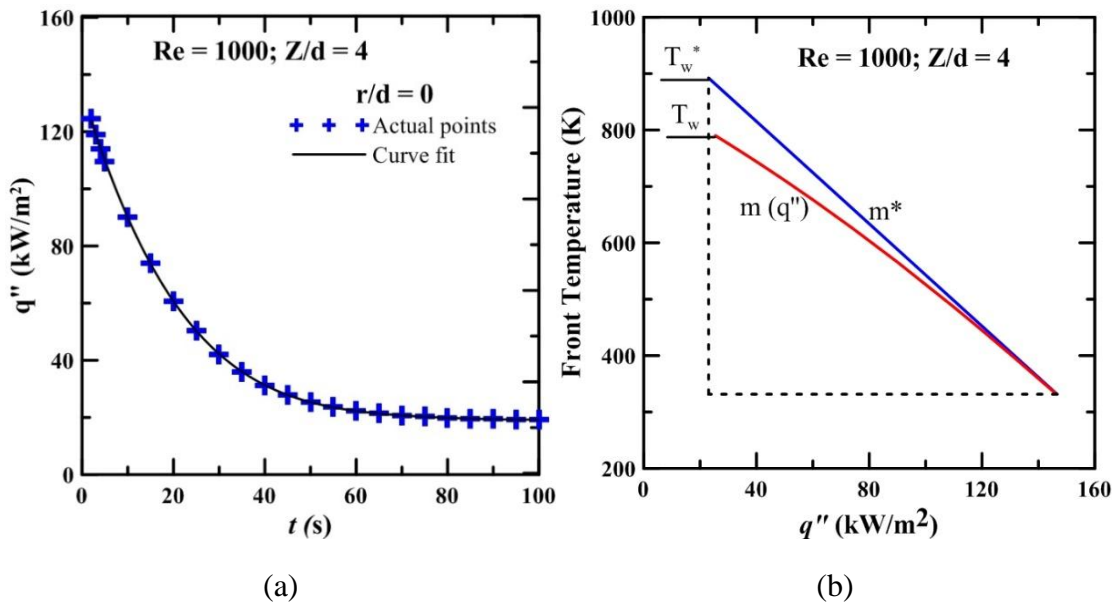


Figure 5.29 a) Extrapolation of flux b) Corrected wall temperature (T_w^*)

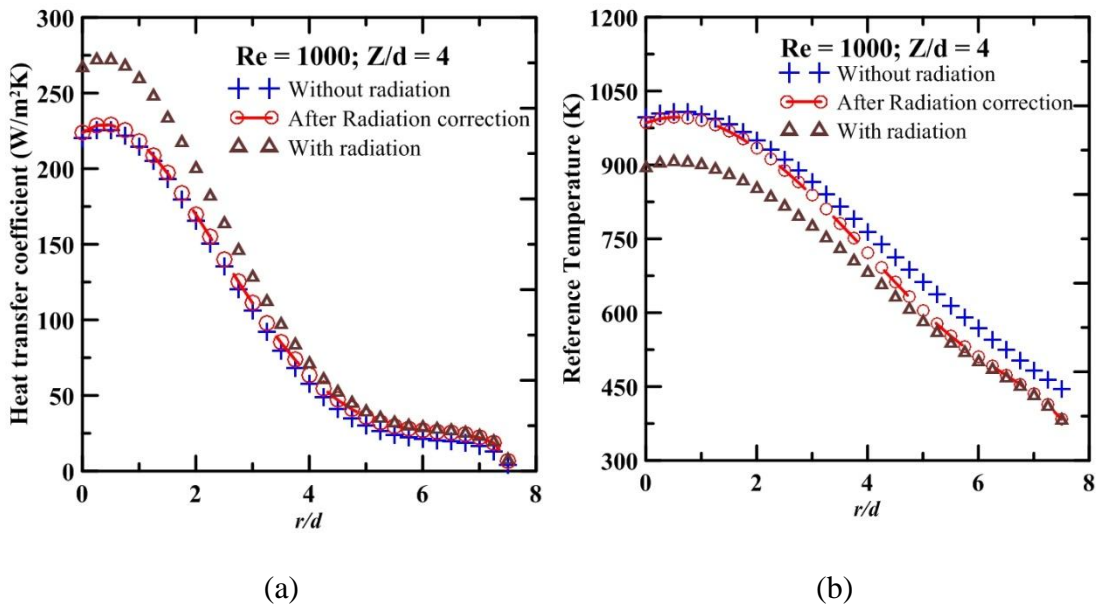


Figure 5.30 a) Corrected heat transfer coefficient (h^*) b) Corrected reference temperature (T_{ref}^*)

5.3.7 Effect of variable thermal conductivity and radiation correction

For larger time interval, the plate temperature increases upto 800 K and 1000 K for 50 seconds at Re 1000 and Re 1600 respectively, hence consideration of thermal conductivity variation and radiation correction becomes important.

Hence, the thermal conductivity variation is considered in the form $k = k_0(1 + \beta T)$ as given in Equation (5.8)

$$k_v = 0.8956(1 + 1.675e^{-3}T) \quad (5.8)$$

The generalized multi-dimensional heat conduction problem with variable thermal conductivity (k_v) for flame jet impinging on a flat plate can be mathematically expressed as given in Equation (5.9).

$$\rho C \frac{\partial T}{\partial t} = \frac{\partial}{\partial x} \left(k_v \frac{\partial T}{\partial x} \right) + \frac{\partial}{\partial y} \left(k_v \frac{\partial T}{\partial y} \right) + \frac{\partial}{\partial z} \left(k_v \frac{\partial T}{\partial z} \right) \quad (5.9)$$

In Equation (5.9), RHS has become non-linear due to temperature dependent thermal conductivity ' k_v '. To transfer non-linear conduction term into linear form, Kirchhoff transformation (Jiji, 2009) has been used and consequently Kirchhoff transformation temperature variable ' θ^* ' is defined as given in Equation (5.10).

$$\theta^*(T) = \frac{1}{k_0} \int_0^T k_v(T) dT \quad (5.10)$$

As $k_v(T)$ is known, relationship between θ^* and T can obtained from Equation (5.8) and Equation (5.10) as given in Equation (5.11).

$$\theta^*(T) = T + \frac{\beta}{2} T^2 \quad (5.11)$$

To determine ' θ^* ', the Equation (5.9) is transformed as given in Equation (5.12).

$$\frac{1}{\alpha} \left(\frac{\partial \theta^*}{\partial t} \right) = \left(\frac{\partial^2 \theta^*}{\partial x^2} + \frac{\partial^2 \theta^*}{\partial y^2} + \frac{\partial^2 \theta^*}{\partial z^2} \right) \quad (5.12)$$

Where $\alpha = \frac{k_v}{\rho C}$ is assumed constant.

Then, 3-D IHCP solution methodology can be adopted to estimate front side temperature. The real front side temperature (T) can be determined by knowing the solution to the quadratic equation (Equation (5.11)) as given in Equation (5.13).

$$T = \sqrt{\left(\frac{1}{\beta^2} + \frac{2}{\beta} \theta^* \right)} - \frac{1}{\beta} \quad (5.13)$$

Further, heat flux can be found out by Eq. (A7). Required temperature gradient can be obtained by two point scheme.

$$q(z, t) = -k_v \left(\frac{\partial T(z, t)}{\partial z} \right)_{z=H} \quad (5.14)$$

The thermal conductivity for Equation (5.14) is taken at average temperature of two points where temperature gradient is calculated.

Only consideration of variable thermal conductivity results in over estimation of the reference temperature by upto 10% and under estimation of heat transfer coefficient by upto 10%. The reference temperature is under estimated by upto 50% and the heat transfer coefficient is over estimated by upto 50% when both the thermal conductivity dependence on temperature and radiation loss are neglected. This is attributed to fourth power dependence of temperature in radiation loss. Figure 5.31a-5.31d shows the plot of heat transfer coefficient and reference temperature for experimental data of Re = 1000 and 1600 at Z/d = 4.

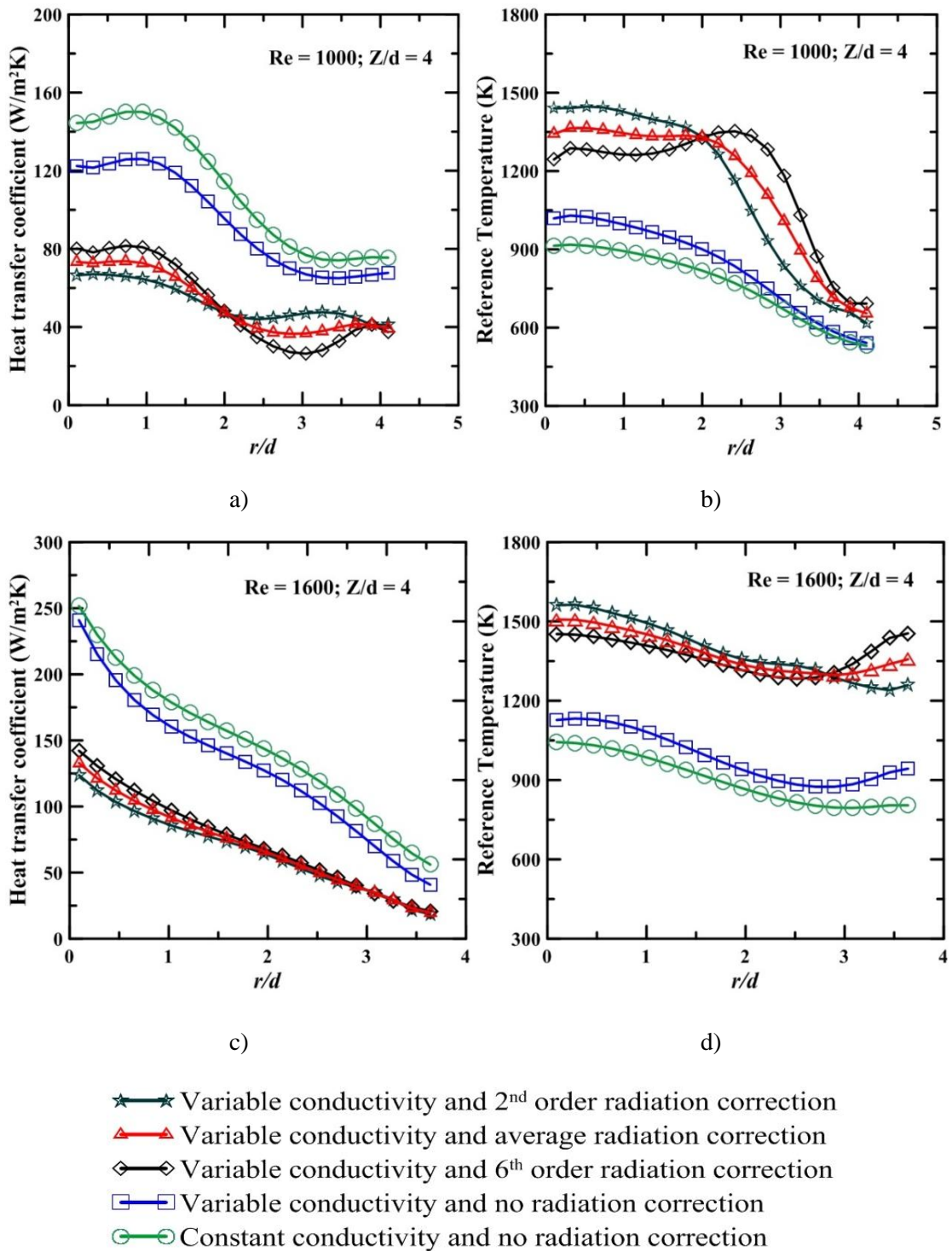


Figure 5.31 Effect of radiation loss and variable thermal conductivity on h and T_{ref} for the experimental data of $Re = 1000$ and 1600 and $Z/d = 4$

5.4 HEAT TRANSFER FROM IMPINGING JETS

Application of The 3-D IHCP solution along with two point scheme is extended further to characterize impinging jets. This section discusses the application of present technique (3-D IHCP + two point) to impinging jets with various configurations such as laminar jet, turbulent jet, hot jet, cold jet and multiple jet. Effect of plate thickness on the accuracy of the present technique is also studied in this section.

5.4.1 Validation of numerical procedure

The present solution is used to characterize both laminar and turbulent jets impinging on a flat plate. Consequently, numerical modelling used for respective jets have been independently validated with related published studies

5.4.1.1 Laminar Jet

For the numerical modelling of laminar impinging jets, the numerical procedure similar to Remie et al. (2008) has been followed. Hot gas at 3000 K is assumed impinging on a flat plate having initial temperature 300 K.

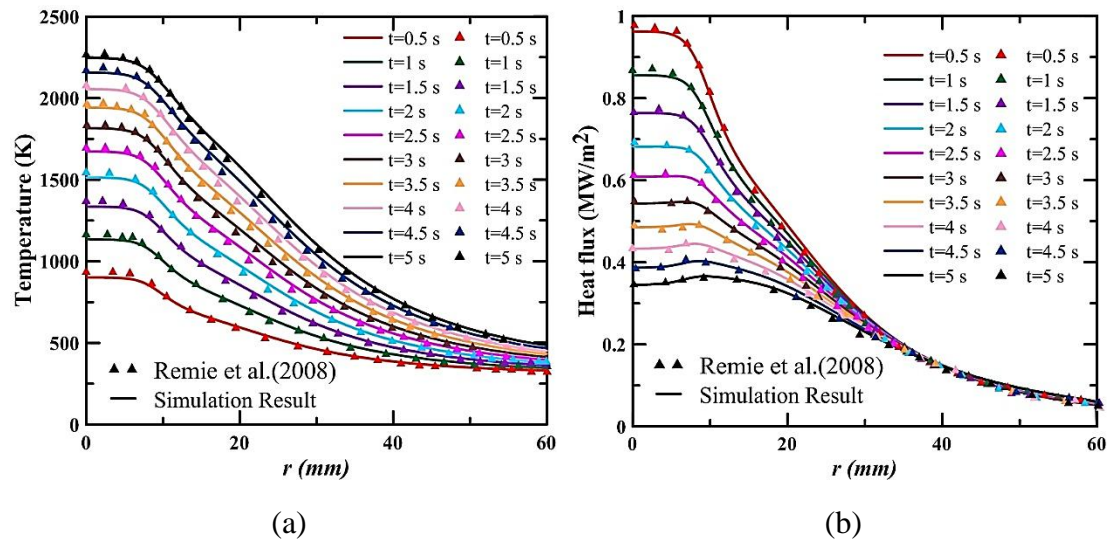


Figure 5.32 Comparison of numerically simulated (a) Front temperature and (b) wall heat flux data

The size of the plate and dimension of burner along with hot gas properties are assumed similar as mentioned in (Remie et al., 2008). The flow simulation is carried out for

burner to plate spacing (Z/d) of 4 at $Re=1333$. The simulated results for front surface temperature and corresponding heat flux are matched with the results of Remie et al. (2008) as illustrated in Figure 5.32a and Figure 5.32b respectively. The match between them is within 2%.

5.4.1.2 Turbulent jet

For the numerical modelling of turbulent impinging jets, the numerical procedure similar to Guo et al. (2017) is considered. Cold turbulent jet at 300 K is assumed impinging on hot target plate having initial temperature of 673 K. Instead three dimensional numerical modelling, simple two dimensional axisymmetric numerical modelling is done in the present study in order to save computational cost and time. The results of present two dimensional numerical simulation for Nusselt number (Nu) distribution are compared with numerical results of Guo et al. (2017) in Figure 5.33.

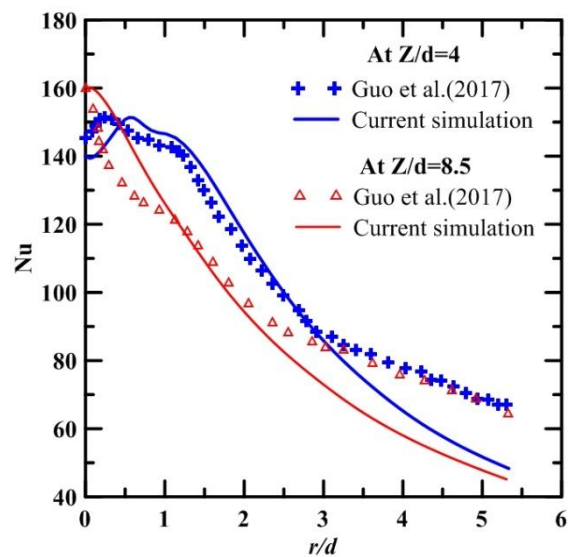


Figure 5.33 Comparison of simulated Nusselt number with Guo et al. (2017)

The Nu is 3% under predicted at stagnation point for $Z/d=4$, whereas for $Z/d=8.5$, it matches exactly with Numerical results of Guo et al. (2017). For both Z/d at larger r/d , Nu estimation is poor because of dissimilarity in mesh density. The mesh density applied at larger r/d is coarse in numerical modelling (Guo et al., 2017) whereas current two dimensional numerical modelling is employed with fine boundary layer near the

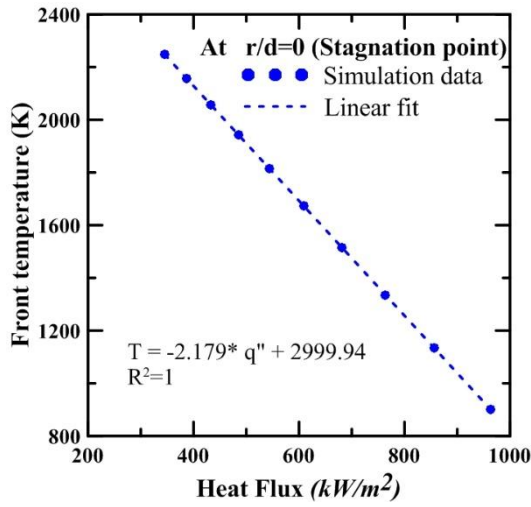
front surface till the end (r/d) of surface. Continuation of boundary layer mesh was necessary to keep the value of orthogonality near 1 in two dimensional modelling with quadrilateral mesh.

5.4.2 Linearity check between heat flux and wall temperature for simulation data

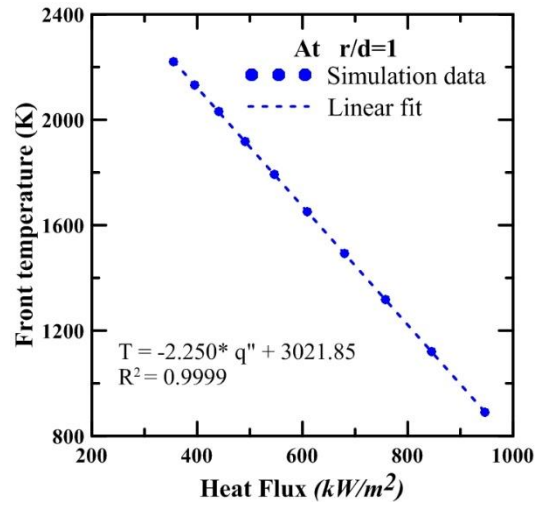
As stated earlier, to estimate heat convection coefficient and reference temperature simultaneously, linearity between wall heat flux and corresponding wall temperature would be utilized. Hence, the linearity check has been done for numerically simulated data. The required data is taken from numerical simulations carried out in section 5.4.1.1. To check linearity, transient wall heat flux is plotted against corresponding wall temperature for various r/d as shown in Figure 5.34. At stagnation point, fit is exactly linear and values of heat convection coefficient and reference temperature seems realistic. The decreasing trend for heat convection coefficient along the radial direction away from the stagnation region is observed which is convincing as similar trends can be found in the literature. However, away from the stagnation point, reference temperature is continuously increasing which is not true. Similar increasing trend for reference temperature is observed also in case of turbulent jet impingement. The reason behind this increase in reference temperature is increase in velocity of the jet after impingement in the region away from the stagnation area. This high kinetic energy results in enthalpy rise which in turn affects reference temperature.

5.4.3 Heat transfer characteristics of impinging jets

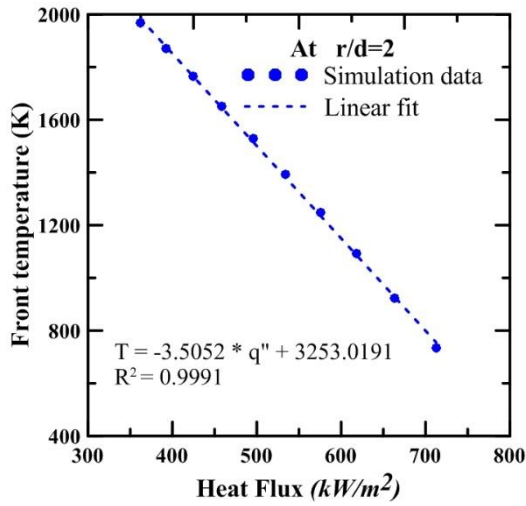
The increase in reference temperature along the radial direction is observed for convective flow simulations, thus flow simulations are avoided. Instead, a simple numerical simulation is carried out only for conduction heat transfer through the plate using heat convection coefficient (h) and reference temperature (T_{ref}) as a convection boundary condition thru user defined function (UDF). In this section, present technique is applied to characterize various configurations of impinging jets. For all the configurations, temperatures and heat flux are estimated at 25 points on the plate along the radial direction at different time interval.



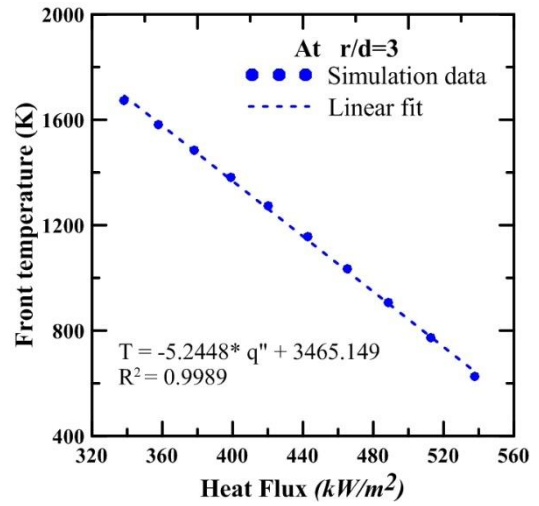
(a)



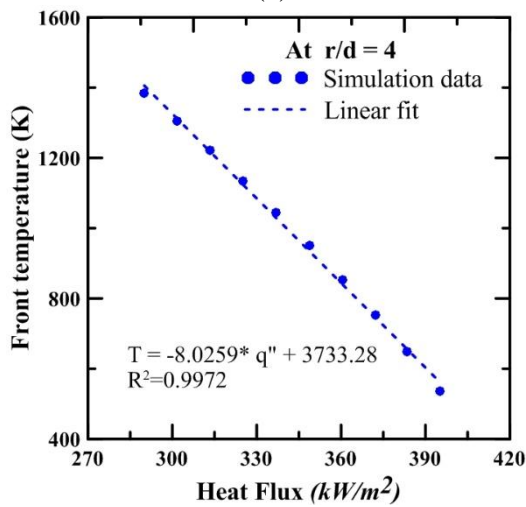
(b)



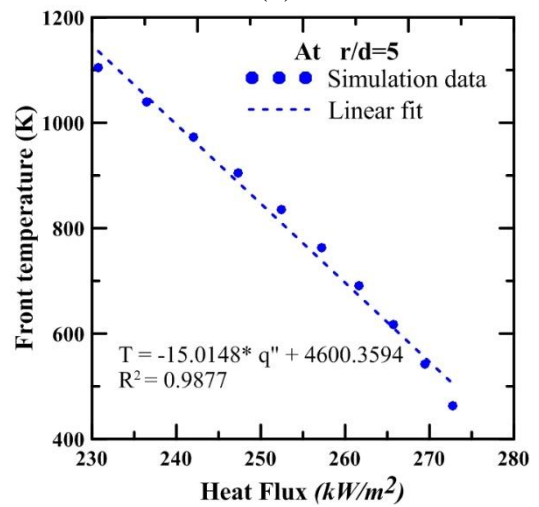
(c)



(d)



(e)



(f)

Figure 5.34 Linear fit at (a) $r/d=0$ (b) $r/d=1$ (c) $r/d=2$ (d) $r/d=3$ (e) $r/d=4$ (f) $r/d=5$

The thickness and length of the plate is assumed as 1 mm and 40 mm respectively. Heat flux is estimated at 0.01 mm inside the plate from the front surface by gradient method.

5.4.3.1 Hot jet

Inverse procedure along with thin foil technique is applied to estimate heat convection coefficient and reference temperature in case of hot jet. The typical variations of heat convection coefficient and reference temperature for hot laminar jet (Plate at 300 K and jet at 373 K) impingement is taken from the reported data of Kuntikana and Prabhu (2016) and fed to numerical code via UDF. The transient data of front surface temperature and heat flux from 1 sec to 10 sec are estimated and considered to evaluate heat convection coefficient and reference temperature. The comparison plots for estimated heat convection coefficient and reference temperature are shown in Figure 5.35a and Figure 5.35b respectively. The estimated data is in very good agreement with the corresponding applied (via UDF) data to numerical code.

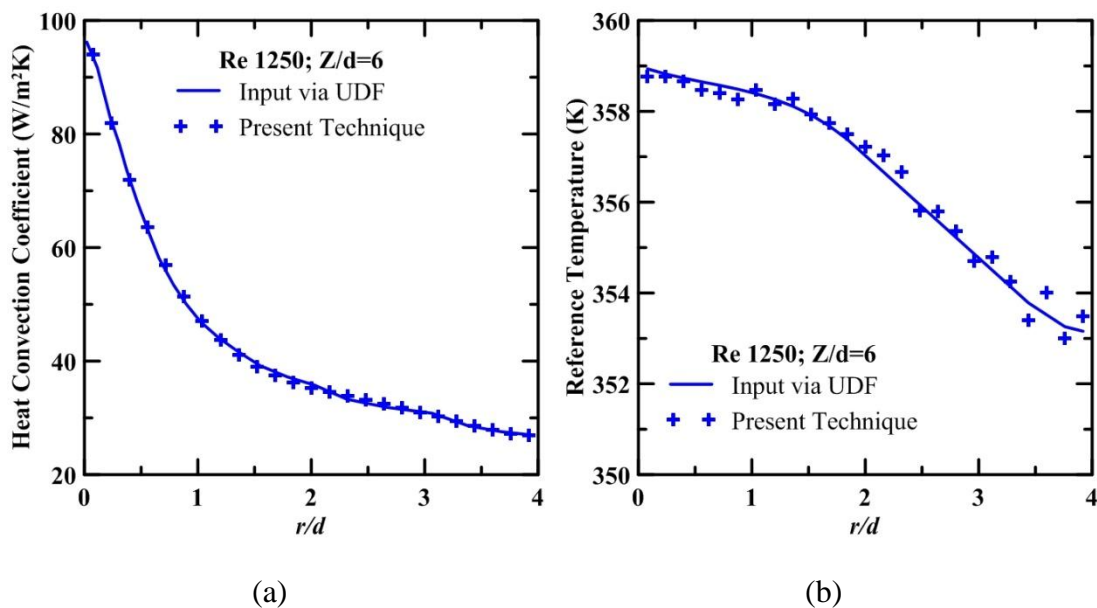


Figure 5.35 Comparison of estimated a) Heat transfer coefficient and b) Reference temperature with applied profile via UDF for hot jet

5.4.3.2 Cold jet

The uniqueness of the present technique is that it can be applied to characterize cold jet as well without a single change in inverse code. The inverse code understands the

cooling or heating process on its own through the temporal variation of input transient temperatures. The typical variations of heat convection coefficient for turbulent cold jet is taken from the work Katti et al. (2011) and applied to numerical code via UDF. Plate is considered at 500 K while impinging jet temperature is assumed at 300 K. The Figure 5.36a shows the matching between the estimated and numerical simulated data. The agreement is found to be very good. To estimate heat convection coefficient, the transient data of front surface temperature (T_{front}) and heat flux from 0.5 sec to 5 sec are evaluated and considered. The Figure 5.36b shows that the estimated data for heat convection coefficient is in good agreement with input data (via UDF).

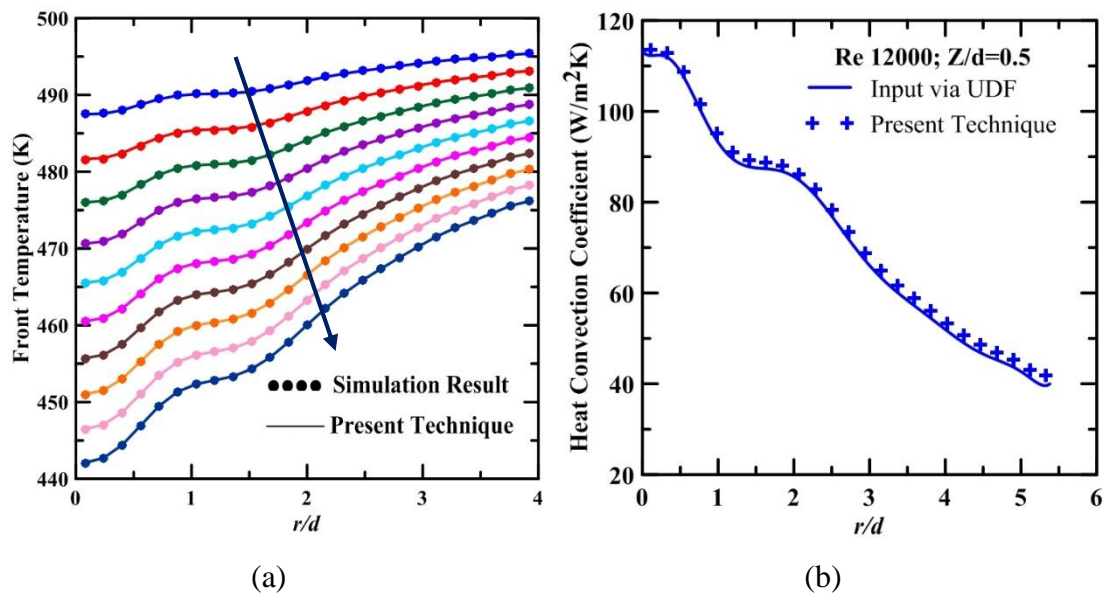


Figure 5.36 Comparison of estimated a) Front temperature with simulation data and b) heat convection coefficient with applied profile via UDF for cold jet. The direction of arrow indicates the increasing value of t from 0.5 to 5 sec in steps of 0.5 sec.

c) Multiple jet: It has been observed that for most of the configurations of impinging jet arrays (Rectangular, circular or elliptical), heat convection coefficient profile is sinusoidal (Caliskan et al., 2014). Thus, sinusoidal profile is applied via UDF to numerical code and simulated back surface temperatures for 0.5 to 5 sec are used as input to inverse code. Plate is considered at temperature 500 K while impinging jet temperature is assumed as 300 K. It can be seen from the Figure 5.37a and Figure 5.37b that estimated front surface temperature and heat convection coefficient are in good match with simulated data.

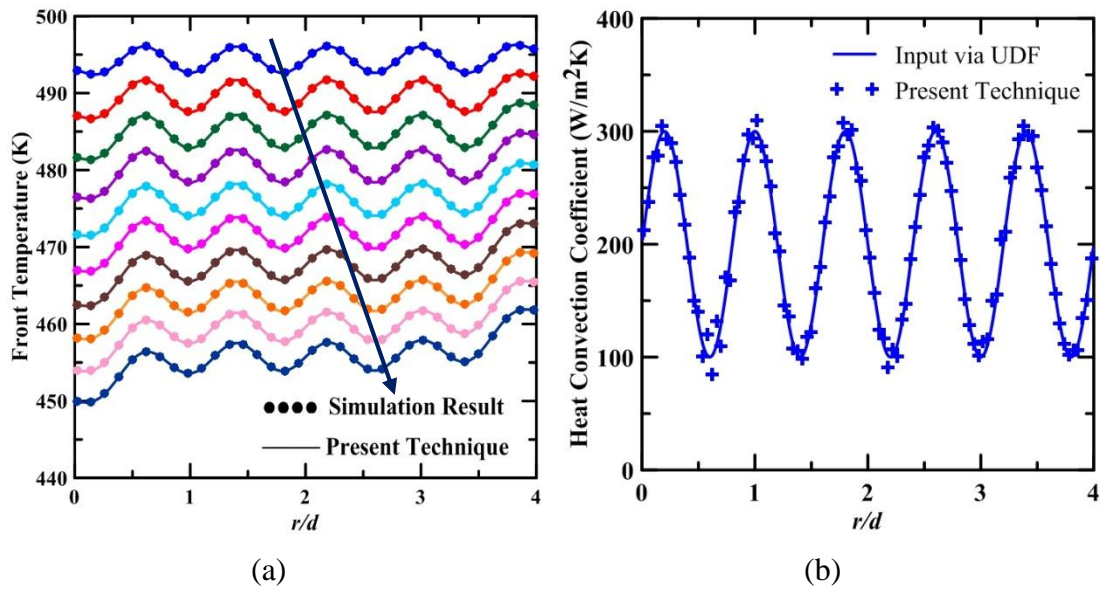


Figure 5.37 Comparison of estimated a) Front temperature with simulated data and b) heat transfer coefficient with applied profile via UDF for multiple jet. The direction of arrow indicates the increasing value of t from 0.5 to 5 sec in steps of 0.5 sec.

5.4.4 Effect of Thickness on 3-D IHCP solution

In this section, effect of plate thickness on the accuracy of inverse estimation of heat convection coefficient and reference temperature is explored. Plates with upto 10 mm thickness are considered at 500 K and typical profile of heat convection coefficient and reference temperature is applied to the front surface of the plate via UDF. Impinging jet temperature is assumed as 300 K. Inverse analysis is done at 25 points on the plate along the radial direction and temporal variation is considered at 10 timings in different interval depending on the thickness of the plate.

5.4.4.1 3mm thick Plate

Present technique is applied to 3 mm thick and 40 mm long plate. The front temperature and corresponding heat flux data for 1 sec to 10 sec is considered during analysis. The comparison of front surface temperature with simulated temperature data is shown in Figure 5.38a. Except at 1 sec, the estimated temperature data is in very good agreement with simulated temperature data. Maximum overestimation of 2.45 K (over 442.6551 K) is found at the first point near the stagnation region which is evaluated as 0.55% more than simulated temperature which can be still considered as good estimation, if

interested only in temperature profiles. Figure 5.38b shows the comparison between the evaluated profiles of heat convection coefficient over the input profile (via UDF). This profile is evaluated by considering the data from 2 sec to 10 sec excluding 1 sec data and it is in close agreement with input profile.

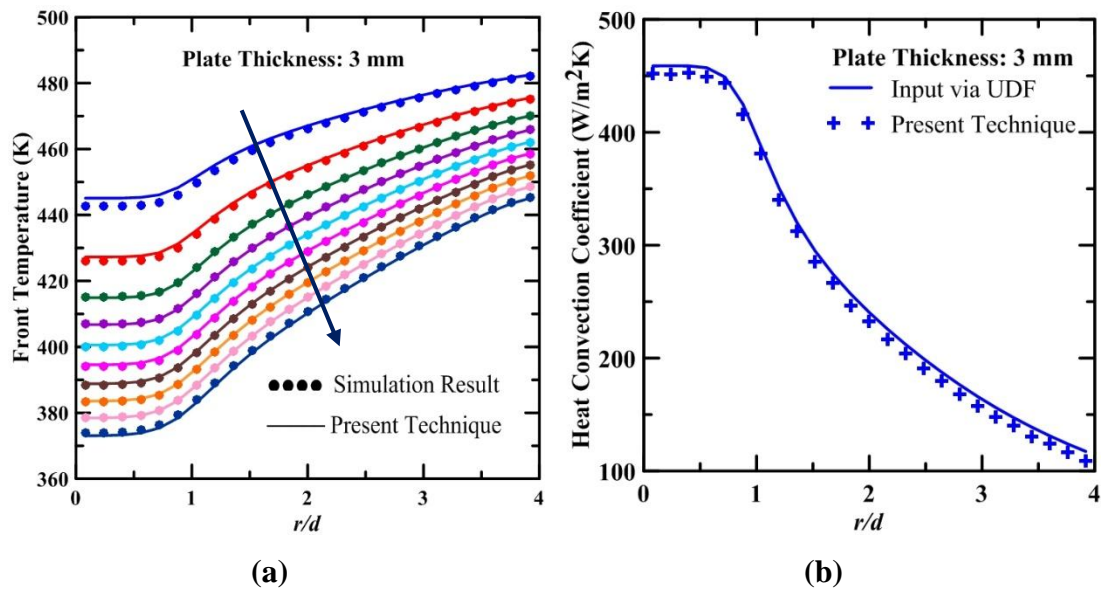


Figure 5.38 Comparison of estimated a) front surface temperature with simulated data and b) Heat convection coefficient with applied profile via UDF for 3 mm plate. The direction of arrow indicates the increasing value of t from 1 to 10 sec in steps of 1 sec.

5.4.4.2 5 mm thick Plate

Present inverse technique is applied to 5 mm thick and 40 mm long plate. For initial seconds (upto 3 sec) appreciable difference (with initial temperature) in back temperature is not found. Thus, the front temperature and corresponding heat flux data for 3 sec to 12 sec is considered during analysis. The comparison of front surface temperature with simulated temperature data is shown in Figure 5.39a. Except at 3 sec and 12 sec, the estimated temperature data matches well with simulated temperature data. Therefore, while evaluating profile of heat convection coefficient, the temperature and heat flux data from 4 sec to 11 sec only considered. Figure 5.39b compares the evaluated profiles of heat convection coefficient with the input profile (via UDF). This evaluated profile matches comparatively poor but still in agreement with the input profile. Maximum deviation around 4% is found at the stagnation point and reduces

further along the radial direction. It is obvious that this deviation is due to small variations in estimated temperatures over the simulated temperatures.

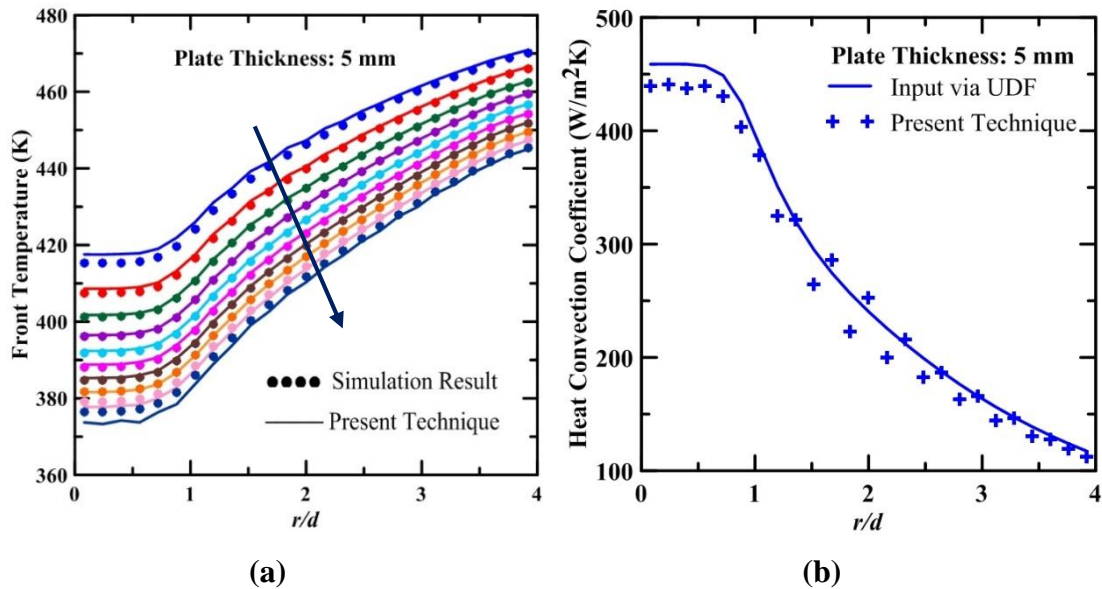


Figure 5.39 Comparison of estimated a) Front surface temperature with simulated data and b) heat convection coefficient with applied profile via UDF for 5 mm plate. The direction of arrow indicates the increasing value of t from 3 to 12 sec in steps of 1 sec.

5.4.4.3 7 mm thick Plate

The application of the present inverse technique is extended to 7 mm thick and 60 mm long plate. Due to absence of significant difference in back surface temperature until 4 sec, front surface temperature and heat flux data is considered between 5 sec to 14 sec for analysis. Estimated temperature data (Figure 5.40a) is in good match with simulated data apart from last 12 sec to 14 sec data. Hence, front temperature and heat flux data between 5 sec to 11 sec is considered to evaluate profile of heat convection coefficient. Evaluated profile of heat convection coefficient is plotted against input profile (via UDF) in Figure 5.40b. Though trend seems matching with the input profile, overestimation around 13% is observed in estimated value of heat convection coefficient at stagnation point. This comparatively more deviation indicates that the accuracy of estimation deteriorates as thickness of the plate increases.

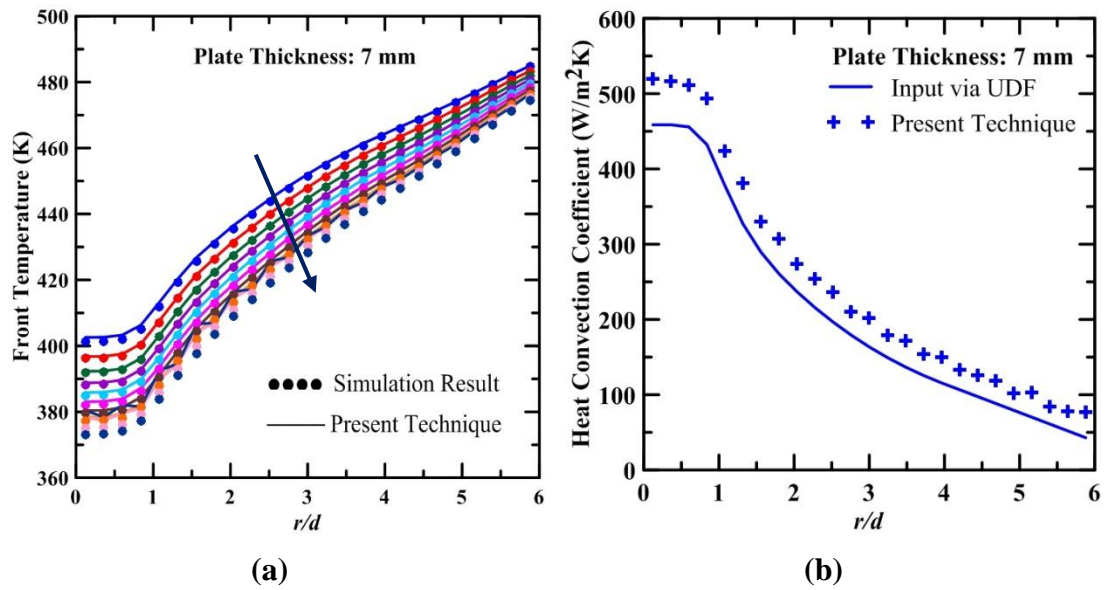


Figure 5.40 Comparison of estimated a) Front surface temperature with simulated data and b) heat convection coefficient with applied profile via UDF for 7 mm plate. The direction of arrow indicates the increasing value of t from 5 to 14 sec in steps of 1 sec.

5.4.4.4 10 mm thick Plate

The final check on the thinness of the plate with the present inverse technique is done on the 10 mm thick and 60 mm long plate. Again up to the time of 7 sec, difference in back surface temperature is not observed much. Thus, for the inverse analysis, front temperature and heat flux data between 8 sec to 17 sec is taken into account. Estimated front temperature data is plotted against corresponding simulated data in Figure 5.41. A lot of fluctuations are observed in estimation of front temperature at almost all the transient timings and it was just not possible to evaluate profile of heat convection coefficient.

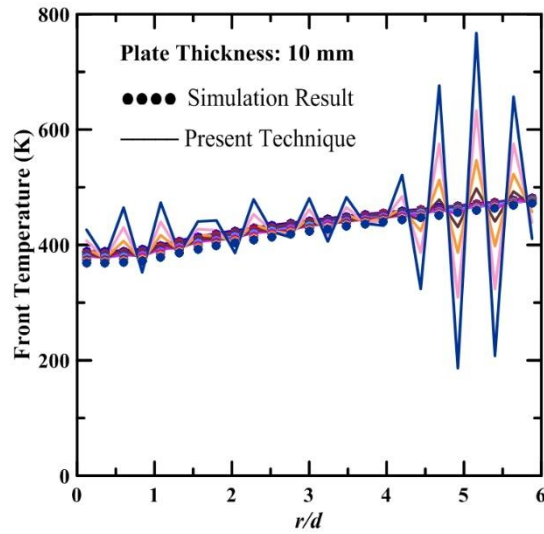


Figure 5.41 Comparison of estimated Front surface temperature with simulated data for 10 mm plate.

5.5 HEAT TRANSFER DISTRIBUTION OF PREMIXED METHANE-AIR LAMINAR FLAME JETS IMPINGING ON RIBBED SURFACES

A few Active methods have been tried to enhance heat transfer rate and to bring out uniformity in the heat transfer distribution in case of flame jet impingement. One way of getting it is making use of multiple jets instead of single set. Another way of improving the heat transfer is by generating swirl inside the burner.

In comparison, extensive study has been done for augmentation of heat transfer rate and to bring out uniformity in the heat transfer distribution in case of air jet impingement. Many Active and passive methods have been tried. One of the passive technique studied largely is rib roughened surfaces. The improvement in heat transfer is credited to flow separation, reattachment, recirculation and disruption of the thermal boundary layer resulted due to presence of rib elements. Moreover ribs increases surface area the way fins do. Many researchers have been studied the heat transfer distribution of rib roughened surfaces for air jet impingement. Thus this study would be good exercise to see the heat transfer distribution in case of flame jets impinging on circular, triangular as well as rectangular rib roughened surfaces. Outcomes of present study are meant to inspire further investigations on passive techniques in the field of flame jet impingement.

5.5.1 Experimental procedure

Experimental set-up used for studying the heat transfer distribution of impinging premixed Methane-air flame jet on ribbed surfaces is explained in section 3.2. Circular stainless steel burner with diameter 10 mm and length 90 mm is used for the impingement. Stainless steel plate (SS 316) having dimension of 200 mm x 150 mm x 3 mm is considered as target plate (Figure 5.42). Plate is blackened with the high temperature flat black spray paint (Bosney make) from non-impingement side (back side) and it is cured in the furnace upto temperature 600°C. Thermal infrared (IR) camera A325sc, FLIR make is used to capture images from the back side.

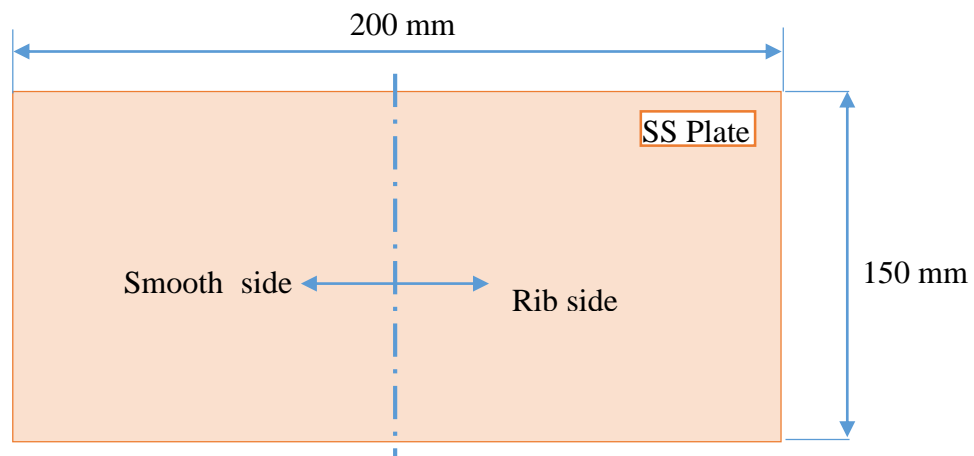
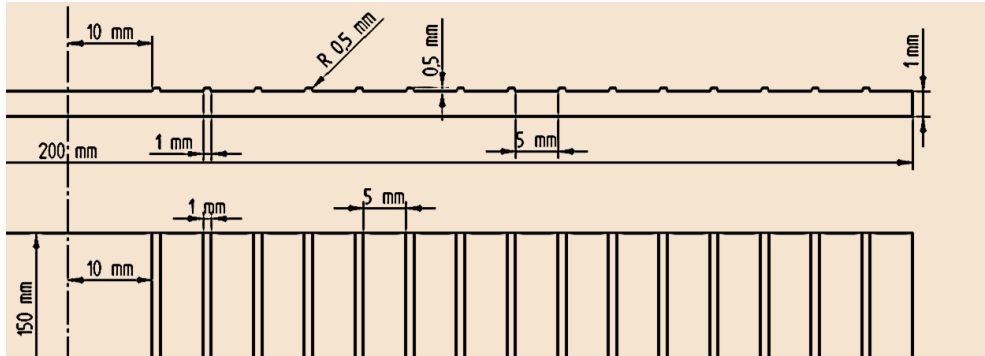
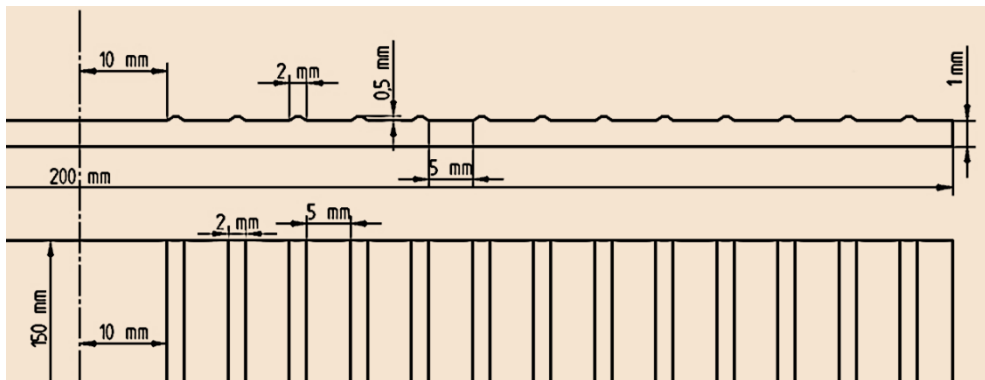


Figure 5.42 Schematic of the test plate

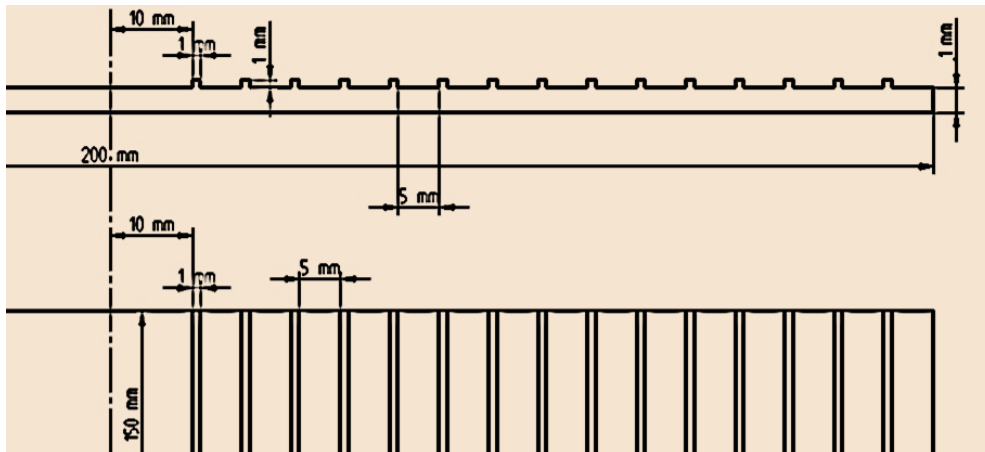
Half side of the plate is machined with VMC (vertical machine centre) to get desired shape of ribbed elements. Three basic geometrical shapes circular, rectangular and triangular are investigated. Effect of width is also considered. In total, six different shapes of ribbed elements are considered in the present investigation as shown in Figure 5.43 and Figure 5.44. The distance between the first rib and stagnation point is kept constant for all the considered geometries. Further 5mm gap is maintained between consecutive ribs. Flame is extinguished as soon as target material temperature reaches around 250 °C to avoid changes in the shape of the plate as it has high coefficient of thermal expansion. Effect of change in conductivity and radiation loss is neglected in the present analysis. Mixture equivalence ratio is maintained at 1.



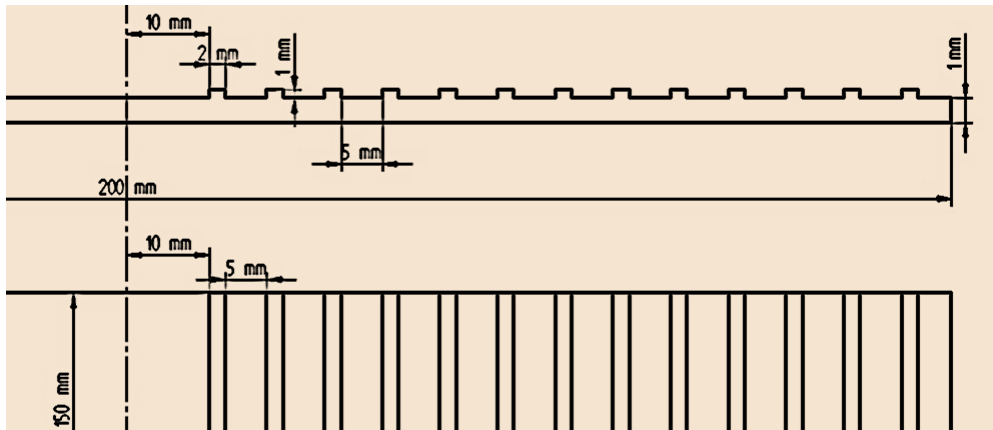
a) Circular ribbed plate



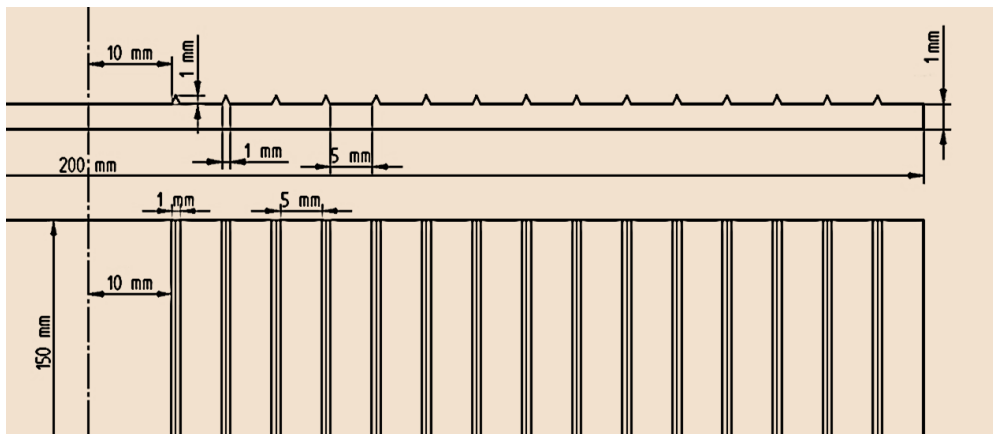
b) Wide circular ribbed plate



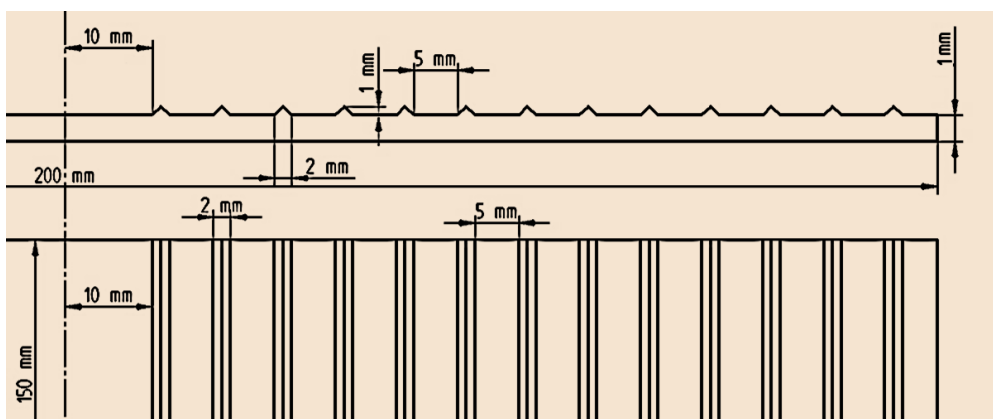
c) Square ribbed plate



d) Rectangular ribbed plate



e) Triangular ribbed plate



f) Wide triangular ribbed plate

Figure 5.43 Schematic of ribbed plates considered in present investigation



a) Circular ribbed plate



b) Wide circular ribbed plate



c) Square ribbed plate



d) Rectangular ribbed plate



e) Triangular ribbed plate



f) Wide triangular ribbed plate

Figure 5.44 Photographs of actual (manufactured) ribbed plates

Initially experiments were conducted on 3 mm thick plates but effect of ribbed elements on the heat transfer is not observed in the transient temperatures measured on the back side. Transient temperature distribution along ribbed side was observed similar to that of smooth side. This is attributed to high thermal conductivity of the material. Thus, thickness of plates is reduced further around 1 mm by using CNC lathe. Assumed mechanical and thermal properties of plate (SS 316) material is given in Table 5.2.

Table 5.2 Mechanical and thermal properties of SS 316 material

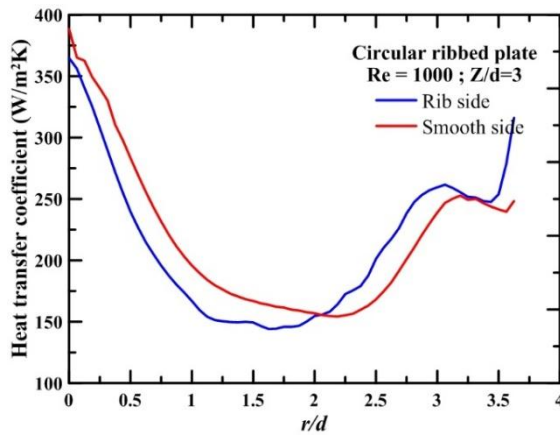
Sr. no.	Properties	Values
1.	Density	8000 Kg/m ³
2.	Specific heat	500 J/kg.K
3.	Thermal Conductivity	16 W/mk
4.	Thermal expansion coefficient	17×10^{-6} /K

5.5.2 Data Smoothing

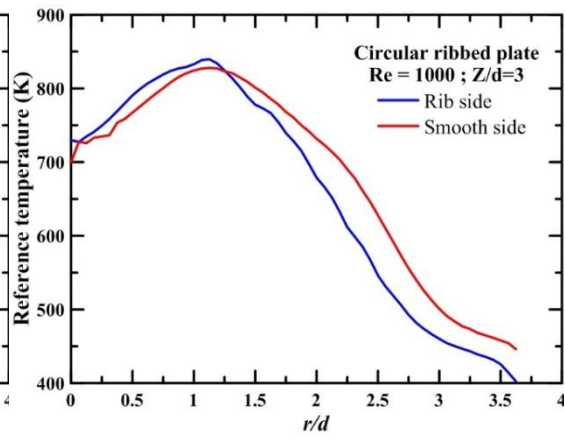
Experimental data is bound to have noise and there are plenty methods to smoothen out it in literature. In present study, peaks and valley in back side temperature data is expected because of presence of ribs. Consequently care has been taken while smoothening the data. Here adjacent averaging with two point of window is used to smoothen the data. This smoothening technique helps in preserving overall nature (peaks and valley) of the data removing only noise which was appearing as localized spikes in temperature data

5.5.3 Heat transfer coefficient and Reference temperature at Re 1000 and Z/d=3

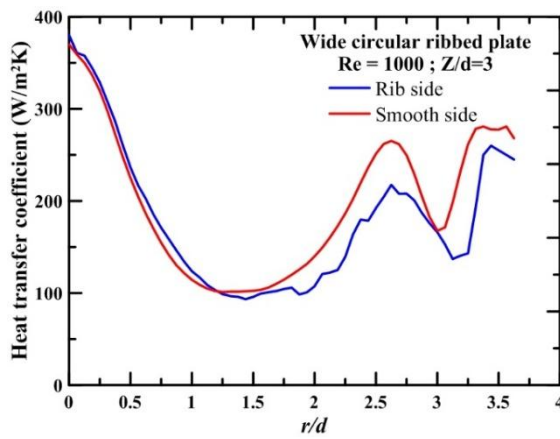
Figure 5.45 shows the heat transfer coefficients and reference temperature values for all considered ribbed plates at Re 1000 and Z/d=3. At this Reynolds number and Z/d, flame is close to plate as a result local heat transfer coefficient is maximum at the stagnation point and decreasing thereafter along the radial direction. For all the cases, initial transient temperature data from 0.2 sec to around 20 sec is considered to estimate heat transfer coefficient and reference temperature.



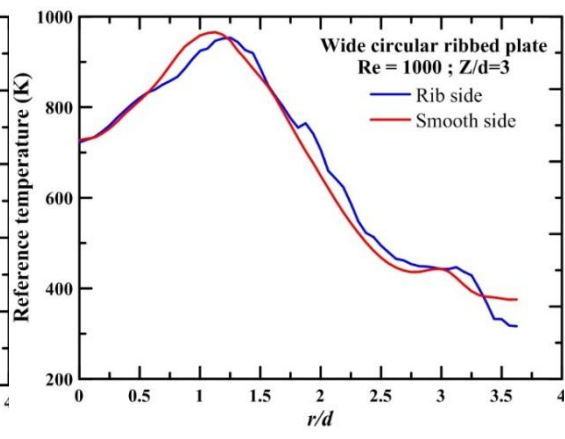
(a)



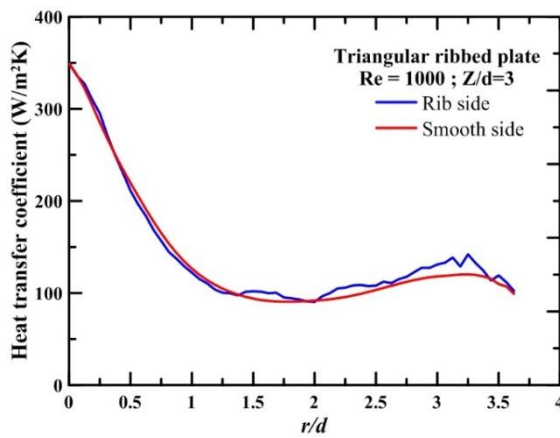
(b)



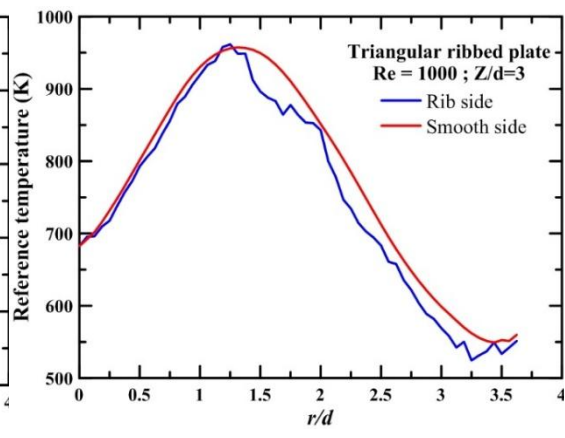
(c)



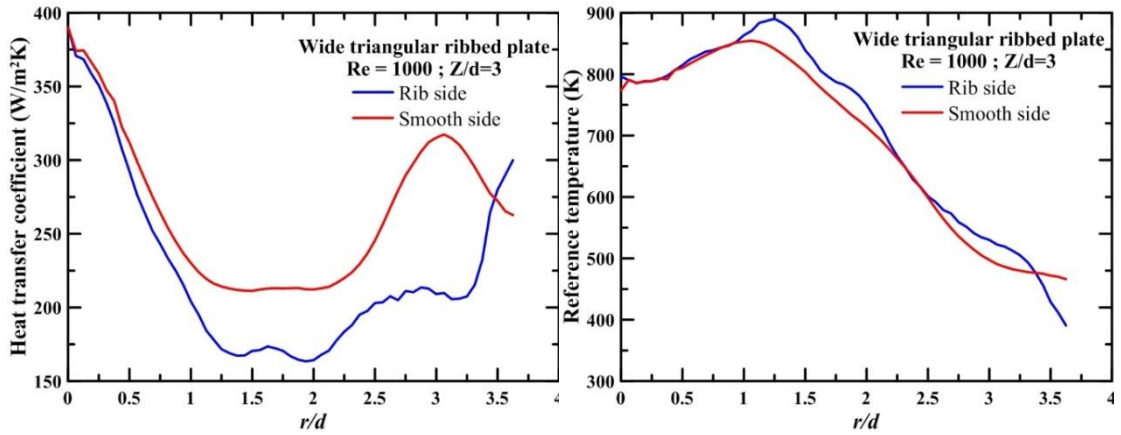
(d)



(e)

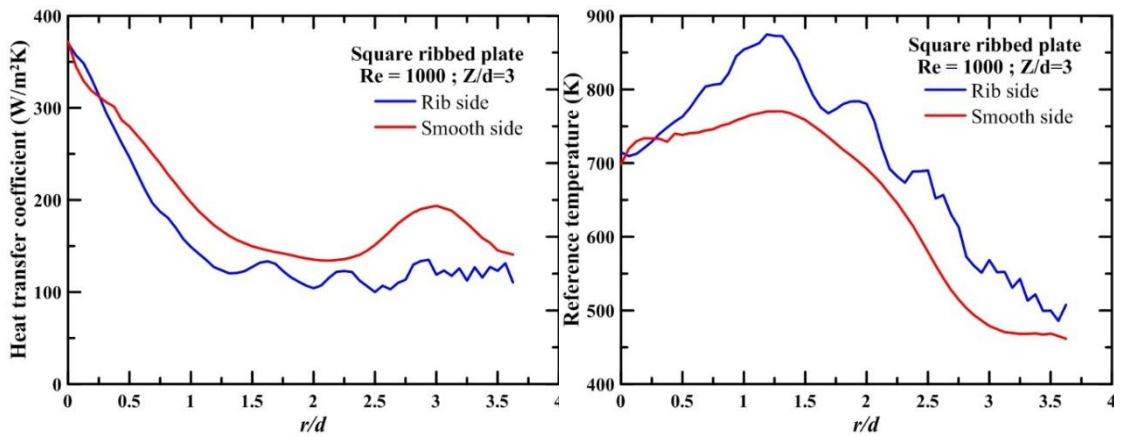


(f)



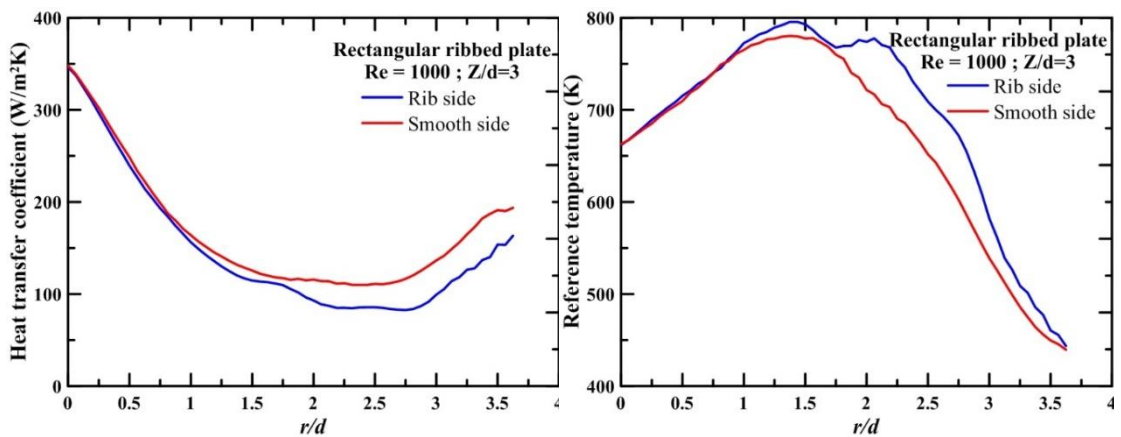
(g)

(h)



(i)

(j)



(k)

(l)

Figure 5.45 Heat transfer coefficient and Reference temperature for various shaped ribbed surfaces at Re 1000 and Z/d=3

Figure 5.46 shows heat flux data at the front side for $Re = 1000$ and $Z/d=3$. It can be observed that upto $r/d = 3$ heat flux values are distinct and from then on heat flux values are almost same for all-time instant. Therefore all the results are plotted upto $r/d=3.6$.

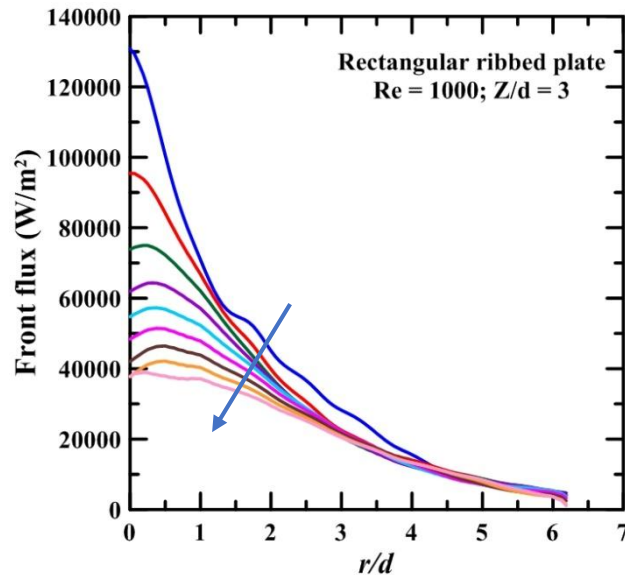
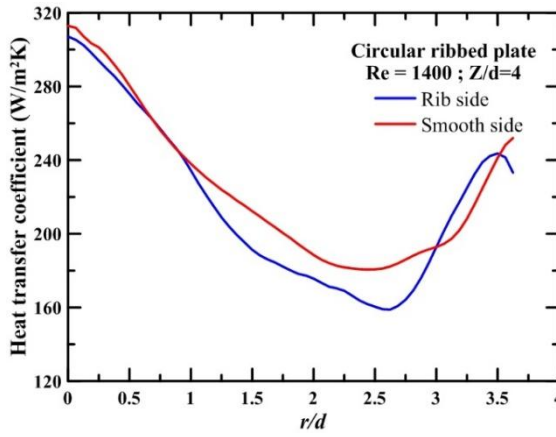


Figure 5.46 Heat flux at the impingement side for rectangular ribbed plate at $Re = 1000$ and $Z/d=3$. The direction of arrow indicates the increasing value of time from 0.2 to 22.6 sec in steps of 2.8 sec.

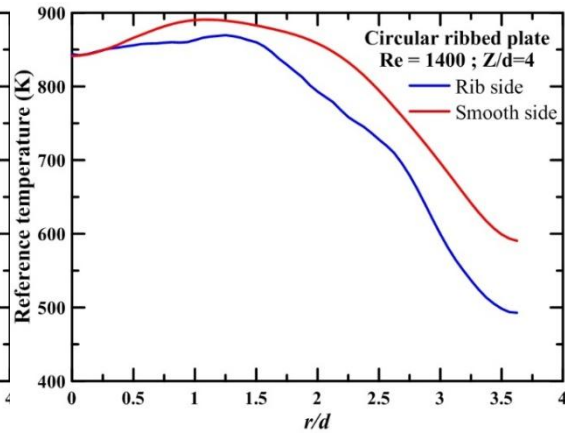
Further it is observed that the heat transfer coefficient values on ribbed side are lower for all plates than the smooth side whereas reference temperature values are comparatively higher on ribbed side than smooth side. Attached ribs are acting like small protrusions over the surface. Hence they are early in contact with the flame which results in increase in reference temperature on ribbed side than smooth side. At the same time, these ribs are obstruction to the flame spreading in wall jet region thus decrease in heat transfer coefficients is observed on the ribbed side.

5.5.4 Heat transfer coefficient and Reference temperature at $Re = 1400$ and $Z/d=4$

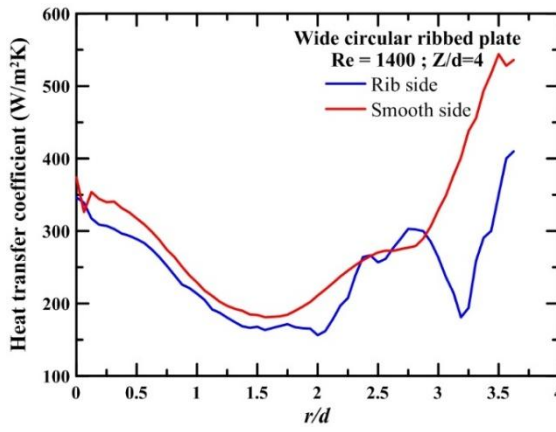
At higher Reynolds number 1400 and $Z/d=4$, heat transfer coefficient and reference temperatures profiles are plotted for all the plates in Figure 5.47. At higher Reynolds number, there is more entrainment of surrounding air so widening of the flame is expected. It can be observed in Figure 5.47 that heat transfer coefficient values in radial direction are comparatively more than the values at $Re = 1000, Z/d=3$.



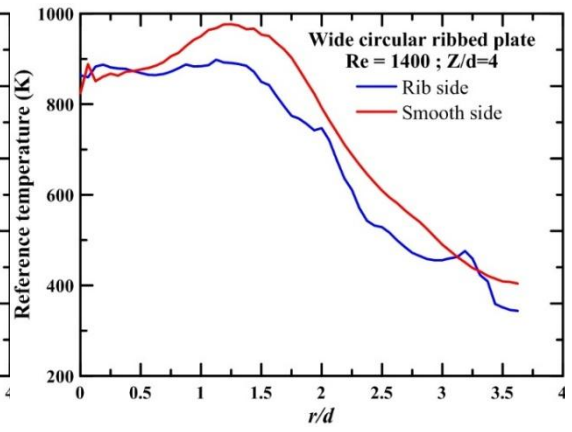
(a)



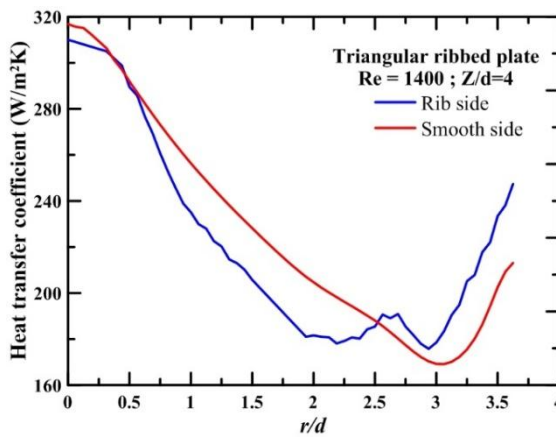
(b)



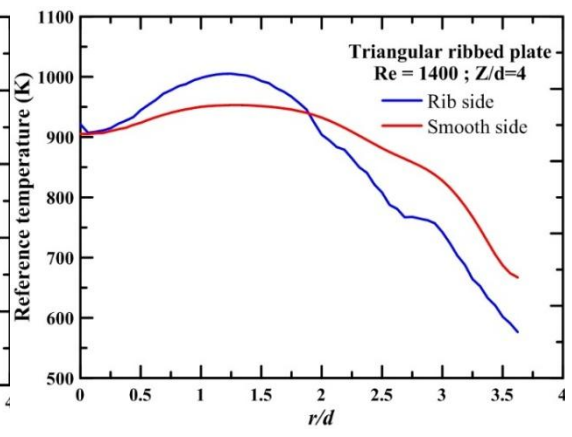
(c)



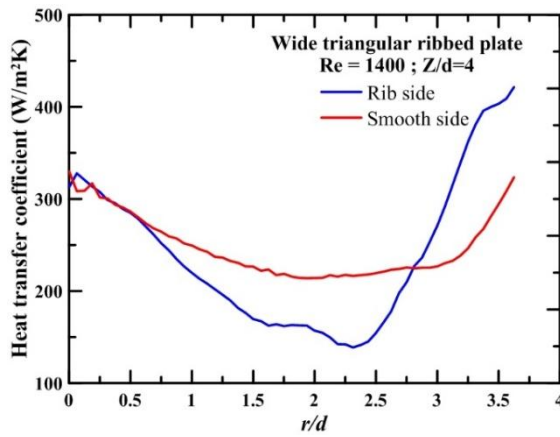
(d)



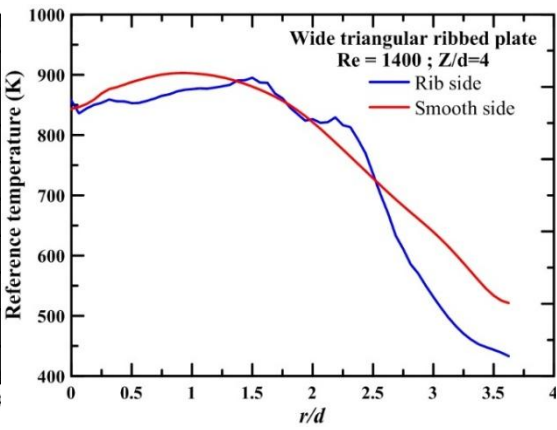
(e)



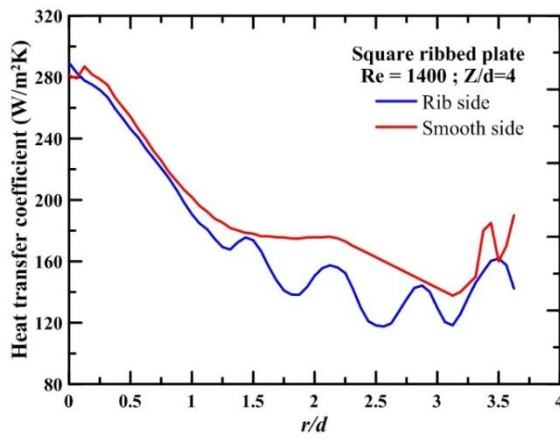
(f)



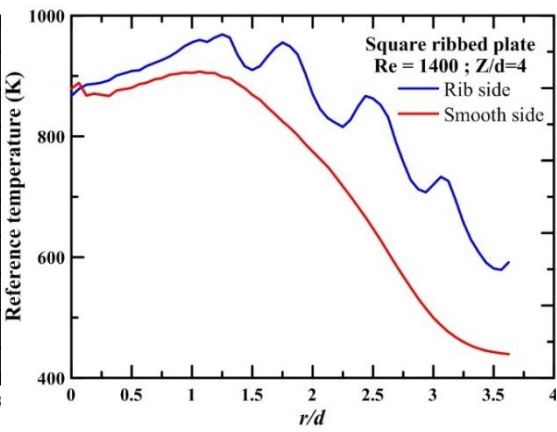
(g)



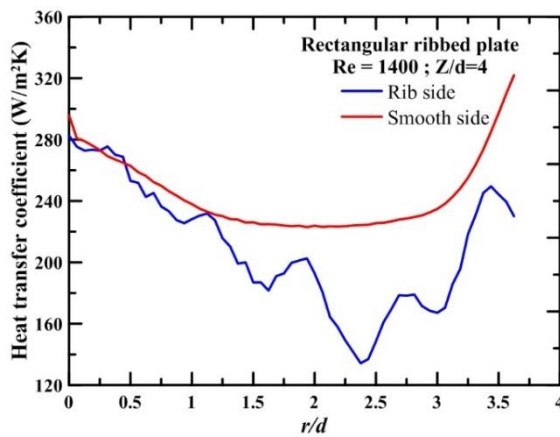
(h)



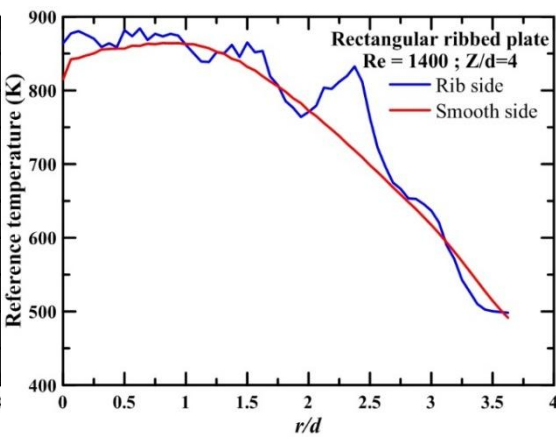
(i)



(j)



(k)



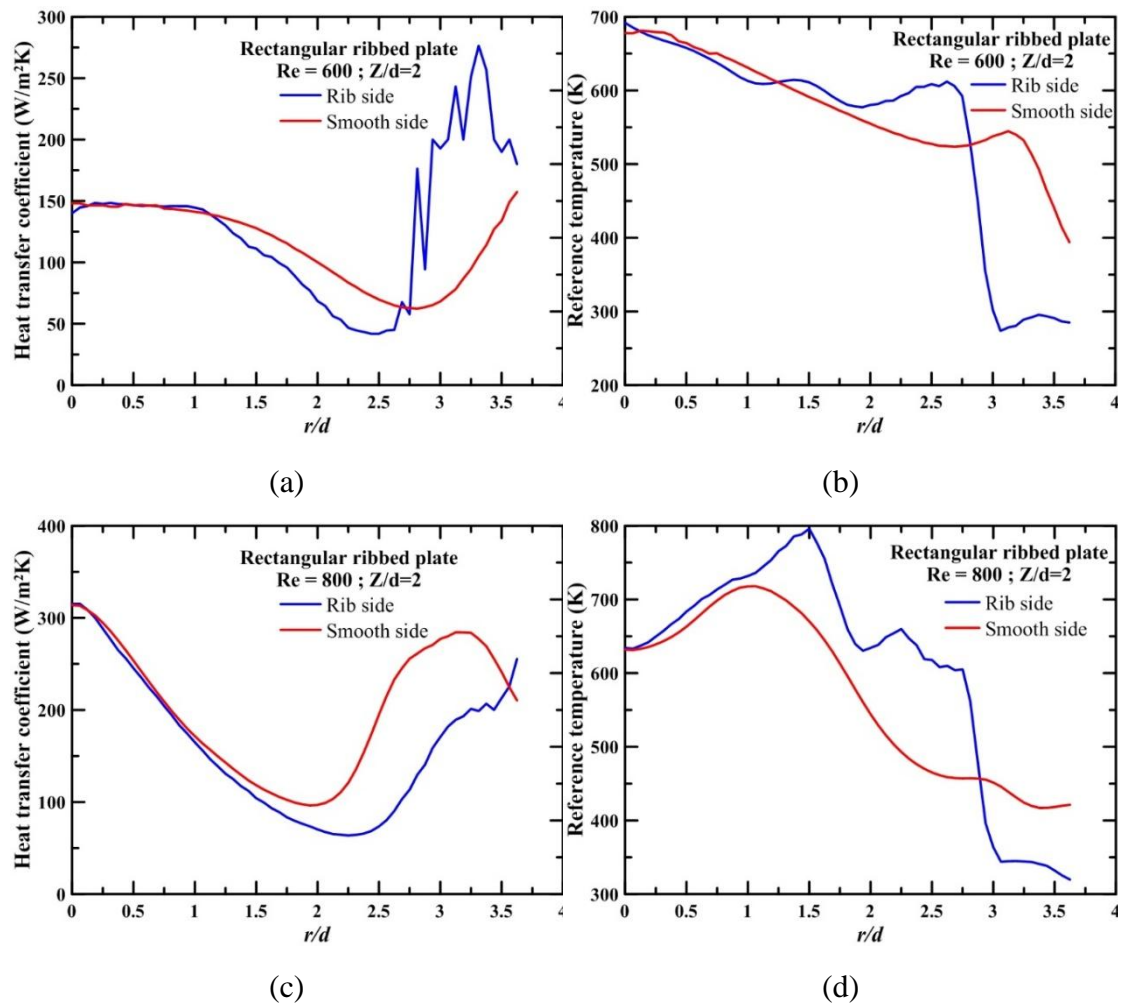
(l)

Figure 5.47 Heat transfer coefficient and Reference temperature for various shaped ribbed surfaces at $Re = 1400$ and $Z/d=4$

From Figure 5.45 and Fig. 5.47, it is observed that local spikes are clearly visible only for square and rectangular ribbed plates. These local spikes are corresponds to extra surface area added to the surface due to ribs. Comparatively square and rectangular ribs are having more surface area than circular and triangular ribs.

5.5.5 Heat transfer coefficient and Reference temperature for Rectangular ribbed plate at various Reynolds number and Z/d

Figure 5.48 to Figure 5.50 shows heat transfer characteristics of rectangular ribbed plates at various Reynolds number and Z/d . As Reynolds number increases, heat transfer coefficient at and around stagnation point found increasing for the cases where flame front is not touching the plate. Almost in all the cases, heat transfer coefficient on ribbed side is at lower side than the smooth side.



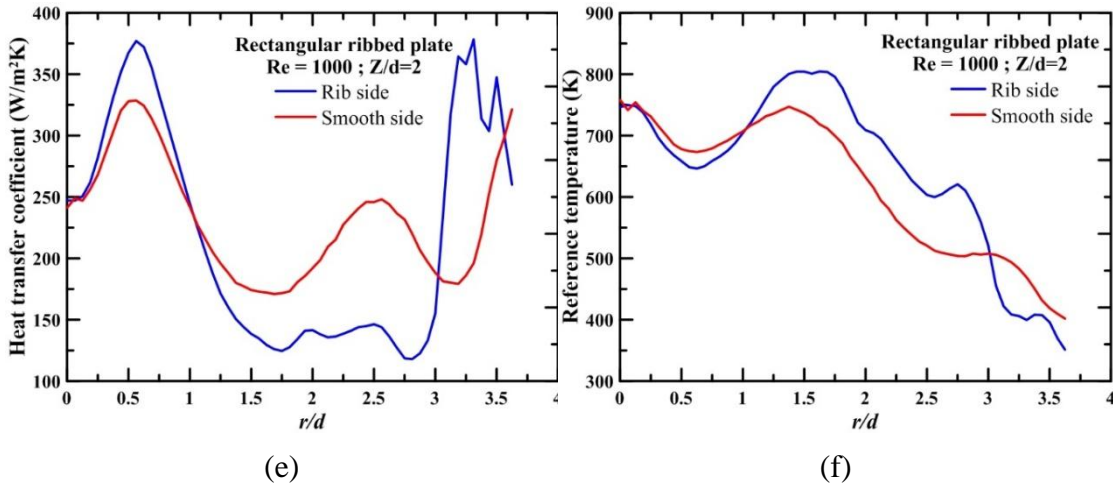
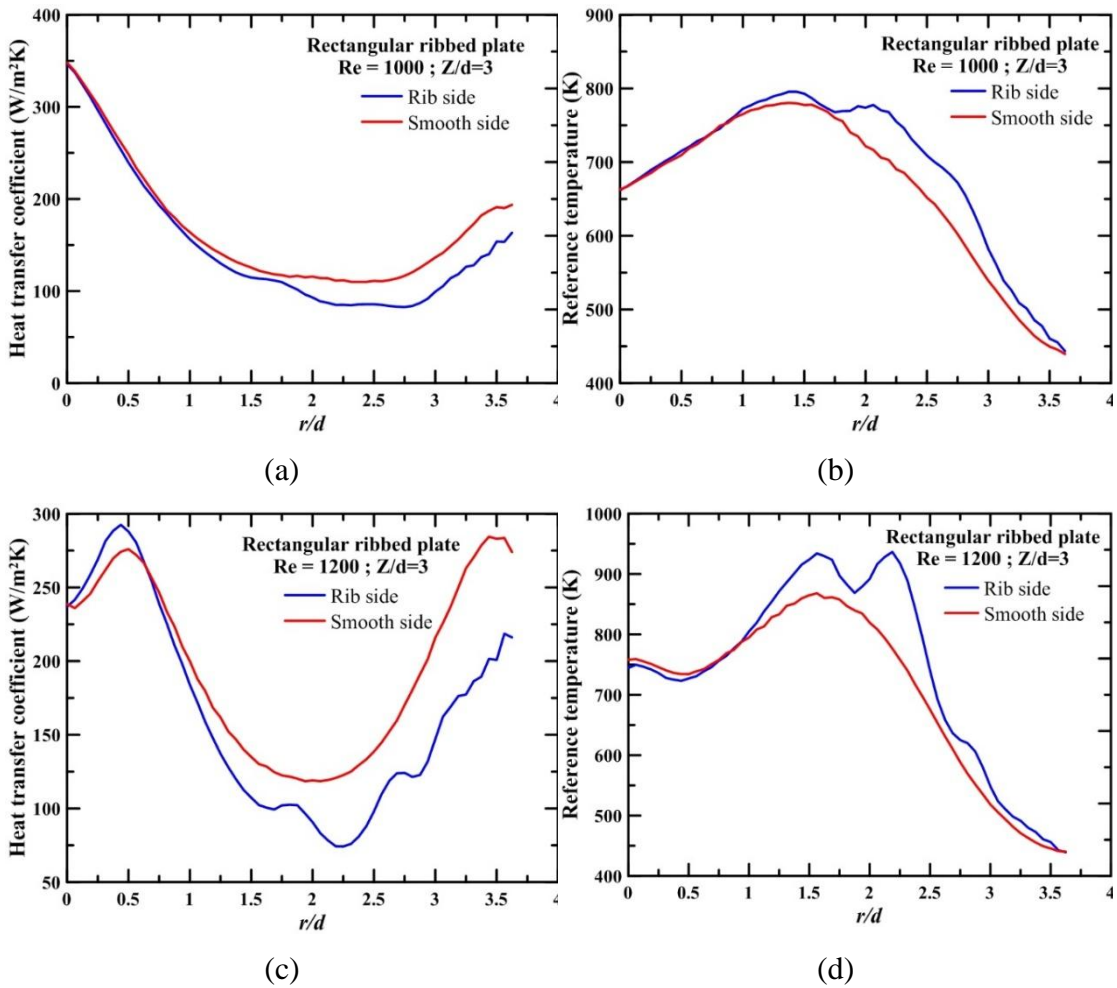


Figure 5.48 Heat transfer coefficient and Reference temperature for Rectangular ribbed plate at different Reynolds number and $Z/d=2$



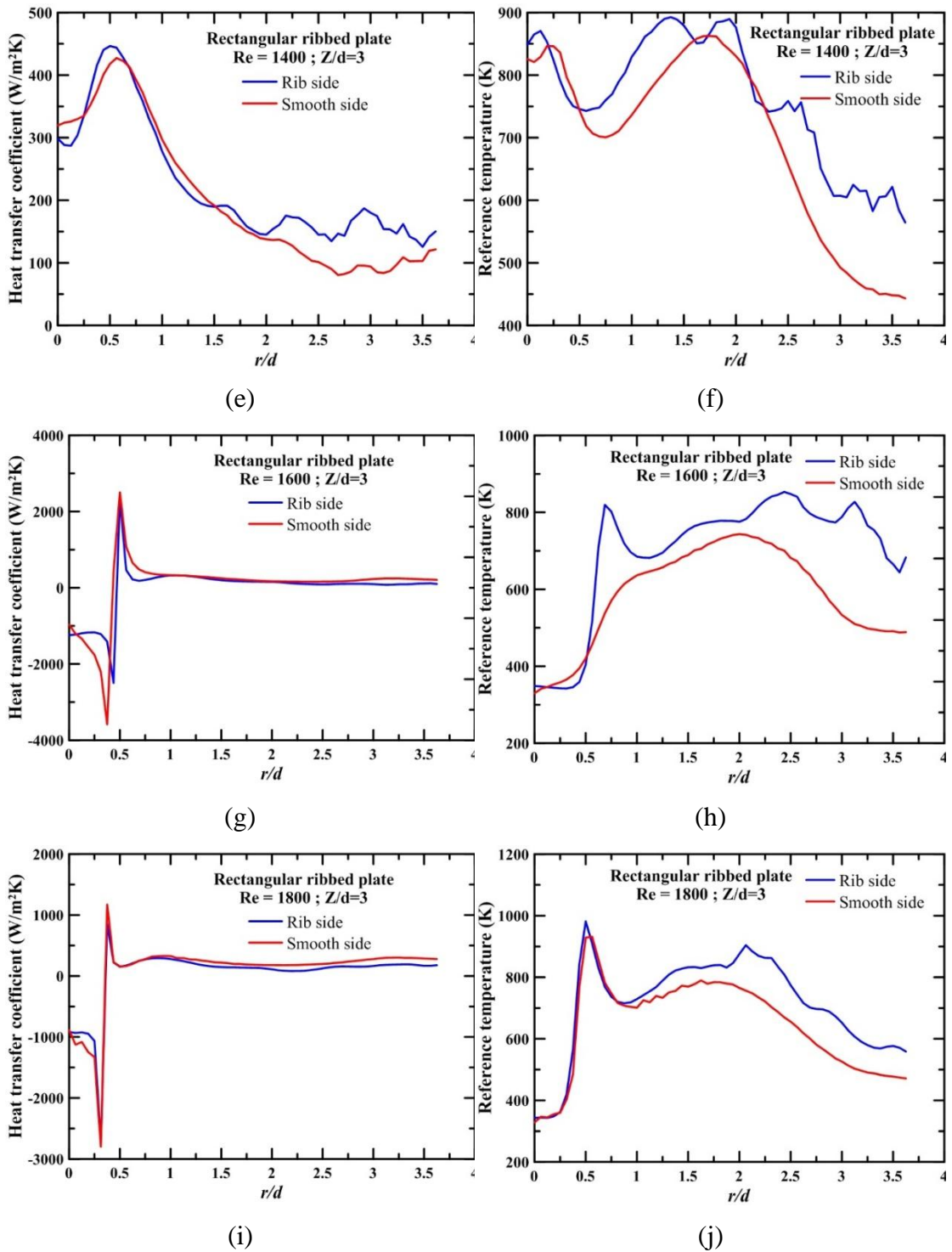
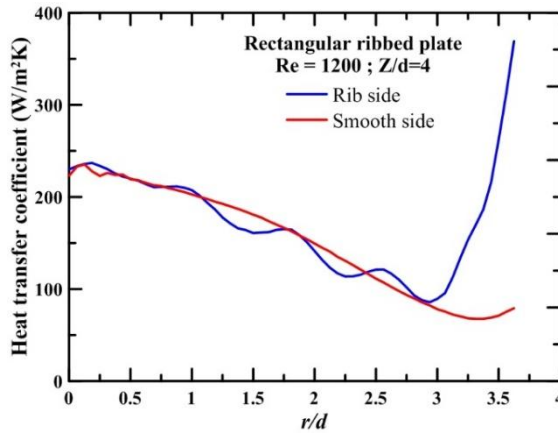
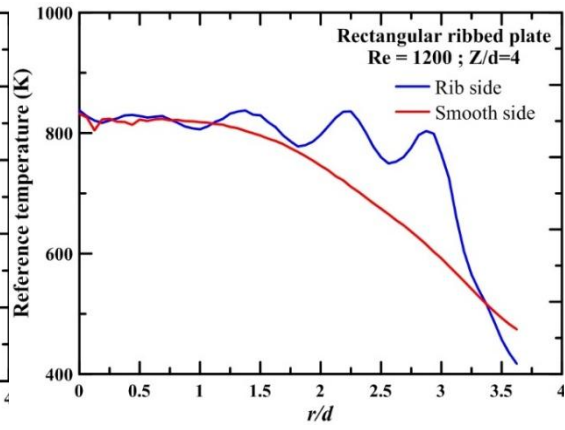


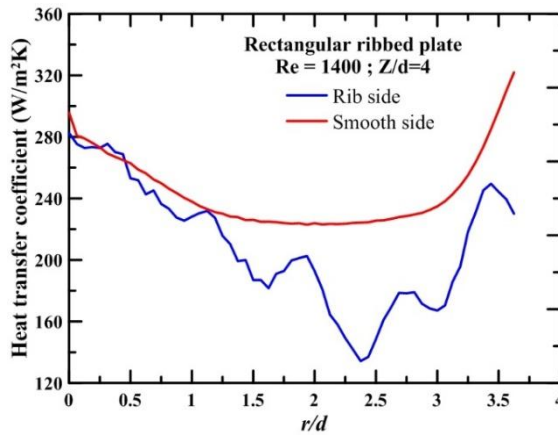
Figure 5.49 Heat transfer coefficient and Reference temperature for Rectangular ribbed plate at different Reynolds number and $Z/d=3$



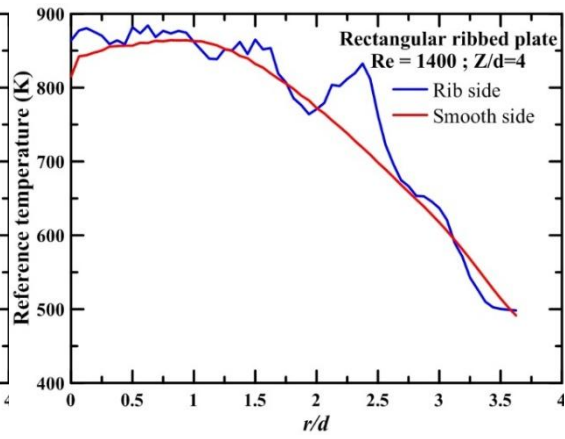
(a)



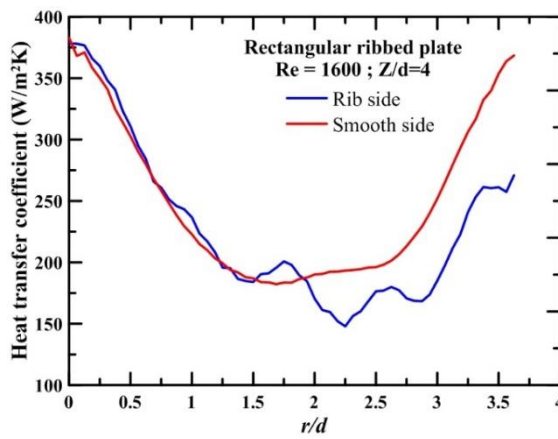
(b)



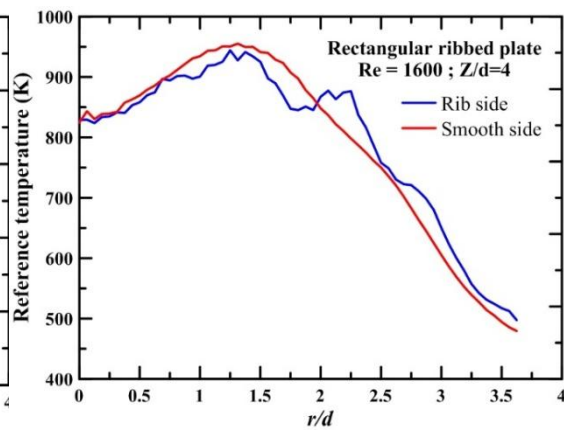
(c)



(d)



(e)



(f)

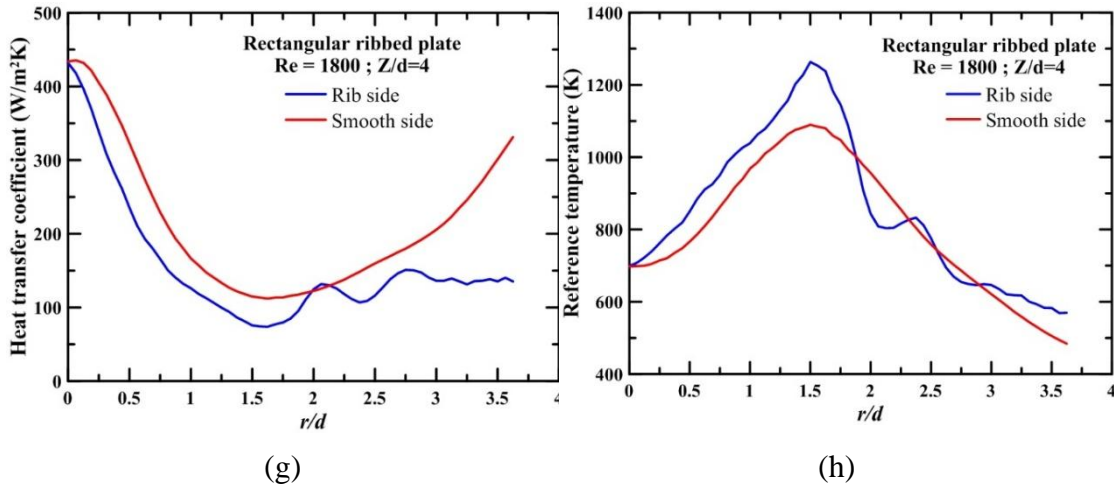


Figure 5.50 Heat transfer coefficient and Reference temperature for Rectangular ribbed plate at different Reynolds number and $Z/d=4$

5.5.6 CFD Simulation results

To understand the flow physics on and around rib elements, numerical simulations are carried out at Re 1400 and $Z/d=4$ for which experimental results are presented above.

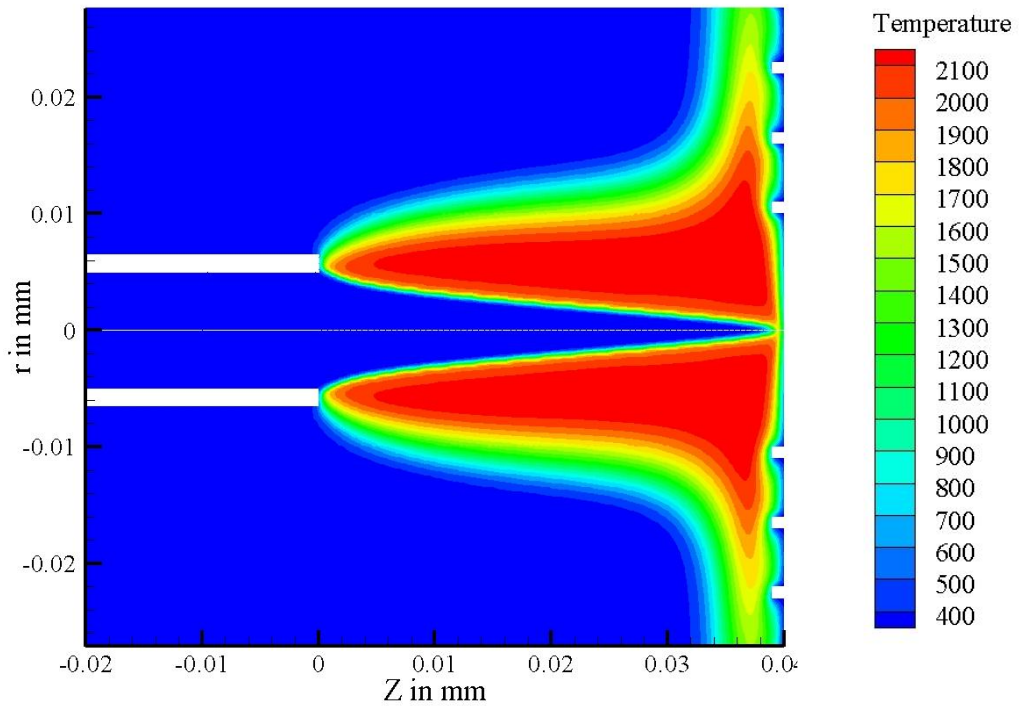


Figure 5.51 Temperature contour for square ribbed plate at Re 1400, $Z/d=4$ and $\phi=1$

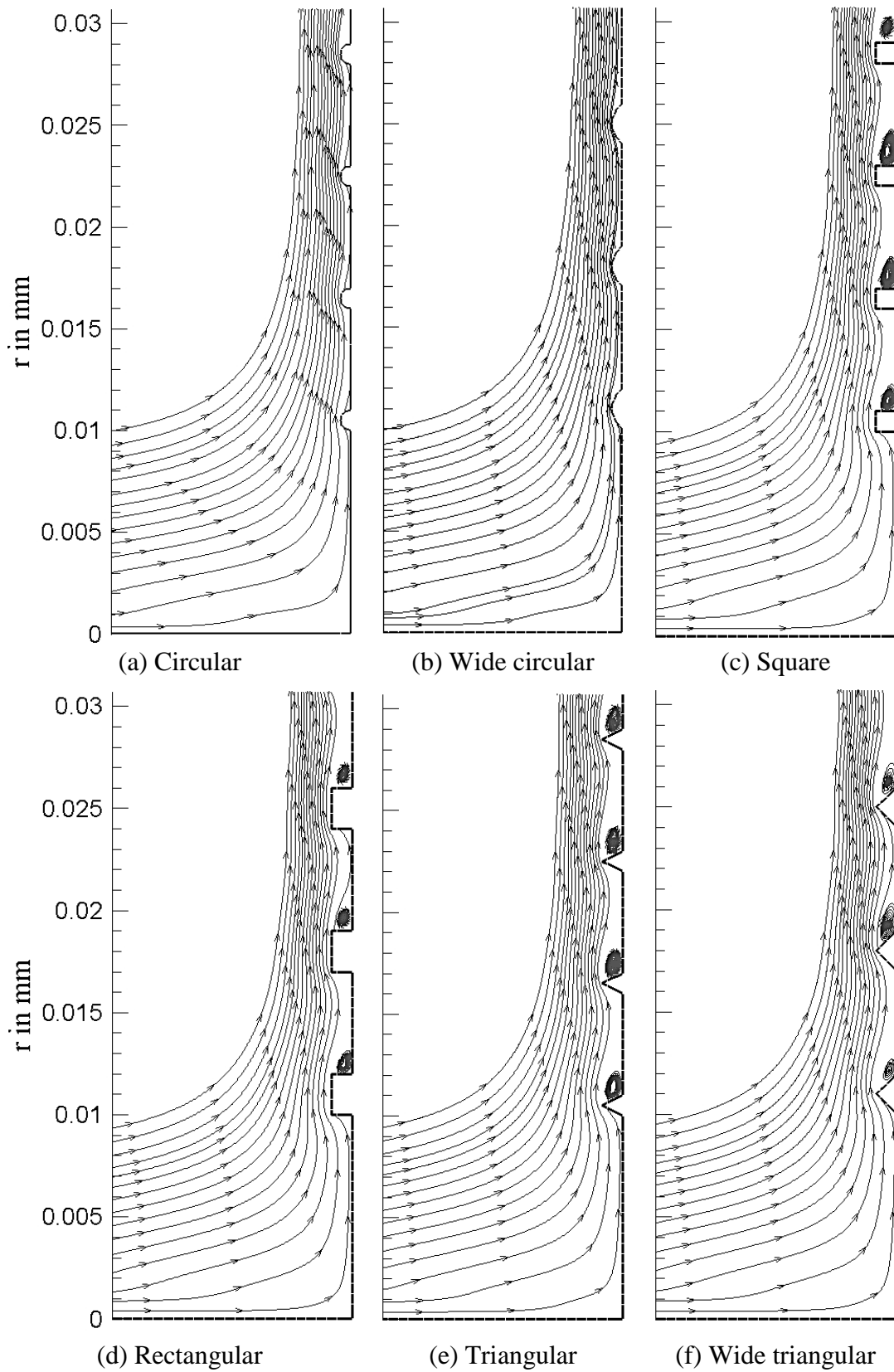


Figure 5.52 Streamlines in the stagnation and wall jet region at $Re = 1400$ and $Z/d = 4$

Figure 5.51 is a representative image for all the simulations carried out. It shows the temperature contour for square ribbed plate. As high temperature zone is near the stagnation region, higher heat transfer also takes place in same region. It was anticipated that these rib elements indeed increase heat transfer to the plate. However heat transfer rate in the presence of ribs is decreased and to explain the possible reasons streamlines are plotted for all the plates as shown in Figure 5.52.

It can be seen that in case of circular ribbed plate (Figure 5.52a), flow over the rib is separated and reattached after a short distance in the downstream of the rib. Comparatively blockage in upstream corner is found less. In case of wide circular ribbed plate, reattachment length after flow separation is found comparatively more than circular plate due to large width of the rib. In both the cases, ribs are acting like guiding elements than the obstruction elements. The reason can be attributed to the lower height of the circular ribs in compare with other ribs. In remaining all cases, flow is getting obstructed due to presence of the rib. As obstruction is more, high momentum flow is getting diverted over the rib. This, flow is getting separated in downstream of the rib. In these cases, reattachment length is also comparatively larger. In all these cases, recirculation zones in the downstream of the rib are observed. Due to these flow separation and recirculation bubbles, penetration of hot fluid is not possible which in turns reduces the heat transfer rate to the plate. Similar observations are found in case of air jet impingement studies (Gau and Lee 1992, Gau and Lee 2002, Labbé 2013).

To support the above discussion, radial velocity contours are shown in Figure 5.53. It can be clearly seen that radial velocity magnitude is minimum in the downstream of the ribs in case of square, rectangle, triangle and wide triangular ribbed plates. At the same time, this lower velocity magnitude area is wider and thick which indicates that penetration of the hot fluid is minimal. As momentum decreases along the wall jet region, thickness of wall jet boundary layer increases. Whereas in case of circular and wide circular ribbed plates, absence of vortex, leads to better mixing in downstream of the rib. Thus, effect of circular and wide circular rib elements on the heat transfer rate to the plate is comparatively less.

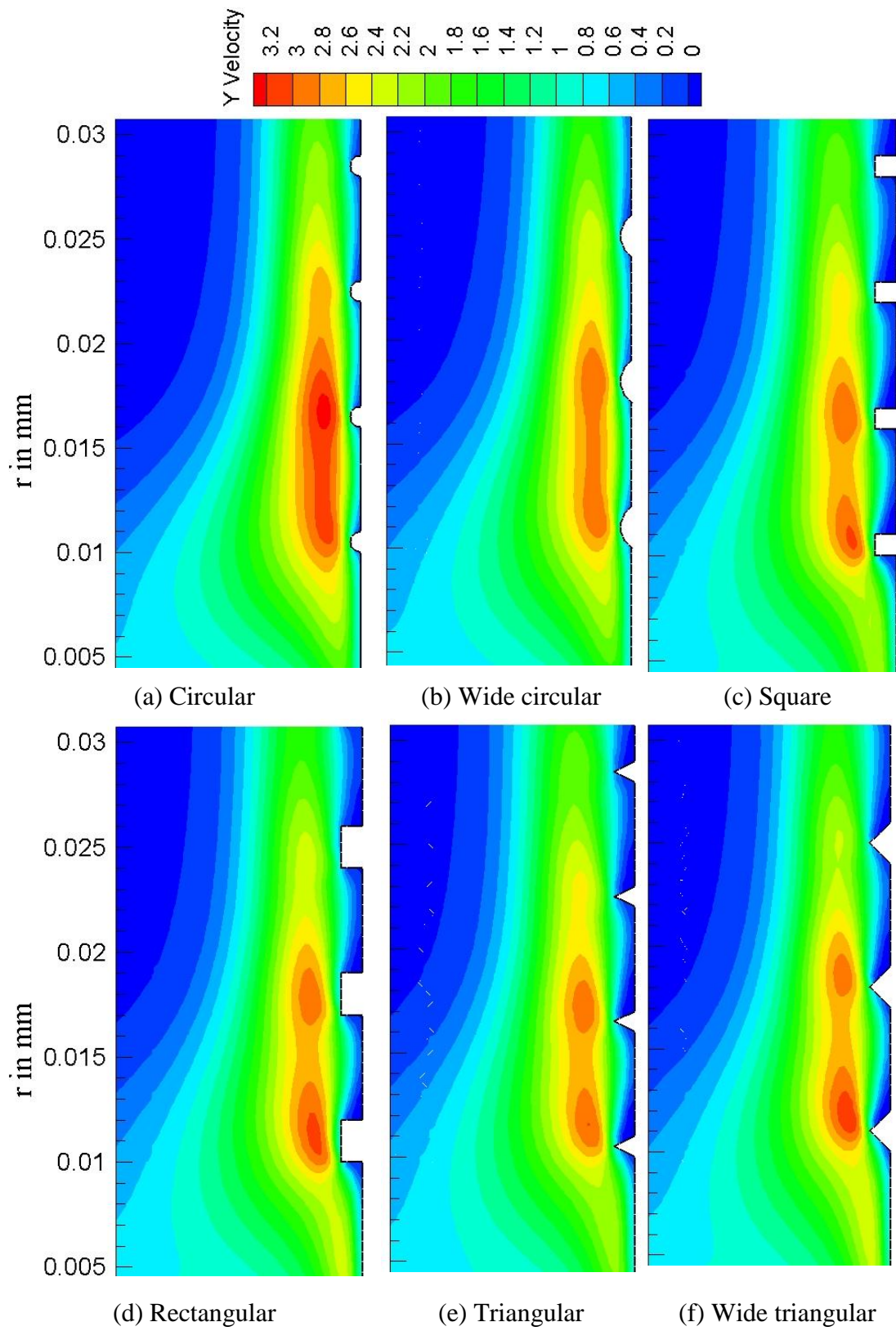


Figure 5.54 Radial Velocity contours for ribbed plates at Re 1400 and Z/d=4

Chapter 6

6 CONCLUSIONS AND SCOPE FOR FUTURE WORK

6.1 CONCLUSIONS

This thesis is directed towards estimation of flame jet impingement heat transfer. More specifically, simultaneous estimation of heat transfer coefficient and reference temperature at the impingement side have been dealt with utmost importance. The simultaneous estimation is carried out with the help of transient temperature measurements at the non-impingement side.

A comparison of heat transfer distribution of impinging flame jet with impinging air jet is carried out from experimental data reported in the literature. A CFD simulation is carried out to give the physical interpretation. The jet velocity increases after burning at the flame front surface and this results in higher heat transfer distribution for the flame jet as compared to air jet especially for $Z/d = 2$. At $Z/d = 4$ and 6 there is a reasonably good match between air jet and flame jet Nusselt numbers at the stagnation region for low Re . Away from the stagnation region, the flame jet Nusselt number is always higher than that of air jet for all Re . For the flame jet, the higher value of experimentally reported Nusselt number away from the stagnation region is due to the much wider spreading of the flame jet in the radial direction as compared to the air jet. From scale analysis, it is found that the inertia force is the most dominant force that has sole influence on the impingement heat transfer distribution at high Re .

Application of Duhamel theorem is found to be given nonlinear fit of wall heat flux with wall temperature for the present data analyzed and therefore the one-dimensional heat diffusion approximation is invalid. The 3-D IHC solution gives a linear fit of wall heat flux with wall temperature and thereby confirming the three-dimensional nature of heat diffusion. The effect of variable thermal conductivity and radiation loss is studied. The assumption of constant thermal conductivity results in under estimation of reference temperature by up to 10% while heat transfer coefficient is over estimated by up to 10%. The deviations of reference temperature and the heat transfer coefficient

due to radiation loss is corrected by applying a novel method which is in good agreement with numerically simulated data. The reference temperature is underestimated by up to 50% and the heat transfer coefficient is overestimated by up to 50% when thermal conductivity dependence on temperature is neglected along with radiation loss.

The present study covers the applications of the hot jet, cold jet and multiple jets with distinct Reynolds numbers and the nozzle-to-plate spacing and results confirm the validity of the technique. Effect of plate thickness on the accuracy of the present technique is studied and it reveals that accuracy deteriorates as thickness increases. Up to 5 mm thick plates can be used in impinging jet applications without compromising much on accuracy.

The experimental results showed no improvement in heat transfer distribution in case of laminar flame jet impingement on ribbed surfaces. The magnitude of heat transfer coefficient is lowered while reference temperature magnitude is raised along the ribbed side than smooth side. Attached ribs are acting like small protrusions over the surface resulting in reducing the momentum of the wall jet. Thus rate of reduction of heat transfer coefficients along the ribbed wall is more. The presence of the recirculation bubbles and flow separation phenomenon observed in case of rectangular and triangular geometrical ribbed plates. This prevents the penetration of hot fluid in the downstream of the ribs which reduces heat transfer rate to the plate.

6.2 KEY CONTRIBUTIONS OF THE PRESENT WORK

Following are the key contribution of the present work.

- Scale analysis of impinging air and flame jets is carried out to explain the effect of various forces and their influence on the heat transfer distribution.
- IHCP technique which can estimate heat transfer coefficient and reference temperature simultaneously from transient measurements is presented.
- The novel technique is proposed for radiation correction based on correcting the experimentally obtained slope of wall heat flux with front surface wall temperature.

- Application of presented inverse technique can be extended to characterize any configuration of jet impingement irrespective of geometry of nozzle (Circular/Rectangular), orientation of nozzle (Orthogonal/inclined), temperature of jet (flame/hot/cold/), Reynolds numbers (Laminar/Turbulent) and the nozzle-to-plate spacing (any Z/d).
- Effect of ribbed elements on the flame jet impingement heat transfer is presented.
- Present technique significantly reduces the experimental cost and time since it works on transient data of just a few seconds.

6.3 SCOPE FOR FUTURE WORK

- (i) The application of the present technique can be extended to problems like turbine blade cooling, thermal protection to launch pad, thermal management of electronic equipment etc.
- (ii) Three dimensional inverse heat conduction problem with convection boundary condition can be explored to get heat transfer coefficient and reference temperature directly.
- (iii) Effect of pulsating flame jet impingement on heat transfer distribution with variation in equivalence ratio and mixture mass can be studied.

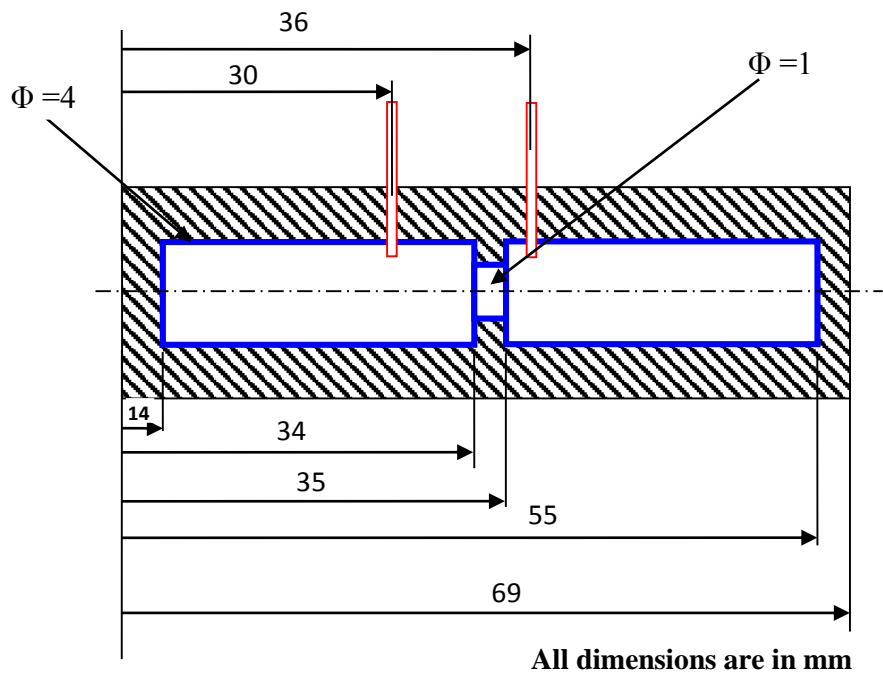


Figure A.2 Design of MOH (Methane Orificemeter for higher range)

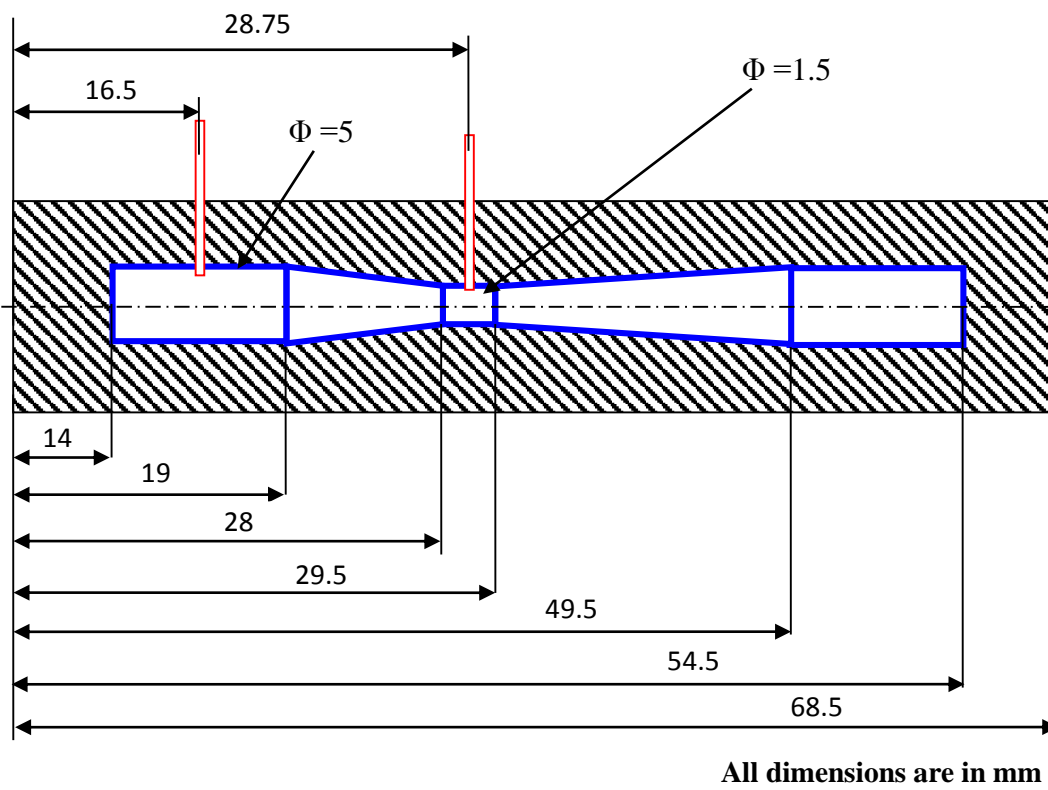


Figure A.3 Design of AVL (Air Venturimeter for lower range)

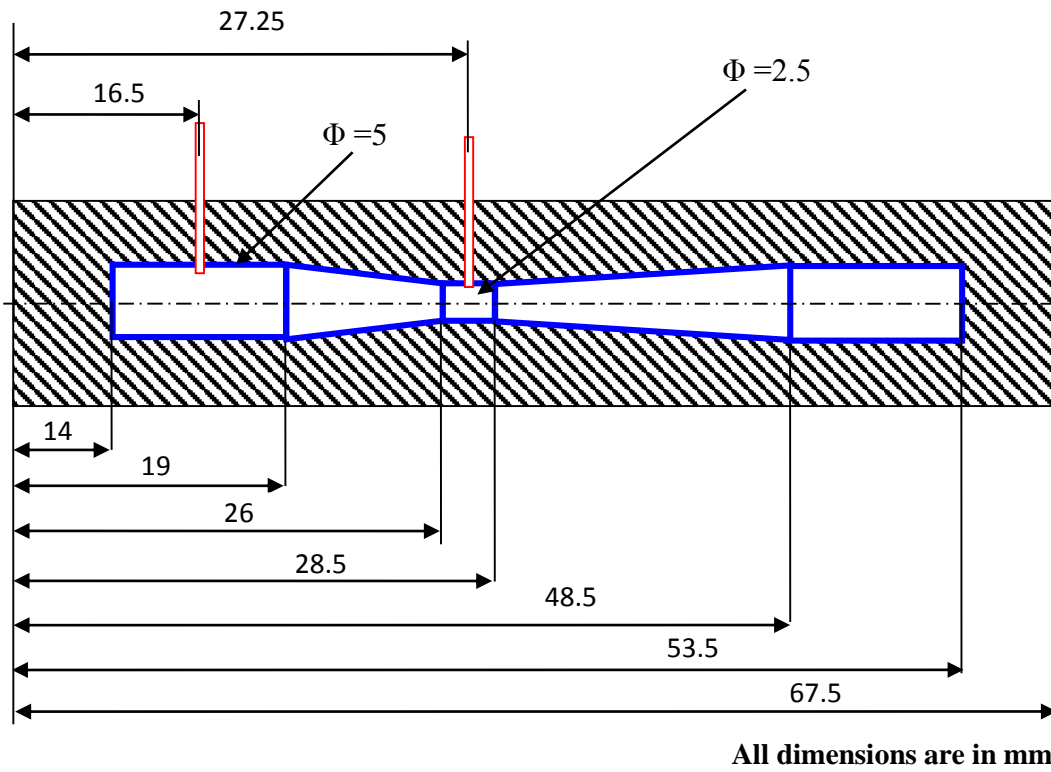


Figure A.4 Design of AVH (Air Venturimeter for high range)

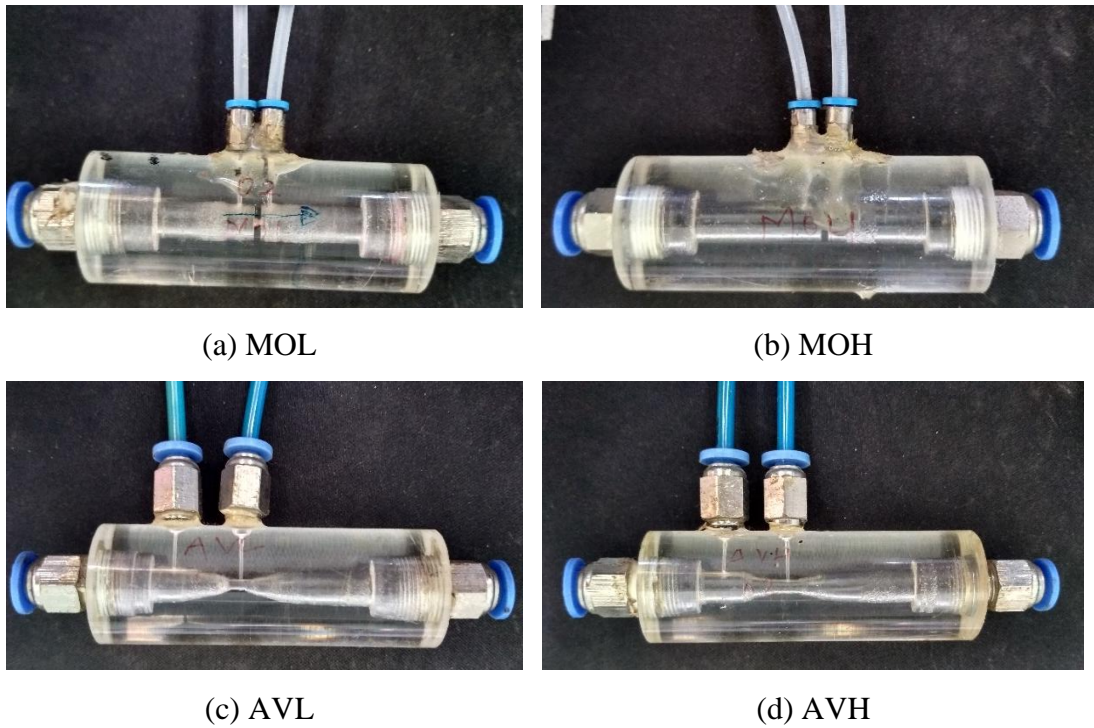


Figure A.5 Fabricated flowmeters

A.2 Calibration of Orificemeters and Venturimeters

Calibration of flowmeters are carried out with the help of DryCal Defender calibrators directly. Data related to calibration is tabulated in Table A.1 to Table A.4 for MOL, MOH, AVL and AVH respectively.

Table A.1 Calibration table for MOL

Trial	Manometer reading	MOL Theoretical mass flow rate	Actual mass flow rate by Calibrator	Coefficient of discharge
	water head (mm)	\dot{m}_{th}	\dot{m}_{act}	C_d
1.	6	9.2225E-06	8.0546E-06	0.87
2.	25	1.8825E-05	1.6703E-05	0.89
3.	48	2.6085E-05	2.2648E-05	0.87
4.	75	3.2607E-05	2.8181E-05	0.86
5.	292	6.4338E-05	5.5692E-05	0.87
6.	430	7.8074E-05	6.7920E-05	0.87
7.	557	8.8859E-05	7.8464E-05	0.88
8.	649	9.5917E-05	8.4857E-05	0.88
9.	755	1.0345E-04	9.2040E-05	0.89
10.	883	1.1188E-04	9.9352E-05	0.89
11.	1009	1.1960E-04	1.0634E-04	0.89
12.	1136	1.2690E-04	1.1240E-04	0.89

Table A.2 Calibration table for MOH

Trial	Manometer reading	MOH Theoretical mass flow rate	Actual mass flow rate by Calibrator	Coefficient of discharge
	water head (mm)	\dot{m}_{th}	\dot{m}_{act}	C_d
1.	5	1.6082E-05	1.4123E-05	0.88
2.	12	2.4915E-05	2.2470E-05	0.90

3.	20	3.2165E-05	2.8541E-05	0.89
4.	89	6.7852E-05	6.0959E-05	0.90
5.	158	9.0406E-05	8.0490E-05	0.89
6.	215	1.0546E-04	9.4241E-05	0.89
7.	273	1.1884E-04	1.0535E-04	0.89
8.	366	1.3760E-04	1.2124E-04	0.88
9.	427	1.4862E-04	1.3097E-04	0.88
10.	530	1.6558E-04	1.4572E-04	0.88
11.	615	1.7836E-04	1.5681E-04	0.88

Table A.3 Calibration table for AVL

Trial	Manometer reading	AVL Theoretical mass flow rate	Actual mass flow rate by Calibrator	Coefficient of discharge
	water head (mm)	\dot{m}_{th}	\dot{m}_{act}	C_d
1.	11	5.4155E-05	3.7835E-05	0.70
2.	28	8.6402E-05	6.0923E-05	0.71
3.	54	1.1999E-04	8.3661E-05	0.70
4.	154	2.0263E-04	1.4128E-04	0.70
5.	257	2.6177E-04	1.8651E-04	0.71
6.	467	3.5286E-04	2.5365E-04	0.72
7.	580	3.9324E-04	2.8315E-04	0.72
8.	765	4.5162E-04	3.2474E-04	0.72
9.	973	5.0933E-04	3.6865E-04	0.72
10.	1057	5.3086E-04	3.8659E-04	0.73
11.	1350	5.9995E-04	4.3352E-04	0.72

Table A.4 Calibration table for AVH

Trial	Manometer reading	AVH Theoretical mass flow rate	Actual mass flow rate by Calibrator	Coefficient of discharge
	water head (mm)	\dot{m}_{th}	\dot{m}_{act}	C_d
1.	17	1.4131E-04	1.2249E-04	0.87
2.	29	1.8456E-04	1.6457E-04	0.89
3.	48	2.3744E-04	2.0856E-04	0.88
4.	63	2.7202E-04	2.3876E-04	0.88
5.	75	2.9680E-04	2.6181E-04	0.88
6.	93	3.3050E-04	2.8959E-04	0.88
7.	117	3.7070E-04	3.2520E-04	0.88
8.	132	3.9375E-04	3.4564E-04	0.88
9.	153	4.2392E-04	3.7393E-04	0.88

A.3 Operating ranges for Orificemeters and Venturimeters

Operating ranges for flowmeters are decided based on deflection that can be measured in the water column of differential manometer. With these flow meters, flow range required for present study between Re 500 to Re 2000 for equivalence ratio 0.7 to 1.4 can be obtained. Higher flow rates in turbulent regime upto Re 10000 are also possible to operate with these flowmeters.

Table A.5 Operating mass flow ranges for flowmeters

Sl no.	Fluid	Device	Mass flow rate (Kg/Sec)	
			Low	High
1	Methane	MOL	2.82014E-06	1.50277E-05
		MOH	1.50277E-05	4.29362E-05
2	Air	AVL	6.51899E-05	0.000137971
		AVH	0.000137971	0.000275942

A.4 Calibration of thermal camera

Thermal infrared (IR) camera A325sc, FLIR make is calibrated using Chromel–Alumel thermocouple (K-type) thermocouple. Plate of Stainless Steel material (Figure A.6a) is heated by the Methane-air flame from bottom side and three thermocouples are attached to other side. Plate is blackened with the high temperature flat black spray paint (Bosney make) from non-impingement side and it is cured in the furnace upto temperature 600°C. The transient temperatures of the plate are measured using a 1.2 mm diameter Chromel–Alumel thermocouples (K-type) placed at three different location using DAQ-USB 6218 (NI make) shown in Figure A.6b. At the same time, transient temperature distribution of the plate is captured with the help of thermal camera having emissivity default set to 0.95.



(a) Plate with thermocouples



(b) NI-DAQ

Figure A.6 Plate and DAQ used in thermal camera calibration

Further to compare the temperature readings captured by the thermal camera with that of thermocouple reading, nearest pixels to thermocouple's location on the plate are selected. Then, emissivity in the thermal camera is chosen such that the measured temperature from the thermocouple matches with the temperature indicated with the thermal camera for the chosen emissivity.

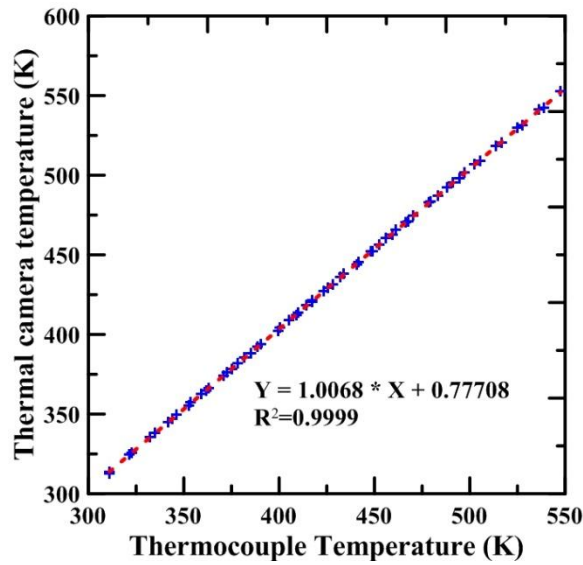


Figure A.7 Calibration chart for thermal IR camera

The emissivity of the applied paint is chosen as 0.98 and changed temperature values are plotted against thermocouple readings to generate calibration chart for camera (Figure A.7). Figure shows the calibration chart for thermal camera. Thus corrected temperature distribution of the plate can be obtained as Equation with maximum deviation of 1%.

$$T_{corrected} = 0.99324T_{thermal\ camera} - 0.77183$$

Appendix B

Uncertainty analysis

The uncertainties associated with the experimental settings and other derived quantities are estimated by the method suggested by Moffat (1986).

B.1 Uncertainties associated with the experimental settings

B.1.1 Mixture mass flow rate

The mixture mass flow rate (\dot{m}_{mix}) is given by

$$\dot{m}_{mix} = \dot{m}_{air} + \dot{m}_{fuel} \quad (\text{B.1})$$

The mass flow rate through the flowmeters is given

$$\dot{m} = C_d \frac{\pi d^2}{4} \sqrt{\frac{2 dp \rho}{1 - \beta^4}} \quad (\text{B.2})$$

and density is estimated as

$$\rho = \frac{p}{RT} \quad (\text{B.3})$$

diameter ratio is given by

$$\beta = \frac{d}{D} \quad (\text{B.4})$$

Uncertainty in each parameter is given by

	$\Delta d = 0.01 \text{ mm}; d = 0.5 \text{ mm}$	$\Delta D = 0.05 \text{ mm}; D = 3 \text{ mm}$
MOL	$\Delta p = 0.05 \text{ bar}; p = 2 \text{ bar}$	$\Delta p = 0.05 \text{ bar}; p = 2 \text{ bar}$
	$\Delta T = 1 \text{ K}; T = 300 \text{ K}$	$\Delta T = 1 \text{ K}; T = 300 \text{ K}$

MOH	$\Delta d = 0.01 \text{ mm}; d = 1 \text{ mm}$ $\Delta p = 0.05 \text{ bar}; p = 2 \text{ bar}$ $\Delta T = 1 \text{ K}; T = 300 \text{ K}$	$\Delta D = 0.05 \text{ mm}; D = 4 \text{ mm}$ $\Delta p = 0.05 \text{ bar}; p = 2 \text{ bar}$ $\Delta T = 1 \text{ K}; T = 300 \text{ K}$
AVL	$\Delta d = 0.01 \text{ mm}; d = 1.5 \text{ mm}$ $\Delta p = 0.05 \text{ bar}; p = 2 \text{ bar}$ $\Delta T = 1 \text{ K}; T = 300 \text{ K}$	$\Delta D = 0.05 \text{ mm}; D = 5 \text{ mm}$ $\Delta p = 0.05 \text{ bar}; p = 2 \text{ bar}$ $\Delta T = 1 \text{ K}; T = 300 \text{ K}$
AVH	$\Delta d = 0.05 \text{ mm}; d = 2.5 \text{ mm}$ $\Delta p = 0.05 \text{ bar}; p = 2 \text{ bar}$ $\Delta T = 1 \text{ K}; T = 300 \text{ K}$	$\Delta D = 0.05 \text{ mm}; D = 5 \text{ mm}$ $\Delta p = 0.05 \text{ bar}; p = 2 \text{ bar}$ $\Delta T = 1 \text{ K}; T = 300 \text{ K}$

Coefficient of discharge $\frac{\Delta C_d}{C_d} = 1.2\%$ (Standard Deviation)

Uncertainty in β is given by

$$\frac{\Delta\beta}{\beta} = \sqrt{\left(\frac{\Delta d}{d}\right)^2 + \left(\frac{\Delta D}{D}\right)^2}$$

$$MOL: \frac{\Delta\beta}{\beta} = \sqrt{\left(\frac{0.01}{0.5}\right)^2 + \left(\frac{0.05}{3}\right)^2} = 2.6\%$$

$$MOH: \frac{\Delta\beta}{\beta} = \sqrt{\left(\frac{0.01}{1}\right)^2 + \left(\frac{0.05}{4}\right)^2} = 1.6\%$$

$$AVL: \frac{\Delta\beta}{\beta} = \sqrt{\left(\frac{0.01}{1.5}\right)^2 + \left(\frac{0.05}{5}\right)^2} = 1.2\%$$

$$AVH: \frac{\Delta\beta}{\beta} = \sqrt{\left(\frac{0.05}{2.5}\right)^2 + \left(\frac{0.05}{5}\right)^2} = 2.24\%$$

Uncertainty in density (ρ) is given by

$$\frac{\Delta\rho}{\rho} = \sqrt{\left(\frac{\Delta p}{p}\right)^2 + \left(\frac{\Delta T}{T}\right)^2}$$

$$\text{Air: } \frac{\Delta\rho_{air}}{\rho_{air}} = \left(\sqrt{\left(\frac{0.05}{2}\right)^2 + \left(\frac{5}{300}\right)^2} \right) = 3\%$$

$$\text{Methane: } \frac{\Delta\rho_{CH_4}}{\rho_{CH_4}} = \left(\sqrt{\left(\frac{0.05}{2}\right)^2 + \left(\frac{5}{300}\right)^2} \right) = 3\%$$

The uncertainty in each mass flowmeter is given by

$$\frac{\Delta\dot{m}}{\dot{m}} = \sqrt{\left(\frac{\Delta Cd}{Cd}\right)^2 + 4\left(\frac{\Delta d}{d}\right)^2 + 0.25\left(\frac{\Delta dp}{dp}\right)^2 + 0.25\left(\frac{\Delta\rho}{\rho}\right)^2 + \left(\frac{2\beta^4}{1-\beta^4}\right)^2 (\Delta\beta)^2}$$

$$\frac{\Delta\dot{m}_{AVL}}{\dot{m}_{AVL}} = \sqrt{\left(0.012\right)^2 + 4\left(\frac{0.01}{1.5}\right)^2 + 0.25\left(\frac{0.05}{2}\right)^2 + 0.25(0.03)^2 + \left(\frac{2 \times (1.5/5)^4}{1 - (1.5/5)^4}\right)^2 (0.012 \times 1.5/5)^2} = 2.65\%$$

$$\frac{\Delta\dot{m}_{AVH}}{\dot{m}_{AVH}} = \sqrt{\left(0.012\right)^2 + 4\left(\frac{0.05}{2.5}\right)^2 + 0.25\left(\frac{0.05}{2}\right)^2 + 0.25(0.03)^2 + \left(\frac{2 \times (2.5/5)^4}{1 - (2.5/5)^4}\right)^2 (0.0224 \times 2.5/5)^2} = 4.76\%$$

$$\frac{\Delta\dot{m}_{MOL}}{\dot{m}_{MOL}} = \sqrt{\left(0.012\right)^2 + 4\left(\frac{0.01}{0.5}\right)^2 + 0.25\left(\frac{0.05}{2}\right)^2 + 0.25(0.03)^2 + \left(\frac{2 \times (0.5/3)^4}{1 - (0.5/3)^4}\right)^2 (0.026 \times 0.5/3)^2} = 4.61\%$$

$$\frac{\Delta\dot{m}_{MOH}}{\dot{m}_{MOH}} = \sqrt{\left(0.012\right)^2 + 4\left(\frac{0.01}{1}\right)^2 + 0.25\left(\frac{0.05}{2}\right)^2 + 0.25(0.03)^2 + \left(\frac{2 \times (1/4)^4}{1 - (1/4)^4}\right)^2 (0.016/4)^2} = 3.04\%$$

The uncertainty in mixture mass flow rates is given by

$$\frac{\Delta \dot{m}_{mix}}{\dot{m}_{mix}} = \sqrt{\left(\frac{\Delta \dot{m}_{fuel}}{\dot{m}_{fuel}}\right)^2 + \left(\frac{\Delta \dot{m}_{air}}{\dot{m}_{air}}\right)^2}$$

$$Low\ Range: \frac{\Delta \dot{m}_{mix}}{\dot{m}_{mix}} = \sqrt{(0.0461)^2 + (0.0265)^2} = 5.31\%$$

$$High\ range: \frac{\Delta \dot{m}_{mix}}{\dot{m}_{mix}} = \sqrt{(0.0304)^2 + (0.0476)^2} = 5.65\%$$

B.1.2 Mixture Reynolds number

The Reynolds number (Re) is given by

$$Re = \frac{\rho_{mix} \bar{u} d_{tube}}{\mu} \quad (B.05)$$

The average velocity (\bar{u}) of the mixture is given by

$$\bar{u} = \frac{\dot{m}_{mix}}{\rho_{mix} A} \quad (B.06)$$

Mixture density (ρ_{mix}) is given by

$$\rho_{mix} = \sum Y_I \rho_I = Y_{air} \frac{P_{air}}{R_{air} T_{air}} + Y_{CH_4} \frac{P_{CH_4}}{R_{CH_4} T_{CH_4}} \quad (B.07)$$

The uncertainty in the mixture density is given by

$$\Rightarrow \frac{\Delta \rho_{mix}}{\rho_{mix}} = \sqrt{\left(\frac{\Delta P_{air}}{P_{air}}\right)^2 + \left(\frac{\Delta T_{air}}{T_{air}}\right)^2 + \left(\frac{\Delta P_{CH_4}}{P_{CH_4}}\right)^2 + \left(\frac{\Delta T_{CH_4}}{T_{CH_4}}\right)^2}$$

Uncertainty in each parameter is given by

$$\Delta p_{air} = 0.05 \text{ bar}; p_{air} = 2 \text{ bar}$$

$$\Delta T_{air} = 1 \text{ K}; T_{air} = 300 \text{ K}$$

$$\Delta p_{CH_4} = 0.05 \text{ bar}; p_{CH_4} = 2 \text{ bar}$$

$$\Delta T_{CH_4} = 1 \text{ K}; T_{CH_4} = 300 \text{ K}$$

Uncertainty in the mixture density is estimated as

$$\frac{\Delta \rho_{mix}}{\rho_{mix}} = \left(\sqrt{2 \left(\frac{0.05}{2} \right)^2 + 2 \left(\frac{5}{300} \right)^2} \right) \times 100 = 4.25\%$$

Flow area is given by

$$A = \frac{\pi}{4} d^2 \quad (\text{B.08})$$

Uncertainty in each parameter is given by

$$\text{Tube Diameter } \Delta d_{tube} = 0.05 \text{ mm} \quad d_{min} = 10 \text{ mm}; d_{max} = 19 \text{ mm}$$

The uncertainty in flow area is given by

$$\text{Maximum: } \frac{\Delta A}{A} = \frac{2\Delta d}{d} = \frac{2 \times 0.05}{10} = 1\% \quad (\text{B.09})$$

$$\text{Minimum: } \frac{\Delta A}{A} = \frac{2\Delta d}{d} = \frac{2 \times 0.05}{19} = 0.53\%$$

The uncertainty (maximum) in average velocity of the mixture is given by

$$\frac{\Delta \bar{u}}{\bar{u}} = \sqrt{\left(\frac{\Delta \dot{m}_{mix}}{\dot{m}_{mix}} \right)^2 + \left(\frac{\Delta \rho}{\rho} \right)^2 + \left(\frac{\Delta A}{A} \right)^2}$$

$$\text{Low range: } \frac{\Delta \bar{u}}{\bar{u}} = \sqrt{(0.0531)^2 + (0.0425)^2 + (0.01)^2} = 6.87\%$$

$$\text{High range: } \frac{\Delta \bar{u}}{\bar{u}} = \sqrt{(0.0565)^2 + (0.0425)^2 + (0.01)^2} = 7.15\%$$

The uncertainty (Maximum) in Reynolds number is given by

$$\frac{\Delta Re}{Re} = \sqrt{\left(\frac{\Delta \bar{u}}{\bar{u}}\right)^2 + \left(\frac{\Delta \rho}{\rho}\right)^2 + \left(\frac{\Delta d}{d}\right)^2}$$

$$\text{Low range: } \frac{\Delta Re}{Re} = \sqrt{(0.0687)^2 + (0.0425)^2 + (0.005)^2} = 8.09\%$$

$$\text{High range: } \frac{\Delta Re}{Re} = \sqrt{(0.0715)^2 + (0.0425)^2 + (0.005)^2} = 8.34\%$$

B.1.3 Equivalence ratio

The air/fuel (A/F) ratio and equivalence ratio (ϕ) are given by

$$\frac{A}{F} = \frac{\dot{m}_{air}}{\dot{m}_{fuel}} \quad (\text{B.10})$$

$$\phi = \frac{(A/F)_{stoic}}{(A/F)_{act}} \quad (\text{B.11})$$

The uncertainty in air/fuel ratio is given by

$$\text{Low range: } \frac{\Delta(A/F)}{A/F} = \sqrt{(0.0265)^2 + (0.0461)^2} = 5.31\%$$

$$\text{High range: } \frac{\Delta(A/F)}{A/F} = \sqrt{(0.0476)^2 + (0.0304)^2} = 5.65\%$$

The uncertainty in equivalence ratio is given by

$$\frac{\Delta\phi}{\phi} = \sqrt{\left(\frac{\Delta(A/F)}{A/F}\right)^2}$$

$$\text{Low range: } \frac{\Delta\phi}{\phi} = \sqrt{(0.0523)^2} = 5.23\%$$

$$\text{High range: } \frac{\Delta\phi}{\phi} = \sqrt{(0.0565)^2} = 5.65\%$$

B.2 Uncertainties in the other derived quantities

B.2.1 Critical velocity gradient

The critical velocity gradient is given by

$$g_b = \frac{\delta \bar{u}}{d} \quad (\text{B.12})$$

The uncertainty in critical velocity gradient is given by

$$\frac{\Delta g_b}{g_b} = \sqrt{\left(\frac{\Delta \bar{u}}{\bar{u}}\right)^2 + \left(\frac{\Delta d}{d}\right)^2}$$

$$\text{Low range: } \frac{\Delta g_b}{g_b} = \sqrt{(0.0687)^2 + (0.005)^2} = 6.88\%$$

$$\text{High range: } \frac{\Delta g_b}{g_b} = \sqrt{(0.0715)^2 + (0.005)^2} = 7.16\%$$

B.2.2 Burning velocity

The burning velocity is given by

$$Su = \frac{r}{l} u_m \quad (\text{B.13})$$

The uncertainty in the burning velocity is given by

$$\frac{\Delta Su}{Su} = \sqrt{\left(\frac{\Delta \bar{u}}{u}\right)^2 + \left(\frac{\Delta r}{r}\right)^2 + \left(\frac{\Delta l}{l}\right)^2}$$

$$\text{Low range: } \frac{\Delta Su}{Su} = \sqrt{(0.0687)^2 + \left(\frac{0.0526}{5}\right)^2 + \left(\frac{0.0526}{32}\right)^2} = 6.95\%$$

$$\text{High range: } \frac{\Delta Su}{Su} = \sqrt{(0.0715)^2 + \left(\frac{0.0526}{5}\right)^2 + \left(\frac{0.0526}{32}\right)^2} = 7.23\%$$

B.2.3 Temperature at the impingement side

Temperature at the impingement side is estimated inversely from the non-impingement side measured temperatures. Iterative procedure as per equations 5.43 and 5.44 is used to obtain front side temperature. Assuming that the uncertainties in material thermal properties negligible, the uncertainty in the front temperature is given as below.

The thermal camera has an uncertainty of 2% in the measured temperature.

$$\text{Plate Thickness } \Delta l_z = 0.05 \text{ mm} \qquad l_{\min} = 1 \text{ mm}; l_{\max} = 3 \text{ mm}$$

$$\frac{\Delta T_{\text{front}}}{T_{\text{front}}} = \sqrt{\left(\frac{\Delta T_{\text{back}}}{T_{\text{back}}}\right)^2 + \left(\frac{\Delta \tau}{\tau}\right)^2}$$

$$\tau = \frac{l_z^2}{\alpha}$$

$$\text{Maximum: } \frac{\Delta \tau}{\tau} = \frac{2 \Delta l_z}{l_z} = \frac{2 \times 0.05}{1} = 10\%$$

$$\text{Minimum: } \frac{\Delta \tau}{\tau} = \frac{2 \Delta l_z}{l_z} = \frac{2 \times 0.05}{3} = 3.33\%$$

$$\text{Maximum: } \frac{\Delta T_{\text{front}}}{T_{\text{front}}} = \sqrt{(0.02)^2 + (0.1)^2} = 10.19\%$$

$$\text{Minimum: } \frac{\Delta T_{\text{front}}}{T_{\text{front}}} = \sqrt{(0.02)^2 + (0.0333)^2} = 3.88\%$$

B.2.4 Heat flux at the impingement side

The wall heat flux at any time t is obtained by Equation (B.14).

$$q(z, t) = -k \left(\frac{\partial T(z, t)}{\partial z} \right)_{z=H} \quad (\text{B.14})$$

$$\text{Maximum: } \frac{\Delta q}{q} = \frac{\Delta T_{front}}{T_{front}} = 10.19\%$$

$$\text{Minimum: } \frac{\Delta q}{q} = \frac{\Delta T_{front}}{T_{front}} = 3.88\%$$

B.2.5 Heat transfer coefficient and Reference Temperature

The heat transfer coefficient and the reference temperatures are estimated simultaneously by curve fitting the transient heat flux data against the corresponding impingement side wall temperature. Thus, uncertainty in heat transfer coefficient and reference temperature is corresponds to uncertainty of slope and intercept of linear fit respectively.

$$\text{Uncertainty in Slope} = \frac{\text{max slope} - \text{min slope}}{2}$$

$$\text{Uncertainty in Intercept} = \frac{\text{max intercept} - \text{min intercept}}{2}$$

$$\text{Maximum: } \frac{\Delta h}{h} = \frac{\Delta \text{slope}}{\text{slope}} = 12.29\%$$

$$\text{Minimum: } \frac{\Delta h}{h} = \frac{\Delta \text{slope}}{\text{slope}} = 5.78\%$$

$$\text{Maximum: } \frac{\Delta T_{ref}}{T_{ref}} = \frac{\Delta \text{Intercept}}{\text{Intercept}} = 2\%$$

$$\text{Minimum: } \frac{\Delta T_{ref}}{T_{ref}} = \frac{\Delta \text{Intercept}}{\text{Intercept}} = 2\%$$

Appendix C

C.1 Weights for seven point quartic fit Savitzky-Golay method

Savitzky-Golay method using seven points fitted with fourth order polynomial is used for smoothing and differentiation the data. This method uses least-square fit of a point and three points on either side of it with a chosen order of polynomial. This methods amounts to a low pass filter. Thus chosen order of polynomial affects the filter. Table C.1 and C.2 gives convolution weights for seven point quartic fit smoothing and first order derivative respectively.

Table C.1 Convolution weights for seven point quartic fit smoothing

i	-3	-2	-1	0	1	2	3
-3	456	25	-35	5	20	-19	5
-2	25	356	155	-30	-65	70	-19
-1	-35	155	212	75	25	-65	20
0	10	-60	150	131	150	-60	10
1	20	-65	25	75	212	155	-35
2	-19	70	-65	-30	155	356	25
3	5	-19	20	5	-35	25	456
Norm	462	462	462	231	462	462	462

Table C.2 Convolution weights for first order derivative

i	-3	-2	-1	0	1	2	3
-3	-4420	-104	158	22	136	20	-746
-2	5059	-25	-1619	-67	-607	-59	2357
-1	1504	68	-50	-58	764	16	-1378
0	-2394	84	1218	0	1218	84	-2394
1	-1378	16	764	58	-50	68	1504
2	2357	-59	-607	67	-1619	-25	5059
3	-746	20	136	-22	158	-104	-4420
Norm	2772	252	2772	252	2772	252	2772

C.2 Real time temperature data before and after noise correction

Temperature data measured by using thermal imaging camera at the non-impingement side is smoothed by Savitzky-Golay method using seven points fitted with fourth order polynomial. Figure before noise correction and after noise correction is added in Appendix of revised thesis as follows:

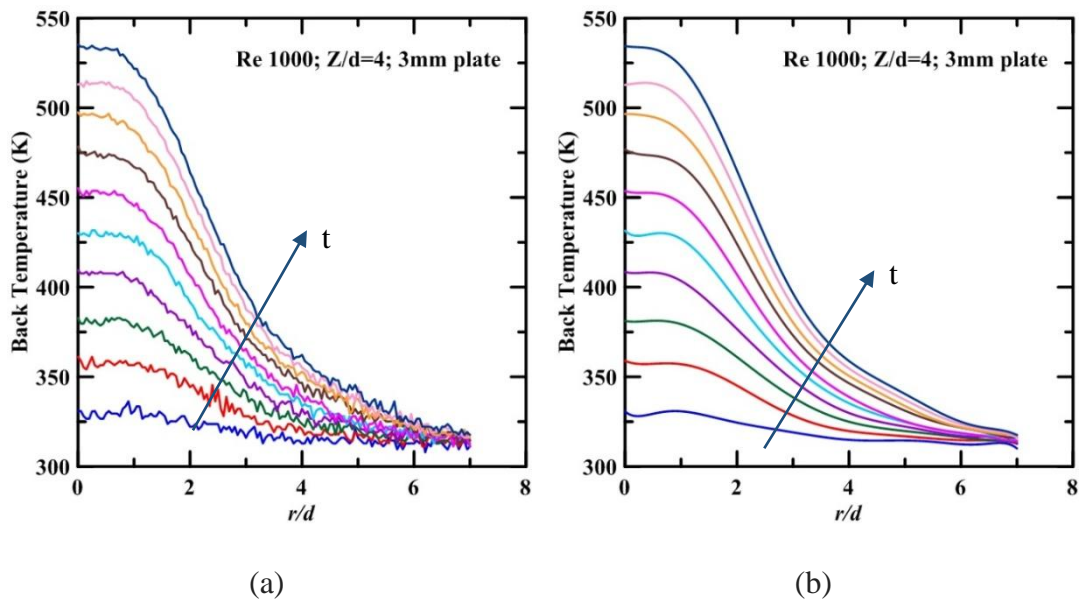


Figure C.1 a) Raw measured back surface temperature data b) Noise corrected back surface temperature data

REFERENCES

- Agrawal, G. K., Suman Chakraborty, and S. K. Som. (2010). "Heat Transfer Characteristics of Premixed Flame Impinging Upwards to Plane Surfaces Inclined with the Flame Jet Axis." *Int. J. Heat Mass Transfer*, 53(9-10), 1899–1907.
- Baukal Jr, and C. E. (2000). "Heat transfer in industrial combustion." *CRC press., N.W. Corporate Blvd., Boca Raton*. ISBN 0-8493-1699-5.
- Baukal, C. E., and Gebhart, B. (1997). "Surface condition effects on flame impingement heat transfer." *Expt. Therm. Fluid Science*, 15(97), 323–335.
- Baukal, C. E., and Gebhart, B. (1996). "A review of semi-analytical solutions for flame impingement heat transfer." *Int. J. Heat Mass Transfer*, 39(14), 2989-3002.
- Caliskan, S. (2013). "Flow and heat transfer characteristics of transverse perforated ribs under impingement jets." *Int. J. Heat Mass Transfer*, 66, 244-260.
- Caliskan, S., Baskaya, S., and Calisir, T. (2014). "Experimental and numerical investigation of geometry effects on multiple impinging air jets." *Int. J. Heat Mass Transfer*, 75, 685-703.
- Chander, S., and Ray, A. (2006). "Influence of burner geometry on heat transfer characteristics of methane/air flame impinging on flat surface." *Expt. Heat Transfer*, 19(1), 15-38.
- Chander, S., and Ray, A. (2007). "Heat transfer characteristics of laminar methane/air flame impinging normal to a cylindrical surface." *Expt Thermal Fluid Sci*, 32(2), 707-721.
- Chander, S., and Ray, A. (2007). "Heat transfer characteristics of three interacting methane/air flame jets impinging on a flat surface." *Int. J. Heat Mass Transfer*, 50(3-4), 640-653.

Chander, Subhash, and Anjan Ray (2008). “An Experimental and Numerical Study of Stagnation Point Heat Transfer for Methane/air Laminar Flame Impinging on a Flat Surface.” *Int. J. Heat Mass Transfer*, 51, 3595–3607.

Chander, Subhash, and Anjan Ray (2011). “Experimental and Numerical Study on the Occurrence of off-Stagnation Peak in Heat Flux for Laminar Methane/air Flame Impinging on a Flat Surface.” *Int. J. Heat Mass Transfer*, 54(5-6), 1179–86.

Chander, Subhash, and Anjan Ray. (2005). “Flame Impingement Heat Transfer: A Review.” *Energy Convers. Mgmt.*, 46, 2803–37.

Chen, Jing-Wei, Chih-Pin Chiu, Shang-Hsuan Mo, and Jing-Tang Yang. (2015). “Combustion Characteristics of Premixed Propane Flame with Added H₂ and CO on a V-Shaped Impinging Burner.” *Int. J. of Hydrogen Energy*, 40(2), 1244–55.

Chen, Y. C., C. F. Ma, M. Qin, and Y. X. Li. (2005). “Theoretical Study on Impingement Heat Transfer with Single-Phase Free-Surface Slot Jets.” *Int. J. Heat Mass Transfer*, 48, 3381–86.

Conolly, R., and Davies, R. M. (1972). “A study of convective heat transfer from flames.” *Int. J. Heat Mass Transfer*, 15(11), 2155-2172.

Cremers, M. F G, M. J. Remie, K. R M Schreel, and L. P H de Goey. (2010). “Thermochemical Heat Release of Laminar Stagnation Flames of Fuel and Oxygen.” *Int. J. Heat Mass Transfer*, 53(5-6), 952–61.

Cui, M., Yang, K., Liu, Y. F., & Gao, X. W. (2012). “Inverse estimation of transient heat flux to slab surface.” *J. of Iron Steel Research Int.*, 19(11), 13-18.

D’Aleo Francesco Paolo and Prasser Horst-Michael (2013), “Transient heat flux deduction for a slab of finite thickness using surface temperature measurements”, *Int. J. Heat Mass Transfer*, 60, 616-623.

Dong, L. L., C. S. Cheung, and C. W. Leung (2013). “Heat Transfer Optimization of an Impinging Port-Array Inverse Diffusion Flame Jet.” *Energy* 49, 182–92.

- Dong, L. L., C. S. Cheung, and C. W. Leung. (2007). "Heat Transfer Characteristics of an Impinging Inverse Diffusion Flame Jet. Part II: Impinging Flame Structure and Impingement Heat Transfer." *Int. J. Heat Mass Transfer*, 50, 5124–38.
- Dong, L. L., C. S. Cheung, and C. W. Leung. (2013). "Characterization of Impingement Region from an Impinging Inverse Diffusion Flame Jet." *Int. J. Heat Mass Transfer*, 56(1-2), 360–69.
- Dong, L. L., C. W. Leung, and C. S. Cheung. (2002). "Heat Transfer Characteristics of Premixed Butane/air Flame Jet Impinging on an Inclined Flat Surface." *Heat Mass Transfer*, 45, 979–992.
- Dong, L. L., Leung, C. W., and Cheung, C. S. (2004). "Heat transfer and wall pressure characteristics of a twin premixed butane/air flame jets." *Int. J. Heat Mass Transfer*, 47, 489–500.
- Dou, R., Wen, Z., and Zhou, G. (2016). "2D axisymmetric transient inverse heat conduction analysis of air jet impinging on stainless steel plate with finite thickness." *App. Therm. Eng.*, 93, 468-475.
- Duda, P. (2015). "Solution of an inverse axisymmetric heat conduction problem in complicated geometry." *Int. J. Heat Mass Transfer*, 82, 419-428.
- Feng Z C, Chen J K, Zhang Yuwen and Griggs James L (2011), "Estimation of front surface temperature and heat flux of a locally heated plate from distributed sensor data on the back surface", *Int. J. Heat Mass Transfer*, 54, 3431-3439.
- Feng, Z. C., Chen, J. K., Zhang, Y., and Montgomery-Smith, S. (2010). "Temperature and heat flux estimation from sampled transient sensor measurements." *Int. J. of Therm. Sci.*, 49(12), 2385-2390.
- Feng, Z.C., Chen, J.K. and Zhang, Y., (2010). "Real-time solution of heat conduction in a finite slab for inverse analysis." *Int. J. of Ther. Sci.*, 49(5), 762–768.

Fénot Matthieu, Vullierme Jean-Jacques and Dorignac Eva, (2005), “A heat transfer measurement of jet impingement with high injection temperature”, *Mécanique C R*, 333, 778–82.

Gau, C., and Lee, C. C. (1992). “Impingement cooling flow structure and heat transfer along rib-roughened walls.” *Int. J. Heat Mass Transfer*, 35(11), 3009-3020.

Gau, C., and I.C. Lee. (2000). “Flow and Impingement Cooling Heat Transfer along Triangular Rib-Roughened Walls.” *Int. J. Heat Mass Transfer* 43(24): 4405–18.

Guo, Q., Wen, Z., and Dou, R. (2017). “Experimental and numerical study on the transient heat-transfer characteristics of circular air-jet impingement on a flat plate.” *Int. J. Heat Mass Transfer*, 104, 1177-1188.

Haghighi, M. G., Eghtesad, M., Malekzadeh, P., and Neculescu, D. S. (2009). “Three-dimensional inverse transient heat transfer analysis of thick functionally graded plates.” *Energy conv. mgmt.*, 50(3), 450-457.

Hao, D. N., Thanh, P. X., and Lesnic, D. (2013). “Determination of the heat transfer coefficients in transient heat conduction.” *Inverse Problems*, 29(9), 095020.

Hindasageri V., Vedula R. P., and Prabhu S. V. (2014), “Heat transfer distribution for impinging methane–air premixed flame jets”, *App. Therm. Eng.*, 73(1), 459–471.

Hindasageri, V., Kuntikana, P., Tajik, A. R., Vedula, R. P., and Prabhu, S. V. (2016). “Axis .switching in impinging premixed methane-air flame jets.” *App. Therm. Engg.*, 107, 144-153.

Hindasageri, V., Vedula, R. P., and Prabhu, S. V. (2013). “Thermocouple error correction for measuring the flame temperature with determination of emissivity and heat transfer coefficient.” *Review of Sci. Instr.*, 84(2), 24902.

Hindasageri, V., Vedula, R. P., and Prabhu, S. V. (2015). “Heat transfer distribution for three interacting methane–air premixed impinging flame jets.” *Int. J. Heat Mass Transfer*, 88, 914-925.

- Hindasageri, Vijaykumar, Rajendra P Vedula, and Siddini V Prabhu. (2014a). "A Novel Method of Estimation of Adiabatic Wall Temperature for Impinging Premixed Flame Jets." *Int. J. Heat Mass Transfer* 77, 185–93.
- Hindasageri, Vijaykumar, Rajendra P. Vedula, and Siddini V. Prabhu. (2014b). "A Novel Concept to Estimate the Steady State Heat Flux from Impinging Premixed Flame Jets in an Enclosure by Numerical IHCP Technique." *Int. J. Heat Mass Transfer*, 79, 342–52.
- Horsely, M. E., Purvis, M. R. I., and Tariq, A. S. (1982). "Convective heat transfer from laminar and turbulent premixed flames." *IN: Heat transfer 1982; Proceedings of the Seventh International Conference, Munich, West Germany, Vol. 3*, 409-415.
- Hou, Shuhn Shyurng, and Yung Chang Ko. (2005). "Influence of Oblique Angle and Heating Height on Flame Structure, Temperature Field and Efficiency of an Impinging Laminar Jet Flame." *Energy Convers. Manage.*, 46, 941–58.
- Huang, X Q, C W Leung Ceng, Fhkie Fimeche, and C K Chan. (2013). "Heat Transfer of Premixed Butane / Air Impinging Circular Flame Jet with Induced Swirl." *Appl. Energy* 37–41.
- Huang, X. Q., Leung, C. W., Chan, C. K., and Probert, S. D. (2006). "Thermal characteristics of a premixed impinging circular laminar-flame jet with induced swirl." *Appl. energy*, 83(4), 401-411.
- Jambunathan, K., Lai, E., Moss, M. A., and Button, B. L. (1992). "A review of heat transfer data for single circular jet impingement." *Int. J. of heat fluid flow*, 13(2), 106-115.
- Jaremiewicz, M. (2018). "Identification of three-dimensional transient temperature fields in thick-walled elements using the inverse method." *Int J. of Numerical Methods Heat Fluid Flow*, 28(1), 138-150.
- Jarray, M., Chetehouna, K., Gascoïn, N., and Bey, F. (2016). "Ceramic panel heating under impinging methane-air premixed flame jets." *Int. J. of Therm. Sci.*, 107, 184–195.

Katti Vadiraj V., Nagesh Yayaswy S. and Prabhu S. V. (2011), “Local heat transfer distribution between smooth flat surface and impinging air jet from a circular nozzle at low Reynolds numbers”, *Heat Mass Transfer*, 47, 237-244.

Katti, Vadiraj, and S. V. Prabhu. (2008). “Heat Transfer Enhancement on a Flat Surface with Axisymmetric Detached Ribs by Normal Impingement of Circular Air Jet.” *Int. J. of Heat and Fluid Flow*, 29(5), 1279–94.

Kito, M., Takezaki, M., Shakouchi, T., Tsujimoto, K., and Ando, T. (2012). “Enhancement of impingement heat transfer on a flat plate with ribs.” *World Academy of Science, Engineering and Technology*, 6, 1367-1373.

Kuntikana P., and Prabhu S.V. (2016), “Isothermal air jet and premixed flame jet impingement: Heat transfer characterization and comparison”, *Int. J. of Therm. Sci.*, 100, 401-415.

Kwok, L. C. (2003). “Heat transfer characteristics of slot and round premixed impinging flame jets.” *Expt. Heat Transfer*, 16(2), 111-137.

Kwok, L. C., C. W. Leung, and C. S. Cheung. (2005). “Heat Transfer Characteristics of an Array of Impinging Pre-Mixed Slot Flame Jets.” *Int. J. Heat Mass Transfer*, 48, 1727–38.

Labbé, O. (2013). “Large-eddy-simulation of flow and heat transfer in a ribbed duct.” *Computers Fluids*, 76, 23-32.

Li, H. B., H. S. Zhen, C. W. Leung, and C. S. Cheung (2011). “Nozzle Effect on Heat Transfer and CO Emission of Impinging Premixed Flames.” *Int. J. Heat Mass Transfer*, 54, 625–35.

Li, H. B., H. S. Zhen, C. W. Leung, and C. S. Cheung. (2010). “Effects of Plate Temperature on Heat Transfer and Emissions of Impinging Flames.” *Int. J. Heat Mass Transfer*, 53, 4176–84.

- Lin, H. C., Cheng, T. S., Chen, B. C., Ho, C. C., and Chao, Y. C. (2009). "A comprehensive study of two interactive parallel premixed methane flames on lean combustion." *Proceedings of the Combustion Institute*, 32(1), 995-1002.
- Loubat, R., Reulet, P., Estebe, B., & Millan, P. (2004). "Heat flux characterisation in hot jet and flame/wall interaction by IHCP resolution coupled with infrared measurements." *Quantitative InfraRed Thermography J.*, 1(2), 205-228.
- Lu, S., Heng, Y., and Mhamdi, A. (2012). "A robust and fast algorithm for three-dimensional transient inverse heat conduction problems." *Int. J. Heat Mass Transfer*, 55(25-26), 7865-7872.
- Lu, T., and Law, C. K. (2008). "A criterion based on computational singular perturbation for the identification of quasi steady state species: A reduced mechanism for methane oxidation with NO chemistry." *Combustion Flame*, 154(4), 761-774.
- Luo, D. D., H. S. Zhen, C. W. Leung, and C. S. Cheung. (2010). "Premixed Flame Impingement Heat Transfer with Induced Swirl." *Int. J. Heat Mass Transfer* 53(19-20): 4333-36.
- Mackowski, D. W. (2011). "Conduction Heat Transfer: Notes for MECH 7210." Mechanical Engineering Department, Auburn University.
- Makmool, U., S. Jugjai, and S. Tia. (2013). "Structures and Performances of Laminar Impinging Multiple Premixed LPG-Air Flames." *Fuel* 112, 254-62.
- Martinez, D. M., Jiang, X., Moulinec, C., and Emerson, D. R. (2013). "Numerical investigation of the effects of fuel variability on the dynamics of syngas impinging jet flames." *Fuel*, 103, 646-662.
- Fénot, M., Vullierme, J. J., & Dorignac, E. (2005). "A heat transfer measurement of jet impingement with high injection temperature." *Comptes Rendus Mécanique*, 333(10), 778-782.

- McDaid, Chloe, Jie Zhou, and Yang Zhang. (2013). "Experimental Observations of Complex Flame Propagations Initiated at Different Locations of an Impingement Configuration." *Fuel* 103, 783–91.
- Miyake, G., Hirata, M., and Kasagi, N. (1994). "Heat transfer characteristics of an axisymmetric jet impinging on a wall with concentric roughness elements." *Expt. Heat Transfer*, 7(2), 121-141.
- Moffat, R.J. (1988), "Describing the uncertainties in experimental results", *Expt Therm Fluid Sci.*, 1, 3-17.
- Najafian Ashrafi, Z., and M. Ashjaee. (2015). "Temperature Field Measurement of an Array of Laminar Premixed Slot Flame Jets Using Mach-Zehnder Interferometry." *Optics Lasers Engg.*, 68, 194–202.
- Narayanan, Vinod, and Vishal a. Patil. (2007). "Oscillatory Thermal Structures Induced by Unconfined Slot Jet Impingement." *Expt. Therm. Fluid Sci.* 32, 682–95.
- Ng, T. K., Leung, C. W., and Cheung, C. S. (2007). "Experimental investigation on the heat transfer of an impinging inverse diffusion flame." *Int. J. Heat Mass Transfer*, 50(17-18), 3366-3375.
- Nortershauser, D., and Millan, P. (2000). "Resolution of a three-dimensional unsteady inverse problem by sequential method using parameter reduction and infrared thermography measurements." *Numerical Heat Transfer; Part A: Applications*, 37(6), 587–611.
- Nuntadusit, C., M. Wae-hayee, a. Bunyajitradulya, and S. Eiamsa-ard. (2012). "Thermal Visualization on Surface with Transverse Perforated Ribs." *Int. Comm. Heat Mass Transfer* 39(5), 634–39.
- O'Donovan, T. S. (2005). "Fluid flow and heat transfer of an impinging air jet." Department of Mechanical and Manufacturing Engineering. PhD Dublin: Trinity College Dublin, 145.

Ozisik M. N. (2012), "Heat Conduction", third edition, Mcgraw Hill publication.

Qi, J. A., Leung, C. W., Wong, W. O., and Probert, S. D. (2006). "Temperature-field measurements of a premixed butane/air circular impinging-flame using reference-beam interferometry." *Applied energy*, 83(12), 1307-1316.

Qi, J. A., Wong, W. O., Leung, C. W., and Yuen, D. W. (2008). "Temperature field measurement of a premixed butane/air slot laminar flame jet with Mach-Zehnder Interferometry." *Appl. Therm. Engg.*, 28(14-15), 1806-1812.

Remie, M. J., Cremers, M. F. G., Schreel, K. R. A. M., and De Goey, L. P. H. (2007). "Analysis of the heat transfer of an impinging laminar flame jet." *Int. J. Heat Mass Transfer*, 50(13-14), 2816-2827.

Remie, M. J., Särner, G., Cremers, M. F. G., Omrane, A., Schreel, K. R. A. M., Aldén, L. E. M., and De Goey, L. P. H. (2008). "Heat-transfer distribution for an impinging laminar flame jet to a flat plate. *Int. J. Heat Mass Transfer*," 51(11-12), 3144-3152.

Rosner, D. E. (1961). "Convective heat transfer with chemical reaction." *Aeron. Res. Lab. Rept.* ARL, 99.

Ryfa A and Bialecki R (2011), "Retrieving the heat transfer coefficient for jet impingement from transient temperature measurements" *Int. J. Heat Fluid Flow*, 32, 1024–1035.

Ryfa, A. and Bialecki, R.A. (2011), "The heat transfer coefficient spatial distribution reconstruction by an inverse technique" *Inv. Prob. Sci Engg*, 19 (1), 117–126.

Shariatmadar, Hamed, Amin Momeni, Amir Karimi, and Mehdi Ashjaee. (2015). "Heat Transfer Characteristics of Laminar Slot Jet Arrays Impinging on a Constant Target Surface Temperature." *Appl. Therm. Engg.* 76, 252–60.

Sibulkin, M. (1952). "Heat transfer near the forward stagnation point of a body of revolution." *J. Aero. Sci.*, 19(8), 570-571.

Singh, G., Chander, S., and Ray, A. (2012). "Heat transfer characteristics of natural gas/air swirling flame impinging on a flat surface." *Expt. Therm. Fluid Sci.*, 41, 165-176.

Singh, S., and Chander, S. (2015). "Heat transfer characteristics of dual swirling flame impinging on a flat surface". *Int. J. Therm. Sci.*, 89, 1-12.

Singh, Satpal, and Subhash Chander. (2014). "Heat Transfer Characteristics of Dual Flame with Outer Swirling and Inner Non-Swirling Flame Impinging on a Flat Surface." *Int. J. Heat Mass Transfer* 77, 995–1007.

Som, S. K., Agrawal, G. K., and Chakraborty, S. (2007). "Thermodynamics of flame impingement heat transfer." *J. Applied Physics*, 102(4), 043506.

Son, C., Dailey, G., Ireland, P., and Gillespie, D. (2005). "An investigation of the application of roughness elements to enhance heat transfer in an impingement cooling system." *In ASME Turbo Expo 2005: Power for Land, Sea, and Air*, American Society of Mechanical Engineers, 465-479.

Son, C., Ireland, P., and Gillespie, D. (2005). "The effect of roughness element fillet radii on the heat transfer enhancement in an impingement cooling system." *In ASME Turbo Expo 2005: Power for Land, Sea, and Air*, American Society of Mechanical Engineers, 263-273.

Tajik, A. R., Kuntikana, P., Prabhu, S. V., & Hindasageri, V. (2015). "Effect of preheated mixture on heat transfer characteristics of impinging methane–air premixed flame jet." *Int. J. Heat Mass Transfer*, 86, 550-562.

Tuttle, S. G., B. W. Webb, and M. Q. McQuay. (2005). "Convective Heat Transfer from a Partially Premixed Impinging Flame Jet. Part II: Time-Resolved Results." *Int. J. Heat Mass Transfer* 48, 1252–66.

Van der Meer, T. H. (1987) "Heat transfer from impinging flame jets". Ph.D. Thesis Technische Hogeschool, Delft (Netherlands)

Van der Meer, T.H. (1991). "Stagnation Point Heat Transfer from Turbulent Low Reynolds Number Jets and Flame Jets." *Expt. Thermal Fluid Sci.*, 4, 115–26.

- Viskanta, R. (1993). "Heat Transfer to Impinging Isothermal Gas and Flame Jets." *Expt. Therm. Fluid. Sci.*, 6, 111–34.
- Wang, Lei, Bengt Sundén, Andreas Borg, and Hans Abrahamsson. (2011). "Control of Jet Impingement Heat Transfer in Crossflow by Using a Rib." *Int. J. Heat Mass Transfer*, 54(19-20), 4157–66.
- Wang, Qian, C.Y. Zhao, and Yang Zhang. (2015). "Time-Resolved 3D Investigation of the Ignition Process of a Methane Diffusion Impinging Flame." *Expt. Thermal Fluid Sci.* 62, 78–84.
- Wikström P, Blasiak W and Berntsson F. (2007), "Estimation of the transient surface temperature and heat flux of a steel slab using an inverse method", *Appl Therm. Eng.*, 27, 2463-2472.
- Zhao, Z., D. W. Yuen, C. W. Leung, and T. T. Wong. (2009). "Thermal Performance of a Premixed Impinging Circular Flame Jet Array with Induced-Swirl." *Appl. Therm. Engg.*, 29(1), 159–166.
- Zhao, Z., T. T. Wong, and C. W. Leung. (2008). "Influences of Material Properties on Thermal Design of Impinging Flame Jets." *Materials Design*, 29, 28–33.
- Zhen, H. S., C. W. Leung, and C. S. Cheung. (2009). "Heat Transfer from a Turbulent Swirling Inverse Diffusion Flame to a Flat Surface." *Int. J. Heat Mass Transfer*, 52(11-12), 2740–48.
- Zhen, H. S., C. W. Leung, and C. S. Cheung. (2012). "Heat Transfer Characteristics of an Impinging Premixed Annular Flame Jet." *Appl. Therm. Engg.*, 36: 386–92.
- Zhen, H. S., Leung, C. W., and Cheung, C. S. (2011). "Emission of impinging swirling and non-swirling inverse diffusion flames." *Applied energy*, 88(5), 1629-1634.
- Zhen, H.S., C.S. Cheung, C.W. Leung, and Y.S. Choy. (2012). "A Comparison of the Emission and Impingement Heat Transfer of LPG–H₂ and CH₄–H₂ Premixed Flames." *Int. J. of Hydro. Energy*, 37(14), 10947–55.

Zografos, A. I., Martin, W. A., & Sunderland, J. E. (1987). "Equations of properties as a function of temperature for seven fluids." *Comp. Methods Appl. Mech. Engineering*, 61(2), 177-187.

Zuckerman N. and Lior N. (2006), "Jet impingement heat transfer: physics, correlations, and numerical modeling", *Adv. Heat Transfer*, 39, 565–631.

<http://www.engr.uconn.edu/~tlu/mechs/mechs.htm>, Mechanism reduction

List of Publications based on PhD Research Work					
Sl. No	Title of the Paper	Authors	Name of the journal/Conferences/Symposium, Vol., No., Pages	Month & Year of publication	Category*
1	Heat transfer distribution of impinging flame and air jets – A comparative study	Anil R. Kadam, Abdul Raouf Tajik, Vijaykumar Hindasageri	Applied Thermal Engineering, 92, 42–49	October, 2015	1
2	Simultaneous estimation of heat transfer coefficient and reference temperature from impinging flame jets	Anil R. Kadam, Siddini V. Prabhu, Vijaykumar Hindasageri	International Journal of Thermal Sciences 131, 48–57	May, 2018	1
3	Transient heat transfer characterization of impinging hot/cold jets by analytical IHCP	Anil R. Kadam, Vijaykumar Hindasageri, Kumar G N	IOP Conference Series: Materials Science and Engineering, 376, 012027 (IConMMEE 2018)	June, 2018	3
4	Estimation of Heat Transfer Coefficient and Reference Temperature in Jet Impingement Using Solution to Inverse Heat Conduction Problem Impingement Holes	Anil R. Kadam, Kumar G N, Vijaykumar Hindasageri	D. Srinivasacharya and K. S. Reddy (eds.), Numerical Heat Transfer and Fluid Flow, Lecture Notes in Mechanical Engineering, 31-37	December, 2018	3
5	Application of Green's Function to Establish a Technique in Predicting Jet Impingement Convective Heat Transfer Rate from Transient Temperature Measurements	Ritesh Kumar Parida, Anil R. Kadam, Vijaykumar Hindasageri and M. Vasudeva	D. Srinivasacharya and K. S. Reddy (eds.), Numerical Heat Transfer and Fluid Flow, Lecture Notes in Mechanical Engineering, 385-391	December, 2018	3
6	Experimental study on effect of pressure on volumetric gas flow rate through a variable area flow meter (Rotameter)	Ritesh Kumar Parida, Anil R. Kadam, Chetan Kumar, Vasudeva. M, Kumar G. N. & Vijaykumar H	International Journal of Mechanical and Production Engineering Research and Development, Vol. 8, Special Issue 7, 1299-1308	October, 2018	3

Category:

1: Journal paper, full paper reviewed

2: Journal paper, Abstract reviewed

3: Conference/Symposium paper, full paper reviewed

4: Conference/Symposium paper, abstract reviewed

5: others (including papers in Workshops, NITK Research Bulletins, Short notes etc.)

(If the paper has been accepted for publication but yet to be published, the supporting documents must be attached.)

Research Scholar
Name & Signature, with Date

Research Guide
Name & Signature, with Date

BIODATA

NAME: KADAM ANIL RAMKISHANRAO

DATE OF BIRTH: 14-08-1984

Mobile No.: +91 8805009978

Email: Kadam.aanil@gmail.com



ADDRESS:

Sr. No-29/1/3/1, flat No. 705, B-4 wing, Anita Residency, Katraj, Pune, INDIA-411046

QUALIFICATION:

Examination	Board/Institute	Year	Percentage/ CGPA
Ph. D (course work)	NITK, Surathkal	2015	9.33
M.Tech (Thermal Engg.)	NITK, Surathkal	2007-09	8.28
B.E. (Mechanical Engg)	JNEC , Aurangabad	2002-06	73.37%

EXPERIENCE:

Sr. no	Name of the college/Institute	Designation	From	To
1.	Parvatibai Genba Moze College of Engg., Wagholi, Pune	Lecturer	10 th August, 2009	25 th July, 2010
2.	Sinhgad College of Engineering, Vadgaon (BK), Pune	Assistant Professor	26 th July, 2010	9 th October, 2012
3.	Flora Institute of Technology, Khopi, Pune	Assistant Professor	10 th October, 2012	31 st December, 2014

ACHIEVEMENTS:

1. 93.24 Percentile in Mechanical Engineering GATE -2007
2. National Scholarship Holder for 10th and 12th standard
3. Maharashtra govt. scholarship for 4th standard